Micro- and Nano- Porous Adsorptive Materials for Removal of Contaminants from Water at Point-of-Use

Ismaiel Yakub

A DISSERTATION

PRESENTED TO THE FACULTY

OF PRINCETON UNIVERSITY

IN CANDIDACY FOR THE DEGREE OF

DOCTOR OF PHILOSOPHY

RECOMMENDED FOR ACCEPTANCE

BY THE DEPARTMENT OF

MECHANICAL AND AEROSPACE ENGINEERING

ADVISER: WINSTON SOBOYEJO

JUNE 2012

© Copyright by Ismaiel Yakub, 2012.

All rights reserved.

Dedication

To my mother, Mrs. Aminat Negi Yakub (néé Musa Ibrahim),

-the molder.

**

And, to my siblings: Mr. Abdul-Kareem, Mrs. Millicent, Mr. Abdul-Azeez, Mrs. Memunatu, Mrs. Fatimatu and Mrs. Idowu,

-the shoulder.

Abstract

Water is food, a basic human need and a fundamental human right, yet hundreds of millions of people around the world do not have access to clean drinking water. As a result, about 5000 people die each day from preventable water borne diseases. This dissertation presents the results of experimental and theoretical studies on three different types of porous materials that were developed for the removal of contaminants from water at point of use (household level).

First, three compositionally distinct porous ceramic water filters (CWFs) were made from a mixture of redart clay and sieved woodchips and processed into frustum shape. The filters were tested for their flow characteristics and bacteria filtration efficiencies. Since, the CWFs are made from brittle materials, and may fail during processing, transportation and usage, the mechanical and physical properties of the porous clays were characterized, and used in modeling designed to provide new insights for the design of filter geometries. The mechanical/physical properties that were characterized include: compressive strength, flexural strength, facture toughness and resistance curve behavior, keeping in mind the anisotropic nature of the filter structure. The measured flow characteristics and mechanical/physical properties were then related to the underlying porosity and characteristic pore size.

In an effort to quantify the adhesive interactions associated with filtration phenomena, atomic force microscopy (AFM) was used to measure the adhesion between bi-material pairs that are relevant to point-of-use ceramic water filters. The force microscopy measurements of pull-off force and adhesion energy were used to rank the adhesive interactions. Similarly, the adsorption of fluoride to hydroxyapatite-doped redart clay was studied using composites of redart clay and hydroxyapatite (C-HA). The removal of fluoride from water was explored by carrying out adsorption experiments on C-HA adsorbents with different ratios of clay to hydroxyapatite (and

sintered at different temperatures). The overall adsorption was controlled using water with varying fluoride concentrations and adsorbent-adsorbate contact times. Prototype frustum-shaped C-HA filters were then fabricated and shown to remove both fluoride and *E.coli* bacteria from water.

Finally, “buckyweb”, which is a foam comprising carbon nanotubes and graphene was made via thermal ablation of graphite, and tested for its deflouridation capacity. Defluoridation was studied in terms of concentration of fluoride, contact time and pH. The structure and adsorption characteristics of buckyweb foams were elucidated via energy dispersive x-ray spectroscopy, transmission electron microscopy and scanning transmission electron microscopy. The implications of the results were then explored for potential applications in water filtration.

Acknowledgments

First and foremost, I would like to express my profound gratefulness to my advisor and mentor, Professor Winston "Wole" Soboyejo. I would like to thank him for the invaluable guidance, assistance, understanding, patience and encouragement throughout my graduate studies. Working with him is the best thing that ever happened to my career; the countless lessons he imparted on me will be extremely useful as I move on in life.

A truly great "obilu" to my first teacher, my mother, and my best friend – Aminat Yakub. You are a true force of nature, and what you mean to me is beyond words. At this juncture, it's only fitting to sing: "*Iya ni wura iyebiye, ti a ko le fowora. Oloyun mi fosu mesan. O pon mi fodun mefa (ah-ah). Iya ni wura iye biye, ti a ko le fowo ra"*. Thank you - for bestowing upon me a love like no other, and for the countless acts, deeds and words that have molded me into what I am today, and what I'll be(come) tomorrow. It is your name that should be engraved on the degree, not mine.

All that I have accomplished in life is hinged to one person, my brother, Abdul-Kareem ("Oyarekhua", "Karym", "Brother Abdul"). From ensuring my education didn't end prematurely, to providing a shoulder on which I could lay, burn and be reborn. To attempt to fully repay you is to attempt the impossible! And, on the scale of what you've done for me, saying "thank you for everything" counts for nothing, but I'll say it anyways – thank you for everything!

Special thanks to my siblings: Millicent Oluwatosin ("Sister Milli"), Abdul-Azeez ("Yabaz", "Bazidon", "Bazzy"), Memunatu Hassanatu ("Hajia", "Taiye"), Fatimatu Hussenatu ("Kenny", "Kehinde"), Rahmat Idowu ("Idee", "Lametu") for the unconditional love, care, support and benevolence throughout my career and life. Thank you all for been my confidant and for been a great source of inspiration. Like the past, the future will be challenging but in you guys I have everything I need to ascend beyond any anticipated zenith (to borrow Yabaz's phrase or name). My sincere gratitude goes to my father, Momodu Yakub for the great assistance and support all through the years.

I must also thank my in-laws: Saidat Kareem, Segun Opawoye, Abdulganiy Akinsunbo, Ayodele Tiamiyu, Kazeem Jayeola, for the unfailing love, compassion and encouragement.

My sincerest gratitude goes to my uncle, Abdulahi I. Musa, for the inestimable support which includes but not limited to “azumi’s” and “iromi’s”. I would like to extend my gratefulness to your lovely wife, Jemila Musa – for been a great aunt, sister and friend. I would also like to thank my aunt, Azalet Immumolen, for the critical role she played during my upbringing.

My gratitude also goes to my “family” in Maryland, Adeleye Adelani, Toyin Adelani, Barakat Adelani and Abdul Salam Adelani, for the encouragement and support and for allowing me to anchor my boat at their shore when the tides are high, and for the great Nigerian foods too!

I would like to thank Rotimi Awoleke for been such a great friend and influence. Thank you for all the lively conversations, and great guidance. I would like to extend my gratefulness to your life-long lover and wife, Diana Awoleke and your son, Gilbert Teniayo.

Infinite thanks to my brothers from another mother: Onobu Akwogu (Ph.D.), Yusuf Oni (Ph.D.), Wali Akande (Ph.D.), and Victor Oyeyemi, for been there whenever I needed them, and for all the great times. Special thanks to Yusuf’s wife, Ajoke Oni-Saliu for the support and fun memories.

I would like to say a special thank you to the members of my research group, past and present: Emily Pretzel (Ph.D.), Juan Meng (Ph.D.), Tiffany Tong, Deying Yu and Wanliang Shan, for the academic and moral support. I am particularly grateful to Jing Du and Xiaozhong “Jakie” Xu (Ph.D.) for the warm and broad shoulders, and for always looking out for me.

I would also like thank my friends: Stephan Priebe, Dan Lev, Steve Brunton, Stephanie Goldfarb, Thanh Nguyen, Anand Ashok, Fadi Abdeljawad, Emerson Sykes, Omar Muhsin Usman, Auxillia Munhutu, Sheila Agiti, Katie Friedman, Wei Ding, Oyenike Oyerinde, Sonia Naidu, Manu Sebastian, Darren Pais, Joanna Coradin and Shuanglei Li for all the assistance, companionship and for making my stay here a memorable one.

During my graduate studies, I had the rare opportunity of working with: Prof. Alfred B. O. Soboyejo, Prof. Larry C. Brown, Prof. Nima Rahbar, Prof. Megan Leftwich, Prof. Francis Nyongesa, Prof. Sam Obwoya, Karen Malatesta (Ph.D.), Yevgeny Raitses (Ph.D.), Nicolas Anuku (Ph.D.), Anand Plappally (Ph.D.), Gerald Poirier, Joe Palmer, Joe Vocaturo and Mike

Vocaturo. I would like to thank them for all the priceless assistance, penetrating insights and intellectual discussions.

My utmost gratefulness goes to my Ph.D committee members: Prof. George Scherer, Prof. Nan Yao, Prof. Michael McAlphine, and Prof. Gigi Martinelli, for the invaluable comments, suggestions, guidance and discussions.

I would also like to thank members of Wesley L. Harris Scientific Society, Black Graduate Caucus, Princeton African Students' Association, Global Development Network, Princeton Haiti Rapid Response Team, the Keller Center, the MAE soccer team and the MAE department for the wonderful experience.

I must also thank Stephanie Landers, Cornelia Huellstrunk, Jill Ray, Jessica O'leary, Prof. S. O. Talabi, Prof. Judith Mathew, Engr. Bayo Ogunmola, Engr. Adekunle Adelaja, Oyinkansademi Adebo, Samson Oloko, Yinka Joseph, Yomi Salako, Kadiri Olayinka, Jamiu Bamire, Fashola Fatai, Shola Fadairo, Victor Daropale, Isaac Ewaleifoh, Seun Magbagbeola, Bioshigun Niran, Yemi Soneye, Misaretu Ajayi, Lateef Anifowose, Abdulahi Anifowose, Kamil Anifowose, Azeezat Anifowose and Wale Olushi for the ancillary but extremely critical support.

Finally, I would like to thank - my nephews: Richard Oluwatobiloba, Flourish Oluwanifemi, Abdulahi Orimadegun, Akram Ogiee and Samuel Oluwadoyinsolami; my nieces: Fathia Toluwalase, Azeemat Effua and Atteeyah Orome, and my cousins: Abdulmajid, Lukman, Lawal, Nasiru, Aliyu, Imran, Becky, Omono, Favour and Ayodele - for been a source of great fun and joy during my trips to Kaduna, Lagos and London.

Obilu and God bless you all.

This dissertation carries the number T-3250 in the records of the Department of Mechanical and Aerospace Engineering

Table of Contents

Dedication iii

Abstract iv

Acknowledgment vi

Table of Contents ix

List of Tables xv

Table of Figures xvii

Chapter 1 1

Background and Introduction 1

1.1 Background and Motivation 1

1.2 Research Objectives 4

1.3 Scope and Organization of Thesis 5

References 7

Chapter 2 10

Literature Review 10

2.1 Contaminants in water and methods of purification: an overview 10

2.2 Clays and Clay-based Materials 23

2.3 Fundamentals of Porosimetry and Flow through Porous Media 35

2.4 Fundamentals of Adsorption 44

2.5 Strength and Fracture of Brittle Materials: The Fundamentals 47

References 58

Chapter 3 74

Porosity and Filtration Characteristics of Frustum-Shaped Ceramic Water Filters..... 74

3.1 Introduction 74

3.2 Experimental Methods 77

3.2.1 Materials and Processing 77

3.2.2 Mercury Intrusion Porosimetry 80

3.2.3 Water Flow Experiments 80

3.2.4 Permeability and Tortuosity 81

3.2.5 *E.coli* Removal Experiments 83

3.3 Modeling 84

3.4 Results and Discussion 86

3.4.1 Porosimetry 86

3.4.2 Flow Rate Measurements, Permeability and Tortuosity 88

3.4.3 Bacterial Filtration 91

3.4.4 Implications 92

3.5 Conclusions 94

Acknowledgments 95

References 96

Chapter 4 117

Mechanical Properties and Design of Porous Clay Ceramics 117

4.1 Introduction 117

4.2 Experimental 118

4.2.1 Materials and Processing 118

4.2.2 Materials Characterization 119

4.2.3 Modulus and Hardness Measurement 120

4.2.4 Strength Measurements 120

4.2.5. Fracture Toughness 122

4.2.6 Resistance-Curve Measurements 122

4. 3 Modeling 123

4. 3.1 Crack-tip Shielding 123

4.3.2 Finite Element Analysis 125

4.4 Results and Discussion 126

4.4.1 Materials Characterization 126

4.4.2 Modulus and Hardness 127

4.4.3 Compressive and Flexural Strength 128

4.4.4 Fracture Toughness and Resistance-curve Behavior 128

4.4.5 Modeling of Filter Stress 129

4.4.6 Implications 131

4.5 Conclusions 132

References 133

Chapter 5 153

Adhesion of E.coli Bacteria to Silver - or Copper - Coated Porous Ceramic Surfaces 153

5.1 Introduction 153

5.2 Theory 156

5.2.1 Adhesion Force Measurement 156

5.2.2 Adhesion Energy 157

5.3 Experimental Procedures 160

5.3.1 Materials 160

5.3.2 Sample Preparation 160

5.3.3 Materials Characterization 162

5.3.4 AFM Measurements 163

5.4 Results and Discussions 164

5.4.1 Characterization of AFM tip and substrate 164

5.4.2 Adhesion Forces 166

5.4.3 Adhesion Energies 168

5.4.4 Implications 169

5.5 Conclusions 170

References 171

Chapter 6 188

Adsorption of Fluoride from Water using Sintered Clay-Hydroxyapatite Composites 188

6.1 Introduction 188

6.2 Experimental 190

6. 2.1 Materials and Processing 190

6.2.2 Materials Characterization 192

6.2.3 Adsorption and Kinetics Studies 193

6.2.4 Proof-of-Concept Study 193

6.3 Results and Discussion 194

6.3.1 Characterization of Adsorbent 194

6.3.2 Effect of Sintering Temperature 196

6.3.3 Effect of HA Content 197

6.3.4 Adsorption Isotherm 198

6.3.5 Change in Free Energy 199

6.3.6 Adsorption Kinetics 200

6.3.7 Frustum-Shaped C-HA Filter 201

6.3.8 Implications 202

6.4 Conclusions 204

References 205

Chapter 7 233

Removal of Fluoride from Water Using the "Buckyweb" 233

7.1 Introduction 233

7.2 Experimental 234

7.2.1 Material Processing 234

7.2.2 Materials Characterization 235

7.2.3 Adsorption and Kinetics Studies 235

7.3 Results and Discussion 236

7.3.1 Characterization of Adsorbent and the Effect of Inclusions 236

7.3.2 Adsorption Isotherm 237

7.3.3 Change in Free Energy 240

7.3.4 Adsorption Kinetics 240

7.3.6 Implications 243

7.4 Conclusions 244

References 246

Chapter 8 262

Concluding Remarks and Suggestions for Future Work 262

8.1 Concluding Remarks 262

8.2 Suggestions for Future Work 265

List of Tables

Table 2.1: Overview of major chemical contaminants in drinking water, their health impacts and a few associated events (Pradeep & Anshup, 2009). 12

Table 2.2: Pathogens transmitted through drinking-water[a] (WHO, 2011b) 13

Table 2.3: Performance requirements for POU/HWT technologies and associated $\log_{10}$ reduction criteria for "interim", "protective" and "highly protective" (WHO, 2011a) 14

Table 3.1: The median pore diameters, the average pore diameters and the porosities of three CWFs tested: (a) Median Pore Diameter of CWFs and (b) Average Pore Diameter of CWFs.. 115

Table 3.2: *E.coli* filtration efficiency obtained for filters with different clay to sawdust volume ratios results expressed as percentages calculated using $\eta_{E.coli} = 1 - \frac{N_f}{N_{pf}}$ where N_f is the number of viable cells per mL of filtrate and N_{pf} is the number of viable cells per mL of pre-filtrate to yield the percentage filtration efficiency. Secondly, as described by Brown and Sobsey (Brown & Sobsey, 2009), the Log_{10} reduction in *E. coli* concentration between the pre-filtrate and the filtrate was obtained from: *Log_{10} reduction value,* $LRV = Log_{10}\left[\frac{C_{pf}}{C_f}\right]$ 116

Table 4.1: Chemical composition of redart clay raw material 135

Table 4.2: Physical properties of porous ceramic. MP is Mercury Porosimeter and HP is Helium Pyncnometer 135

Table 4.3: Summary of mechanical properties of the porous ceramics 136

Table 4.4: The maximum principal stress (in kPa) in the "lip edge" and "bottom edge" of the frustum-shaped filter under different support condition 137

Table 5.1: Average rms roughness values 178

Table 5.2: Spring constants of the bare and coated AFM tips 178

Table 5.3: Adhesion force between coated AFM tips and substrate for (a) *E.coli* bacteria interactions and (b) Ceramic interactions 179

Table 6.1: Different types of adsorbent studied. *Sawdust was added to the matrix (i.e. Clay and HA) in a ratio of 2 to 1 by volume. The adsorbent was sintered at five different temperatures of 500°C, 600°C, 700°C, 800°C and 900°C. 212

Table 6.2: The Freundlich Isotherm parameters and Gibbs free energy obtained for all adsorbent type. 213

Table 6.3: Particle- and intra – particle rate constant for two adsorbents (C-HA = 0:100 and C-HA = 75:25) 214

Table 6.4: Proof-of-concept results using frustum-shaped C-HA filter. *Averaged over a cumulative volume of ~500mL 214

Table 7.1: Chemical composition of the treated buckyweb 251

Table 7.2: The Freundlich Isotherm parameters and Gibbs free energy obtained for the adsorbent treated with different pH 251

Table of Figures

Figure 2.1: Temperature versus time relationships for safe water pasteurization (Feachem *et al.*, 1983) 19

Figure 2.2: Mother of all graphitic forms. It can be wrapped up into 0D buckyballs, rolled into 1D nanotubes or stacked into 3D graphite (Geim & Novoselov, 2007) 23

Figure 2.3: Mineralogical classifications associated with clay minerals (Shackelford & Doremus, 2008) 27

Figure 2.4: Atomic arrangements of Si_2O_5 and $AlO(OH)_2$ layers. Patterns (a) and (b) are idealized, and (c) and (d) are the distorted arrangement found to occur in kaolinite and dickite. (Kingery, 1958) 29

Figure 2.5: Perspective drawing of kaolinite with Si-O tetrahedrons on the bottom half of the layer and Al-O, OH octahedrons on the top half (Kingery, 1958). 30

Figure 2.6: Different techniques for processing of advanced ceramics (Askeland & Phulé, 2006) 34

Figure 2.7: Contact angle, θ of two liquids placed on a surface: (a) $\theta < 90$, a wetting liquid and (b) $\theta > 90$, a wetting liquid 36

Figure 2.8: Behavior of: (a) wetting and (b) non-wetting liquids with respect to a capillary tube (Webb, 2001) 37

Figure 2.9: Liquid in a pore with radius r_p 39

Figure 2.10: Flow through a permeable media with thickness t 41

Figure 2.11: Schematics of the stress-strain behavior of brittle materials compared with that of more ductile material. 49

Figure 2.12: Schematic of typical nanoindentation load-displacement plot. U_I is the unrecoverable elastic energy and U_E is the recovered elastic energy during unloading (He *et al.*, 2008) 50

Figure 2.13: An elliptical flaw of size *2a* at the centre of a plate with thickness, *B*, subjected to uniaxial loading..... 52

Figure 2.14: The three different modes of failure: (I) Opening mode; (II) Sliding mode and (III) Tearing mode 55

Figure 2.15: In-plane coordinate system ahead of a crack tip 55

Figure 3.1: Geometry of the two-piece aluminum molds that were used to form the CWF into a frustum shape: (a) Male Mold and (b) Female Mold (Major dimensions are shown in mm) 103

Figure 3.2: Schematic of a CWF with key variables labeled. The four sites from which samples for the MIP analyses were obtained are demarcated with black rectangles 104

Figure 3.3: Pore-size distribution for samples taken from the bases of: (a) PFP filter; (b) 50:50 filter; (c) 65:35 filter, and (d) 75:25 filter..... 106

Figure 3.4: Comparison of the average pore size of a CWF to the sizes of a water molecule, different microbes and cells, and a multi-cellular hair, all of which can be found in contaminated water..... 107

Figure 3.5: Dependence of porosity on the volume fraction of sawdust used in filter fabrication: (a) Base porosity levels and (b) Overall average porosity from sides and base 108

Figure 3.6: Plots of effluent discharge as a function of time: (a) Day-long (24 hour) effluent discharge and (b) “Overnight” (8 hour) effluent discharge 109

Figure 3.7: Plots of volume flow rate against time – comparisons of experimental data and Darcy fits: (a) 50:50: CWF; (b) 65:35 CWF and (c) 75:25 CWF 111

Figure 3.8: Dependence of the effective CWF intrinsic permeability on the volume percentage of sawdust 112

Figure 3.9: Comparing the permeability obtained from Darcy fit with the K-T method 113

Figure 3.10: Bar chart showing the tortuosity of the CWFs. The tortuosity was found by combining the Jörgen Hager approach with: 1. The permeability obtained from the Darcy fit and 2. The permeability obtained using the K-T method. The skeletal density used was obtained using helium pycnometer 114

Figure 4.1: Finite element models of the filters for (a) frustum filter model, (b) uniform thickness frustum filter model, (c) ellipsoid filter model, (d) semi-spherical filter model, (e) cylindrical filter model, and (f) inverted frustum filter model 138

Figure 4.2: Different support configurations modeled. Figure shows support spanning (a) first quarter of lip, (b) second quarter of lip, (c) third quarter of lip, (d) fourth quarter of lip, (e) half of lip, (f) three-quarter of lip and (g) the entire lip 139

Figure 4.3: Environmental scanning electron microscopy micrographs of (a) the woodchips (sawdust) used and (b) a typical pore structure of the porous ceramics 140

Figure 4.4: Linear relationship between porosity measured using helium pycnometer and mercury porosimeter 141

Figure 4.5: XRD pattern of Redart clay (bottom/blue) and the porous ceramic (top/red) 142

Figure 4.6: Variation of elastic modulus and hardness with porosity and average pore diameter 144

Figure 4.7: Dependence of compressive strength on porosity of the porous ceramics 145

Figure 4.8: Dependence of flexural strength on porosity of the porous ceramics 146

Figure 4.9: Dependence of fracture toughness on porosity of the porous ceramic 147

Figure 4.10: Resistance curve behavior of the porous ceramic 148

Figure 4.11: ESEM image of a porous ceramic showing evidence of crack bridging 149

Figure 4.12: Variation of the maximum principal stress on the "lip edge" and the "bottom edge" of the frustum-shaped filter as the pressure head of water changes 150

Figure 4.13: Variation of the maximum principal stress on the "lip edge" (dash lines) and "bottom edge" (solid lines) of the filter models as the pressure head of water changes 151

Figure 5.1: Schematic of a typical cantilever deflection-displacement plot with highlights of the various stages (A-E) of the AFM tip as it is brought into and out of sample at a fixed point (adapted from Shahin et al., 2005)..... 180

Figure 5.2: Schematic illustration of adhesion between coated AFM tips and surfaces relevant to ceramic water filter 181

Figure 5.3: ESEM images and EDX spectrum of (a) uncoated tip, (b) copper coated tip, (c) silver coated tip, (d) colloidal silver coated tip, and (e) ceramic coated tip 182

Figure 5.4: Measurement of AFM tips radii using ESEM micrograph (scale bar of insert = 100 nm). The metallic silver coated AFM tip shown has a tip radius of ~ 87 nm..... 183

Figure 5.5: Sample of 5μm AFM tapping mode image of (a) porous ceramic and (b) *E.coli* bacteria surfaces..... 184

Figure 5.6: Typical AFM force-displacement characteristics for copper coated tip and (a) porous ceramics and (b) *E.coli* bacteria..... 185

Figure 5.7: Comparison of adhesion force obtained for (a) *E.coli* interactions and (b) Porous ceramics interactions 186

Figure 5.8: Adhesion energies obtained for (a) *E.coli* interactions and (b) Porous ceramics interactions 187

Figure 6.1: EDX analysis of C-HA adsorbent 216

Figure 6.2: XRD analysis of C-HA adsorbent 218

Figure 6.3: STEM image of the HA used in making the C-HA adsorbents, the C-HA = 0:100 adsorbent and the C-HA = 75:25 adsorbent 220

Figure 6.4: Backscattered electron (BSE) image of the C-HA adsorbent in this case C-HA = 75:25 221

Figure 6.5: Effect of sintering temperature of the adsorbent on the amount of fluoride that is adsorbed from water with at an initial fluoride level of: (a) 10mg/L; (b) 20mg/L; (c) 30mg/L; (d) 40mg/L and (e) 100mg/L 224

Figure 6.6: Freundlich Isotherm for C-HA adsorbent 229

Figure 6.7: C-HA adsorption kinetics 231

Figure 6.8: Change in concentration of fluoride with cumulative volume of water collected for: (a) C_o = 2.5mg/L and (b) C_o = 20mg/L. 232

Figure 7.1: Schematics of set up used for making buckyweb (Raitses *et al.*, 2008) 252

Figure 7.2: Representative SEM and TEM images of various carbon deposits collected in different collection areas. (a–c) Low-, medium-, and high magnification SEM images of the samples containing graphene layers, collected from the top and side surfaces of the magnet. (d, e)

TEM image of folded graphene layers in the carbon sample collected from the top and side surfaces of the magnet, respectively. (f) TEM image of the sample containing carbon nanotube bundles 253

Figure 7.3: STEM and TEM micrograph of buckyweb: [a] STEM image showing ropes of carbon and catalyst deposits (scale bar = 3 μm), and [b] TEM image showing graphene sheets and catalyst deposits (scale bar = 50 nm) 254

Figure 7.4: Chemical composition analysis: [a] EDX spectrum of buckyweb (Insert: Environmental Scanning Electron Image of the treated web) and [b] EDX mapping of Carbon, Oxygen, Fluorine, Sodium, Nickel and Yttrium (from top to bottom)..... 255

Figure 7.5: Variation of amount of fluoride adsorbed as a function of pH values 256

Figure 7.6: Freundlich Isotherm for the fluoride adsorption on buckyweb..... 257

Figure 7.7: The intercept of the plot of ln(Qe/Ce) against Ce is an indication of the thermodynamic distribution coefficient of the adsorption process (Khan, 1987) 258

Figure 7.8: Amount of fluoride adsorbed with time on buckyweb at pH 6.5..... 259

Figure 7.9: Diffusion-based models: [a] Particle diffusion modeling and [b] Intraparticle/pore diffusion modeling for the buckyweb at pH 6.5 260

Figure 7.10: Reaction-based models: [a] Pseudo-first-order kinetic model and [b] Pseudo-second-order model of fluoride adsorption kinetics on the buckyweb at pH 6.5 261

Chapter 1

Background and Introduction

1.1 Background and Motivation

Water is food and the importance of drinking clean water cannot be overemphasized. It is a solvent for biochemical reactions, essential for maintaining vascular volume, serves as a medium for transport within the body by supplying nutrients (such as calcium and magnesium which are important in bone health and cardio vascular health and selenium which helps the body build immunity against germs to mention a few) and removing waste (DRI, 2004). Cellular hydration has been suggested to be an important signal in the regulation of cellular metabolism, cellular function and gene expression (Haussinger *et al.*, 1994).

However, around 884 million people in the world do not have access to improved water supplies (WHO/UNICEF, 2008). These people are left with no choice but to drink water that is contaminated with chemicals and pathogens. Consequently, millions die each year from preventable water-borne diseases such as diarrhea, dysentery, poliomyleitis, cholera, typhoid, ascariasis, and leptospirosis and other enteric illnesses, as well as sequelae and indirect effects, such as neurological syndromes and reactive arthritis (reiter syndrome) and electrolyte imbalance. Moreover, drinking an insufficient amount of water (or no water at all) can lead to

malnutrition, arrested growth and development, dehydration and death (Checkley *et al.*, 2004; Kosek *et al.*, 2003; Lantagne, 2001c; Sobsey *et al.*, 2008; Wenhold & Faber, 2009).

Diarrhea, a preventable disease, is the most commonly occurring water related disease. It is estimated to cause 4 billion episodes of diarrhea every year, leading to at least 1.8 million deaths every year (UNICEF, 2008). This greatly increases the mortality rates and the disease burden in developing countries, especially in children younger than 5 years old. Waterborne diseases kill more young children than AIDS, malaria and measles combined (UNICEF/WHO, 2009).

When the population of humans who lacks access to proper sanitation and hygiene is considered, the number of water-associated deaths rockets to a staggering 3.4 million deaths per year (UNICEF, 2008). This figure, although alarming, is not hard to imagine. Each year, 300 million people suffer from malaria, 160 million people are infected with schistosomaisis, 6 million people are blind from trachoma and 10% of the developing world is infected with intestinal worms, just to mention a few (Kindhauser, 2003; UNICEF, 2008).

While microbiological contamination is the largest public health threat, water contaminated with chemicals such as fluoride, arsenic, nitrate, mercury, lead, halogenated organics (Pradeep & Anshup, 2009) can cause serious health problems. Ground water with high fluoride concentrations can be found in many areas of the world. Ingesting water containing fluoride of concentration greater than ~1.5 mg/L over a prolonged period of time can also lead to different forms of fluorosis. An example is dental fluorosis, which is a condition characterized with the staining, pitting and mottling of the dental enamel. A much larger concentration of fluoride (about 4 mg/L) and long time exposure can lead to crippling skeletal fluorosis and osteoporosis (Inyang, 2004; Mandinic *et al.*, 2010; WHO, 2011).

Furthermore, the lack of access to safe and adequate drinking water supplies contributes significantly to ongoing poverty in many poor communities both through the economic cost of poor health and in the high proportion of household expenditure on water supplies, arising from the need to purchase water and/or time and energy expended in collection (WHO, 2003). There have been continued efforts by governments, civil society and the international community, to solve the problem of contaminated water by providing "improved" water supply, such as household connections, public standpipes and boreholes – the problem with such methods is that they are not sustainable and the water is often contaminated at the point of use. Also, the age and the type of materials used in the installed pipes often leads to corrosion and the leaching of chemicals into the water.

In order to tackle this worldwide problem, a number of new techniques, methods, and devices have been developed. The point of use (POU), sometimes referred to as the household water treatment technique, is a way of purifying water at the household level. A major advantage of POU technologies is that they drastically reduce the chance of secondary contamination of water occurring (since water is often polluted between source and point of use). A promising method for the purification of water at the point of use is the clay-based porous ceramic water filter (CWF). Even though studies have shown that the ceramic filters, locally or commercially produced, are effective in removal of microbial pathogens in water (Clasen & Boisson, 2006; Lantagne *et al.*, 2010; Lantagne, 2001a,2001b,2001c; PFP; Sobsey *et al.*, 2008; Yakub *et al.*, Submitted for publication), there are few fundamental scientific studies of POU CWFs. Moreover, the current designs of the ceramic water filters have some draw backs. It is not effective at removing chemical contaminants – a problem that can be solved by exploiting clays' adsorption properties. Also, because of their brittle nature, the POW CWFs are subject to

breakage during processing, transportation and usage. There is, therefore, a need for strength and cracking resistance of porous clays that are relevant to water filtration.

There is also the need and opportunity to optimize and/or re-design the frustum-shaped CWF. Besides ordinarily supplying clean drinking water, the technology should also be extended to providing clean water for washing, cooking, bathing etc and this can be achieved through a scale-up approach. The porous ceramics can be made even more robust by integrating it with other porous structures that could range from clean cloth to advanced materials such as "buckyweb" structures.

This dissertation adds to the limited knowledge of the fundamental scientific knowledge of porous ceramic water filters and the possibility of the adoption of the device as means of water purification, not only in the developing world, but also globally. It also proposes the use of a new type of clay-based ceramic composites water filters and "buckyweb" structures that may be used as standalone devices (for biochemical filtration) or used to augment other types of POU technologies (including the CWFs).

1.2 Research Objectives

The thesis presents a combination of experimental, theoretical and computational modeling that provides new insights for the design of a robust water filtration technique. The innovations range from materials that are easily available, sustainable and cheap, to much advanced materials. The objectives of the current work are to:

(a) Develop a fundamental understanding of porous structures of CWFs, and their effects on fluid (water) flow and filtration characteristics;

(b) Use atomic force microscopy to gain insights into adhesion phenomena associated with bi-material pairs that are relevant to ceramic water filter;

(c) Develop a basic understanding of the effects of porosity on the strength (compressive and flexural), modulus, hardness and fracture behavior of the porous media;

(d) Explore the potential for the re-design and/or scale up of CWFs using a finite element models;

(e) Extend the current filter from the removal of microorganism contaminants to the removal of chemical contaminants that are dangerous to public health;

(f) Study the effectiveness of next generation of carbon-based (carbon nanotube and graphene) web materials for water purification.

1.3 Scope and Organization of Thesis

Following the background and introduction presented in this section, the relevant literature is reviewed in chapter 2. Chapter 3 then presents the results of an experimental study of the effects of porosity on the flow rate and *E.coli* filtration characteristics of porous ceramic water filters (CWFs) with well controlled porosities. A theoretical model, based on Darcy's equation, is used to determine the effective permeabilities. These values are then compared with values obtained via the Katz-Thompson method.

The mechanical properties (modulus, hardness, compressive strength, flexural strength, fracture toughness and R-curve behavior) of the ceramic filter materials are presented in chapter 4. The chapter also examines the potential for scaling-up the CWFs, using finite element analyses.

Chapter 5 presents the results of an atomic force microscopy (AFM) study of the adhesion between bi-material pairs that are related to bacteria removal/water purification using porous ceramic filters with silver, colloidal silver and copper coatings. Since AFM measurements are highly sensitive to roughness and surface asperities, the AFM tip radii as well as the substrate roughness were measured and incorporated into adhesion models that were used to establish the adhesion energies.

This is followed by chapter 6 in which fluoride removal from drinking water is presented. The adsorption characteristics are explored in clay-hydroxyapatite (C-HA) composites. *E.coli* filtration is also shown to occur in the HA-doped filter. Chapter 7 explores the removal of fluoride in novel structures that consist of carbon nanotube and graphene. Salient conclusions arising from this work are summarized in chapter 8, along with suggestions for future work.

References

Checkley, W., Gilman, R. H., Black, R. E., Epstein, L. D., Cabrera, L., Sterling, C. R., & Moulton, L. H. (2004). Effect of water and sanitation on childhood health in a poor Peruvian peri-urban community. *Lancet, 363*(9403), 112-118.

Clasen, T., & Boisson, S. (2006). Household-based ceramic water filters for the treatment of drinking water in disaster response: An assessment of a pilot programme in the Dominican Republic. *Water Practice & Technology, 1*(2).

DRI. (2004). Dietary Reference Intakes (DRI) for water, potassium, sodium, chloride and sulphate. *National Academy of Sciences*.

Haussinger, D., Lang, F., & Gerok, W. (1994). Regulation of cell function by the cellular hydration state. *Am J Physiol, 267*(3 Pt 1), E343-355.

Inyang, H. I. (2004). Geochemical and Health Policy Dimensions of the Controversy about Fluorides in Water Resources. *Journal of Environmental Engineering, 130*(2), 113.

Kindhauser, M. K. (2003). Global defence against the infectious disease threat. Communicable Diseases 2002. *World Health Organization, Geneva*.

Kosek, M., Bern, C., & Guerrant, R. L. (2003). The global burden of diarrhoeal disease, as estimated from studies published between 1992 and 2000. *Bulletin of the World Health Organization, 81*(3), 197-204.

Lantagne, D., Klarman, M., Mayer, A., Preston, K., Napotnik, J., & Jellison, K. (2010). Effect of production variables on microbiological removal in locally-produced ceramic filters for

household water treatment. *International Journal of Environmental Health Research, 20*(3), 171-187.

Lantagne, D. S. (2001a). *Investigation of the Potters for Peace Colloidal Silver-Impregnated Ceramic Filter: Intrinsic Effectiveness and Field Performance in Rural Nicaragua*: Istanbul Conference, Turkey.

Lantagne, D. S. (2001b). *Investigation of the Potters for Peace Colloidal Silver Impregnated Ceramic Filter Report II: Field Investigations*: Alethia International.

Lantagne, D. S. (2001c). *Investigation of the Potters for Peace Colloidal Silver Impregnated Ceramic Filter. Report 1: Intrinsic Effectiveness*: Alethia Environmental, Allston, Massachusetts.

Mandinic, Z., Curcic, M., Antonijevic, B., Carevic, M., Mandic, J., Djukic-Cosic, D., & Lekic, C. P. (2010). Fluoride in drinking water and dental fluorosis. *Science of The Total Environment, 408*(17), 3507-3512.

PFP. Potters for Peace. Retrieved from <http://www.pottersforpeace.org>

Pradeep, T., & Anshup. (2009). Noble metal nanoparticles for water purification: A critical review. *Thin Solid Films, 517*(24), 6441-6478.

Sobsey, M. D., Stauber, C. E., Casanova, L. M., Brown, J. M., & Elliott, M. A. (2008). Point of use household drinking water filtration: A practical, effective solution for providing sustained access to safe drinking water in the developing world. *Environmental Science & Technology, 42*(12), 4261-4267.

UNICEF. (2008). UNICEF Handbook on Water Quality. *United Nations Children's Fund (UNICEF), New York*.

UNICEF/WHO. (2009). *Diarrhoea: why children are still dying and what can be done*. New York: United Nations Children's Fund.

Wenhold, F., & Faber, M. (2009). Water in nutritional health of individuals and households: An overview. *Water Sa, 35*(1), 61-71.

WHO. (2003). *Domestic Water Quantity, Service, Level and Health*. Geneva, Switzerland.

WHO. (2011). *Guidelines for Drinking-Water Quality* (4 ed.). Geneva, Switzerland.

WHO/UNICEF. (2008). *Progress on Drinking Water and Sanitation: Special Focus on Sanitation; World Health Organization and United Nations Children's Fund Joint Monitoring Programme for Water Supply and Sanitation*. Geneva, Switzerland.

Yakub, I., Plappally, A., Leftwich, M., Malatesta, K., Friedman, K. C., Obwoya, S., Nyongesa, F., Maiga, A. H., Soboyejo, A. B. O., et al. (Submitted for publication). Porosity and Filtration Characteristics of Frustum-Shaped Ceramic Water Filters.

Chapter 2

Literature Review

2.1 Contaminants in water and methods of purification: an overview

The importance of water for health and development has been reflected in the outcomes of a series of international policy forums. These include: water-oriented conferences such as 1977 World Water Conference in Mar del Plata, Argentina, which launched the water supply and sanitation decade of 1981-1990, as well as the Millennium Development Goals (MDG) adopted by the General Assembly of the United Nations (UN) in 2000, and the outcome of the Johannesburg World Summit for Sustainable Development in 2002 (WHO, 2011b). Most recently, the UN General Assembly declared the period from 2005 to 2015 as the International Decade for Action, "Water for Life" (WHO, 2011b).

Access to safe drinking-water is essential to health and a fundamental human right. Yet, as noted in chapter 1, about 13% (884 million) of the people in the world lack access to portable water (WHO/UNICEF, 2008). The MDG called for the proportion of people without *sustainable* access to potable water to be reduced by half by 2015 (WHO, 2007). For that happen, significant efforts must be made to provide sufficient (quantity) and safe (quality) drinking water, especially in rural areas of world where up to 743 million people are affected (WHO/UNICEF, 2010). This can be done with the development, deployment (by stakeholders) and application (by end-user)

of the appropriate technology for the effective inactivation and/or removal of contaminants that may be present in the water.

There are three main types of contaminants in water. They are: radiological contaminants, chemical contaminants and microbial contaminants. Although, drinking water may contain radioactive substances that could present a risk to human health, except in extreme circumstances, those risks are normally small, compared to the risks from chemicals and microbes that may be present in the water (WHO, 2011b).

Water contaminated with chemicals, such as fluoride, arsenic, nitrate, mercury, lead, halogenated organics (Pradeep & Anshup, 2009), can cause serious health problems when beyond permissible dose is taken for a prolonged period of time. Table 2.1 shows some of the major contaminants and the associated health effects due to ingestion. While the health risk of ingesting chemical contaminants is serious, microbes/pathogens that may be transmitted through drinking contaminated water pose the largest public health threat – as 1.8 million deaths every year from diarrhea related deaths alone (UNICEF, 2008). The pathogens are diverse in characteristics, behavior and resistance. General information on pathogens that are relevant to drinking-water supply management is provided in Table 2.2 (WHO, 2011b). Table 2.3 (WHO, 2011a) shows the acceptable levels to which the three main classes of microbial contaminants must be reduced to.

Major pollutant	Origin	Permissible limits	Affected countries	Population at risk	Health effects	Specific incidents
Pesticides	- Farming, effluents, home use	DDT: 1 ppb; Carbofuran: 40 ppb; Simazine: 4 ppb	US, Kenya, Egypt, India, European Union, Africa, China, Australia	Poisoning: 28 million agricultural workers in the developing countries. ~ 18,000 deaths	Cancer, cardiovascular/reproductive/neurological disorders, liver/kidney problems	Pesticide contamination in soft drinks, the Union Carbide Bhopal tragedy (India)
Halogenated organics	Chlorination, effluents, home insecticide	CCl_4: 5 ppb; TCE: 5 ppb; TTHMs: 80 ppb	Japan, Central Asia, Arabian Peninsula, Sweden, Poland, Germany, USA, Egypt, China	~ 180 million people in US consume chloraminated water	CCl_4: High toxicity to liver and kidney, carcinogenic. TCE: Lung/liver tumor	25 million pounds of TCE were released into the U.S. environment by manufacturing plants in 1995
Fluoride	- Geological origin, mineral weathering, coal mining	- 2 ppm	Asia, Mexico, Australia, Argentina, Africa, New Zealand	62 million (India)	Dental and skeletal fluorosis, Muscle fibre regeneration, nervous system malfunction	In 1999, a union of 1200 scientists, doctors and lawyers announced their opposition to water fluoridation (M. J. Solomon *et al.*)
Arsenic	- Geological origin	10 ppb	Bangladesh, India, China, Pakistan, Nepal, Myanmar, Vietnam	65 million (Asia)	High blood pressure, glucosuria, hyperpigmentation, keratoses, cancer	1 in 100 people (Conc: 0.05 mg/l) and 10 in 100 people (Conc: 0.5 mg/l) die due to cancer in long-term
Mercury	- Industrial pollution, dental filling, Food (fish)	- 2 ppb	Indonesia, China, Africa, Philippines, Japan, Kazakhstan, USA, Brazil, Australia, Taiwan, EU	~ 630,000 infants are born with high Hg content in the blood every year (USEPA)	Neurotoxicant, tremors, respiratory failure, gastrointestinal failures, and kidney damage	- ~ 30% of the mercury in US comes from abroad e.g., China -Unilever plant, Kodaikanal (India). Minamata, Niigata (Japan), River Nura (Kazakhstan).
Lead	- Old piping lines, mineral weathering, paint	15 ppb	Egypt, EU, USA, Thailand, China, Cambodia	> 300,000 US children and 65% of Shanghai children have high lead concentration	Delays in physical/mental development, Kidney problem, high blood pressure	- Incidence of Gout due to leaded wine and rum - Use of lead in paints and discharge in environment - Use of lead in paints and discharge in environment

Table 2.1: Overview of major chemical contaminants in drinking water, their health impacts and a few associated events (Pradeep & Anshup, 2009).

Pathogen	Health Significance[b]	Persistence in water supplies[c]	Resistance to chlorine[d]	Relative infectivity[e]	Important animal source
Bacteria					
Burkholderia pseudomallei	High	May multiply	Low	Low	No
Campylobacter jejuni, C.coli	High	Moderate	Low	Moderate	Yes
Escherichia coli - Pathogenic[f]	High	Moderate	Low	Low	Yes
E.coli - Enterohaemorrhagic	High	Moderate	Low	High	Yes
Francisella tularensis	High	Long	Low	High	Yes
Legionella spp.	High	May multiply	Low	Moderate	No
Leptospira	High	Long	Low	High	Yes
Mycobacteria (non-tuberculous)	High	May multiply	Low	Low	No
Salmonella Typhi	High	Moderate	Low	Low	No
Other salmonellae	High	May multiply	Low	Low	Yes
Shigella spp	High	Short	Low	High	No
Vibrio cholerae	High	Short to long[g]	Low	Low	No
Viruses					
Adenoviruses	Moderate	Long	Moderate	High	No
Astroviruses	Moderate	Long	Moderate	High	No
Enteroviruses	High	Long	Moderate	High	No
Hepatitis A virus	High	Long	Moderate	High	No
Hepatitis E virus	High	Long	Moderate	High	Potentially
Noroviruses	High	Long	Moderate	High	Potentially
Rotaviruses	High	Long	Moderate	High	No
Sapoviruses	High	Long	Moderate	High	Potentially
Protozoa					
Acanthamoeba spp.	High	May multiply	High	High	No
Cryptosporidium hominis/ parvum	High	Long	High	High	Yes
Cyclospora cayetanensis	High	Long	High	High	No
Entamoeba histolytica	High	Moderate	High	High	No
Giardia intestinalis	High	Moderate	High	High	Yes
Naegleria fowleri	High	May multiply[h]	Low	Moderate	No
Helminths					
Dracunculus medinensis	High	Moderate	Moderate	High	No
Schistosoma spp.	High	Short	Moderate	High	Yes

Table 2.2: Pathogens transmitted through drinking-water[a] (WHO, 2011b)

[a] This table contains pathogens for which there is some evidence of health significance related to their occurrence in drinking-water supplies.
[b] Health significance relates to the incidence and severity of disease, including association with outbreaks.

[c] Detection period for infective stage in water at 20 °C: short, up to 1 week; moderate, 1 week to 1 month; long, over 1 month.
[d] When the infective stage is freely suspended in water treated at conventional doses and contact times and pH between 7 and 8. Low means 99% inactivation at 20°C generally in < 1 min, moderate 1–30 min and high > 30 min. It should be noted that organisms that survive and grow in biofilms, such as *Legionella* and mycobacteria, will be protected from chlorination.
[e] From experiments with human volunteers, from epidemiological evidence and from experimental animal studies. High means infective doses can be 1–102 organisms or particles, moderate 102–104 and low > 104.
[f] Includes enteropathogenic, enterotoxigenic, enteroinvasive, diffusely adherent and enteroaggregative.
[g] *Vibrio cholerae* may persist for long periods in association with copepods and other aquatic organisms.
[h] In warm water.

Reference microbe used in dose-response model	Assumed number of microbes per liter in risk calculations[a]	Pathogen class	Log_{10} reduction required[b]		
			Interim	Protective[c]	Highly protective[c]
			Requires correct, consistent and continuous use to meet performance levels		
Campylobacter jejuni	1	**Bacteria**	Achieves "protective" target for two classes of pathogens and results in health gains	**≥ 2**	**≥ 4**
Rotavirus[d]	1	**Viruses**		**≥ 3**	**≥ 5**
Cryptosporidium	0.1	**Protozoa**		**≥ 2**	**≥ 4**

Table 2.3: Performance requirements for POU/HWT technologies and associated log_{10} reduction criteria for "interim", "protective" and "highly protective" (WHO, 2011a)

[a] Assumptions for background water quality used to derive microbial reduction targets where local data are not available. These are based on an assumed wastewater content in untreated water of 0.01% by volume, using estimated background wastewater concentrations of reference microbes from Volume 2 of the WHO Guidelines for the safe use of wastewater, excreta and greywater (WHO, 2006). Local water quality data should be used if available and representative enough to inform QMRA using bacteria, viruses and protozoa. The use of alternative background water quality data will result in different log10 reductions required to achieve the relevant risk-based targets using the QMRA models as described in the GDWQ (WHO, 2011b).

[b] Computed as $\log_{10} (C_{\text{untreated water}} / C_{\text{treated water}})$, where C = microbe concentration in water.

[c] Treated water achieving the $\log_{10}$ reduction required to meet the health-based target of 10^{-4} ("protective") and 10^{-6} ("highly protective") DALY per person per year, based on the given assumptions for background water quality and using the QMRA models as described in the GDWQ (WHO, 2011b).

[d] The concentration of rotavirus is derived from high-income regions as presented in Table 7.4 of the GDWQ. Refer to the GDWQ for further explanation and validity for application in low-income regions (WHO, 2011b).

A common metric of comparing health outcomes, i.e. comparing the burden of disease associated with different water-related hazards, is the disability-adjusted life year (DALY) (Havelaar & Melse, 2003; WHO, 2011b). DALY is the sum of the years of life lost due to mortality (YLL) and the years of life lived with disability due to illness (YLD). For example, a top-tier standard of "highly protective" (Table 2.3) represents those technologies that, if used correctly, and consistently over an entire year will limit drinking water disease burden to 10^{-6} DALY per person (WHO, 2011a). This upper-limit DALY, is equivalent to one excess case of cancer per 100,000 people ingesting treated drinking-water over a 70-year period (WHO, 2011a,2011b). A more realistic target is 10^{-4} DALY per person per year, which can be achieved by middle-tier "protective" technology (Table 2.3). This includes technologies that do not meet the highly conservative target of 10^{-6} DALY per person per year, but may contribute to a substantial reduction in waterborne disease risk, particularly when the burden of disease is high (WHO, 2011a). The bottom tier, "interim", are "protective" technologies which are only able to satisfactorily remove two out of the three classes of pathogens (Table 2.3).

The removal of contaminants from water is best achieved at the point-of-use (POU) using different household water treatment technologies (HWTs) (Sobsey *et al.*, 2008). The HWTs that are commonly used can be classified into *disinfection* and *filtration* technologies (Sobsey *et al.*, 2008). Although the interventions have their merits, they may also have their drawbacks. Some examples of disinfection technologies include:

Chemical coagulation and/or flocculation: It involves the use of compounds such as "Alum" (hydrated potassium aluminium sulfate, $KAl(SO_4)_2 \cdot 12H_2O$), aluminium hydroxide ($Al(OH)_3$) and iron salts (e.g. ferric chloride), which neutralizes the electric double layer surrounding the suspended particles in water allowing them to stick together (flocculate) to form bigger particles.

In this way, the coagulated particles may then be easily filtered out using some other means. The downfall is it requires careful control of chemical dose, pH and consideration of the quality of the water being treated, as well as the appropriate mixing conditions for optimal flocculation in order to achieve the maximum reduction of turbidity and the inactivation of microbial contaminants (Sobsey, 2002). It is of moderate cost and requires a constant supply of chemicals.

Sedimentation: This method of water treatment cannot really be classified under *disinfection*. It involves slowly flowing water (Stokes flow) through a large tank, large reservoirs or large settling basin. The suspended particles, including microbes, in the water are separated by means of gravity (WHO, 2011b). The drawback is that it is not effective at removing microbes and the water has to sit in the tank long enough for the desired particle size to be removed (the finer the particle the longer the time it takes for it to settle down as sediments).

Chlorination and Chlorine dioxide: These are the most widely used disinfectants that are used for the purification of drinking water (Sobsey, 2002). With the right dose and contact time, the addition of free chlorine (or chlorine dioxide, a bleaching agent) to water is known to inactivate many waterborne pathogens, except for cryptosporidium and some viruses (Table 2.2; (WHO, 2011b)). Though it is effective at killing pathogens, it does not remove the turbidity of the water. Furthermore, it requires a constant supply of chemicals that consumers must be willing and able to purchase regularly. Also, the addition of chlorine to water with high organic matter and particles causes the production of compounds with objectionable tastes and odors (as a result of formation of chemical by-products) which may be toxic.

Ozonation: As the name suggests, it involves the use of ozone gas (O_3) which can be produced by passing oxygen gas through ultraviolet light. The ozone is unstable and when dissolved in

water it decomposes into oxygen gas and nascent oxygen which is harmful to microbial organism in water. Ozonation systems are also expensive to operate. The method is best suited for community or other centralized water systems where the specialized equipment and delivery systems required for its use can be properly applied by trained personnel (Sobsey, 2002).

Hydrogen Peroxide: Is similar to ozonation and chlorination in that it relies on oxidation process for inactivation of microorganism in water. However, storing hydrogen peroxide is an issue because of its rapid degradation. It also requires constant supply of the chemicals.

Solar disinfection (SODIS): This is an initiative of the Swiss Federal Institute of Aquatic Sciences and Technology (EAWAG/SANDEC, 2002). It is known to inactivate bacteria and viruses through combination of UV radiation and elevated water temperature (Sommer *et al.*, 1997; Sommer *et al.*, 1996). It is a low cost solution, as it uses clear plastic bottles, such as the preferred polyethylene terephthalate (PET) (which is less likely to leach harmful chemicals or substances into the water and/or affect the taste and odor of the water). Polyethylene bags may also be used (B. Sommer *et al.*, 1997). The main drawback is it requires about 6 hours to reach required heat on a sunny day and up to 48 hours on a cloudy day (Oates *et al.*, 2003; SODIS, 2011) and also time to cool. Also, the water has to have a low turbidity (< 30 NTU) for radiation to penetrate sufficiently and does not remove turbidity (EAWAG/SANDEC, 2002). A high level of turbidity may not only protect the microorganism from disinfection but can also stimulate growth of bacteria (WHO, 2011b). One way of preventing such occurrence is the use of other chemical disinfectants, such as hydrogen peroxide (Sciacca *et al.*, 2010). However, SODIS does not remove chemical contaminants.

Ultraviolet radiation: It is an easy and effective way of disinfecting drinking water. A UV lamp producing monochromatic UV radiation at a germicidal wavelength of 254 nm can be used as the UV source (WHO, 2011). However, like the SODIS method the turbidity of the water has to be low this is because of scattering and absorption of the radiation by the suspended particulate in the water. A reliable and affordable source of electricity is required. If a UV lamp is used, the lamp has to be replaced periodically, due to its finite lifespan (Sobsey, 2002).

Boiling: It is well known that heating water to boiling point temperature is capable of disinfecting most waterborne pathogens. The major advantage of boiling is that all the major pathogens can be killed – independent of pH, turbidity and other factors that influences alternative methods. The cost of boiling water is around $0.02/L (Andreatta *et al.*, 1994), which is relatively higher than many of the other methods. Moreover, it requires time to gather fuel (usually fire wood), causes environmental damage and requires time for heating and cooling and does not reduce turbidity.

Pasteurization: This is different from boiling of water in that the water is heated at a much lower temperature and around the temperature similar to milk pasteurization. Solar thermal systems may be used (Ciochetti & Metcalf, 1984). The time and temperature it takes to effectively inactivate some microbes is given in Figure 2.1. It has the same pros as boiling but the drawback of pasteurization is that the system has a higher life-cycle cost than other interventions (Burch & Thomas, 1998) and it is somewhat hard to maintain a constant heating temperature.

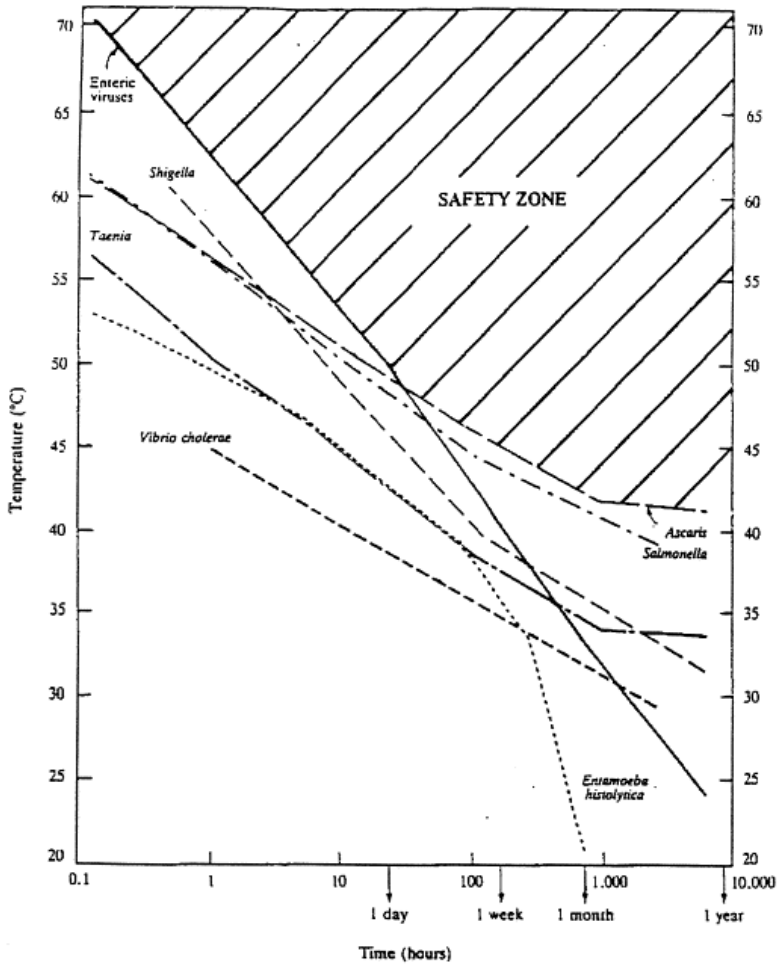

Figure 2.1: Temperature versus time relationships for safe water pasteurization (Feachem *et al.*, 1983)

Filtration technologies are different from disinfection methods in that they rely largely on size exclusion for the removal of microbes from water. Table 2.2 shows the pathogens that are transmitted through drinking water. They may also rely not only on a single porous surface but on multiple or different pore-structured surfaces. Moreover, some of the filters may employ chemical antimicrobial or bacteriostatic surfaces or chemical modifications that cause microbes

and chemicals to become adsorbed to filter media (WHO, 2011b). Examples of point of use filtration technologies include:

Slow sand filter: Is a type of granular media filter. Slow sand filters are filters with graded layers of sand – the finest sand at the top and the coarsest sand at the bottom. It is effective in removing micro-organism but the drawback is that the effectiveness of the system largely depends on the coarseness of the sand and putting fine sand on top of the coarse sands causes clogging of the filter.

Biosand filter: Biosand filters are slow sand filter with a bioactive layer that is often called the "schmutzdecke" layer. This serves to retain microbes and often leads to their inactivation and biodegradation (WHO, 2011a). It, however, requires periodic cleansing by manually scraping the top few centimeters of sand and it is expensive, costing between $25 – 100 per unit depending on the country and implementer (Sobsey *et al.*, 2008).

Porous ceramic filter: This is a filter made from the sintering of the mixture of clay and a combustible material (such as sawdust, rice husk, coffee husk). It is generally either in a pot shape or candle shape and cost around $8 – 10 (Sobsey *et al.*, 2008). They are usually coated with colloidal silver which acts as a disinfectant and prevents the formation of biofilm on the surface of the filter (Silvestry-Rodriguez *et al.*, 2008). Besides effectively removing bacteria from water, it is also capable of reducing the turbidity of the water. It is also very sustainable and has the potential to generate wealth. The major disadvantage is that it is brittle and not effective at removing chemical contaminants. It also requires periodic cleaning (because turbid water clogs the filter) and is expected to be replaced every two years.

Due to the limitations of the conventional technologies described above, the identification of more and more contaminants, the rapid growth of world's population and industrial activities, and diminishing availability of water resources (Zhou & Smith, 2001), there is need to develop more advance water filter methodology, technologies and material. Some of the processes and technologies currently in use include:

PuR: Are technologies developed by Procter and Gamble (P&G). They take two forms. The activated-charcoal based filters (PUR, 2011b) and calcium hypochlorite-based powder (Lougheed, 2006). While the former purifies the water by a combination of particle exclusion and adsorption, the latter relies on a combination coagulation and disinfection. At around $0.075/L - $0.125/L (PUR, 2011a), the former is significantly more expensive of the two types of intervention. The cost of a PuR sachet ranges from $0.003/L (production cost) to > $ 0.010/L (end user cost without subsidy), hence a relatively expensive method (Sobsey *et al.*, 2008).

Reverse Osmosis: In reverse osmosis, contaminated water is forced through a semi-permeable membrane filter that stops the passage of impurities. It is one of the three main "pressure-driven" membrane type technology; the others being ultrafiltration and microfiltration (Grimm *et al.*, 1998). It does not alter the taste or smell of water and can be effective in removal of chemical contaminants. The drawbacks include: high cost, it requires mechanical energy, the purified water is usually devoid of useful minerals, the membrane can be clogged after prolonged usage, and costly to maintain.

Some novel materials that are currently under investigation include: noble metal nanoparticles (Pradeep & Anshup, 2009); conformal nanoporous biomimetic silica-based membranes (Cygan *et al.*, 2008; Jiang *et al.*, 2006); inorganic metal-oxo polynuclear ions plus surfactants or

amphiphiles (Cygan *et al.*, 2008); nanofibrous filter e.g. polysulfone (PSU) and NanoCeram (Kaur *et al.*, 2008; Tepper *et al.*, 2002) and functional DNA based water contaminants sensors (Wernette *et al.*, 2008) amongst others.

Carbon, in the form of activated carbon/charcoal, is the most widely used industrial adsorbent for removal of contaminants and pollutants from gaseous, aqueous, and nonaqueous solution because of its large surface area, complex porous structure, with associated energetic as well as chemical heterogeneities (Brennan *et al.*, 2001; Colella *et al.*, 1998; Nevskaia *et al.*, 2004; Roque-Malherbe, 2007; Singh *et al.*, 1996). However, the discovery of the carbon nanotube (CNT) (Iijima, 1991) has attracted the attention of many scientists due to its unique mechanical properties, electronic, thermal (Ruoff & Lorents, 1995; Salvetat *et al.*, 1999; Xie *et al.*, 2000), physical (large specific surface area), and chemical properties (surface chemistry) (Loh *et al.*, 2010; Tasis *et al.*, 2006). The last two properties are of great interest to researchers who are interested in fundamental studies of CNTs adsorptive properties (Li *et al.*, 2001; Li *et al.*, 2003; Pan & Xing, 2008) and those interested in making an adsorption media out of CNTs (Srivastava *et al.*, 2004). Li et al. (2003) have found that the fluorine-ion sorption capacities of multiwalled carbon nanotube (MWCNTs) are 3-4 times greater than those of activated carbon.

Furthermore, the discovery of graphene (Novoselov *et al.*, 2004), which may be regarded as mother of all graphitic forms (Figure 2.2) has also attracted a lot of attention (Geim & Novoselov, 2007). Like CNTs, graphene has been suggested as a water purifier due to its attractive characteristics (Li & Kaner, 2008). Hence, this thesis will explore the chemical adsorption characteristics of a carbon form ("buckyweb") that contains both carbon nanotubes and graphene.

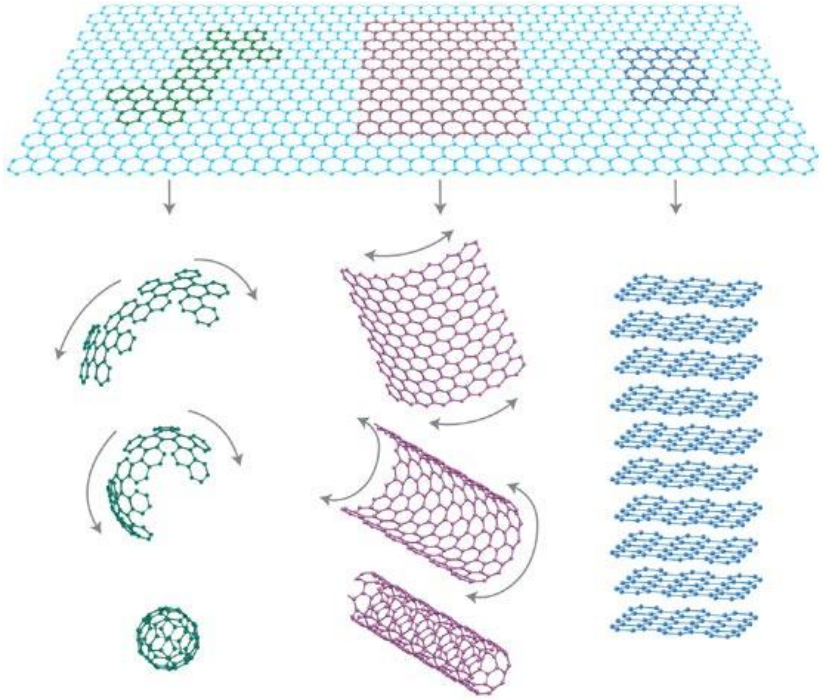

Figure 2.2: Mother of all graphitic forms. It can be wrapped up into 0D buckyballs, rolled into 1D nanotubes or stacked into 3D graphite (Geim & Novoselov, 2007)

2.2 Clays and Clay-based Materials

The uses of clay are ubiquitous and diverse. On a global scale, clays are of major economic significance. They are applied in virtually every aspect of our daily lives. The applications range from medicines to cosmetics, from drilling fluids to paint, and from paper to cups and saucers. It is very difficult to over-estimate their use and importance (Benna *et al.*, 1999; Reeves *et al.*, 2006). So, what exactly is "clay"?

Georgius Agricola, in 1546, was the first to formalize the definition of "clay". He defined clay as (Bandy & Bandy, 1955):

"…mineral bodies that can be worked in the hands when they are moistened and from which mud can be made when they are saturated with water."

This definition has however been revised many times since 1546 (Guggenheim & Martin, 1995). A glance at any comprehensive dictionary will show that clay has a plethora of definitions, scientific and colloquial, often steeped in history and clearly demonstrating that the definition of the word "clay" depends on the context in which it is used, each having developed, over the years, a definition, appropriate for its requirements. The reason for this situation undoubtedly lies in the many and diverse industries in which clay is used, each having developed, over the years, a definition appropriate for its requirements (Reeves *et al.*, 2006).

In 1948, during the 18th International Geological Congress (IGC), clay scientists decided to cooperate on clay research and to form an international group, the Comité Internationale Pour l'Etude des Argiles (CIPEA). A few years later, CIPEA morphed into a new organization, the Association Internationale pour l'Etude des Argile (AIPEA, 2011). The AIPEA nomenclature committees together with the Clay Mineral Society (CMS) nomenclature committees in a joint report has recommended that clay should be defined as (Guggenheim & Martin, 1995):

"*... a naturally occurring material composed primarily of fine-grained minerals, which is generally plastic at appropriate water contents and will harden with [sic] dried or fired. Although clay usually contains phyllosilicates (Figure. 2.3), it may contain other materials that impart plasticity and harden when dried or fired. Associated phases in clay may include materials that do not impart plasticity and organic matter*."

Furthermore, "plasticity" refers to the ability of the clay material to be molded into any shape (Guggenheim & Martin, 1995). Moreover, plasticity can also mean that, within a certain range of

moisture content, the material will deform under application of pressure, the deformed shape being retained when the deforming force is removed (Reeves *et al.*, 2006). "Clay" can be used as a rock term and also can be used as a particle size term in mechanical analysis of sedimentary rocks or soils (Reeves *et al.*, 2006). The definition of clay is not complete without the mention of what clay mineral is. According to the joint committee of AIPEA and CMS:

"The term "clay mineral" refers to phyllosilicate minerals and to minerals which impart plasticity to clay and which harden upon drying or firing"

Clays (and clay minerals) are products of *in situ* alteration or alternatively deposited as sediment during erosional cycle or developed *in situ* as authigenic clay deposit (Reeves *et al.*, 2006). In order words, clays are formed by two paths: (1) near the surface of the Earth by the action of liquid water that originates either on the surface or ground water that is percolating toward the surface (Ries, 1927), and (2) formed under pressure at greater depths due to the action of heated liquid-water or liquid-vapor mixtures (Kerr, 1955). For both conditions, three different possible mechanisms have been proposed for the conversion of aluminosilicate minerals to clays, this are: (a) the direct reaction with water, (b) dissolution and removal of carbonate minerals, leaving insoluble clay impurities behind, or (c) the action of water on compacted shale sediments (Ries, 1927; Shackelford & Doremus, 2008). The classic equation for the chemical reaction for clay formation by decomposition of potash feldspar is given below (Grim, 1962):

$$K_2O \cdot Al_2O_3 \cdot 6SiO_{2(s)} + 2H_2O + CO_{2(aq)} \rightarrow Al_2O_3 \cdot 2SiO_2 \cdot 2H_2O \cdot 2H_2O_{(s)} + 4SiO_{2(s)} + K_2CO_{3(aq)} \quad (1)$$

The reaction involves the disintegration of potash feldspar, due to the action of water-containing dissolved carbon oxide to form insoluble kaolinite, which is the most common clay mineral,

(Figure 2.3, Figure 2.5) and soluble ionic species (Klein *et al.*, 1993; Shackelford & Doremus, 2008). Moreover, different spars [such as albite ($Na_2O \cdot Al_2O_3 \cdot 6SiO_2$) and anorthite ($CaO \cdot Al_2O_3 \cdot 6SiO_2$)], along with many other aluminosilicate mineral can undergo conversion to kaolinite. In reality, the formation of clays is much more complex than depicted in Reaction 1, this is due to the variability in the composition of the feldspar and the minerals that reacts to form clays (Klein *et al.*, 1993) amongst other factors.

Clay minerals are classed as phyllosilicates (Figure 2.3) because they are characterized by two-dimensional sheets which form a layered structure (Klein *et al.*, 1993). The crystal structures of common clay minerals are based on combination of an $(Si_2O_5)_n$ layer (Figure 2.4(a and b)) of SiO_4 tetrahedra joined at the corners with an $AlO(OH)_2$ layer (Figure 2.4(c and d)) of alumina octahedral (Kingery *et al.*, 1976). Kaolinite (Reaction 1) is produced when the oxygen in the Si_2O_5 tetrahedra sheet is shared with the $AlO(OH)_2$ octahedral sheet to give rise to $Al_2(Si_2O_5)(OH)_4$. This schematic for the Kaolinite structure is given in Figure 2.5. While the bonding *within* each unit is covalent and the bonding *between* each unit is relatively weak (usually van der Waal type).

Clay (or clay mineral) is classified based on the way its octahedral and tetrahedral sheets are stacked into layers. If there is one octahedral and one tetrahedral sheet in each layer such clay is called a 1:1 clay. An example is kaolinite. Alternatively, when an octahedral sheet is sandwiched between two tetrahedral sheets, the clay formed is a 2:1 clay. Examples include illite, talc and montmorillonite. Redart clay, which is the host material for the fabrication of the ceramic water filter studied in this thesis, is primarily composed of 10% kyanite; 40% illite; 30% free quartz; 7% red iron and 15% mixed layered clays (Davis & Davis, 2004).

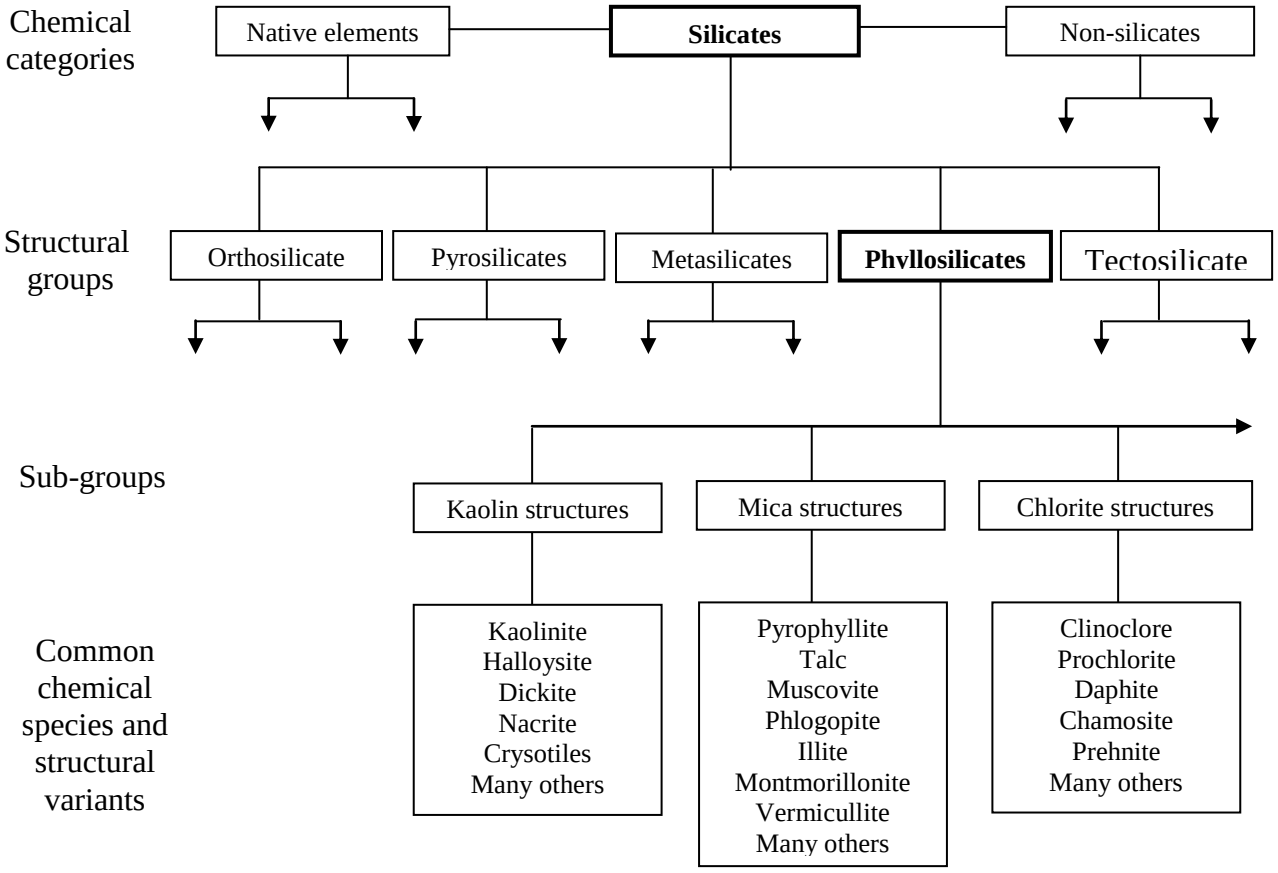

Figure 2.3: Mineralogical classifications associated with clay minerals (Shackelford & Doremus, 2008)

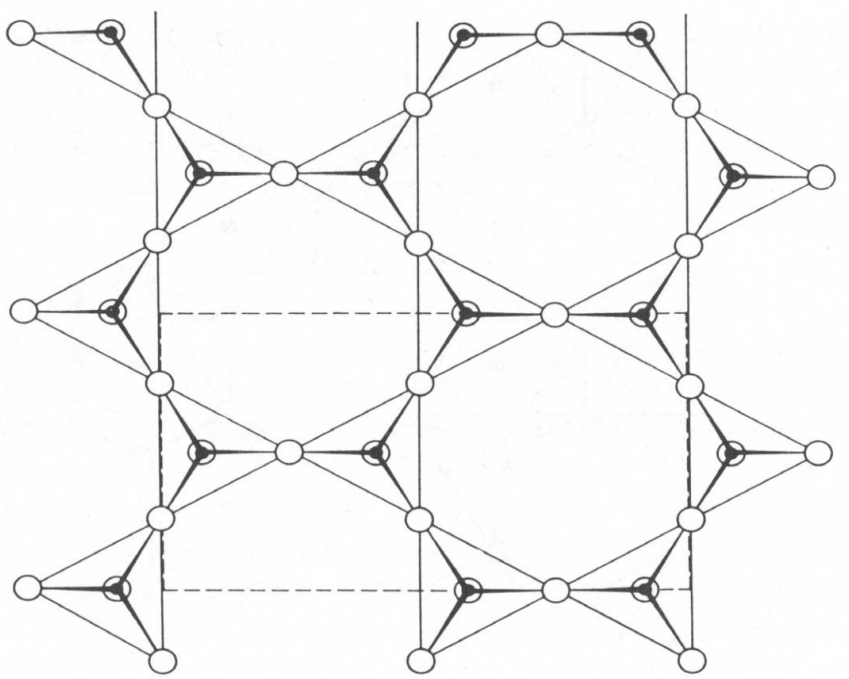

(a)

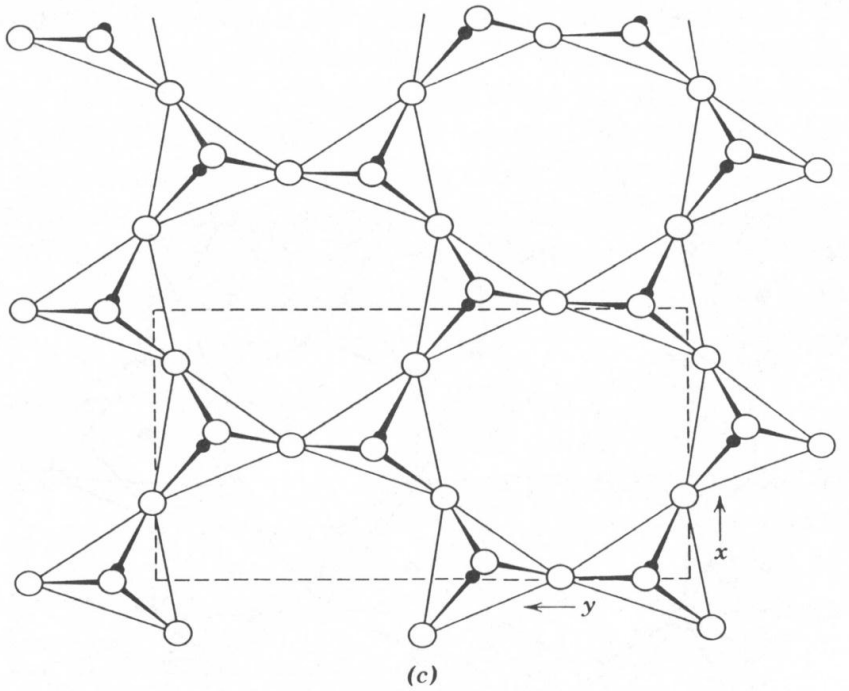

(c)

● Silicon ○ Oxygen

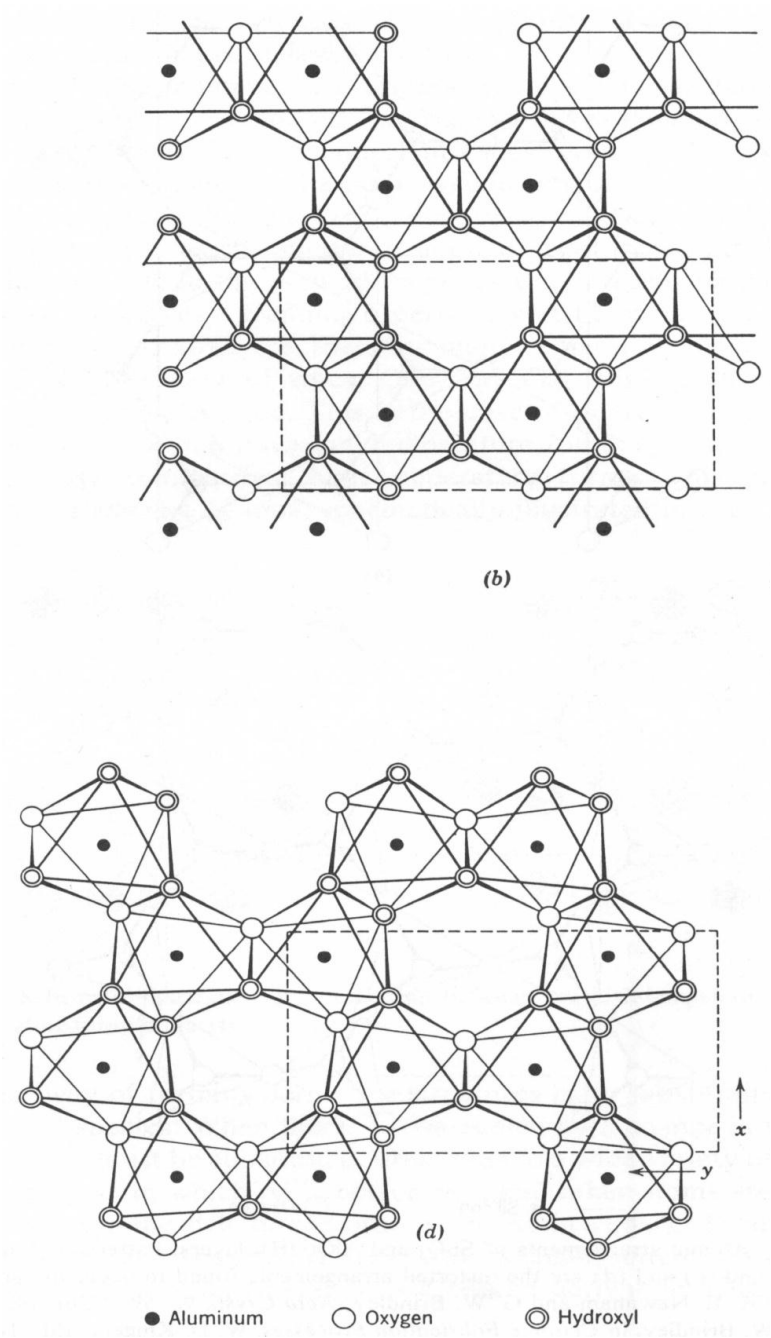

Figure 2.4: Atomic arrangements of Si_2O_5 and $AlO(OH)_2$ layers. Patterns (a) and (b) are idealized, and (c) and (d) are the distorted arrangement found to occur in kaolinite and dickite. (Kingery, 1958)

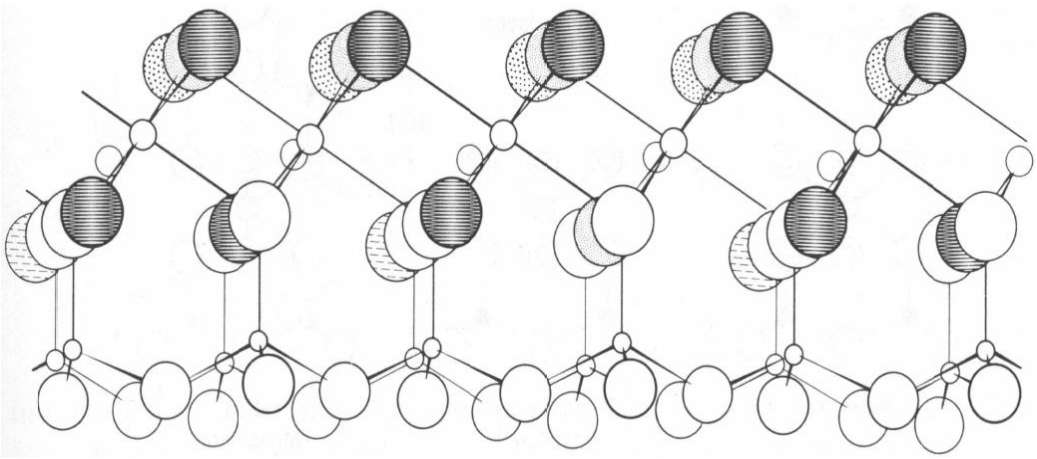

Figure 2.5: Perspective drawing of kaolinite with Si-O tetrahedrons on the bottom half of the layer and Al-O, OH octahedrons on the top half (Kingery, 1958).

Besides clay being built from different layer combinations it is also built with different cation combinations. Clay minerals can combines with different cations by isomorphous substitution or any other means. This may involve the substitution of Al^{3+} ion in the octahedral sheet with Fe^{3+} or Mg^{2+} ion to form more complex structures. It is also possible for the Al^{3+} ion in the octahedral sheet, and/or Fe^{3+}, to substitute the Si^{4+} ion in the tetrahedral sheet. However, the substitutions results in a net negative charge in the structure. The resulting charge is nullified by alkali (Na^{+}, K^{+}) or alkaline earth (Ca^{2+}, Mg^{2+}) cations which binds either between the layers of the structural units or within the open space inside the Si_2O_5 tetrahedral or on the surface the particle (Kingery *et al.*, 1976; Shackelford & Doremus, 2008). The substituted ions are responsible for the clays base exchange capacity. For example, a natural clay containing absorbed Ca^{2+} can react with sodium silicate to form insoluble calcium silicate and the sodium clay, as given in Reaction 2 (Kingery *et al.*, 1976):

$$Clay\text{ - }Ca^{2+} + Na_2SiO_3 = Clay \begin{matrix} \diagup Na^+ \\ \diagdown Na^+ \end{matrix} + CaSiO_3 \qquad (2)$$

Reaction 2 is an important determinant of the behavior of clays in aqueous solution. Furthermore, such a reaction may be responsible for the removal of fluoride from water, as the calcium (or any other substituted ion) may react with the fluorine ion in water to form calcium fluoride (Yakub & Soboyejo, Submitted for publication). In addition, by varying site occupancy and layer orders an almost infinite number of clay minerals can be conceived (Shackelford & Doremus, 2008).

One of the most important properties of clay is its rheological properties. It is known to be a function of pH of solution, structure, particle size, shape, and surface characteristics of the dispersed phase (Solomon *et al.*, 2001). Controlling the rheological property of clay is often indispensable in industrial processes and practical applications involving ceramics processing (melt-processing behavior such as injection molding) or paper coating (Penner & Lagaly, 2001; Solomon *et al.*, 2001). Moreover, this property has allowed for the development of clay-based composites and nanocomposite materials.

Numerous types of polymers/clay hybrids have been made by blending different polymers with (mainly organophilic) clays. Such polymers include the use of polypropylene (Kawasumi *et al.*, 1997; Solomon *et al.*, 2001, Reichert *et al.*, 2000), nylon 6 (Cho & Paul, 2001), polyimides (Zhu *et al.*, 1999), polyethylene oxide (Vaia *et al.*, 1997), polycaprolactone (Jimenez *et al.*, 1997), polymethyl methacrylate (Biasci *et al.*, 1994), epoxy resin (Messersmith & Giannelis, 1994; H. H. Wang & Shiao, 1994; Z. Wang & Pinnavaia, 1998), polyolefins (Furuichi *et al.*, 1996; Kato *et al.*, 2011), polyurethanes (Wang & Shiao, 1994), polycarbonate (Kato *et al.*, 2011; Lee *et al.*, 2011), rubber (Kato *et al.*, 2011) and so on. Clay has also been blended with combustible

materials (e.g. sawdust) (Yakub *et al.*, Submitted for publication-a; Yakub *et al.*, Submitted for publication-b), hydroxyapatite (Friedman, 2010; Yakub & Soboyejo, Submitted for publication), iron oxide (Brown & Sobsey, 2009; Tsao, 2011) to mention a few.

While polymers are usually hydrophobic, clay is hydrophilic in nature. The synthesis of polymer-clay composites (PCCs) involves the preparation of organophilic clay. This can be accomplished by introducing surfactants (such as aliphatic amines) and alkylammonium salt (such as dioctadecyldimenthyl ammonium bromide) into the clay layer by cation exchange reaction (Solomon & Hawthorne, 1991). The intercalated amine species improves the compatibility of the clay with the polymer (Usuki *et al.*, 1993). There are two main types of methods of making PCC: *in situ* polymerization or melt mixing method. For the *in situ* polymerization method, the polymer precursor is infiltrated into intercalated organophilic clay where it polymerizes (Solomon *et al.*, 2001). The second method simply involves simply melt mixing the organophilic clay with the polymer (Vaia *et al.*, 1993). The blended polymer may then be further processed using the different processing techniques (Figure 2.3). Like the formation of alloys with metals, the formation of composites usually results in desirable and enhanced physical, chemical, mechanical and thermal properties (Cho & Paul, 2001; Friedman, 2010; Jimenez *et al.*, 1997; Kawasumi *et al.*, 1997; Reichert *et al.*, 2000; Solomon *et al.*, 2001; Tsao, 2011; Vaia *et al.*, 1997; Yakub *et al.*, Submitted for publication-a; Yakub *et al.*, Submitted for publication-b; Yakub & Soboyejo, Submitted for publication).

Figure 2.6 highlights the different methodologies by which clay (or ceramic) powder, mixed with or without other types of materials including clay, may be processed into green ware and then finally into sintered ceramic. First, the clay powder (or different clay powders and other materials) is produce by crushing the lump of material into fine particles using milling or other

techniques. The fine powder may then be blended with other materials, e.g. sawdust in the case of ceramic water filters (Yakub *et al.*, Submitted for publication-b), or with a surfactant (as described in the previous paragraph) or otherwise. The resulting mixture, which may or may not be dried, is then mixed with a binder, e.g. water, in the case of ceramic water filters (Yakub *et al.*, Submitted for publication-b) or plasticizers (as described in previous paragraph) or otherwise. This concludes the powder processing stage.

The processed powder may be further formed using techniques such as: slip (or solid and drain) casting, tape casting, dry pressing, extrusion, injection molding and compaction (Figure 2.6). Though compaction is the easiest, fastest and most cost-effective shaping method, the choice of forming method is often dictated by the desired shape of the final product (Shackelford & Doremus, 2008). The ceramic water filters are usually compacted into frustum shaped greenware using an hydraulic or manual press (Yakub *et al.*, Submitted for publication-a; Yakub *et al.*, Submitted for publication-b) and then allowed to dry in ambient condition. The drying rate must not be too high as this may result in warping and possibly cracks.

The next process involves sintering (or firing) of greenware at high temperature. The firing temperature is determined by the desired properties and composition of the end product. The rate of increase in temperature is usually determined by trial and error and/or experience. Care must be taken as firing at a high rate may lead to breakage of the greenware due to thermal shocking. Sintering results in the consolidation of greenware materials by reduction of its surface area. Most ceramic materials are crystalline and the transport process that permits sintering is diffusion (otherwise the transport process is viscous flow for amorphous (glassy) greenware materials).

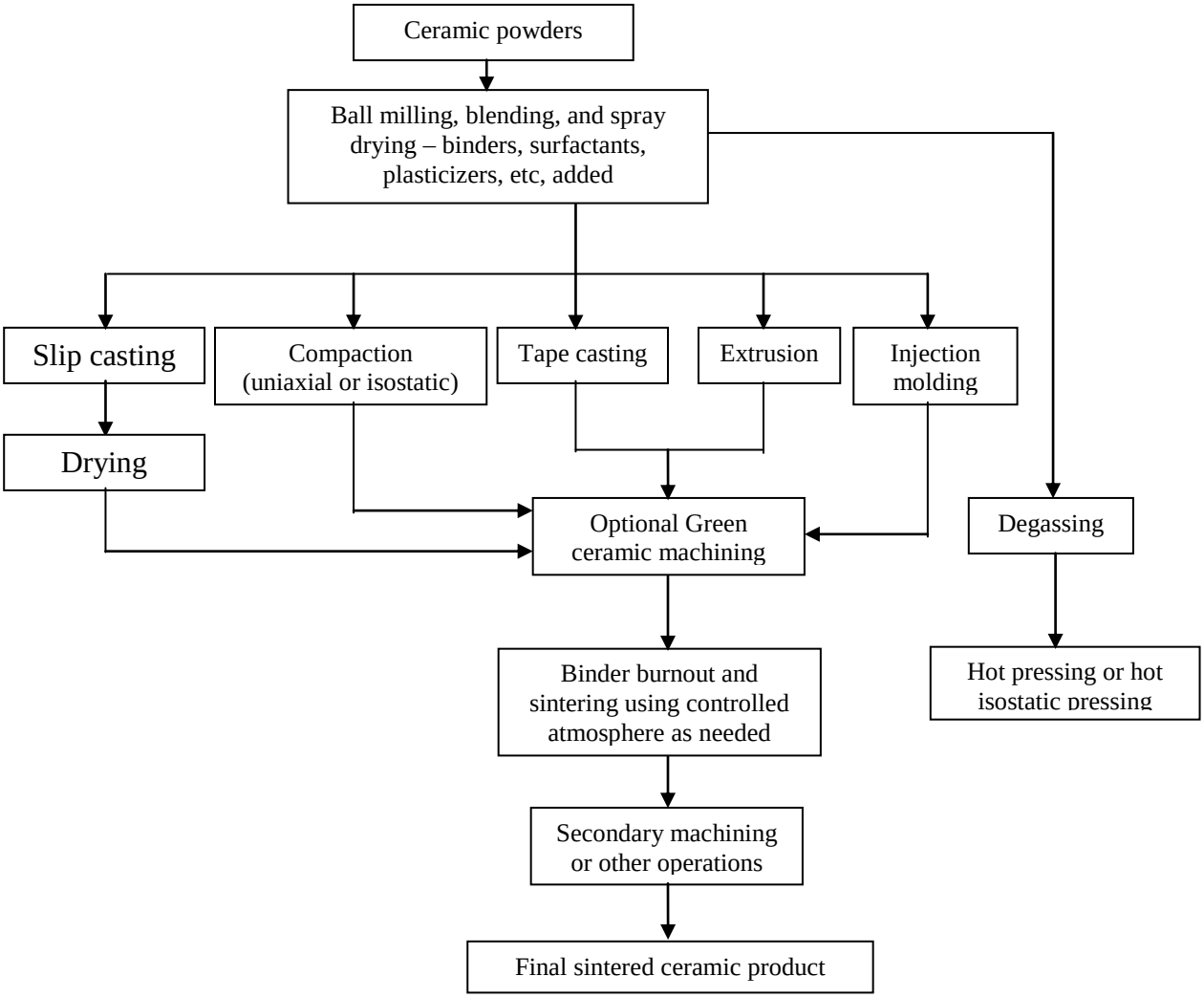

Figure 2.6: Different techniques for processing of advanced ceramics (Askeland & Phulé, 2006)

Sintering (or firing) usually results in (further) reduction in porosity, increase in density (densification) and an increase in strength of the material. During sintering, the volume shrinkage which occurs is just equal to the porosity decrease and varies from a few to 30 or 40 vol%, depending on the forming process and the ultimate density of the fired ware (Kingery *et al.*, 1976). The sintered ceramic may then be further processed, depending on the intended application, by processes such as: cutting, e.g. preparation of elongated bars for fracture mechanics testing (Yakub *et al.*, Submitted for publication-a); polishing, e.g. for microstructure analysis; or dip-coated with silver (Oyanedel-Craver & Smith, 2008).

2.3 Fundamentals of Porosimetry and Flow through Porous Media

All water filtration technologies have one thing in common, they contain pores. For the filters to work effectively, they must contain pores that are small enough that prevent the passage of microbes yet large enough for water to flow through. For porous ceramics, the shape and distribution of the pores, as well as the porosity (defined as the percentage of the ratio of total volume of pore to total volume of solid matrix and pore), not only determines how well the media filters out particulates suspended in liquid but also the strength properties of the media. Other important factors include the volumetric flow rate of fluid through the filter and the bacteria removal efficiency. These may scale, respectively, with the intrinsic permeability and tortuosity. It is, therefore, imperative to characterize the porous structures of ceramics that are used in water filtration.

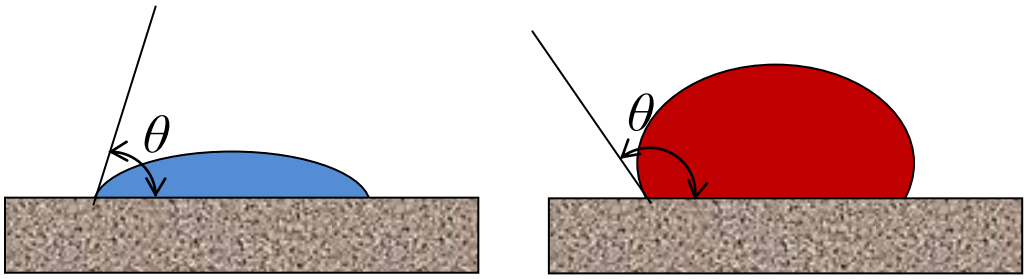

Figure 2.7: Contact angle, θ of two liquids placed on a surface: (a) θ < 90, a wetting liquid and (b) θ > 90, a wetting liquid

Figure 2.7 presents schematics of a wetting liquid (e.g water) droplet and non-wetting liquid (e.g. mercury) droplet placed on a solid substrate. Water, like many other liquids, is seen to have a contact angle < 90°, while the mercury has a contact angle > 90°. This is because of the relative difference in surface energy (or surface tension) of the liquids and the substrate. In general, when a liquid has a lower surface energy than its substrate it tends to spread out (or "wets" the surface) and forms an acute angle with the substrate. However, if the liquid has a higher surface energy than its substrate, it tends to form a bead and make an obtuse angle with the substrate. One implication of this is the acute contact angle that is observed in capillary tubes that contain water (Figure 2.8a) and obtuse angle of contact in capillary tubes that contain non-wetting fluids such as mercury (Figure 2.8b).

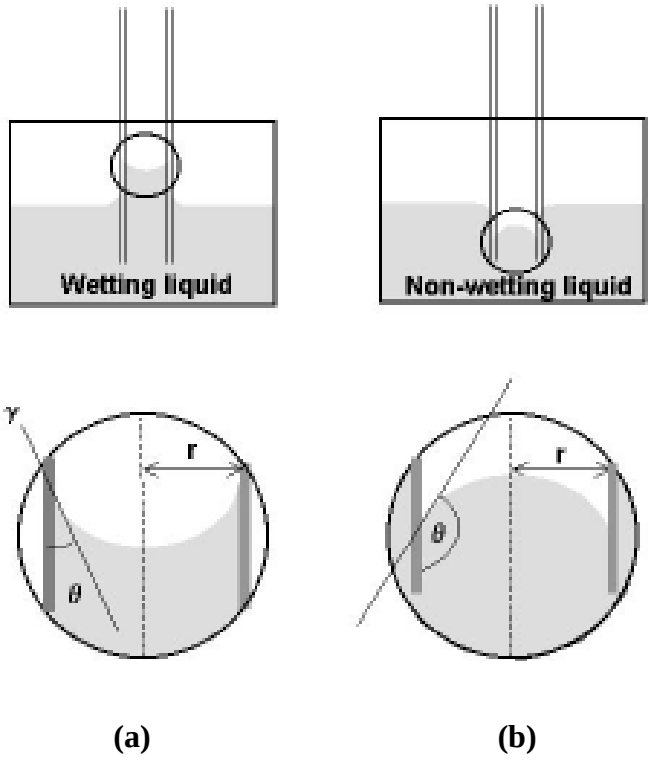

Figure 2.8: Behavior of: (a) wetting and (b) non-wetting liquids with respect to a capillary tube (Webb, 2001)

Figure 2.8 shows what will happen when a capillary tube is inserted in containers holding a wetting and a non-wetting liquid, respectively. As shown in the figure, the wetting liquid rose in the tube and the non-wetting liquid experienced a capillary depression. The consequence of the latter is that pressure (greater than ambient) will have to be applied to the non-wetting fluid in other for it to rise in the tube. The fact that mercury is non-wetting and that pressure is needed to force it through channels is what makes mercury a substance of choice for the characterization.

The pressure required to push a liquid into a pore of a given radius can be derived from Laplace's equation, which may be expressed as:

$$\Delta P = \gamma_{LG} k_{LG} \qquad (1)$$

where is ΔP is the difference between the pressure in the liquid and in the gas, i.e $P_L - P_G$, and for the purpose of porosimetry, ΔP is equivalent to the applied pressure; γ_{LV} is the liquid/gas interfacial free energy and $k_{LG}\,(= -\,k_{GL})$ is the curvature of the liquid surface in the gas medium, which may be defined by:

$$k = \frac{dA}{dV} \qquad (2)$$

where A is the surface area and V is the volume of the liquid. For a cylindrical liquid with $A = 2\pi rl$ and $V = \pi r^2 l$, the curvature of the surface (if the length, l can be extended while keeping the radius, r constant) is:

$$k = \frac{2\pi r \cdot dl}{\pi r^2 \cdot dl} = \frac{2}{r} \qquad (3)$$

Now if the liquid is a pore with radius r_p and if the contact angle between the liquid and pore wall is θ (Figure 2.9), the radius of meniscus, r is given by:

$$r = -\frac{r_p}{\cos(\theta)} \qquad (4)$$

Substituting equation (2) and (3) into equation (1):

$$\Delta P = \frac{-2 \cdot \cos(\theta) \cdot \gamma_{LV}}{r_p} \qquad (5)$$

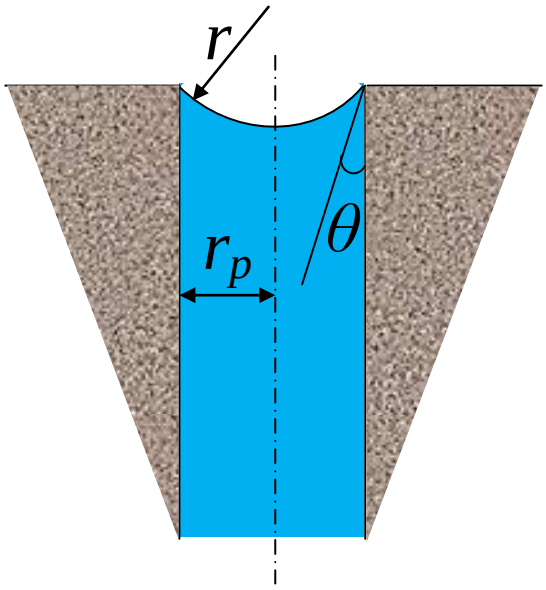

Figure 2.9: Liquid in a pore with radius r_p

The expression above is called the Washburn equation. It is named after the person who first derived it and suggested that it can be used to characterize the pore size of materials using mercury (Washburn, 1921). It was not until about 20 years after the derivation of the equation that Henderson *et al.* applied the suggestions of Washburn to determine the pore size distribution of a number of clays and bauxite. Subsequently, 4 years later, Ritter and Drake constructed the first mercury porosimeter (Ramachandran *et al.*, 2001; Vanbrakel *et al.*, 1981).

Despite the wide variety of mercury porosimeters that have been built over the years, the principle of operation remains the same (Ramachandran *et al.*, 2001). The operation involves: placing the sample into a container (dilatometer or penetrometer), evacuating the container to remove any contaminant gases, water vapor and adsorbate that may be present and then allowing mercury to fill the container (Webb, 2001).

Pressure on the mercury is then raised slowly to the maximum pressure, which is typically around 414 MPa (60,000 psia). The build-up of the pressure must not be too high, since time is needed for the transport of mercury through the porous network of the material (Ramachandran *et al.*, 2001). As the pressure is raised, more and more pores as well as smaller size pore are invaded with mercury. The size of the intruded pores is found from the Washburn equation (equation 5). Also, the volume of the invaded pores is related to the volume of mercury that has been forced into it. This can be used to find the *porosity* of the material (once the total intrusion volume is known). Although, with an applied pressure of 414 MPa, a mercury porosimeter should be able to detect a pore radius of ~1.66 nm, some porous materials have much smaller pore radius. Therefore, for more accurate result, mercury porosimetry is complemented with gas adsorption techniques such as helium pycnometers and nitrogen adsorption.

Beyond the porosity, it is also important to characterize the permeability of a porous material. The permeability of a material may be described as the ease by which a fluid flows through the material. The work of Katz and Thompson provides a way of determining the permeability of a material from mercury intrusion experimental data. The Katz-Thompson equation is given by (Katz & Thompson, 1987):

$$k = \frac{1}{89} L_{max}^2 \frac{L_{max}}{L_c} \emptyset S(L_{max}) \qquad (6)$$

where, k is intrinsic permeability; L_{max} is the pore size at which conductance is maximum; L_c is the pore breakthrough size, which is determined from the mercury depression curve; $\emptyset$ is the porosity of the filter and $S(L_{max})$ is the fractional volume of connected pore space composed of pore widths of size L_{max} and larger.

This equation has been used to determine the permeability of a wide range of porous materials (Crowley *et al.*, 2004; Eldieb & Hooton, 1994; Garboczi & Bentz, 2001; Hooton *et al.*, 2001; Van Halem, 2006).

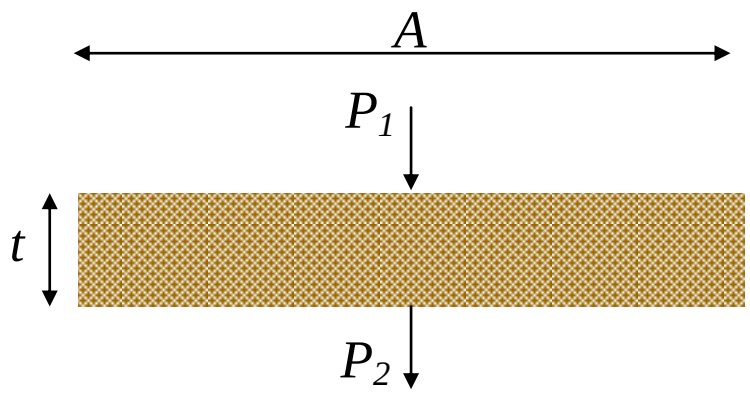

Figure 2.10: Flow through a permeable media with thickness *t*

Flow through a porous material may be described by Darcy's law. Figure 2.10 is an example of a permeable media with a pressure on the faces as shown. According to Darcy's law, the flow rate, *Q*, of fluid through the media is:

$$Q = \frac{\kappa A}{\mu t}\Delta P \qquad (7)$$

where κ is the permeability of the material, *A* is the cross-sectional area, *t* is the thickness of the material, μ is the dynamic viscosity of the fluid (water) and ΔP is the pressure difference from the top to the bottom of the surface (i.e. $P_1 - P_2$) or the initial and final pressure.

Darcy's law can be used to describe flow of fluid through different geometries and shapes. Fahlin (Fahlin, 2003) and van Halem (Van Halem, 2006) has previously applied different variations of the equation to the modeling of flow through porous ceramic water filters.

Another important equation for flow through pipe channels is the Poiseuille law (or sometimes called the Hagen-Poiseiulle law). This law is applicable to laminar, viscous and incompressible flow and is given by:

$$Q = \frac{\pi r^4}{8\mu l}\Delta P \qquad (8)$$

Where, Q is the volumetric flow rate, r is the radius of the pipe, μ is the dynamic viscosity of the fluid (water) and ΔP is the pressure drop across the pipe of length, l.

Furthermore, tortuosity of a porous medium is another important parameter. While the level of permeability of a porous ceramic gives a measure of the relative ease at which water (or any other fluid) will flow through it, the tortuosity gives an indication of the chances of capture of contaminants, say *E.coli* bacteria, carried along with the water by processes such as adsorption, geometrical occlusion and sedimentation. Tortuosity may be defined as the ratio of the effective length of a connected (or through) pore to actual length (or thickness) of the porous media.

By combining Darcy's law (equation 6) with the Poiseuille's law (equation 7) and applying what is known as the capillary bundle model (in which pores are treated as bundle of capillary tubes of varying sizes), Hager (Hager, 1998) derived an expression for the tortuosity. This is given by:

$$\tau = \sqrt{\frac{\rho_S}{24k(1 + \rho_S V_{tot})}\int_{\zeta = r_{c,min}}^{\zeta = r_{c,max}} \zeta^2 f_v(\zeta) d\zeta} \qquad (9)$$

where, τ is materials' tortuosity; ρ_s is the material skeletal density; k is material permeability; V_{tot} is the total pore volume of the material and $\int_{\zeta=r_{c,min}}^{\zeta=r_{c,max}} \zeta^2 f_v(\zeta) d\zeta$ is the pore volume distribution by pore size.

It is important to note here that the tortuosity, τ, defined by equation 9 can be obtained from parameters found using the mercury intrusion porosimetry. However, because mercury cannot intrude into all of the small pores, a more accurate value of tortuosity is obtained from skeletal density determined from gas pycnometry (Webb, 2001).

The four main types of biological contaminants in water are: helminthes, protozoans, bacteria and viruses (Table 2.2). Though, helminthes are not unicellular organisms, they are important waterborne pathogens because their ova (eggs) and waterborne larval stages can be waterborne (Sobsey, 2002). Protozoa are around ~ 3 – 30 µm in size. They are biggest unicelullar waterborne pathogens. Next are bacteria with sizes around ~ 0.5 - 3µm. They are somewhat smaller than protozoa. Viruses are the smallest waterbone microbes, ~20 – 100 nm (Sobsey, 2002). Filter design should have pores that are smaller in size than biological pathogens. Filters should also have a high tortuosity, high permeabilities and flow rates to consistently supply the required amount of water to their user. For drinking, the required daily consumption of water is approximately 2 liters per day for adults (WHO, 2011b).

The daily water need of each individual can vary widely, and as a result there is currently no recommended dietary allowance (which is the intake that meets the nutrient needs of almost all individuals) for water because scientific evidence is inadequate to set an estimated average requirement (which is the intake that meets the estimated nutrient needs of 50% of individuals per gender in a given life-stage) (Wenhold & Faber, 2009). Furthermore, adequate domestic

water is needed for food preparation, laundry and person and domestic hygiene (WHO, 2011b) and so it has been proposed that each person have access to 50 liters of clean water per day (Gleick, 1998).

2.4 Fundamentals of Adsorption

While the removal of microbes from water is done using particle size occlusion, chemical contaminants can also be removed from water by a process of adsorption. Adsorption is the enrichment of one or more component in an interfacial layer (Gregg & Sing, 1982). Adsorption is different from absorption, where molecules enter the solid phase. Adsorbent is the term used to describe the material onto which adsorption occurs, while the adsorbate is the adsorbed material or species. Adsorption processes may include: physical adsorption (usually van der Waals or dispersion forces), chemical adsorption (or chemisorption), chelation and ion exchange.

Adsorption from liquid phase depends on the system conditions, such as initial concentration of adsorbent, type and surface area of adsorbent, adsorbent surface chemistry, mass of adsorbent (or solid-liquid ratio), solution pH, ionic strength of solution, contact time, solubility of adsorbate in the solvent, and temperature (Bower & Hatcher, 1967; Chen *et al.*, 2010; Díaz-Nava *et al.*, 2002; Meenakshi *et al.*, 2008; Roque-Malherbe, 2007; Sundaram *et al.*, 2008). For the removal of contaminants from water, there are two physicochemical aspects for the evaluation of an adsorption process. These are the equilibrium adsorption capacity of the adsorbent and the adsorption kinetics (Ho *et al.*, 2000).

For a solution containing adsorbent and adsorbate, the amount of adsorbate adsorbed at equilibrium, or adsorption capacity of the adsorbent, q_e (mg/g), is defined as the mass of the adsorbate adsorbed per unit mass of adsorbent. This is given by:

$$q_e = \frac{10^{-3}(C_i - C_e)V}{m} \qquad (10)$$

where C_i (mg/L) is the initial concentration of the adsorbate, C_e (mg/L) is the concentration of adsorbate at equilibrium, V (mL) is the volume of the solution, and m (mg) is the mass of the adsorbent used.

Equilibrium is said to be established when the concentration of the adsorbate in the bulk solution is in dynamic balance with that of the interface of the adsorbent(Ho *et al.*, 2000). The equilibrium adsorption capacity of an adsorbent changes with the equilibrium concentration of the solution. One way of modeling such dependency is the use of isotherms. Adsorption isotherms express the specific relation between the concentration of adsorbate and its degree of accumulation onto adsorbent surface at constant temperature (Sundaram *et al.*, 2008). The most widely used isotherm models are the Freundlich and Langmuir isotherms (Roque-Malherbe, 2007). The Langmuir isotherm can be derived from kinetic gas theory (Gregg & Sing, 1982; Liu *et al.*, 2005), while the Freundlich isotherm has historically been an empirical equation, although there have been attempts to derive it from first principles (Appel, 1973; Liu *et al.*, 2005; Sips, 1948; Skopp, 2009; Yang, 1998). The respective mathematical representations of the Freundlich and Langmuir models are:

$$q_e = K_f \, C_e^{1/n} \qquad (11)$$

$$q_e = \frac{q_m K_l C_e}{1 + K_l C_e} \qquad (12)$$

Where $1/n$ and K_f ($mg^{1-1/n}L^{1/n}g^{-1}$) are Freundlich constant related to adsorption intensity and adsorption capacity, respectively, while q_m (mg/g) and K_l (L/mg) are Langmuir constants related to adsorption capacity and the affinity of the binding cite, respectively.

The linearized forms of Equations 11 and 12 are given below:

$$\ln(q_e) = \frac{1}{n}\ln(C_e) + \ln(K_f) \qquad (13)$$

$$\frac{1}{q_e} = \frac{1}{q_m b}\frac{1}{C_e} + \frac{1}{q_m} \qquad (14)$$

The Freundlich constants are extrapolated from the plots of $\ln(q_e)$ versus $\ln(C_e)$, while the Langmuir constants can be extracted from plots of $\frac{1}{q_e}$ versus $\frac{1}{C_e}$

It is also important to be able to characterize the adsorption kinetics process. Theoretically, the mass transport of adsorbate in porous adsorbent normally takes three consecutive stages (Chen *et al.*, 2010; Fan, 2003; Meenakshi *et al.*, 2008):

(a) The first stage is the mass transfer or diffusion across the bulk fluid to the external surface of the adsorbent (sometimes called bulk diffusion or external mass transfer);

(b) The next stage is the intra particle (or pore) diffusion of the species through the liquid-filled pores and

(c) The final stage is the adsorption of adsorbate at the adsorption sites of the adsorbent (or the equilibrium adsorption stage).

The rate-limiting step is the step that determines or controls the overall rate of uptake. The third step is usually rapid and does not contribute to the rate of adsorption of the adsorbent. The rate of adsorption is usually controlled by either stage 1 or 2 or both. The adsorption kinetics of chemicals from water (by the walls of a porous material) is controlled by diffusion. In order to understand this process diffusion-based models, such as models developed by Chanda *et al.* (1983), equation 15, and Weber and Morris (Weber & Morris, 1964), equation 16, may be applied to adsorption kinetics data:

$$\ln(1-\alpha) = -k_p t \qquad (15)$$

$$\mathrm{q_t} = k_d t^{0.5} \qquad (16)$$

where, α is the fractional attainment of equilibrium, i.e, the ratio of the amount of the adsorptive ion removed from water at any given time, t (min), to that removed from water at equilibrium; $\mathrm{q_t}$ is the amount of adsorptive ion that is adsorbed at any given time, k_p ($\mathrm{min^{-1}}$) is particle rate constant and k_d ($\mathrm{mg/g\ min^{½}}$) is the intra particle rate constant

Furthermore, adsorption is not only limited to the removal of chemical species, but also particulates including microbes – a process which may be termed "Adhesion". A brief overview of the fundamentals of adhesion and contact mechanics is given in theory section of Chapter 4.

2.5 Strength and Fracture of Brittle Materials: The Fundamentals

Brittle Material Behavior

Ceramic water filters (CWFs) are brittle, so it is important to review the strength and fracture of brittle materials. Also, as mentioned earlier, a key attribute of the ceramic water filter is that it

contains pores. This allows them to filter out microbes, while allowing water to pass through. Ironically, the presence of the pores (or flaws) is what makes them susceptible to failure (especially during transportation of the filters). Moreover, the strength of a ceramic is dependent on its porosity, pore morphology, distribution of flaw sizes, grain size and microstructure (Deng *et al.*, 2001; Knudsen, 1959; Rice, 1993,1996). There is, therefore, a need to understand the behavior of compositionally different CWFs under the application of stress.

It is difficult to measure the mechanical strength of a brittle ceramic material by normal tensile testing, which requires mounting the specimen in tight grips without fracturing the material (Chung, 2007). Moreover, they are very weak in tension and fail after relatively low strains (Figure 2.11). However, filters are relatively strong in compression, similar to most ceramics that can support high levels of compressive stress. As a matter of fact, the weight of an entire firetruck can be supported on four ceramic coffee cups (Askeland *et al.*, 2010).

Furthermore, because of the difficulty in gripping brittle materials, they are usually tested using three- or four- point bend loading conditions. This technique can be used to find the modulus of rupture (or flexural strength) of the material, which is measure of the material's strength. A measure of the stiffness of a brittle material is the elastic modulus. Although the elastic modulus may be found by applying the standard formula for finding the elasticity of a beam (Equation 17) to a bend test, the problem is the result is very dependent on the accuracy of the measured deflection.

$$E = \frac{PS^3}{48I\delta} \qquad (for\ three\ point\ loading) \qquad (17)$$

where S is the loading span, P is the applied load, I is second moment of area (in this case, given by $WB^3/12$. Where B is the breadth and W is width, of the specimen), and δ is the deflection of beam.

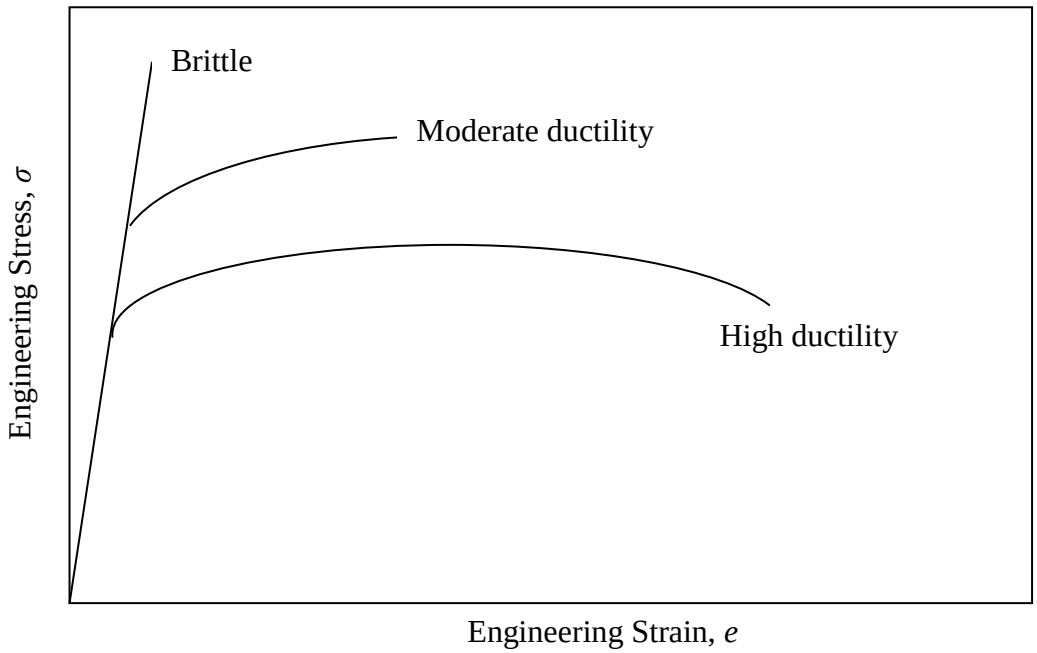

Figure 2.11: Schematics of the stress-strain behavior of brittle materials compared with that of more ductile material.

A more reliable way of measuring the modulus of a material is by nanoindentation. The process involves the use of a hard (usually diamond) tip that is pressed into the specimen. This causes some deformation and leaves a residual impression from which mechanical properties such as elastic modulus and hardness can be measured. However, a more suitable method is the use of the recorded load-displacement data (Fig. 2.12).

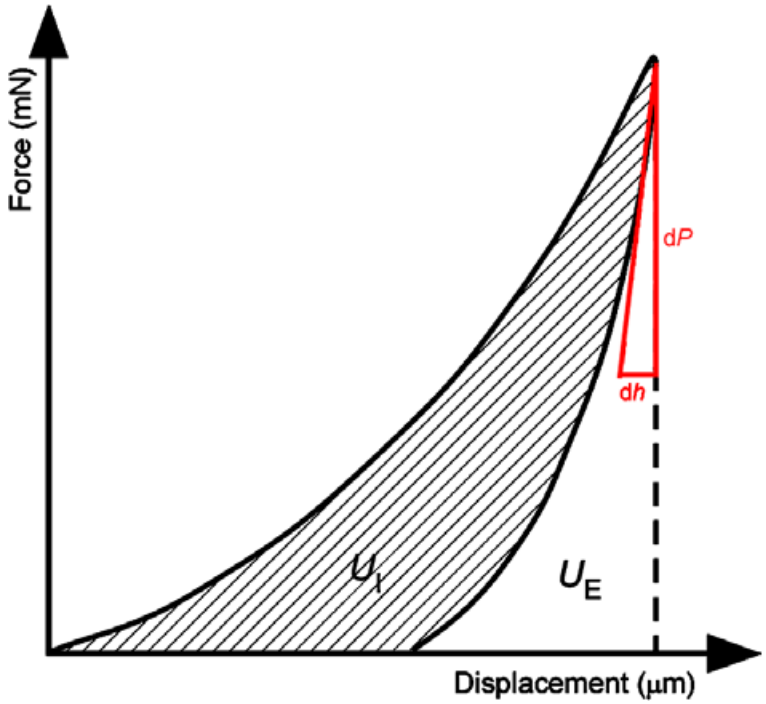

Figure 2.12: Schematic of typical nanoindentation load-displacement plot. U_I is the unrecoverable elastic energy and U_E is the recovered elastic energy during unloading (He *et al.*, 2008)

The figure shows a schematic representation of a typical load-displacement curve obtained from one indentation loading and unloading plot. The standard procedure for obtaining the Young's modulus and hardness from the load-displacement characteristics was developed by Doerner and Nix (Doerner & Nix, 2011) and Oliver and Pharr (Oliver & Pharr, 1992). The contact stiffness, *S* is found from the slope of the initial unloading curve. This is given by:

$$S = \frac{dP}{dh} = \frac{2E_r}{\sqrt{\pi}}\sqrt{A} \qquad (18)$$

where, P is the indentation load, h is the indentation depth relative to the initial untouched surface, E_r is the reduced elastic modulus and A is the projected contact area which is found from the area function:

$$A(h_c) = C_0 h_c^2 + C_1 h_c + C_2 h_c^{\frac{1}{2}} + C_3 h_c^{\frac{1}{4}} + C_4 h_c^{\frac{1}{8}} + C_5 h_c^{\frac{1}{16}} \qquad (19)$$

The constants C_1 through C_5 can be determined by carrying out a series of indentations at different depths on a standard material (e.g. fused silica) and employing curve- fitting procedure. For an indenter with spherical tip geometry (with radius R), $C_0 = -\pi$ and $C_1 = 2\pi R$. Equation (18) may be re-written as:

$$E_r = \frac{S}{2}\frac{\sqrt{\pi}}{\sqrt{A}} \qquad (20)$$

However, the reduced modulus E_r accounts for the fact that the measured displacement includes contribution from both the specimen and the indenter (Hysitron, 2010). The reduced modulus is related to the elastic modulus of the indenter and specimen according to:

$$\frac{1}{E_r} = \left(\frac{1-v^2}{E}\right)_{indenter} + \left(\frac{1-v^2}{E}\right)_{specimen} \qquad (21)$$

where, v represents the poisson ratio. While the elastic modulus of the specimen is found from Equation 21, the hardness, H, of the specimen is found from:

$$H = \frac{P_{max}}{A} \qquad (22)$$

Furthermore, it is important to be able to quantify the resistance of the material to resist cracking (or fracture toughness), and the resistance-curve (or R-curve) behavior of the material as the crack propagates. These will be described later after presenting some fundamentals of fracture mechanics.

Griffith was the first person to propose a thermodynamic criterion for unstable crack extension in a brittle solid (Griffith, 1921). The law states that:

"A crack will advance if the release of strain energy is greater than the energy invested to create the new surface (i.e., exposed surface of the crack)"

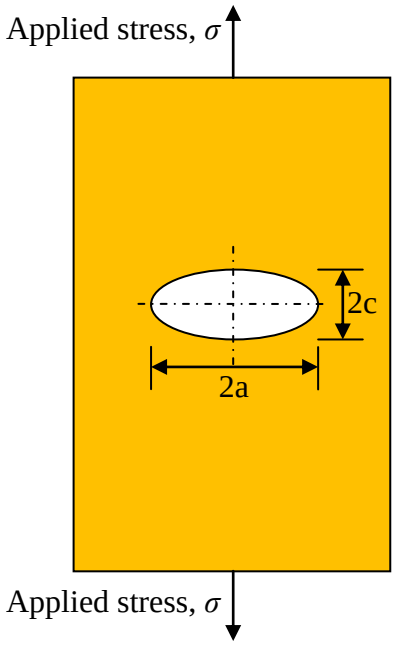

Figure 2.13: An elliptical flaw of size *2a* at the centre of a plate with thickness, *B*, subjected to uniaxial loading

Using thermodynamic arguments and the concept of notch concentration factors from previously developed by Inglis (Inglis, 1913) for an elliptical flaw in a plate subjected to uniaxial loading (Fig. 2.13), Griffith was able to obtain a condition for unstable crack growth in brittle materials, such as glass. This is given by:

$$U = -\frac{\pi\sigma^2 a^2 B}{E'} + 4aB\gamma_s \qquad (23)$$

where, σ is the applied stress, a is the crack length, B is the thickness of the plate, $E' = E/(1-\nu^2)$ for plane strain condition and $E' = E$ for plane stress condition, E is the Young's modulus of the material, ν is the poisson ratio, γ_s is the free surface energy per unit area and the product $4aB$ is the total surface area of the crack faces. Moreover, the first term represents the net potential energy or the stored strain energy in the body and the second term represents the surface energy of the crack in the plate. The criterion for crack stability is:

$$\frac{dU}{da} = 0 \qquad (24)$$

Thus, the critical stress for unstable equilibrium or fracture is:

$$\sigma_c = \sqrt{\frac{2\gamma_s E'}{\pi a}} \qquad (25)$$

Equation 25 is only applicable to brittle materials in which no plastic work is done during crack extension. Another important concept in fracture mechanics is the strain energy release rate, G, which was first proposed by Irwin (Soboyejo, 2003). This is defined as the rate of reduction of the total potential energy of a loading system with respect to crack length per unit thickness and is given by:

$$G = -\frac{1}{B}\frac{d(U_L + U_E)}{da} \qquad (26)$$

where , U_L is the potential energy of the loading system and U_E is the strain energy of the body. For materials that do not undergo plastic deformation prior to failure, a crack will extend when G reaches a critical value G_c given by:

$$G_c = 2\gamma_s \qquad (27)$$

In other words, G is a measure of crack driving force and G_c is a measure of the initial resistance of a brittle material to resist cracking which is key measure of a materials' reliability.

A more comprehensive understanding of the propagation of cracks can be obtained by using linear elastic fracture mechanics (LEFM). LEFM is based on the analysis of stress in an elastic continuum which means there is an infinite stress at the crack tip.

Figure 2.14 shows the three different modes of failure associated with three different modes of loading (tensile stress, in-plane shear and out-of-plane shear respectively). However, the stresses in all the cases are of the form (Westergaard, 1939):

$$\sigma_{ij} = \frac{K_m}{\sqrt{2\pi r}} f_{ij}(\theta), \qquad m = I, II, or\ III \qquad (28)$$

Where σ_{ij} is the applied stress tensor, f_{ij} is a dimensionless function of θ, K_m is the stress intensity factor corresponding to mode m and is the magnitude of the crack-tip stress field under linear elastic conditions. The r and θ are the polar coordinates ahead of the crack tip (Fig. 2.15)

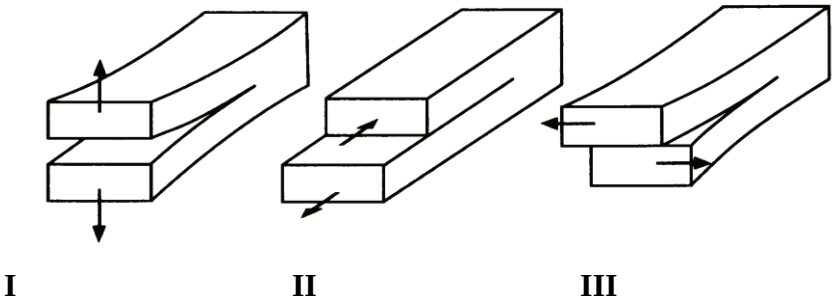

Figure 2.14: The three different modes of failure: (I) Opening mode; (II) Sliding mode and (III) Tearing mode

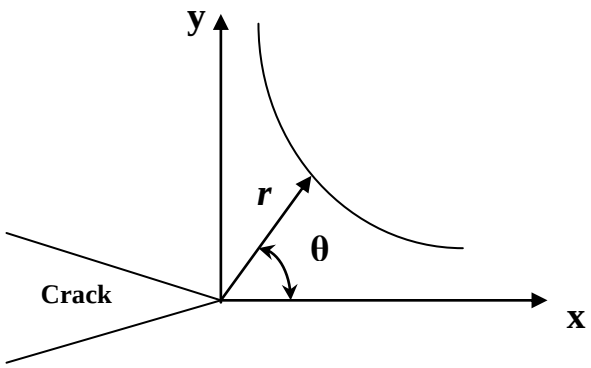

Figure 2.15: In-plane coordinate system ahead of a crack tip

The stress intensity factor for each failure mode, K_m (provided that the material is subjected to uniform applied loading), generally takes the form:

$$K_m = Y\sigma_a\sqrt{\pi a}, \qquad m = I, II, or\ III \tag{29}$$

where, Y is dimensionless factor of order unity and depends on the geometry of the specimen,

In this dissertation, we are only interested in mode I type fracture. The relationship between the strain energy release rate, *G*, and the stress intensity factor *K* for mode I loading is given by:

$$G_I = \frac{K_I^2}{E} \qquad (for\ plane\ stress) \tag{30}$$

And,

$$G_I = \frac{(1-v^2)K_I^2}{E} \qquad (for\ plane\ strain) \tag{31}$$

Also,

$$G_{II} = \frac{(1-v^2)K_{II}^2}{E} \qquad (for\ mode\ II\ fracture) \tag{32}$$

$$G_{III} = \frac{(1+v)K_{III}^2}{E} \qquad (for\ mode\ III\ fracture) \tag{33}$$

The energy release rate is a scalar quantity and may be added up for the different mode of crack opening, therefore:

$$G_T = G_I + G_{II} + G_{III}$$

$$= \frac{(1-v^2)(K_I^2 + K_{II}^2)}{E} + \frac{(1+v)K_{III}^2}{E} \qquad (for\ plane\ strain) \tag{34}$$

And,

$$G_T = G_I + G_{II} + G_{III} = \frac{K_I^2 + K_{II}^2}{E} \qquad (for\ plane\ stress) \tag{35}$$

While the energy release rate is additive for the different modes of fracture, the stress intensity factor are only additive for different load components for a given mode of failure (because the form of the stress field is fixed).

Fracture specimens are usually loaded in incremental stages, under displacement or load control, until stable crack growth is observed or initiated (Soboyejo, 2003). The stress intensity factor at which this happens is called the fracture toughness. After crack initiation, most materials exhibit some resistance curve (or R-curve) behavior, which may be represented by plotting the stress intensity factor against crack displacement. The observed R-curve behavior depends on the toughening (or the energy dissipative), intrinsic or extrinsic, mechanism of the material. For the case of shielding due to crack bridging, the R-curve behavior can be modeled using small- and large-scale bridging models. More details on the modeling of crack bridging are presented in the modeling section of Chapter 5.

References

AIPEA. (2011, October, 10 2011). History, from http://www.aipea.org/history.html

Andreatta, D., Yegian, D., Connelly, L., & Metcalf, R. (1994). *Recent Advances for The Heat Pasteurization of Drinking Water in The Developing World.* Proceedings of the 29th Intersociety Energy Conversion Engineering Conference.

Appel, J. (1973). Freundlichs Adsorption Isotherm. *Surface Science, 39*(1), 237-244.

Askeland, D. R., Fulay, P. P., & Wright, W. J. (2010). *Essentials of materials science and engineering* (2nd ed.). Stamford, C.T. ; United kingdom: Cengage Learning.

Askeland, D. R., & Phulé, P. P. (2006). The science and engineering of materials 5th.

Bandy, M. C., & Bandy, J. A. (1955). Translation of "De Natura Fossilium" by G. Agricola (1546). *Geological Society of America Special Paper, 63*.

Benna, M., Kbir-Ariguib, N., Magnin, A., & Bergaya, F. (1999). Effect of pH on rheological properties of purified sodium bentonite suspensions. *Journal of Colloid and Interface Science, 218*(2), 442-455.

Biasci, L., Aglietto, M., Ruggeri, G., & Ciardelli, F. (1994). Functionalization of Montmorillonite by Methyl-Methacrylate Polymers Containing Side-Chain Ammonium Cations. *Polymer, 35*(15), 3296-3304.

Bower, C. A., & Hatcher, J. T. (1967). Adsorption of Fluoride by Soils and Minerals. *Soil Science, 103*(3), 151-&.

Brennan, J. K., Bandosz, T. J., Thomson, K. T., & Gubbins, K. E. (2001). Water in porous carbons. *Colloids and Surfaces a-Physicochemical and Engineering Aspects, 187*, 539-568.

Brown, J., & Sobsey, M. D. (2009). Ceramic media amended with metal oxide for the capture of viruses in drinking water. *Environmental Technology, 30*(4), 379-391.

Burch, J. D., & Thomas, K. E. (1998). Water disinfection for developing countries and potential for solar thermal pasteurization. *Solar Energy, 64*(1-3), 87-97.

Carter, C. B., & Norton, M. G. (2007). *Ceramic materials : science and engineering*. New York ; London: Springer.

Chanda, M., Odriscoll, K., & Rempel, G. (1983). Sorption of phenolics onto cross-linked poly(4-vinyl pyridine). *Reactive Polymers, Ion Exchangers, Sorbents, 1*(4), 281-293.

Chen, N., Zhang, Z. Y., Feng, C. P., Sugiura, N., Li, M., & Chen, R. Z. (2010). Fluoride removal from water by granular ceramic adsorption. *Journal of Colloid and Interface Science, 348*(2), 579-584.

Cho, J. W., & Paul, D. R. (2001). Nylon 6 nanocomposites by melt compounding. *Polymer, 42*(3), 1083-1094.

Chung, Y.-w. (2007). *Introduction to materials science and engineering*. Boca Raton: CRC/Taylor & Francis.

Ciochetti, D. A., & Metcalf, R. H. (1984). Pasteurization of naturally contaminated water with solar energy. *Appl Environ Microbiol, 47*(2), 223-228.

Colella, L. S., Armenante, P. M., Kafkewitz, D., Allen, S. J., & Balasundaram, V. (1998). Adsorption isotherms for chlorinated phenols on activated carbons. *Journal of Chemical and Engineering Data, 43*(4), 573-579.

Crowley, M. M., Schroeder, B., Fredersdorf, A., Obara, S., Talarico, M., Kucera, S., & McGinity, J. W. (2004). Physicochemical properties and mechanism of drug release from ethyl cellulose matrix tablets prepared by direct compression and hot-melt extrusion. *International Journal of Pharmaceutics, 269*(2), 509-522.

Cygan, R. T., Brinker, C. J., Nyman, M. D., Leung, K., & Rempe, S. B. (2008). A molecular basis for advanced materials in water treatment. *Mrs Bulletin, 33*(1), 42-47.

Davis, J., & Davis, J. (2004). US Patent No. US 6,695,674 B1: U. S. Patent.

Deng, Z. Y., Fukasawa, T., Ando, M., Zhang, G. J., & Ohji, T. (2001). Microstructure and mechanical properties of porous alumina ceramics fabricated by the decomposition of aluminum hydroxide. *Journal of the American Ceramic Society, 84*(11), 2638-2644.

Díaz-Nava, C., Olguín, M. T., & Solache-Ríos, M. (2002). Water Defluoridation by Mexican Heulandite–Clinoptilolite. *Separation Science and Technology, 37*(13), 3109-3128.

Doerner, M. F., & Nix, W. D. (2011). A method for interpreting the data from depth-sensing indentation instruments. *Journal of Materials Research, 1*(04), 601-609.

EAWAG/SANDEC. (2002). SODIS Solar Water Disinfection. Dübendorf, Switzerland: SANDEC (Water & Sanitation in Developing Countries) at EAWAG. Swiss Federal Institute for Environmental Science and Technology.

Eldieb, A. S., & Hooton, R. D. (1994). Evaluation of the Katz-Thompson Model for Estimating the Water Permeability of Cement-Based Materials from Mercury Intrusion Porosimetry Data. *Cement and Concrete Research, 24*(3), 443-455.

Fahlin, C. J. (2003). Hydraulic Properties Investigation of the Potters For Peace Colloidal Silver Impregnated, Ceramic Filter: College of Engineering. University of Colorado at Boulder.

Fan, X. (2003). Adsorption kinetics of fluoride on low cost materials. *Water Research, 37*(20), 4929-4937.

Feachem, R. G., Bradley, D. J., Garelick, H., & Mara, D. (1983). *Sanitation and disease : health aspects of excreta and wastewater management*. Chichester West Sussex ; New York: Published for the World Bank by Wiley.

Friedman, K. C. (2010). *Design and Characterization of Hydroxyapatite-Clay Filters for Water Purification.* Bachelor of Science in Engineering Princeton University, Princeton, NJ.

Furuichi, N., Kurokawa, Y., Fujita, K., Oya, A., Yasuda, H., & Kiso, M. (1996). Preparation and properties of polypropylene reinforced by smectite. *Journal of Materials Science, 31*(16), 4307-4310.

Garboczi, E. J., & Bentz, D. P. (2001). The effect of statistical fluctuation, finite size error, and digital resolution on the phase percolation and transport properties of the NIST cement hydration model. *Cement and Concrete Research, 31*(10), 1501-1514.

Geim, A. K., & Novoselov, K. S. (2007). The rise of graphene. *Nature Materials, 6*(3), 183-191.

Gleick, P. (1998). The human right to water. *Water Policy, 1*(5), 487-503.

Gregg, S. J., & Sing, K. S. W. (1982). *Adsorption, surface area, and porosity* (2nd ed.). London ; New York: Academic Press.

Griffith, A. A. (1921). The phenomenon of rupture and flow in solids *Philosophical Transactions of the Royal Society* (Vol. A221, pp. 163-197). London.

Grim, R. E. (1962). *Applied clay mineralogy*. New York,: McGraw-Hill.

Grimm, J., Bessarabov, D., & Sanderson, R. (1998). Review of electro-assisted methods for water purification. *Desalination, 115*(3), 285-294.

Guggenheim, S., & Martin, R. T. (1995). Definition of Clay and Clay Mineral - Joint Report of the Aipea Nomenclature and Cms Nomenclature Committees. *Clays and Clay Minerals, 43*(2), 255-256.

Hager, J. (1998). *Steam Drying of Porous Media.* Ph.D, Lund University.

Havelaar, A., & Melse, J. M. (2003). Quantifying public health risk in the WHO Guidelines for drinking-water quality: A burden of disease approach. Bilthoven: National Institute for Public Health and the Environment.

He, L. H., Standard, O. C., Huanga, T. T. Y., Latella, B. A., & Swain, M. V. (2008). Mechanical behaviour of porous hydroxyapatite. *Acta Biomaterialia, 4*(3), 577-586.

Ho, Y. S., Ng, J. C. Y., & McKay, G. (2000). Kinetics of Pollutant Sorption by Biosorbents: Review. *Separation & Purification Reviews, 29*(2), 189-232.

Hooton, R. D., Thomas, M. D. A., Marchand, J., & Beaudoin, J. J. (Eds.). (2001). *Materials Science of Concrete Special Volume: Ion and Mass Transport in Cement-Based Materials*. Westerville, OH Am. Ceram. Soc.

Hysitron. (2010). TriboScope user manual. Minneapolis: Hysitron Inc.

Iijima, S. (1991). Helical Microtubules of Graphitic Carbon. *Nature, 354*(6348), 56-58.

Inglis, C. E. (1913). Stress in a plate due to the presence of cracks and sharp corners. *Transactions of the Institute of Naval Architects, 55*, 219-241.

Jiang, Y. B., Liu, N. G., Gerung, H., Cecchi, J. L., & Brinker, C. J. (2006). Nanometer-thick conformal pore sealing of self-assembled mesoporous silica by plasma-assisted atomic layer deposition. *Journal of the American Chemical Society, 128*(34), 11018-11019.

Jimenez, G., Ogata, N., Kawai, H., & Ogihara, T. (1997). Structure and thermal/mechanical properties of poly(epsilon-caprolactone)-clay blend. *Journal of Applied Polymer Science, 64*(11), 2211-2220.

Kato, M., Usuki, A., Hasegawa, N., Okamoto, H., & Kawasumi, M. (2011). Development and applications of polyolefin- and rubber-clay nanocomposites. *Polymer Journal, 43*(7), 583-593.

Katz, A. J., & Thompson, A. H. (1987). Prediction of Rock Electrical-Conductivity from Mercury Injection Measurements. *Journal of Geophysical Research-Solid Earth and Planets, 92*(B1), 599-607.

Kaur, S., Gopal, R., Ng, W. J., Ramakrishna, S., & Matsuura, T. (2008). Next-generation fibrous media for water treatment. *Mrs Bulletin, 33*(1), 21-26.

Kawasumi, M., Hasegawa, N., Kato, M., Usuki, A., & Okada, A. (1997). Preparation and mechanical properties of polypropylene-clay hybrids. *Macromolecules, 30*(20), 6333-6338.

Kerr, P. F. (1955). *Formation and occurrence of clay minerals.* Proceedings of the First National Conference on Clays and Clay Technology, California Division of Mines, San Francisco.

Kingery, W. D. (Ed.). (1958). *Ceramic fabrication processes*. New York: John Wiley & Sons, Inc.

Kingery, W. D., Bowen, H. K., & Uhlmann, D. R. (1976). *Introduction to ceramics* (2d ed.). New York: Wiley.

Klein, C., Hurlbut, C. S., & Dana, J. D. (1993). *Manual of mineralogy* (21st ed / ed.). New York: Wiley.

Knudsen, F. P. (1959). Dependence of Mechanical Strength of Brittle Polycrystalline Specimens on Porosity and Grain Size. *Journal of the American Ceramic Society, 42*(8), 376-387.

Lee, C. H., Kato, M., & Usuki, A. (2011). Preparation and properties of bio-based polycarbonate/clay nanocomposites. *Journal of Materials Chemistry, 21*(19), 6844-6847.

Li, D., & Kaner, R. B. (2008). Materials science - Graphene-based materials. *Science, 320*(5880), 1170-1171.

Li, Y.-H., Wang, S., Cao, A., Zhao, D., Zhang, X., Xu, C., Luan, Z., Ruan, D., Liang, J., et al. (2001). Adsorption of fluoride from water by amorphous alumina supported on carbon nanotubes. *Chemical Physics Letters, 350*(5-6), 412-416.

Li, Y. H., Wang, S., Zhang, X., Wei, J., Xu, C., Luan, Z., Wu, D., & Wei, B. (2003). Removal of fluoride from water by carbon nanotube supported alumina. *Environmental Technology, 24*(3), 391-398.

Liu, Y., Xu, H., & Tay, J. H. (2005). Derivation of a general adsorption isotherm model. *Journal of Environmental Engineering-Asce, 131*(10), 1466-1468.

Loh, K. P., Bao, Q. L., Ang, P. K., & Yang, J. X. (2010). The chemistry of graphene. *Journal of Materials Chemistry, 20*(12), 2277-2289.

Lougheed, T. (2006). A clear solution for dirty water. *Environmental Health Perspectives, 114*(7), A424-A427.

Meenakshi, S., Sundaram, C. S., & Sukumar, R. (2008). Enhanced fluoride sorption by mechanochemically activated kaolinites. *Journal of Hazardous Materials, 153*(1-2), 164-172.

Messersmith, P. B., & Giannelis, E. P. (1994). Synthesis and Characterization of Layered Silicate-Epoxy Nanocomposites. *Chemistry of Materials, 6*(10), 1719-1725.

Nevskaia, D. M., Castillejos-Lopez, E., Munoz, V., & Guerrero-Ruiz, A. (2004). Adsorption of aromatic compounds from water by treated carbon materials. *Environmental Science & Technology, 38*(21), 5786-5796.

Novoselov, K. S., Geim, A. K., Morozov, S. V., Jiang, D., Zhang, Y., Dubonos, S. V., Grigorieva, I. V., & Firsov, A. A. (2004). Electric field effect in atomically thin carbon films. *Science, 306*(5696), 666-669.

Oates, P. M., Shanahan, P., & Polz, M. F. (2003). Solar disinfection (SODIS): simulation of solar radiation for global assessment and application for point-of-use water treatment in Haiti. *Water Research, 37*(1), 47-54.

Oliver, W. C., & Pharr, G. M. (1992). An Improved Technique for Determining Hardness and Elastic-Modulus Using Load and Displacement Sensing Indentation Experiments. *Journal of Materials Research, 7*(6), 1564-1583.

Oyanedel-Craver, V. A., & Smith, J. A. (2008). Sustainable colloidal-silver-impregnated ceramic filter for point-of-use water treatment. *Environmental Science & Technology, 42*(3), 927-933.

Pan, B., & Xing, B. S. (2008). Adsorption Mechanisms of Organic Chemicals on Carbon Nanotubes. *Environmental Science & Technology, 42*(24), 9005-9013.

Penner, D., & Lagaly, G. (2001). Influence of anions on the theological properties of clay mineral dispersions. *Applied Clay Science, 19*(1-6), 131-142.

Pradeep, T., & Anshup. (2009). Noble metal nanoparticles for water purification: A critical review. *Thin Solid Films, 517*(24), 6441-6478.

PUR. (2011a). PUR Product. Retrieved from http://www.purwater.com/pur-products/

PUR. (2011b). PUR Technology. Retrieved from http://www.purwater.com/pur-technology/

Ramachandran, V. S., Beaudoin, J. J., & Knovel (Firm) (Eds.). (2001). *Handbook of analytical techniques in concrete science and technology*. Park Ridge, N.J.Norwich, N.Y.: Noyes Publications ; William Andrew Pub.

Reeves, G. M., Sims, I., & Cripps, J. C. (Eds.). (2006). *Clay Materials Used in Construction* (Vol. 21). London: The Geological Society.

Reichert, P., Nitz, H., Klinke, S., Brandsch, R., Thomann, R., & Mulhaupt, R. (2000). Poly(propylene)/organoclay nanocomposite formation: Influence of compatibilizer functionality and organoclay modification. *Macromolecular Materials and Engineering, 275*(2), 8-17.

Rice, R. W. (1993). Comparison of stress concentration versus minimum solid area based mechanical property-porosity relations. *Journal of Materials Science, 28*(8), 2187-2190.

Rice, R. W. (1996). Grain size and porosity dependence of ceramic fracture energy and toughness at 22 degrees C. *Journal of Materials Science, 31*(8), 1969-1983.

Ries, H. (1927). *Clays, their occurrence, properties, and uses, with especial reference to those of the United States and Canada* (3d ed.). New York, London,: J. Wiley & Sons; Chapman & Hall.

Roque-Malherbe, R. M. A. (2007). *Adsorption and diffusion in nanoporous materials*. Boca Raton: CRC Press.

Ruoff, R. S., & Lorents, D. C. (1995). Mechanical and Thermal-Properties of Carbon Nanotubes. *Carbon, 33*(7), 925-930.

Salvetat, J. P., Bonard, J. M., Thomson, N. H., Kulik, A. J., Forro, L., Benoit, W., & Zuppiroli, L. (1999). Mechanical properties of carbon nanotubes. *Applied Physics a-Materials Science & Processing, 69*(3), 255-260.

Sciacca, F., Rengifo-Herrera, J. A., Wethe, J., & Pulgarin, C. (2010). Dramatic enhancement of solar disinfection (SODIS) of wild Salmonella sp in PET bottles by H(2)O(2) addition on natural water of Burkina Faso containing dissolved iron. *Chemosphere, 78*(9), 1186-1191.

Shackelford, J. F., & Doremus, R. H. (Eds.). (2008). *Ceramic and glass materials : structure, properties and processing*. New York: Springer.

Silvestry-Rodriguez, N., Bright, K. R., Slack, D. C., Uhlmann, D. R., & Gerba, C. P. (2008). Silver as a residual disinfectant to prevent biofilm formation in water distribution systems. *Applied and Environmental Microbiology, 74*(5), 1639-1641.

Singh, B., Madhusudhanan, S., Dubey, V., Nath, R., & Rao, N. B. S. N. (1996). Active carbon for removal of toxic chemicals from contaminated water. *Carbon, 34*(3), 327-330.

Sips, R. (1948). On the Structure of a Catalyst Surface. *Journal of Chemical Physics, 16*(5), 490-495.

Skopp, J. (2009). Derivation of the Freundlich Adsorption Isotherm from Kinetics. *Journal of Chemical Education, 86*(11), 1341-1343.

Soboyejo, W. O. (2003). *Mechanical properties of engineered materials*. New York: Marcel Dekker.

Sobsey, M. D. (2002). *Managing water in the home : accelerated health gains from improved water supply*. Geneva, Switzerland: World Health Organization (WHO).

Sobsey, M. D., Stauber, C. E., Casanova, L. M., Brown, J. M., & Elliott, M. A. (2008). Point of use household drinking water filtration: A practical, effective solution for providing sustained

access to safe drinking water in the developing world. *Environmental Science & Technology, 42*(12), 4261-4267.

SODIS. (2011). How does it work?

Solomon, D. H., & Hawthorne, D. G. (1991). *Chemistry of pigments and fillers*. Malabar, Fla.: Krieger Pub. Co.

Solomon, M. J., Almusallam, A. S., Seefeldt, K. F., Somwangthanaroj, A., & Varadan, P. (2001). Rheology of polypropylene/clay hybrid materials. *Macromolecules, 34*(6), 1864-1872.

Sommer, B., Marino, A., Solarte, Y., Salas, M. L., Dierolf, C., Valiente, C., Mora, D., Rechsteiner, R., Setter, P., et al. (1997). SODIS - An emerging water treatment process. *Journal of Water Supply Research and Technology-Aqua, 46*(3), 127-137.

Sommer, R., Cabaj, A., & Haider, T. (1996). Microbicidal effect of reflected UV radiation in devices for water disinfection. *Water Science and Technology, 34*(7-8), 173-177.

Srivastava, A., Srivastava, O. N., Talapatra, S., Vajtai, R., & Ajayan, P. M. (2004). Carbon nanotube filters. *Nature Materials, 3*(9), 610-614.

Sundaram, C. S., Viswanathan, N., & Meenakshi, S. (2008). Defluoridation chemistry of synthetic hydroxyapatite at nano scale: Equilibrium and kinetic studies. *Journal of Hazardous Materials, 155*(1-2), 206-215.

Tasis, D., Tagmatarchis, N., Bianco, A., & Prato, M. (2006). Chemistry of carbon nanotubes. *Chemical Reviews, 106*(3), 1105-1136.

Tepper, F., Rivkin, T., & Lukasic, G. (2002). Novel nanofibre filter medium attracts waterborne pathogens. *Filtration & Separation, 39*(6), 16-19.

Tsao, N. H. (2011). *Virus filtration in porous iron oxide doped ceramic water filter.* Bachelor of Science in Engineering Princeton University, Princeton, NJ. .

UNICEF. (2008). UNICEF Handbook on Water Quality. *United Nations Children's Fund (UNICEF), New York*.

Usuki, A., Kojima, Y., Kawasumi, M., Okada, A., Fukushima, Y., Kurauchi, T., & Kamigaito, O. (1993). Synthesis of Nylon 6-Clay Hybrid. *Journal of Materials Research, 8*(5), 1179-1184.

Vaia, R. A., Ishii, H., & Giannelis, E. P. (1993). Synthesis and Properties of 2-Dimensional Nanostructures by Direct Intercalation of Polymer Melts in Layered Silicates. *Chemistry of Materials, 5*(12), 1694-1696.

Vaia, R. A., Sauer, B. B., Tse, O. K., & Giannelis, E. P. (1997). Relaxations of confined chains in polymer nanocomposites: Glass transition properties of poly(ethylene oxide) intercalated in montmorillonite. *Journal of Polymer Science Part B-Polymer Physics, 35*(1), 59-67.

Van Halem, D. (2006). *Ceramic Silver Impregnated Pot Filters for Household Drinking Water Treatment in Developing Countries.* Master of Science Delft University of Technology, The Netherlands.

Vanbrakel, J., Modry, S., & Svata, M. (1981). Mercury Porosimetry - State of the Art. *Powder Technology, 29*(1), 1-12.

Wang, H. H., & Shiao, K. R. (1994). Preparation and Physical-Properties of Polyurethane Modified with Poly(4,4'-Diphenylsulfone Terephthalamide). *Journal of Applied Polymer Science, 52*(7), 847-855.

Wang, Z., & Pinnavaia, T. J. (1998). Nanolayer reinforcement of elastomeric polyurethane. *Chemistry of Materials, 10*(12), 3769-+.

Washburn, E. W. (1921). Note on a method of determining the distribution of pore sizes in a porous material. *Proceedings of the National Academy of Sciences of the United States of America, 7*, 115-116.

Webb, P. A. (2001). An Introduction to the Physical Characterization of Materials by Mercury Intrusion Porosimetry with Emphasis on Reduction and Presentation of Experimental Data. Retrieved from http://www.micromeritics.com/pdf/mercurypaper.pdf

Weber, W. J., & Morris, J. C. (1964). Equilibria and capacities for adsorption on carbon. *J. Sanitary Eng. Div, 90*(SA3), 79-107.

Wenhold, F., & Faber, M. (2009). Water in nutritional health of individuals and households: An overview. *Water Sa, 35*(1), 61-71.

Wernette, D. P., Liu, J. W., Bohn, P. W., & Lu, Y. (2008). Functional-DNA-Based nanoscale materials and devices for sensing trace contaminants in water. *Mrs Bulletin, 33*(1), 34-41.

Westergaard, H. M. (1939). Bearing pressures and cracks. *Journal of Applied Mechanics, 6*, A49 - 53.

WHO. (2006). *Guidelines for the safe use of wastewater, excreta and greywater. Volume 2. Wastewater use in agriculture*. Geneva, Switzerland.

WHO. (2007). *Combating Waterborne Disease at the Household Level*. Geneva, Switzerland.

WHO. (2011a). *Evaluating Household Water Treatment Options: Health-based targets and microbial performance specifications*. Geneva, Switzerland.

WHO. (2011b). *Guidelines for Drinking-Water Quality* (4 ed.). Geneva, Switzerland.

WHO/UNICEF. (2008). *Progress on Drinking Water and Sanitation: Special Focus on Sanitation; World Health Organization and United Nations Children's Fund Joint Monitoring Programme for Water Supply and Sanitation*. Geneva, Switzerland.

WHO/UNICEF. (2010). *Progress on sanitation and drinking water - 2010 update*. Geneva: World Health Organization and United Nations Children's Fund Joint Monitoring Programme for Water Supply and Sanitation.

Xie, S. S., Li, W. Z., Pan, Z. W., Chang, B. H., & Sun, L. F. (2000). Mechanical and physical properties on carbon nanotube. *Journal of Physics and Chemistry of Solids, 61*(7), 1153-1158.

Yakub, I., Du, J., & Soboyejo, W. O. (Submitted for publication-a). Mechanical Properties and Design of Porous Clay-based Ceramics.

Yakub, I., Plappally, A., Leftwich, M., Malatesta, K., Friedman, K. C., Obwoya, S., Nyongesa, F., Maiga, A. H., Soboyejo, A. B. O., et al. (Submitted for publication-b). Porosity and Filtration Characteristics of Frustum-Shaped Ceramic Water Filters.

Yakub, I., & Soboyejo, W. O. (Submitted for publication). Adsorption of Fluoride from Water using Sintered Clay-Hydroxyapatite Composite.

Yang, C. H. (1998). Statistical mechanical study on the Freundlich isotherm equation. *Journal of Colloid and Interface Science, 208*(2), 379-387.

Zhou, H., & Smith, D. W. (2001). Advanced technologies in water and wastewater treatment. *Canadian Journal of Civil Engineering, 28*, 49-66.

Zhu, Z. K., Yang, Y., Yin, J., Wang, X. Y., Ke, Y. C., & Qi, Z. N. (1999). Preparation and properties of organosoluble montmorillonite polyimide hybrid materials. *Journal of Applied Polymer Science, 73*(11), 2063-2068.

Chapter 3

Porosity and Filtration Characteristics of Frustum-Shaped Ceramic Water Filters

3.1 Introduction

Although clean water and effective sanitation are essential to good health and wellbeing, they are not available globally. Around 884 million people in the world do not have access to clean drinking water (WHO/UNICEF, 2008). Consequently, about 5000 people die each day from preventable water-borne diseases such as diarrhea, dysentery, poliomyleitis, typhoid, ascariasis, and leptospirosis (Kosek *et al.*, 2003; Lantagne, 2001c; Wenhold & Faber, 2009). These diseases greatly increase the mortality rates and the disease burden in developing countries, especially in children younger than 5 years old (UNICEF/WHO, 2009).

In 1981, in an effort to address health and mortality issues associated with the consumption of contaminated water, the Inter-American Bank organized a competition to promote the development of an affordable filter that could remove bacteria while enabling sufficient water flow for the consumption needs of families in developing countries. This stimulated Dr. Fernando Mazariegos of the Central American Research Institute-Guaetamala (ICAITI) to make the first frustum-shaped ceramic water filter with a colloidal silver coating (PFP, 2008). The filter relied on gravity flow and the use of colloidal silver to remove or inactivate bacteria and other pathogens (Lantagne, 2001c). Subsequently, the Medical Assistance Program trained potters in Ecuador and ICAITI, and a number of Non-Governmental Organizations (NGOs) started to make the filters (Lantagne, 2001c).

In 1998, Potters For Peace (PFP) standardized the Mazariegos design and started mass production of these filters, named Filtròn, in 1999 in Nicaragua (PFP, 2008), where PFP developed a new strategy of helping poor communities across the world to establish water filter factories that make and sell the filters to rural and urban populations in developing countries (Donachy, 2004; PFP, 2008). Since 1999 PFP has helped to establish water filter factories in over 20 countries, this includes: Mexico, Cambodia, Haiti, Guatemala, El Salvador, Nepal, Pakistan, Uzbekistan, Sudan, Kenya, Benin, Ghana and Nigeria (Brown *et al.*, 2009; Dies, 2003; Donachy, 2004; Hwang, 2003; Lantagne, 2001a,2001b; Lantagne *et al.*, 2010; Lee, 2009; Oyanedel-Craver & Smith, 2008; PFP, 2008; Swanton, 2008; Van Halem, 2006). In an effort to enhance the availability of the filters across borders in the developing world, the filter has not been patented.

Although there are other methods for the treatment of water in developing countries (boiling, pasteurization, chlorination, flocculation disinfection, solar disinfection, and biosand filter

(Clasen *et al.*, 2007; Fewtrell *et al.*, 2005; Sobsey *et al.*, 2008)), point-of-use ceramic filters are one of the most promising solutions available (Sobsey *et al.*, 2008). This is largely due to their low-cost, ease of fabrication, ease of use, and the ability to effectively filter out bacteria from water. They are also attractive because they represent a sustainable solution with the potential for large scale adoption. So far, about 500,000 people have adopted some form of porous ceramic filter technology in the developing world (Sobsey *et al.*, 2008).

Clay based ceramic water filters (CWFs) are usually produced by mixing of clay, sawdust (woodchips) and water. Other combustible organic material, such as rice husk, coffee husk or flour can also be used (Oyanedel-Craver & Smith, 2008). By careful control of the clay and woodchip mixture proportions, as well as the processes that are used for the fabrication of CWFs, initial water flow rates of around 2 Liters outflow, in the first hour, have been shown consistently to result in the removal of many microbes and pathogens in water (Brown *et al.*, 2008; Lantagne, 2001a,2001b,2001c; Lantagne *et al.*, 2010; PFP, 2008). However, the flow rates decrease gradually with increasing filter use during the 2 – 3 year recommended lifetime of the CWFs. This is due to gradual blockage of the pores by trapped contaminants (Brown *et al.*, 2008; Lantagne, 2001b).

During use, PFP recommends that the CWF be cleaned by fire heating, scrubbing and brushing to remove caked impurities that form with time (Lantagne, 2001b). Furthermore, the clay-water mixture is a combination that has a rheological property, which not only permits shaping, but also allows for doping with other materials. This can potentially give the CWFs the robustness required for the removal of other contaminants besides microbial contaminants from water. For instance, the removal of chemical contaminants, such as arsenic, iron and fluoride has also been reported (Dies, 2003; Friedman, 2010; Yakub & Soboyejo, Submitted for publication).

Furthermore, it has also been shown that with the right amount of iron oxide doping, the CWFs are capable of removing viruses (Brown & Sobsey, 2009; Tsao, 2011).

Although porous CWFs have been used successfully in the field (Albert *et al.*, 2010; Brown *et al.*, 2009; Dies, 2003; Hwang, 2003; Lantagne, 2001a,2001b,2001c; Lee, 2009; Oyanedel-Craver & Smith, 2008; PFP, 2008; Swanton, 2008; Van Halem, 2006) for over a decade, scientific understanding of the effects of porosity on the water flow rate and filtration efficiency is still very limited. There is, therefore, a need for scientific studies of the effects of porosity on the water filtration properties of CWFs. This chapter presents the results of an experimental study of the effects of porosity on water flow and filtration characteristics of CWFs. The effects of porosity are explored using ceramics produced from different, well-controlled mixtures of redart clay and wood chips. The effective permeabilities of the CWFs were determined from fits to the Darcy equation and also by using Katz and Thompson method. The tortuosity of the filters was found using Jörgen Hager's equation. The efficiencies of bacterial removal (filtration) were elucidated for the same range of CWFs. The implications of the results are then discussed for applications of CWFs in the developing world.

3.2 Experimental Methods

3.2.1 Materials and Processing

CWFs were made by mixing clay (Cedar Heights Redart Airfloated Clay, Pittsburgh, PA) composed of illite and kaolinite clays with sawdust consisting of 80% oak and 20% Spanish cedar (Hamilton Building Supplies, Trenton, NJ). In order to vary the porosity after sintering,

three different proportions of clay to sawdust by volume (50:50, 65:35, and 75:25) were used to produce the CWFs.

Prior to mixing, the sawdust was manually sieved using 35-1000 mesh wire sieves. The initial blending of sieved sawdust and clay was then done manually to ensure a thorough mixing and to avoid the formation of clustered pores. The dry mixture of clay and sawdust was transferred to an industrial mixer (Model A-200, The Hobart Manufacturing Company, Troy, OH) and thoroughly mixed again for approximately 5 minutes before the addition of water. Half (0.9 L) of the required amount of water (usually 1.8 – 2 L for a 50:50 CWF) was gradually added during mixing, and the mixture was again blended for 5 – 10 minutes. Next, half of the remaining water (one quarter of the total amount or 0.45 L) was added, and the mixture was mixed for another 5 – 10 minutes. The remaining water (approximately 0.45 L) was added in small increments until the mixture began to coalesce into large clumps and no longer adhered to the walls of the mixer. No additional water was added after coalescence occurred.

Approximately 12 pounds of the blended mixture were then manually formed into a ball, which was pressed tightly together so that no cracks were visible on its surface. This ball was compacted in a two-piece aluminum mold (Figure 3.1) that was covered with a 13-gallon plastic bag to prevent the greenware from sticking to the walls of the mold during pressing. The blended ball mixture was placed into the female part of the mold before applying a pressure of 140 kPa (20 psi) to the male part of the mold using a 50 ton hydraulic press (TRD55002, Torin Jacks, Inc., Ontario, Canada).

After pressing, the CWFs were dried in laboratory air at a temperature of about 25°C and a relative humidity of about 40%. The time required for drying the greenwares varied between 5

and 8 days, depending on the porosity level. After drying, the greenwares were sintered in a gas kiln (Ceramics Art Department, Princeton University, Princeton, NJ). This involved the preheating of the CWFs to 450-550°C for three hours (to burn off the sawdust), followed by heating to the sintering temperature of 955°C in the same gas kiln. The initial heating rate of 50°C per hour was increased to 100°C per hour beyond a furnace temperature of 200°C. The CWFs were sintered for 5 hours at a peak temperature of about 955° C. They were then furnace cooled in air to room temperature.

The frustum-shaped CWFs consisted of two sections, the base (or disc part) and the side (or curved part). The disc had a radius of ~ 91.5 mm and a thickness of ~ 15 mm. The side had a slant height of ~ 240 mm and a thickness of ~ 10 mm. The CWFs were ~ 237 mm deep and hence have a capacity of about 10 liters. After cooling, the porosities of the CWFs were characterized using Mercury Intrusion Porosimetry (MIP). The flow rates and bacterial filtration characteristics of the filters were also characterized. A standard PFP reference filter, produced by Potters for Peace in Managua, Nicaragua, was used as a reference in the porosimetry and flow tests. The typical PFP reference filter was made from a 60:40 mixture of clay to sawdust by weight, rather than by volume. This was also coated with colloidal silver, and had a flow rate of between ~ 1-2 L per hour (Lantagne, 2001b). This was estimated by measuring the volume of water that drained from an initially full filter over a period of 1hour. A more accurate dynamic method of measuring the water flow rate will be presented in section 2.3.

3.2.2 Mercury Intrusion Porosimetry

The porosities of the CWFs were characterized using Mercury Intrusion Porosimetry (MIP). MIP measurements were carried out in a MicroMetrics Autopore III 9400 analyzer (MicroMetrics, Norcross, GA). The two-stage MIP experiments were used to characterize the nano- and the micro-scale pore size distributions. The MIP tests were performed on pieces with dimensions of ~ 3 mm x 3 mm x 3 mm that were cut from the three different CWFs (50:50, 65:35 and 75:25) and the PFP reference filter Samples were cut from four different locations in each CWF [the "base" and three locations (the "top", "middle", "bottom") on the side of the filter], as shown in Figure 3.2.

3.2.3 Water Flow Experiments

Prior to the water flow experiments, the CWFs were saturated by complete submersion in a vat containing purified water (Model D8611, Barnstead/Thermolyne, Hampton, NH) for about 12 hours to remove internal air bubbles. The flow rates of purified water were then measured through the three CWFs (50:50, 65:35 and 75:25). Flow rates across the PFP reference filter were also determined as a control. The flow rates were obtained by measuring the volume of water discharged from the CWFs as a function of time. The flow measurement system was enclosed in a plastic container to minimize possible contamination and mass loss by evaporation.

The ceramic pot was first placed into a plastic receptacle that was fitted with a large plastic funnel. The filter and receptacle-funnel were suspended above an empty collection bucket that rested on a load cell (Model LSC 7000-50, Omega Engineering Incorporated, Stamford, CT). The load cell was connected to a LabView card (NI PCI-6259, National Instruments, Austin,

TX) via a 68-Pin Digital and Trigger I/O Terminal Block (CB-68LP, National Instruments, Austin, TX) to LabView software (Version 8.0, National Instruments, Austin, TX) that recorded the mass of the water as it flowed into the collection bucket.

At the start of each experiment, a water-saturated CWF was filled completely with approximately 10 Liters of purified water and covered with a plastic lid. The water was allowed to drain passively from the CWF being tested. No additional water was added to the CWF during the experiment. In this way, time durations between three and twenty-one days were required to drain the range of CWFs examined in this study.

3.2.4 Permeability and Tortuosity

The permeability of the porous CWFs was determined using two methods. The first method involved fitting the flow rate data to an equation derived from the Darcy's equation (see section on Modeling). The second method for determining permeability was based on data obtained from mercury intrusion porosimetry measurements. The equation, given below, was derived by Katz and Thompson (Katz & Thompson, 1987) and has been used to find the permeability of a wide range of porous materials (Crowley *et al.*, 2004; Eldieb & Hooton, 1994; Garboczi & Bentz, 2001; Hooton *et al.*, 2001; Van Halem, 2006).

$$k = \frac{1}{89} L_{max}^2 \frac{L_{max}}{L_c} \emptyset S(L_{max}) \qquad (1)$$

where k (darcy) is intrinsic permeability; L_{max} (μm) is the pore size at which conductance is maximum; L_c (μm) is the pore breathrough size which is determined from the mercury

depression curve; ∅ is the porosity of the filter and $S(L_{max})$ is the fractional volume of connected pore space composed of pore widths of size L_{max} and larger.

Hager (Hager, 1998) derived an expression for material permeability, in which pores are treated as bundle of capillary tubes of varying sizes. By re-writing the equation of the permeability and making tortuosity the subject of the formula, we have:

$$\tau = \sqrt{\frac{\rho_S}{24k(1+\rho_S V_{tot})} \int_{\zeta = r_{c,min}}^{\zeta = r_{c,max}} \zeta^2 f_v(\zeta) d\zeta} \qquad (2)$$

where, τ is tortuosity; ρ_s (g/mL) is the skeletal density; k (m^2) is permeability; V_{tot} (mL/g) is the total pore volume of the material and $\int_{\zeta = r_{c,min}}^{\zeta = r_{c,max}} \zeta^2 f_v(\zeta) d\zeta$ is the pore volume distribution by pore size. Except for the tortuosity, all these parameters can be obtained from the mercury intrusion porosimetry tests.

Since mercury cannot intrude into small micropores a more accurate value of tortuosity is obtained by using the value of skeletal density obtained by gas pycnometry (Webb, 2001). In this chapter the skeletal density obtained from helium pycnometry method was used (Yakub *et al.*, Submitted for publication). Moreover, the tortuosity for each CWF type was computed using both the value of permeability obtained from the Katz and Thompson (K-T) method with permeability obtained from the Darcy fits (see section on Modeling).

3.2.5 *E.coli* Removal Experiments

E.coli filtration experiments were performed on CWFs with volume ratios of clay to sawdust of 50:50 and 65:35. To determine the removal efficiencies, 10 – 20 milliliter (mL) cultures of the non-pathogenic *E. coli* K-12 strain W3110 [(Bachmann, 1972); Obtained from N. Ruiz, The Ohio State University] were grown in Miller's LB Broth (Miller, 1972) at 37°C for 18 – 24 hrs. The growth was completed with vigorous aeration, either by shaking at approximately 200 – 220 revolutions per minute (Model G-24 Incubator Shaker, New Brunswick Scientific), or by stirring using a digital stirrer/hotplate (Model 735-HPS, VWR, West Chester, PA).

Four milliliters of the stationary phase culture were mixed into 4 L of sterile, purified water, producing a pre-filtrate suspension containing 10^6 to 10^7 cells/mL, which is similar to the concentration used by Bielefeldt *et al.* (2009), and also to the maximum bacterial concentration determined for surface drinking water in South Africa (Obi *et al.*, 2003). This concentration of *E.coli* is approximately 1,000-fold greater than the density rated as "very high risk" for drinking water quality guidelines of World Health Organization (WHO) for rural drinking water supplies (WHO, 2011b). The entire 4 L of pre-filtrate was poured rapidly into a water-saturated CWF, and 3 – 4 L of the filtrate was collected in a 5-gallon plastic bucket lined with sterile plastic bag after 24 hr of filtration. The numbers of viable cells in the pre-filtrate and filtrate suspensions were determined by appropriate dilution into sterile purified water and plating onto Miller's LB agar (Miller, 1972). Other experiments have confirmed that the viability of the W3110 strain of *E.coli* in purified water decreased less than 0.15 LRV (Log_{10} reduction value) during the 24-hr duration of filtration (unpublished results).

The number of colonies (CFU) in the pre-filtrate and filtrate was counted after overnight incubation at 37°C. When the viable count of the filtrate was low, the cells present in larger

filtrate samples (10 - 100 mL) were collected using sterile filtration assemblies (MVHAWG124, Millipore Corp., Billerica, MA). The membrane filter was then removed from the filtration assembly, placed directly onto Miller's LB agar and incubated overnight at 37°C. To decontaminate CWFs between experiments, they were rinsed thoroughly with purified water and dried in full sunlight for 5 – 8 hrs to mimic conditions in the field..The efficiency of *E. coli* filtration is expressed both as a percentage and a log reduction value (Brown & Sobsey, 2009).

3.3 Modeling

An analytical hydrodynamic model was developed to describe the flow of water through the filters due to the effect of gravity. Flow continued until the filter had emptied to levels where there was not enough pressure head to overcome the resistance of the membrane/filter. Figure 3.2 is a schematic of the water filter with the important variables labeled. Flow through the porous filters was assumed to follow Darcy's Law, which is given by (Bear, 1972):

$$Q = \frac{\kappa A}{\mu L}\Delta p \tag{3}$$

where κ is the permeability of the material, A is the surface area, L is the thickness of the material, μ is the dynamic viscosity of the fluid (water) and Δp is the pressure difference from the top to the bottom of the surface. In this case, the bottom and sides of the filter are considered separately (denoted Q_b and Q_s, respectively) and the corners are neglected. The pressure change between the surfaces is equal to the hydrostatic pressure of the water (as the flow is very slow, a quasi-steady approximation is appropriate). For the flow through the bottom, the change in pressure from the inside bottom surface to the outside bottom surface (the distance of porous

media through which the water flows) is equal to the hydrostatic pressure of the fluid at that time. This is given by:

$$\Delta p = \rho g h(t) \tag{4}$$

Equation 4 is substituted into equation 3. Additionally, the area of the bottom of the filter ($A = \pi r_o^2$) is the surface area that the flow is acting on; the thickness of permeable material is $L=t_b$; and the permeability is considered to be constant. Thus, the flow rate through the *bottom* of the filter is given by:

$$Q_b = \frac{\kappa}{\mu}\frac{\pi r_0^2 \rho g h(t)}{t_b} \tag{5}$$

On the sides of the filter, the pressure is a function of the position y and is given by $\Delta p=\rho g(h(t)-y)$. The area of the filter is also a function of y. The radius changes along the filter height of the filter and is expressed as $r(y) = r_0+y\tan\theta$. The permeability coefficient is again considered to be constant and to be the same as on the bottom of the filter. Thus, the flow rate through the side of the filter is given by:

$$Q_s = \int_0^{h(t)} \frac{\kappa}{\mu}\frac{\pi\rho g\left(h(t)-y\right)}{t_s} 2\left(r_0 + y\tan\theta\right)dy\,. \tag{6}$$

Integration of equation 6 gives:

$$Q_s = \frac{\kappa}{\mu}\frac{\pi\rho g 2h^2(t)}{t_s}\left[\frac{r_0}{2} - \frac{h(t)}{3}\tan\theta\right]. \tag{7}$$

Furthermore, by adding equations (5) and (7), the following expression for the total mass flow rate is obtained for the total mass flow rate, *Q*:

$$Q = \frac{\kappa}{\mu}\pi\rho g h(t)\left[\frac{r_0^2}{t_b} + \frac{r_0 h(t)}{t_s} - \frac{2h^2(t)}{3t_s}\tan\theta\right] \tag{8}$$

Thus, an expression is derived for the flow rate through the ceramic filter, as a function of the height of water in the filter. The values of *h(t)* were found from the following expression for the volume of water, *V(t)*, contained in the frustum-shaped filter at any given time t:

$$V(t) = \pi\left[R^2 h(t) + R h(t)^2 \tan\theta + \frac{h(t)^3 \tan^2\theta}{2}\right] \tag{9}$$

The values of κ were used to fit equation (8) to the experimental measurements of flow rate that were obtained using the methods described earlier in section 2.3.

3.4 Results and Discussion

3.4.1 Porosimetry

The pore-size distribution results obtained for CWFs with clay to sawdust ratios of 50:50, 65:35 and 75:25 are compared with those from the base of the PFP reference filter (60:40 by weight) in Figures 3.3(a) – 3.3(d). All CWFs tested had a range of pore sizes between the nano- and micron-scales. The fact that each CWF has both nano- and micron-scale porosities is important because the micron-scale pores can trap larger microbes and multi-cellular organisms (Figure 3.4), while the nano-scale pores may trap viruses. A unimodal distribution of pore sizes was observed in the PFP reference filter and the 50:50 CWF [Figures 3.3(a) and 3.3(b)]. In contrast,

the 65:35 and 75:25 CWFs had bimodal micro- and nano-scale pore size distributions [Figures 3.3(c) and 3.3(d)]. The median pore diameters and the average pore diameters of the three CWFs tested are summarized in Tables 3.1(a) – 3.1(b), respectively.

In all cases, most of the pores in the three different CWFs were between 0.05 and 1 µm in size. This is smaller than the typical sizes of most bacteria and non-viral pathogens, which are usually ~ 1 - 3µm in size (Weart *et al.*, 2007; Willey *et al.*, 2008). All three CWFs should, therefore, be effective in removing bacteria, as well as larger cells such as helminth ova, which are typically between 10 µm and a few hundred microns in size (Crompton & Joyner, 1980). The presence of a significant fraction of nano-scale pores is also of some importance, since it raises the possibility of using CWFs in the nano-scale filtration of viruses, which are typically between 10-100 nm in size (Willey *et al.*, 2008). One way of confirming that the filter is capable of removing virus by particle size occlusion is the use of a surrogate in the form of fluorescent labeled polystyrene beads (Bales *et al.*, 1997; Bielefeldt *et al.*, 2010; Dai & Hozalski, 2003; Hendricks *et al.*, 2005). It has been shown that the removal of microspherical-beads from water by CWF decreases with decreasing bead size (Bielefeldt *et al.*, 2010). This means that to effectively filter out viruses from water the CWFs cannot rely on size occlusion alone. One solution that is currently been explored is to doping the CWFs with materials that have affinity for viruses (Brown & Sobsey, 2009; Tsao, 2011).

The porosities determined from the MIP analyses showed that the porosity of the base of the CWF (Figure 3.2) increased with increasing volume fraction of sawdust [Figure 3.5(a)]. Similarly, the porosity of each of the three samples extracted from the top, middle and bottom of the sides of the CWFs (Figure 3.2) also increased with the volume fraction of sawdust.

Consequently, the average porosity obtained from all four samples (from each specific CWF) increased with increasing volume fraction of sawdust [Figure 3.5(b)].

Furthermore, by taking samples from different regions of the CWF, porosimetry tests should give an indication of how homogenous the CWF is, since the pressure used in the manufacturing process is not equal over the height of the filter (Van Halem, 2006). With a standard deviation of ~5.52%, ~ 4.88% and ~3.92%, for CWFs with volume fraction of sawdust of 25, 35 and 50 respectively, the filter can be said to be homogenous.

3.4.2 Flow Rate Measurements, Permeability and Tortuosity

The short term (8 hour) and long term (24 hour) discharge rates of the CWFs are presented in Figures 3.6(a) and 3.6(b). While the pore size and pore size distribution of a filter are important in determining the filters' efficacy at removing particulates from water, the porosity and permeability are important in determining how the rate of fluid flow through the filter. The most porous of the filters studied, the 50:50 CWF, exhibited the fastest discharge, followed by the PFP reference filter. The slowest discharge rates, for both the short- and long-term, were associated with the 75:25 CWF. Therefore, the rate of water discharge by CWF increases with porosity, or in other words with the volume fraction of sawdust used in making the filter. The flow rates obtained for the 50:50 CWF were between ~ 1.3 and 2 L/hr during the first two hours, which is the range that is typical of PFP filters (Lantagne, 2001b). Flow rates for the 65:35 and 75:25 CWFs were well below this level [Figures 3.6(a) and 3.6(b)].

It is important to note that the amount of water through the 50:50 CWF approached an asymptote, as the pressure head decreased with increasing flow. Hence, the flow-time plots

became increasingly non-linear with increasing flow, as shown in Figure 3.6(a). This asymptotic behavior was recently mathematically simulated with a stochastic birth process model specific to respective amounts of organic raw material used in the manufacturing of these filters (Plappally *et al.*, 2009). However, asymptotic regimes were not observed for the 65:35 and 75:25 CWFs [Figures 3.6(a) and 3.6(b)], since the amount of flow was low, even after 24 hours. In these cases, the pressure head is insufficient to drive significant amount of flow through the porous CWFs, as the water level reduced. Figure 3.7(a) – 3.7(c) shows how the measured volume flow rate of the different filters changes with time. Darcy fits are also presented to show how well the measured flow rate data fit the theory. The effective intrinsic permeabilities obtained for each of the CWFs from the Darcy fit (described in section 3) are plotted against the volume fraction of sawdust in Figure 3.8. This shows that the effective permeabilities of the filters increase with increasing volume fraction of sawdust.

Figure 3.9 shows the comparison between the permeability obtained from the Darcy fit to that obtained using the K-T method. For a particular filter composition the variability in the value of permeability obtained using the K-T approach is *largely* due to the variation of the porosity of the filter with respect to the location from which the sample was taken for the mercury porosimetry test, and also in part due to L_c, L_{max} and $S(L_{max})$ (see equation 1). The variability in the permeability obtained from the Darcy fit may be attributed to pores opening and clogging during multiple flow experiments and possibly the effect of the degree of saturation of the CWF prior to testing. The permeabilties of the filters studied (obtained by both methods) were found to be between ~ 10^{-15} m^2 to ~ 5.0 x 10^{-14} m^2 (i.e. ~ 1 millidarcy to ~50 millidarcy), which means the filters can be classified as semi-pervious (Bear, 1972). The value of the permeability is of the same order as that reported by van Halem (Van Halem, 2006). The difference may be due to the

choice of inflexion point (Webb, 2001) and the effects of production variables during fabrication of the CWFs (Lantagne *et al.*, 2010).

While the level of permeability of a porous ceramics gives a measure of the relative ease at which water (or any other fluid) will flow through it, the tortuosity gives an indication of the chances of capture of contaminants, such as *E.coli* bacteria, that are carried along with the water by processes such as adsorption, geometrical occlusion and sedimentation. The results for the tortuosity of the CWFs found by using Jörgen Hager equation (combined with the permeability obtained from Darcy fit and K-T method respectively) are presented in Figure 3.10. In general, the tortuosity is found to increase with increasing clay content. The material tortuosity ranged from ~10 to ~60. A tortuosity value of, say 10, means that in other for a particle (traveling with the water) to get through the CWF it must travel an effective length 10 times the actual length (or thickness) of the CWF. While the data presented in Figure 3.10 represents the average value of the tortuosity, it should be noted that not all of the channels of the filter have the same effective length. Some effective lengths may be shorter or longer than the 'average' effective lengths and hence, compositionally different filters may have a large fraction of similar effective lengths. The overlapping error bars in Figure 3.10 partially testify to this fact. This may also explain why there is no significant difference in the filtration efficiencies of the CWFs studied, despite the fact that the filters have different porosities (see section 4.3 on bacteria filtration). Furthermore, the 50-50 filter, which has a composition similar to filters used in the field, has a tortuosity value that is comparable to that reported by van Halen (Van Halem, 2006).

3.4.3 Bacterial Filtration

Following the flow rate tests, *E.coli* filtration experiments were performed on the two CWFs with the fastest flow rates, the 50:50 CWF and the 65:35 CWF. Each of these two CWFs were tested twice using pre-filtrate with a high *E.coli* density as described earlier. The percentage and the $\log_{10}$ reduction value (LRV) of *E.coli* removed by the CWFs are presented in Table 3.2. Both CWFs tested were highly efficient at removing *E.coli* from aqueous suspensions. The CWFs showed average percentages of filtration of 99.97 and 99.99% and average log reduction values (LRVs) of 5.67 and 6.36 respectively. Thus, the removal efficiency of the 65:35 CWF was slightly greater than that of the 50:50 CWF. Both CWFs meet the WHO standard for water treatment (WHO, 2011a). In comparison, the filtration efficiency of the PFP filter has been reported to be approximately 99.99% with LRV of ~ 2 – 6 (Lantagne, 2001a; Oyanedel-Craver & Smith, 2008; Sobsey *et al.*, 2008).

Following the first set of filtration experiments, a second set of experiments was performed on the same CWFs to explore possible performance differences as a function of increased CWF use. Only small differences in filtration efficiencies were observed between the first and the second sets of tests (Table 3.2). These results suggest that CWF pores did not become significantly clogged or plugged during the first test because of the high *E.coli* density in the pre-filtrate suspensions. Further work is clearly needed to study the dependence of flow and filtration characteristics of the CWFs on the number of filtration cycles. In addition to tests using a pre-filtrate volume of 4 L, a pre-filtrate volume of 8 L was also used to determine whether the efficiency of filtration would be affected by the volume of the pre-filtrate. Base on a study of two different 50:50 CWFs, the average LRV did not change significantly using an 8 L pre-filtrate compared to a 4 L pre-filtrate ($LRV_{4L} = 5.67 \pm 2.50$ and $LRV_{8L} = 4.61 \pm 0.53$).

3.4.4 Implications

The implications of the above results are quite significant. First, they suggest that point-of-use CWFs with well-controlled porosities can be used to filter out most of the bacterial pathogens in water. With *E. coli* removal rates of approximately 99.9%, the use of the CWFs can contribute significantly to the removal of microbial pathogens from drinking water in the developing world, where about 5,000 people die every day from the effects of consuming contaminated water. Social marketing has played a major role in helping the water filter dissemination evolve and progress. However, further work is needed to develop entrepreneurial models and public/private partnerships for increased distribution of the CWFs to people in rural and urban areas in the developing world.

Moreover, the frequency of use of filters by individuals and households cannot be controlled because of many unpredictable conditions such as job nature, behavior, education and untimely social events (Plappally, 2010). A survey in Bolivia found that only 70% of the filters distributed were regularly used (Clasen *et al.*, 2006). It is always important to study the setting of the society to which the filter is going to be distributed (Plappally, 2010). Recontamination due to improper use of the CWF is also an issue, which can be combatted by proper education and behavioral change programs (Brown & Sobsey, 2006). The problem of recontamination also supports the use of household intervention to the problem of waterborne diseases (Plappally *et al.*, 2011). Time of filter use, education, socio-economic status, number of people using the filters, survey feedback and maintenance are some parameters that will influence the health of the people using the ceramic water filter (Plappally *et al.*, 2011).

The porosimetry data also provide some useful insights into how the different ranges of pore sizes can contribute to the trapping of bacteria (Figures 3.3 and 3.4). Based on the current results,

the range of nano- and micron-scale pores can trap single-celled and multi-cellular organisms that cause water-borne diseases. However, the nano-scale pores may not be sufficient to trap viruses that have sizes of about 10 – 30 nm. This suggests a need for adsorbing surfaces that attract viruses during flow through the CWFs. Further work is clearly needed to develop such surfaces.

The successful fitting of Darcy's equation to most of the flow data suggests that much of the flow through the CWFs is well described by continuum flow through porous membranes. However, experiments carried out with filters that were not pre-soaked with water (results not shown) suggest some discrepancies between the measured and the fitted data during the initial stages of the flow. The discrepancies between the initial flow data are attributed to the initial transient flow required for the transport of water from the inner to the outer surface of the CWF. Once this occurs (or if the filter is pre-soaked), the conditions for "continuum" flow appear to be established, and the data is well described by Darcy's equation [Figure 3.7(a) – 3.7(c)]. Furthermore, during the latter stages of the experiments, the hydraulic pressures are insufficient to drive the fluid flow through the porous ceramic walls. Under such conditions, the flow rates decrease, and the flow asymptotes.

Before closing, it is important to note that the flow data presented in Figures 3.6 and 3.7 are highly non-linear. Hence, the simple use of initial flow rate data in CWF quality control provides only a limited perspective of the CWF flow and filtration characteristics. At best, these represent average flow rates during the initial stages. Moreover, studies on the flow rates of the CWFs that have been performed using less sophisticated equipment such as stopwatches, graduated cylinders and/weight scales (Lantagne *et al.*, 2010; Van Halem, 2006). This is more or less a single snapshot flow approach and does not give an accurate picture of the flow characteristics of

a CWF. Better accuracy was achieved in this chapter with the aid of an automated flow measuring device. This method should be complemented with bacterial filtration testing, especially when different batches or sources of clay are used in the fabrication of CWFs.

For the greatest precision, the effective permeabilities should be extracted from the measured flow data, and also used as quality control measures at CWFs factories. However, this may not be practical in rural environments in developing countries, where the CWFs are produced by people with limited capacity to analyze fluid flow data. This suggests a need for simple software and materials process design charts that combine the theories presented in this chapter into guidelines useful to CWF producers in the developing world. These are clearly some of the challenges for future work.

3.5 Conclusions

This chapter presents the results of an experimental study of the water flow and *E.coli* removal efficacy of porous semi-pervious CWFs produced by the sintering of well controlled mixtures of redart clay and sawdust. The flow was well described by Darcy's law and continuum theory. The permeability obtained from the Darcy fit is comparable to that obtained using the Katz and Thompson method. The porosity, intrinsic permeability and overall flow rates increase with increasing volume fraction of sawdust. The tortuosity, however, decreases with increasing volume fraction of sawdust. An optimum flow rate of ~2 Liters per hour was obtained from the CWFs with a sawdust volume fraction of 50%. This filter also removed more than 99.96% or 5.67 LRV of *E.coli* from aqueous suspensions. However, the filtration efficiency did not change significantly with volume fraction of sawdust. The *E.coli* removal was attributed largely to the

geometrical occlusion provided by micron-scale pores and quite possibly by adsorption due to the high tortousity value.

Acknowledgments

This chapter is dedicated to the life and work of Ron Rivera, who was devoted to bringing clean water to poor people across the world.

References

Albert, J., Luoto, J., & Levine, D. (2010). End-User Preferences for and Performance of Competing POU Water Treatment Technologies among the Rural Poor of Kenya. *Environmental Science & Technology, 44*(12), 4426-4432.

Bachmann, B. J. (1972). Pedigrees of some mutant strains of Escherichia coli K-12. *Bacteriol Rev, 36*(4), 525-557.

Bales, R. C., Li, S. M., Yeh, T. C. J., Lenczewski, M. E., & Gerba, C. P. (1997). Bacteriophage and microsphere transport in saturated porous media: Forced-gradient experiment at Borden, Ontario. *Water Resources Research, 33*(4), 639-648.

Bear, J. (1972). *Dynamics of fluids in porous media*. New York,: American Elsevier Pub. Co.

Bielefeldt, A. R., Kowalski, K., Schilling, C., Schreier, S., Kohler, A., & Summers, R. S. (2010). Removal of virus to protozoan sized particles in point-of-use ceramic water filters. *Water Research, 44*(5), 1482-1488.

Bielefeldt, A. R., Kowalski, K., & Summers, R. S. (2009). Bacterial treatment effectiveness of point-of-use ceramic water filters. *Water Research, 43*(14), 3559-3565.

Brown, J., Proum, S., & Sobsey, M. D. (2009). Sustained use of a household-scale water filtration device in rural Cambodia. *Journal of Water and Health, 7*(3), 404-412.

Brown, J., & Sobsey, M. (2006). *Independent Appraisal of Ceramic Water Filtration Interventions in Cambodia*: University of North Carolina of Public Health, Department of Environmental Sciences and Engineering.

Brown, J., & Sobsey, M. D. (2009). Ceramic media amended with metal oxide for the capture of viruses in drinking water. *Environmental Technology, 30*(4), 379-391.

Brown, J., Sobsey, M. D., & Loomis, D. (2008). Local drinking water filters reduce diarrheal disease in Cambodia: a randomized, controlled trial of the ceramic water purifier. *Am J Trop Med Hyg, 79*(3), 394-400.

Clasen, T., Nadakatti, S., & Menon, S. (2006). Microbiological performance of a water treatment unit designed for household use in developing countries. *Tropical Medicine & International Health, 11*(9), 1399-1405.

Clasen, T., Schmidt, W. P., Rabie, T., Roberts, I., & Cairncross, S. (2007). Interventions to improve water quality for preventing diarrhoea: systematic review and meta-analysis. *BMJ, 334*(7597), 782.

Crompton, D. W. T., & Joyner, S. M. (1980). *Parasitic worms*. New York: Crane, Russak.

Crowley, M. M., Schroeder, B., Fredersdorf, A., Obara, S., Talarico, M., Kucera, S., & McGinity, J. W. (2004). Physicochemical properties and mechanism of drug release from ethyl cellulose matrix tablets prepared by direct compression and hot-melt extrusion. *International Journal of Pharmaceutics, 269*(2), 509-522.

Dai, X. J., & Hozalski, R. M. (2003). Evaluation of microspheres as surrogates for Cryptosporidium parvum oocysts in filtration experiments. *Environmental Science & Technology, 37*(5), 1037-1042.

Dies, R. W. (2003). *Development of a ceramic water filter for Nepal.* M Eng, Massachusetts Institute of Technology. Retrieved from http://dspace.mit.edu/handle/1721.1/29553

Donachy, B. (2004). *Manual/Guide for Health Trainers and Others Involved in the Monitoring of the Colloidal Silver Ceramic Water Filter*. Potters for Peace, Managua, Nicaragua.

Eldieb, A. S., & Hooton, R. D. (1994). Evaluation of the Katz-Thompson Model for Estimating the Water Permeability of Cement-Based Materials from Mercury Intrusion Porosimetry Data. *Cement and Concrete Research, 24*(3), 443-455.

Fewtrell, L., Kaufmann, R. B., Kay, D., Enanoria, W., Haller, L., & Colford, J. M., Jr. (2005). Water, sanitation, and hygiene interventions to reduce diarrhoea in less developed countries: a systematic review and meta-analysis. *Lancet Infect Dis, 5*(1), 42-52.

Friedman, K. C. (2010). *Design and Characterization of Hydroxyapatite-Clay Filters for Water Purification.* Bachelor of Science in Engineering Princeton University, Princeton, NJ.

Garboczi, E. J., & Bentz, D. P. (2001). The effect of statistical fluctuation, finite size error, and digital resolution on the phase percolation and transport properties of the NIST cement hydration model. *Cement and Concrete Research, 31*(10), 1501-1514.

Hager, J. (1998). *Steam Drying of Porous Media.* Ph.D, Lund University.

Hendricks, D. W., Clunie, W. F., Sturbaum, G. D., Klein, D. A., Champlin, T. L., Kugrens, P., Hirsch, J., McCourt, B., Nordby, G. R., et al. (2005). Filtration removals of microorganisms and particles. *Journal of Environmental Engineering-Asce, 131*(12), 1621-1632.

Hooton, R. D., Thomas, M. D. A., Marchand, J., & Beaudoin, J. J. (Eds.). (2001). *Materials Science of Concrete Special Volume: Ion and Mass Transport in Cement-Based Materials*. Westerville, OH Am. Ceram. Soc.

Hwang, R. E. Y. (2003). *Six-month field monitoring of point-of-use ceramic water filter by using H\2082S paper strip most probable number method in San Francisco Libre, Nicaragua.* M Eng, Massachusetts Institute of Technology. Retrieved from http://dspace.mit.edu/handle/1721.1/29556

Katz, A. J., & Thompson, A. H. (1987). Prediction of Rock Electrical-Conductivity from Mercury Injection Measurements. *Journal of Geophysical Research-Solid Earth and Planets, 92*(B1), 599-607.

Kosek, M., Bern, C., & Guerrant, R. L. (2003). The global burden of diarrhoeal disease, as estimated from studies published between 1992 and 2000. *Bulletin of the World Health Organization, 81*(3), 197-204.

Lantagne, D. (2001a). Investigation of the Potters for Peace Colloidal Silver-Impregnated Ceramic Filter: Intrinsic Effectiveness and Field Performance in Rural Nicaragua.

Lantagne, D. (2001b). Investigation of the Potters for Peace Colloidal Silver Impregnated Ceramic Filter Report II: Field Investigations.

Lantagne, D. (2001c). Investigation of the Potters for Peace Colloidal Silver Impregnated Ceramic Filter. Report 1: Intrinsic Effectiveness.

Lantagne, D., Klarman, M., Mayer, A., Preston, K., Napotnik, J., & Jellison, K. (2010). Effect of production variables on microbiological removal in locally-produced ceramic filters for household water treatment. *International Journal of Environmental Health Research, 20*(3), 171-187.

Lee, C. (2009). Investigation into the Properties of Filtron. Retrieved from <http://www.edc-cu.org/pdf/scotland%20study.pdf>

Miller, J. H. (1972). *Experiments in molecular genetics*. Cold Spring Harbor, N.Y.: Cold Spring Harbor Laboratory.

Obi, C. L., Potgieter, N., Bessong, P. O., & Matsaung, G. (2003). Scope of potential bacterial agents of diarrhoea and microbial assessment of quality of river water sources in rural Venda communities in South Africa. *Water Science and Technology*, *47*(3), 59-64.

Oyanedel-Craver, V. A., & Smith, J. A. (2008). Sustainable colloidal-silver-impregnated ceramic filter for point-of-use water treatment. *Environmental Science & Technology*, *42*(3), 927-933.

PFP. (2008). Potters for Peace. Retrieved from http://www.pottersforpeace.org.

Plappally, A., Chen, H., Ayinde, W., Alayande, S., Usoro, A., Friedman, K. C., Dare, E., Ogunyale, T., Yakub, I., et al. (2011). A Field Study on the Use of Clay Ceramic Water Filters and Influences on the General Health in Nigeria. *Journal of Health Behavior and Public Health, 1*(1), 14.

Plappally, A. K. (2010). Theoretical and empirical modeling of flow, strength, leaching and micro-structural characteristics of V shaped porous ceramic water (pp. xxiii, 219 p.). Retrieved from http://rave.ohiolink.edu/etdc/view.cgi?acc%5Fnum=osu1276860054

Plappally, A. K., Yakub, I., Brown, L. C., Soboyejo, W. O., & Soboyejo, A. B. O. (2009). Theoretical and Experimental Investigation of Water Flow through Porous Ceramic Clay Composite Water Filter. *FDMP, 5*(4), 373-398.

Sobsey, M. D., Stauber, C. E., Casanova, L. M., Brown, J. M., & Elliott, M. A. (2008). Point of use household drinking water filtration: A practical, effective solution for providing sustained access to safe drinking water in the developing world. *Environmental Science & Technology, 42*(12), 4261-4267.

Swanton, A. A. (2008). *Evaluation of the complementary use of the ceramic (Kosim) filter and Aquatabs in Northern Region, Ghana.* M Eng, Massachusetts Institute of Technology. Retrieved from http://dspace.mit.edu/handle/1721.1/43897

Tsao, N. H. (2011). *Virus filtration in porous iron oxide doped ceramic water filter.* Bachelor of Science in Engineering Princeton University, Princeton, NJ. .

UNICEF/WHO. (2009). *Diarrhoea: why children are still dying and what can be done*. New York: United Nations Children's Fund.

Van Halem, D. (2006). *Ceramic Silver Impregnated Pot Filters for Household Drinking Water Treatment in Developing Countries.* Master of Science Delft University of Technology, The Netherlands.

Weart, R. B., Lee, A. H., Chien, A. C., Haeusser, D. P., Hill, N. S., & Levin, P. A. (2007). A metabolic sensor governing cell size in bacteria. *Cell, 130*(2), 335-347.

Webb, P. A. (2001). An Introduction to the Physical Characterization of Materials by Mercury Intrusion Porosimetry with Emphasis on Reduction and Presentation of Experimental Data. Retrieved from http://www.micromeritics.com/pdf/mercurypaper.pdf

Wenhold, F., & Faber, M. (2009). Water in nutritional health of individuals and households: An overview. *Water Sa, 35*(1), 61-71.

WHO. (2011a). *Evaluating Household Water Treatment Options: Health-based targets and microbial performance specifications*. Geneva, Switzerland.

WHO. (2011b). *Guidelines for Drinking-Water Quality* (4 ed.). Geneva, Switzerland.

WHO/UNICEF. (2008). *Progress on Drinking Water and Sanitation: Special Focus on Sanitation; World Health Organization and United Nations Children's Fund Joint Monitoring Programme for Water Supply and Sanitation*. Geneva, Switzerland.

Willey, J. M., Sherwood, L., Woolverton, C. J., & Prescott, L. M. (2008). *Prescott, Harley, and Klein's microbiology* (7th ed.). New York: McGraw-Hill Higher Education.

Yakub, I., Du, J., & Soboyejo, W. O. (Submitted for publication). Mechanical Properties and Design of Porous Clay Ceramics.

Yakub, I., & Soboyejo, W. O. (Submitted for publication). Adsorption of Fluoride from Water using Sintered Clay-Hydroxyapatite Composite.

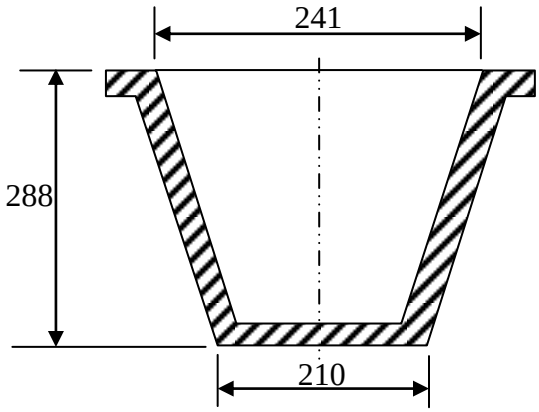

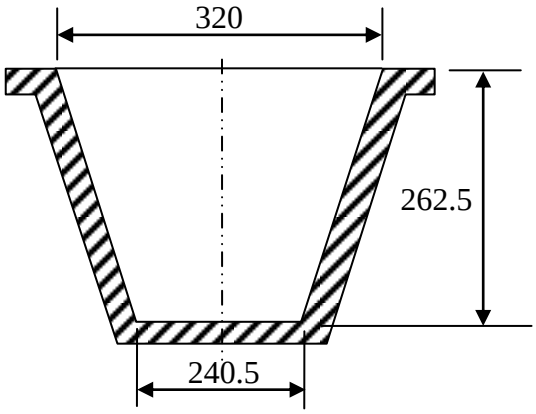

Figure 3.1(a): Male Mold **Figure 3.1(b):** Female Mold

Figure 3.1: Geometry of the two-piece aluminum molds that were used to form the CWF into a frustum shape: (a) Male Mold and (b) Female Mold (Major dimensions are shown in mm)

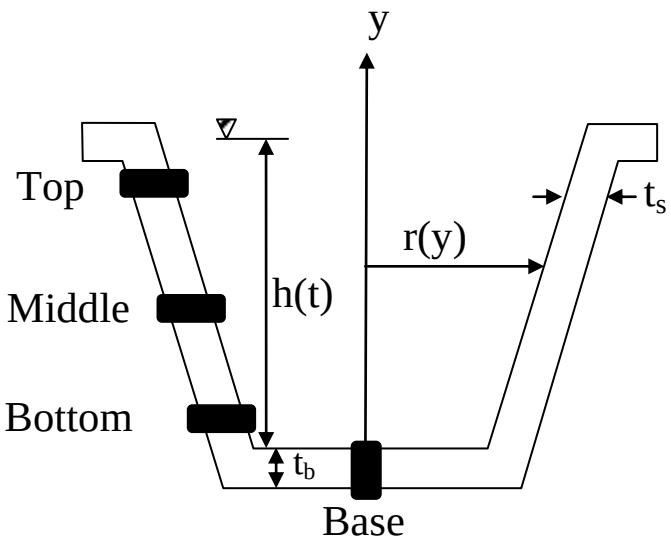

Figure 3.2: Schematic of a CWF with key variables labeled. The four sites from which samples for the MIP analyses were obtained are demarcated with black rectangles

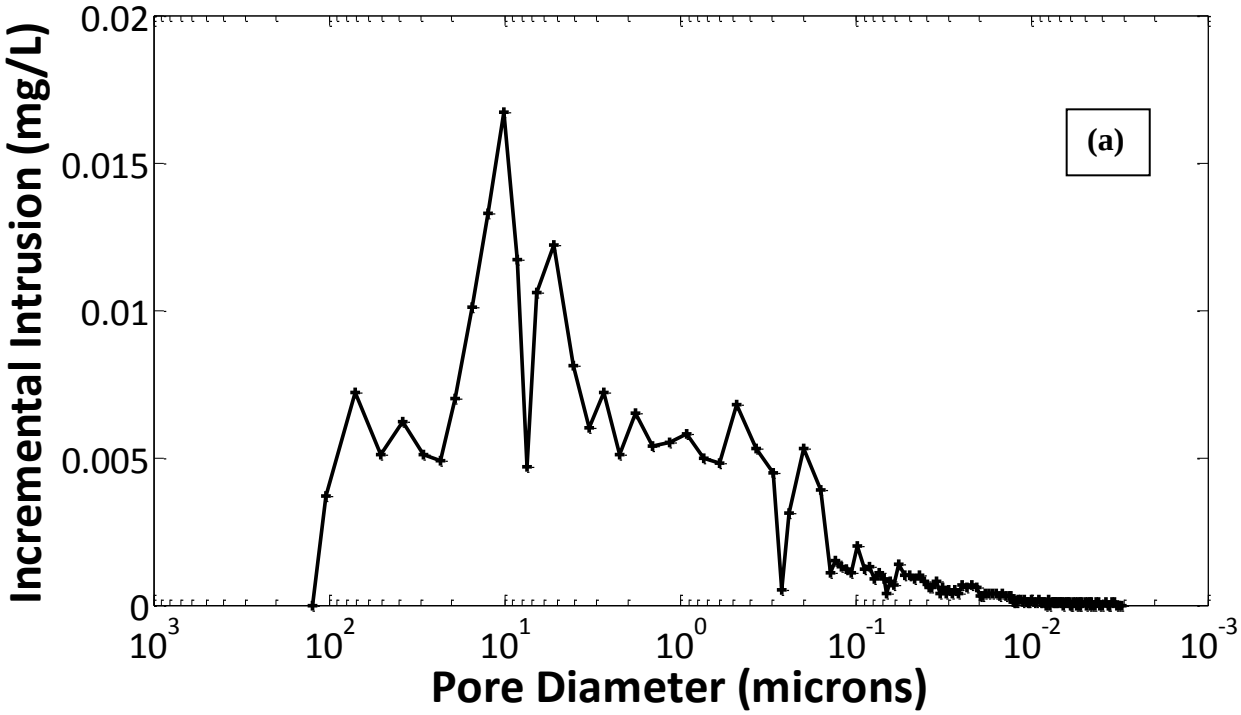
(a)
Incremental Intrusion (mg/L)
0.02
0.015
0.01
0.005
0
10^{3}
10^{2}
10^{1}
10^{0}
10^{-1}
10^{-2}
10^{-3}
Pore Diameter (microns)

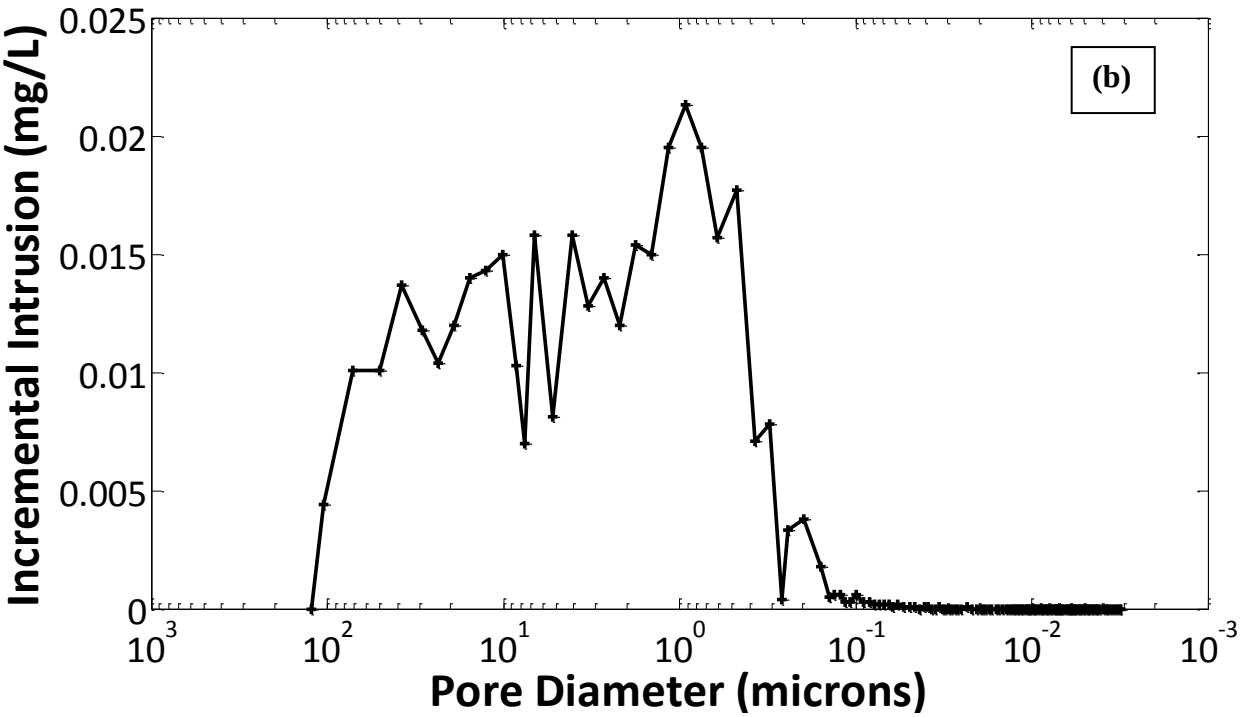
(b)
Incremental Intrusion (mg/L)
0.025
0.02
0.015
0.01
0.005
0
10^{3}
10^{2}
10^{1}
10^{0}
10^{-1}
10^{-2}
10^{-3}
Pore Diameter (microns)

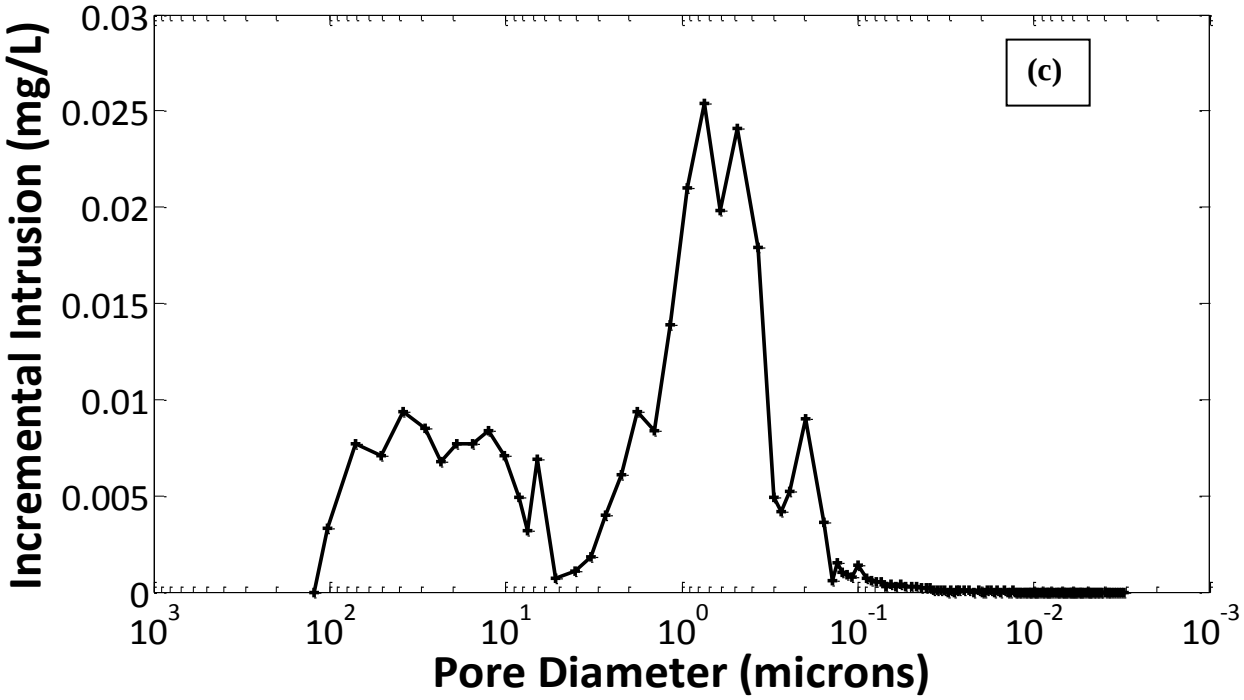

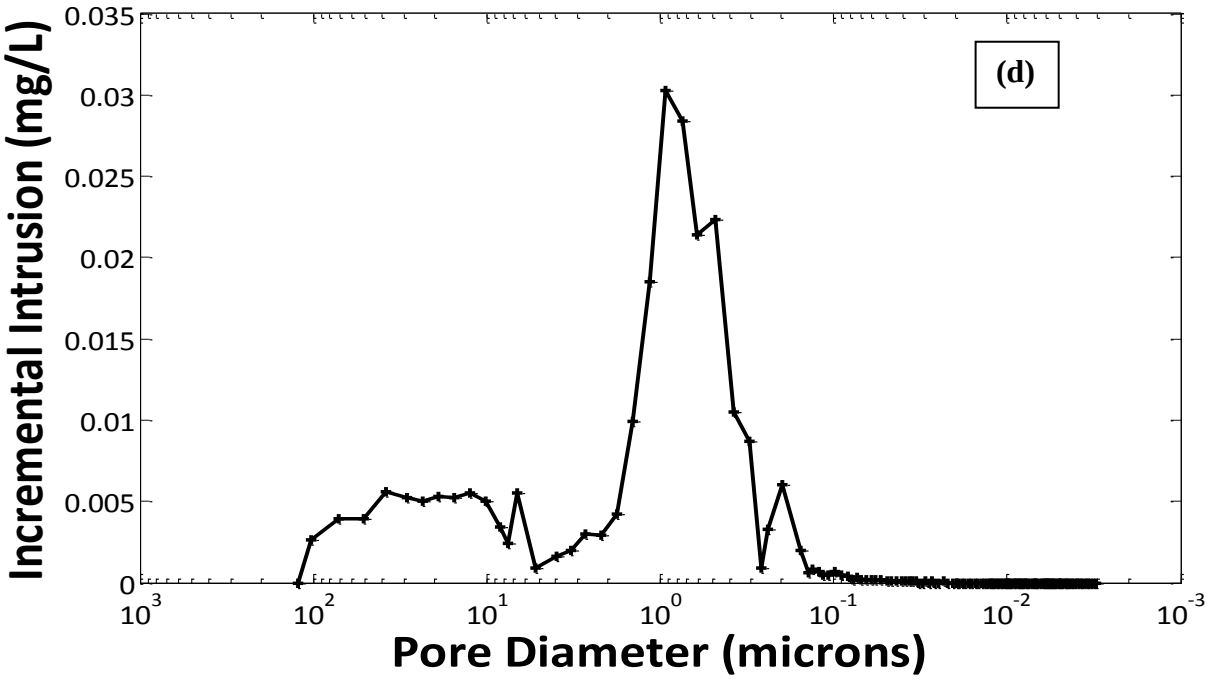

Figure 3.3: Pore-size distribution for samples taken from the bases of: (a) PFP filter; (b) 50:50 filter; (c) 65:35 filter, and (d) 75:25 filter

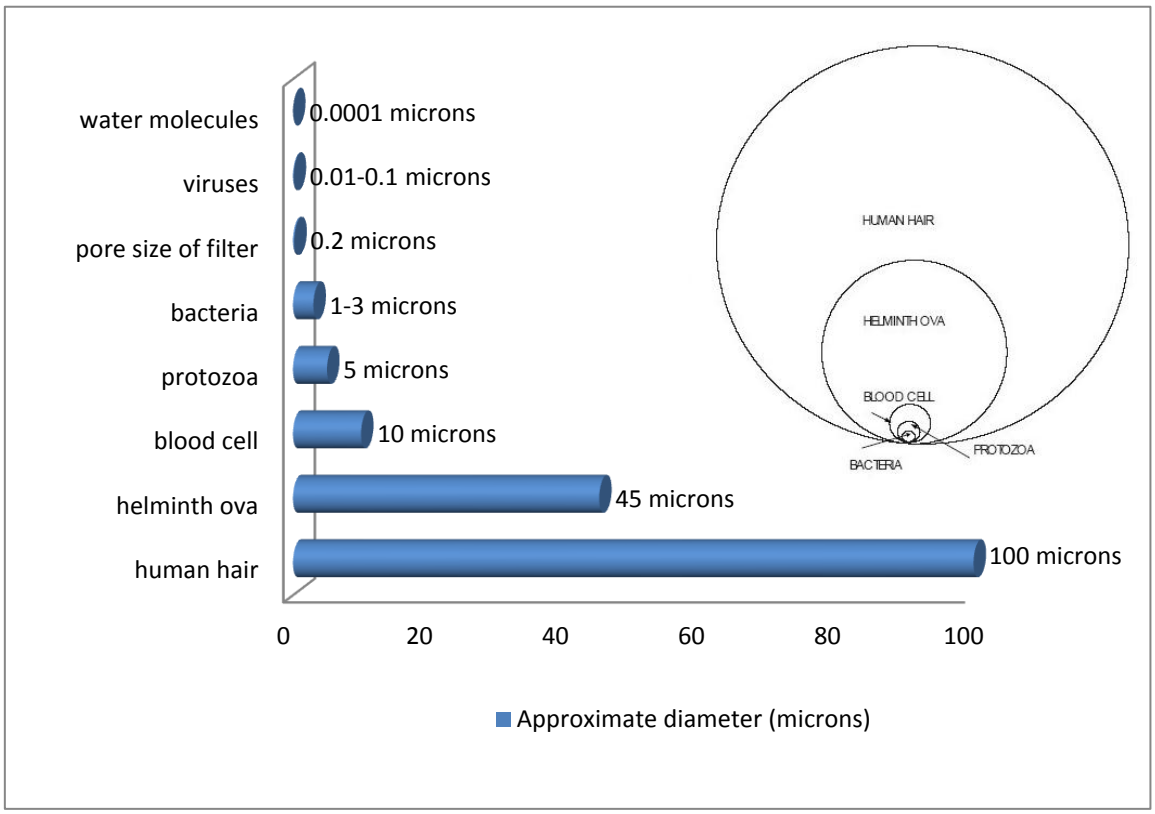

Figure 3.4: Comparison of the average pore size of a CWF to the sizes of a water molecule, different microbes and cells, and a multi-cellular hair, all of which can be found in contaminated water

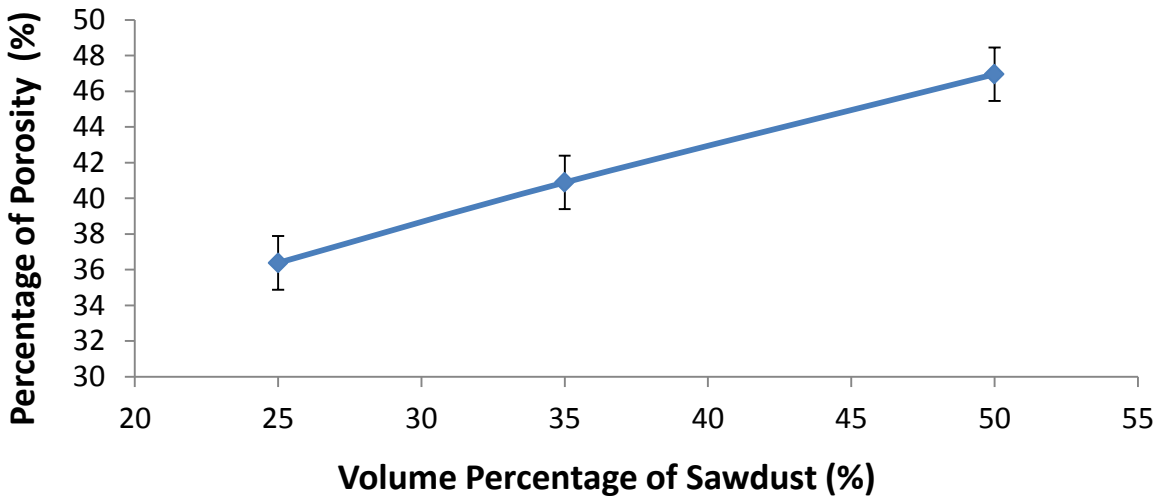

Figure 3.5(a): Porosity dependence on the volume fraction of sawdust (CWF Base)

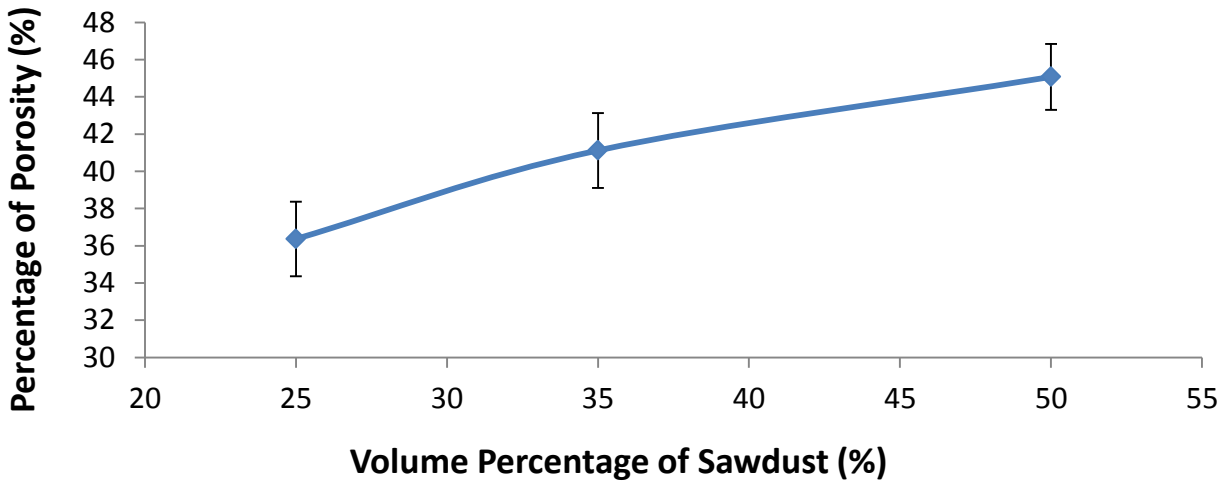

Figure 3.5(b): Variation of porosity with the volume fraction of sawdust. The value of the porosity shown in the plot represents the average of the porosities for each volume fraction of sawdust

Figure 3.5: Dependence of porosity on the volume fraction of sawdust used in filter fabrication: (a) Base porosity levels and (b) Overall average porosity from sides and base

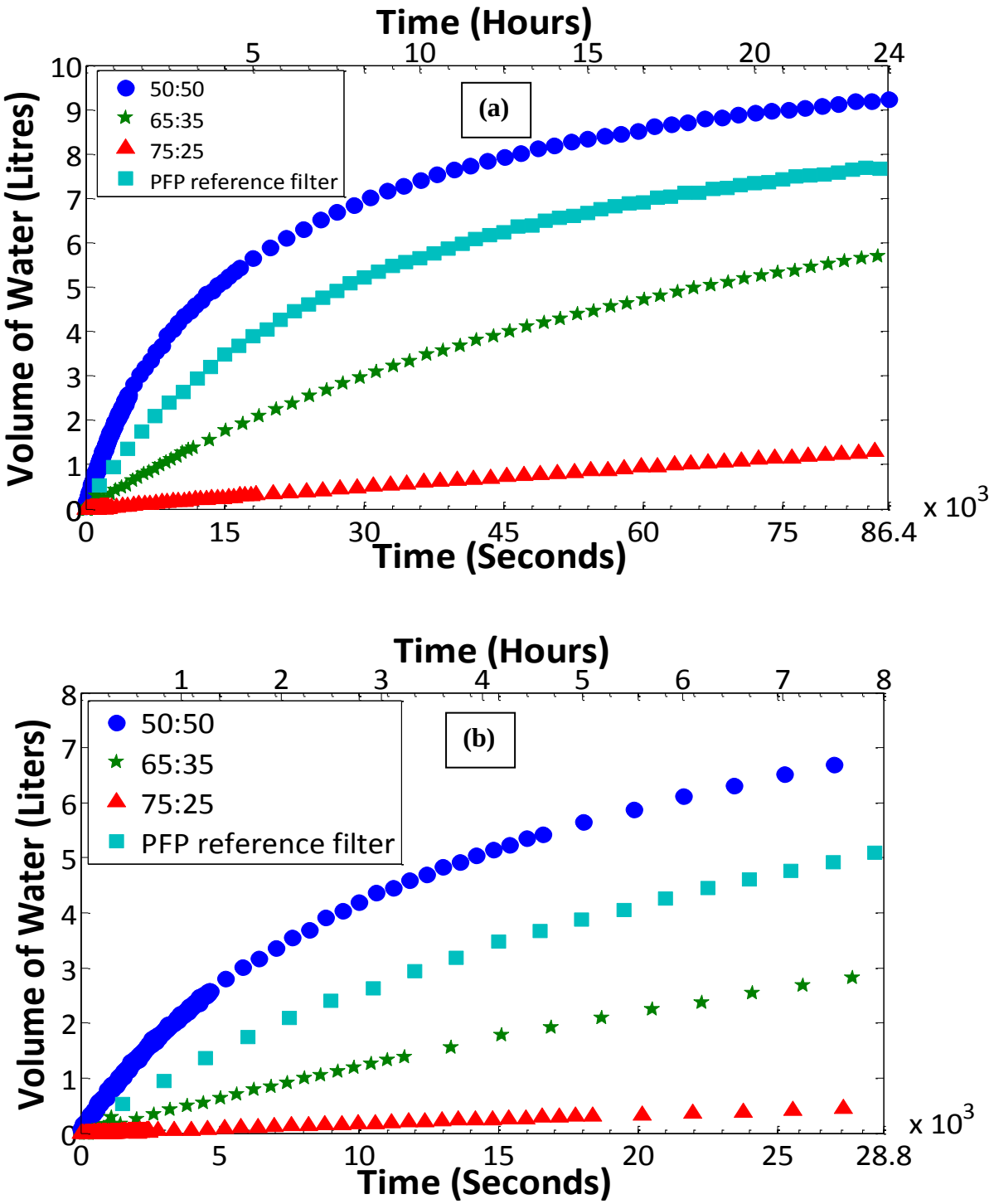

Figure 3.6: Plots of effluent discharge as a function of time: (a) Day-long (24 hour) effluent discharge and (b) "Overnight" (8 hour) effluent discharge

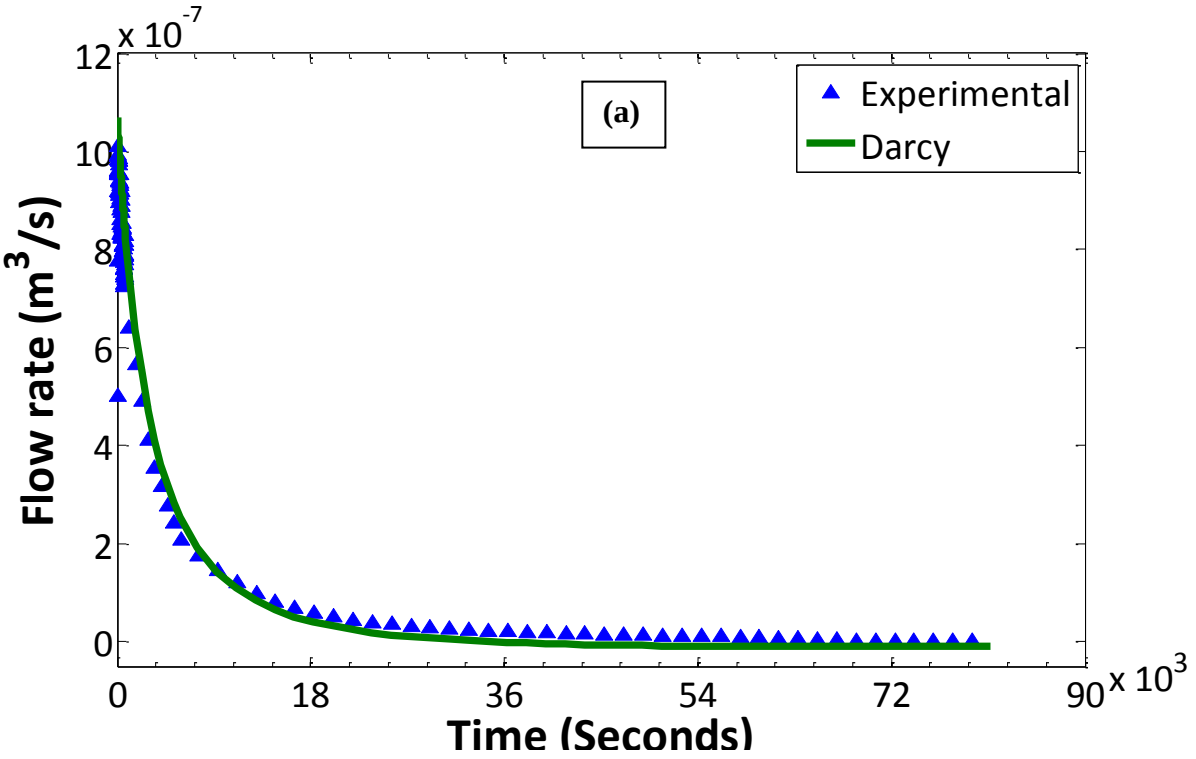
x 10^-7
12
10
8
6
4
2
0
Flow rate (m^3/s)
(a)
Experimental
Darcy
0
18
36
54
72
90
x 10^3
Time (Seconds)

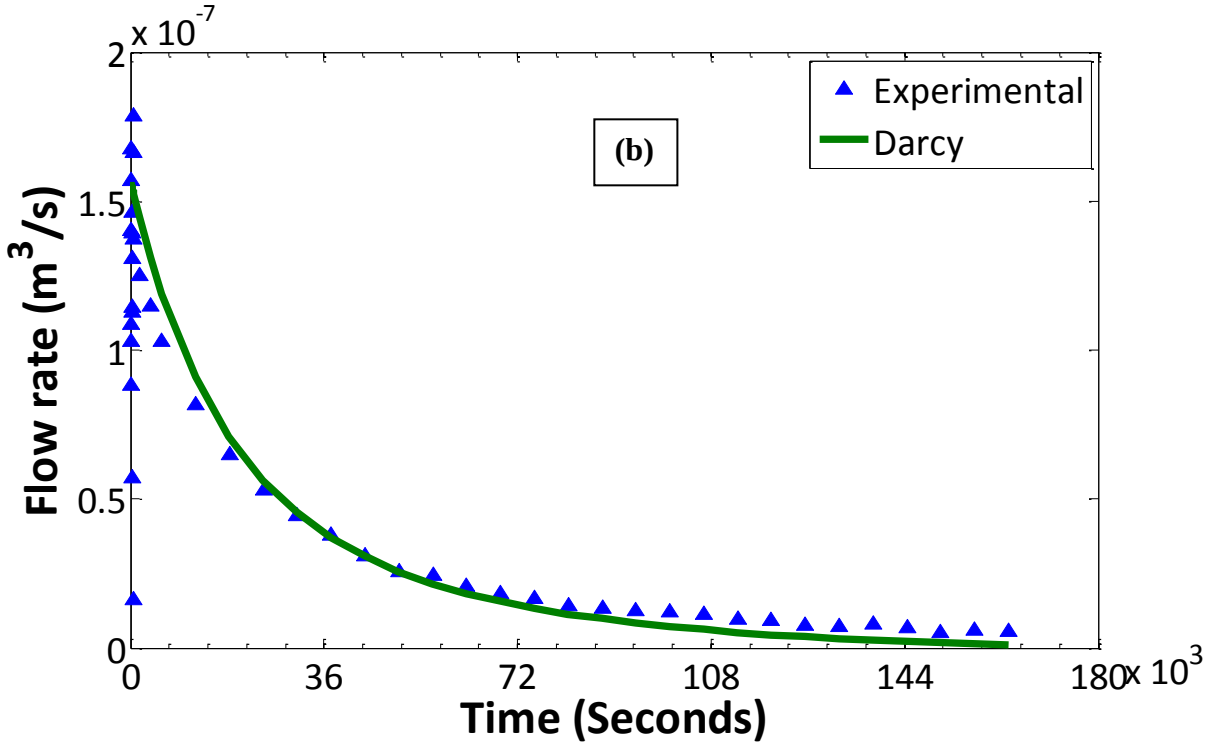
x 10^-7
2
1.5
1
0.5
0
Flow rate (m^3/s)
(b)
Experimental
Darcy
0
36
72
108
144
180
x 10^3
Time (Seconds)

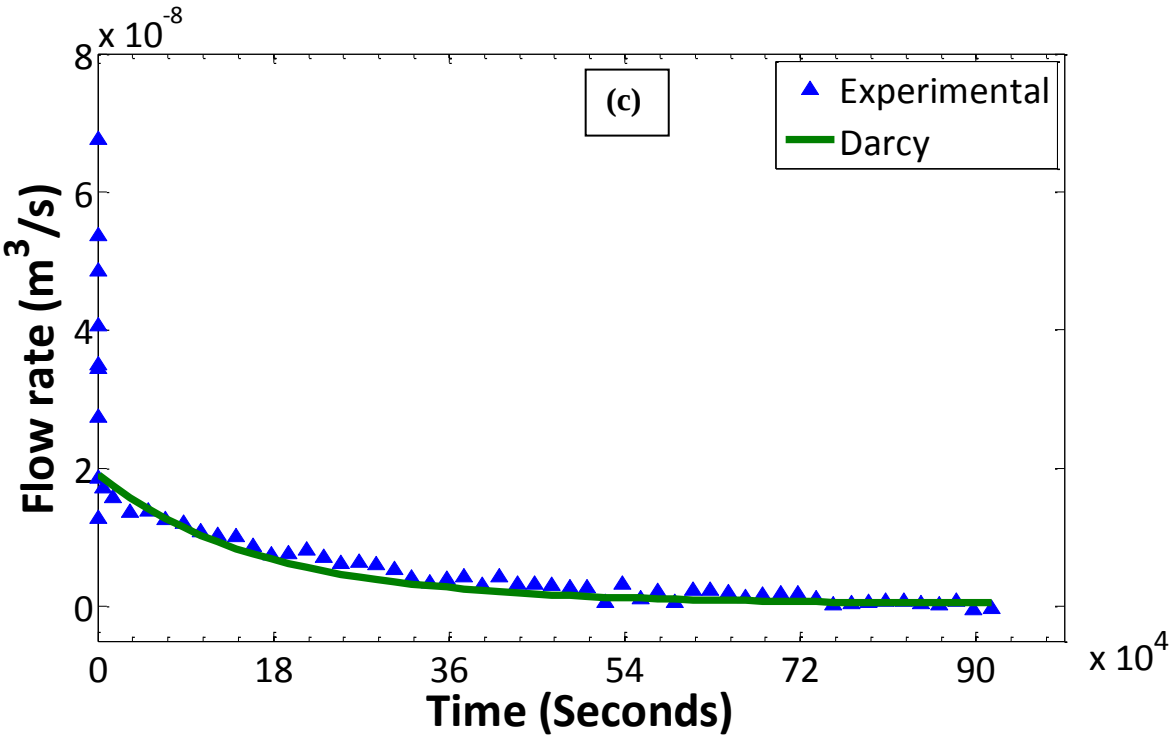

Figure 3.7: Plots of volume flow rate against time – comparisons of experimental data and Darcy fits: (a) 50:50: CWF; (b) 65:35 CWF and (c) 75:25 CWF

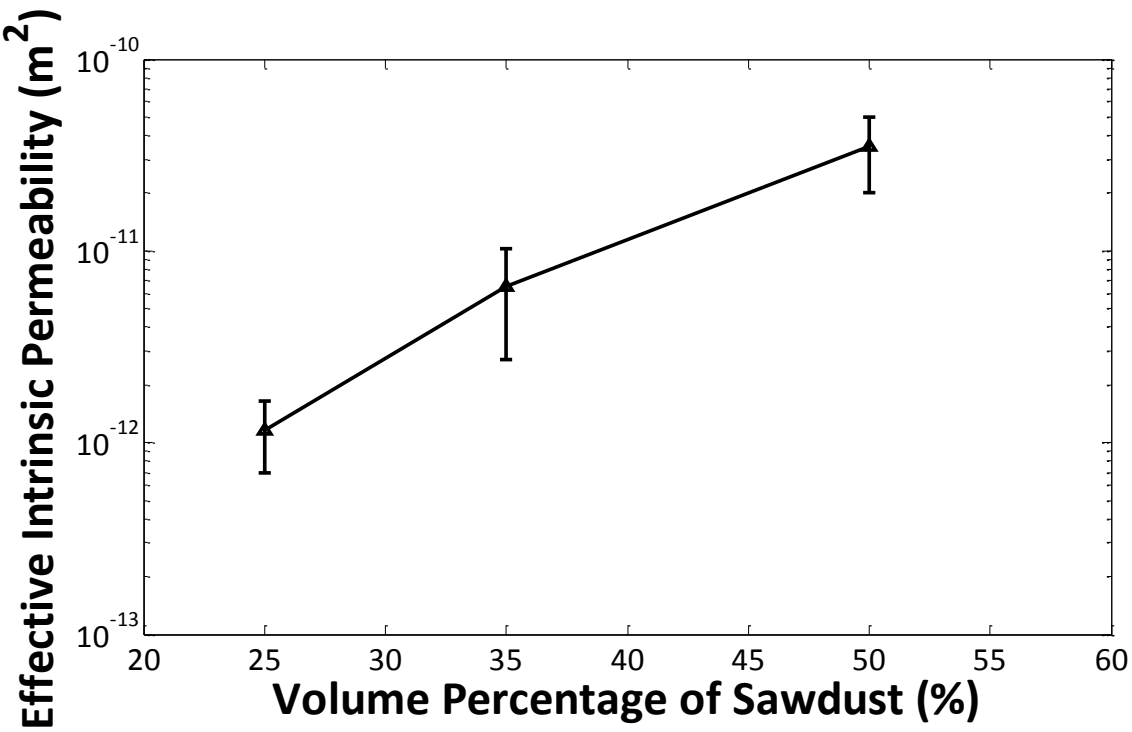

Figure 3.8: Dependence of the effective CWF intrinsic permeability on the volume percentage of sawdust

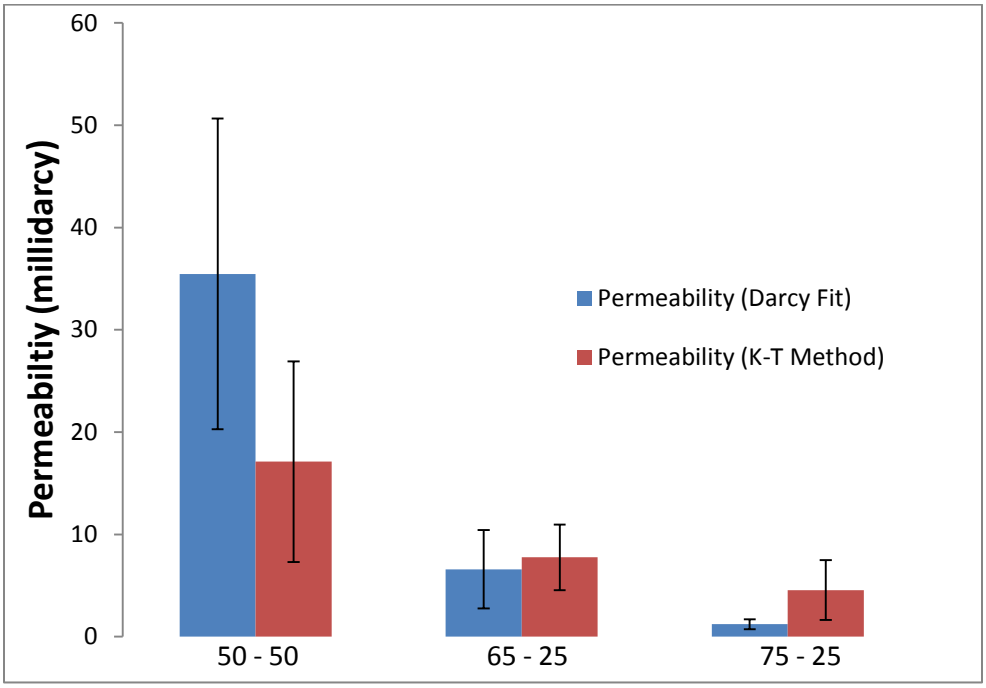

Figure 3.9: Comparing the permeability obtained from Darcy fit with the K-T method

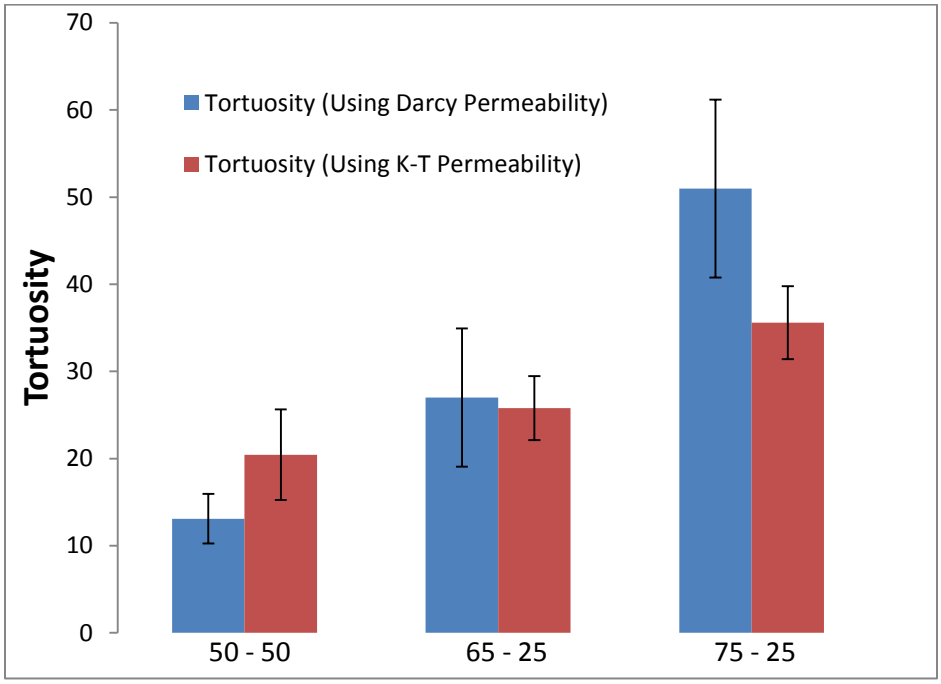

Figure 3.10: Bar chart showing the tortuosity of the CWFs. The tortuosity was found by combining the Jörgen Hager approach with: 1. The permeability obtained from the Darcy fit and 2. The permeability obtained using the K-T method. The skeletal density used was obtained using helium pycnometer

(a)

Volume Fraction of Sawdust	Median Pore Diameter (μm)				Average
	Base	Lower	Middle	Upper	
25	0.88	1.00	0.96	0.94	0.94
35	1.02	0.80	1.05	0.88	0.94
50	3.12	6.05	3.27	3.31	3.94

(b)

Volume Fraction of Sawdust	Average Pore Diameter (μm)				Average
	Base	Lower	Middle	Upper	
25	0.60	0.73	0.71	0.68	0.68
35	0.59	0.46	0.51	0.48	0.51
50	1.07	1.02	1.13	1.04	1.07

Table 3.1: The median pore diameters, the average pore diameters and the porosities of three CWFs tested: (a) Median Pore Diameter of CWFs and (b) Average Pore Diameter of CWFs

Volume Fraction Clay : Sawdust	Percent E.coli Removal Average ± S.D	Log Reduction Value *E.coli* Removal Average ± S.D
50:50	99.96 ± 0.04	5.67 ± 2.50
65:35	99.99 ± 0.00	6.36 ± 0.76

Table 3.2: *E.coli* filtration efficiency obtained for filters with different clay to sawdust volume ratios results expressed as percentages calculated using $\eta_{E.coli} = 1 - \frac{N_f}{N_{pf}}$ where N_f is the number of viable cells per mL of filtrate and N_{pf} is the number of viable cells per mL of pre-filtrate to yield the percentage filtration efficiency. Secondly, as described by Brown and Sobsey (Brown & Sobsey, 2009), the Log_{10} reduction in *E. coli* concentration between the pre-filtrate and the filtrate was obtained from: *Log_{10} reduction value,* $LRV = Log_{10}\left[\frac{C_{pf}}{C_f}\right]$

Chapter 4

Mechanical Properties and Design of Porous Clay Ceramics

4.1 Introduction

The porous nature of the CWFs makes them susceptible to failure. This leads to filter breakage during processing, distribution (transportation) and usage. The latter is because the filter has to be able to support its own weight on its lips (which rests on the rim of a receptacle) during operation (due to the hydrostatic pressure of water). There is, therefore, a need to relate the mechanical properties of the porous clay ceramics to their porosity and pore size distributions. There is also a need to fabricate filters with improved structural integrity. This can be achieved by re-designing the filter geometries and by finding ways to toughen them.

In this chapter, clay ceramics with three different levels of porosity were produced by the sintering of clay/sawdust mixture with ratios of 50:50, 65:35 and 75:25 by volume. The structure

and mechanical properties (elastic modulus, hardness, compressive strength, flexural strength, fracture toughness and resistance-curve behavior) were studied using a combination of experiments and models. The finite element method (FEM) was then used to study the stress distributions due to the hydrostatic pressures exerted on the filter walls with different shapes and support configurations. The implications of the results are then discussed for the scale up of ceramic water filtration and the design of filter shapes and structures with improved robustness.

4.2 Experimental

4.2.1 Materials and Processing

The (redart) clay that was used in this study was obtained from Cedar Heights (Cedar Heights Redart Airfloated Clay, Pittsburgh, PA). The chemical composition of the clay is given in Table 4.1. The sawdust (woodchips) used was obtained from a local sawmill (Hamilton Building Supplies, Trenton, NJ). The clay was mixed with the sawdust in three different ratios (clay-to-sawdust) by volume, viz: 50:50, 65:35 and 75:25. Prior to mixing, the sawdust was manually sieved using 35-1000 mesh wire sieves. The clay was then blended with sawdust in an industrial mixer (Model A-200, The Hobart Manufacturing Company, Troy, OH), with water as the binding agent.

The resulting mixture (clay, sawdust and water) was formed into a dough shape (about 5.5 kg / 12 lbs is required to make a CWFs). The dough was then formed into a frustum-shape, with a two-piece frustum-shaped aluminum mold. This was done using a 50 tonne hydraulic press (TRD55002, Torin Jacks, Inc., Ontario, Canada). The resulting greenware was dried in laboratory air (temperature of 25°C, humidity of 40%) for about 5 to 8 days. After drying, the

greenware was sintered in a gas kiln (Ceramics Art Department, Princeton University, Princeton, NJ). The firing involved pre-heating of the greenware to 450-550°C for three hours (to burn off the sawdust), followed by heating to the sintering temperature of 955°C in the same gas kiln. The initial heating rate of 50°C per hour was increased to 100°C per hour beyond a furnace temperature of 200°C. The CWFs were sintered for 5 hours at the peak temperature of about 955°C. They were then furnace-cooled in air to room-temperature.

The frustum-shaped CWFs consists of two sections, the base (or disc part) and the side (or curved part). The disc has a radius of ~ 91.5 mm and a thickness of ~ 15 mm. The side has a slant height of ~ 240 mm and is ~ 10 mm thick. The CWFs is ~ 237 mm deep, and hence has a capacity of about 10 liters. In this study, only the base (or disc part) of the CWFs was used in the characterization of the structure and mechanical properties of the porous clays ceramics. The sides were not used due to their curvature.

4.2.2 Materials Characterization

The porosities, (average) pore-size, bulk density and skeletal density of the porous clay ceramics were measured using a Mercury Porosimeter (MP). The porosimetry measurements were carried out in a MicroMetrics Autopore III 9400 analyzer (MicroMetrics, Norcross, GA). The two-stage MP experiments were performed on pieces with dimensions of ~ 3 mm x 3 mm x 3 mm that were cut from the three different porous ceramics (50:50, 65:35 and 75:25). The skeletal density of the porous ceramic was also found using a AccuPyc 1330 Helium Pyncometer (HP) (MicroMetrics, Norcross, GA).

The surface morphology of the woodchips and the porous ceramic was carried out using the Environmental Scanning Electron Microscope (ESEM) (Quanta 200 FE-ESEM, FEI, Hillboro,

OR). The elements present in the redart clay and porous clay ceramics were also verified using the Oxford EDX detector (Oxford Instruments, Oxfordshire, UK) on the Environmental SEM. X-ray diffraction (XRD) was performed on powders of redart clay and porous clay ceramics to determine their phase compositions. This was done using a Bruker D8 Advance diffractometer, with secondary graphite monochoromator and Cu-Kα radiation (λ=0.15418 nm). The scan step was 0.02^{o} and the step time was 0.8 seconds per step. The measurement was done over the interval $10° < 2\theta < 70°$. The entire operation was carried out at room temperature ($25^{o}C$).

4.2.3 Modulus and Hardness Measurement

Nanoindentation was used to obtain the moduli and hardness values of the porous ceramic. The indentation studies were performed in a TriboScope nanomechanical testing system (Hysitron Inc., Minneapolis, MN), coupled to a Dimension 3100 scanning probe microscope (Veeco Instruments Inc., Woodbury, NY). A three-plate capacitive transducer was used by the TriboScope to control the applied load. A conical (spherical-tipped) indenter with a norminal tip radius of ~100 μm was used. The loading profile consisted of the following three steps: loading at a rate of 5μN/s to a peak load of 1000 μN; holding at the peak load for 5s, and returning to zero load at an unloading rate of 5μN/s.

4.2.4 Strength Measurements

Both the compressive strength and flexural strength testing were carried out in an Instron Model 8872 servo-hydraulic testing machine (Instron, Canton, MA) instrumented with a load cell of 25 kN. The compressive strengths of the porous clay ceramics were obtained by compressive

loading of bars of height, H = 35 mm, width, W = 12.63 mm, and breadth, B = 12.63 mm was used. These were loaded to failure at a rate of 0.1 $N.s^{-1}$. The compressive strength was then evaluated from the following expression:

$$\sigma_c = \frac{P}{BW} \tag{1}$$

where P is the load at failure; B and W are the respective breadth and width of the rectangular specimens.

The flexural strengths or moduli of rupture (MOR) were obtained by the bend testing of bars of height, H, of 12.63 mm, width, W, of 12.63 mm, and length, L, of 76 mm. Two types of specimens were made due to the anisotropic nature of the porous clay ceramics. The specimens were oriented for fracture in the short transverse and traverse orientations, referred to here as "S-Type" and "T-Type" specimen respectively. The MOR experiment was done under three-point bend loading at a cross-head speed of 0.1 $N.s^{-1}$ and a loading span of 40 mm.

The MOR was then evaluated from the following expression (Kingery *et al.*, 1976):

$$MOR(\sigma) = \frac{3PS}{2B^2W} \tag{2}$$

where S is the loading span, P is the applied load at the onset of failure, while the other constants have their usual meanings.

4.2.5. Fracture Toughness

Due to the anisotropic nature of the porous clay ceramics, fracture toughness (K_{Ic}) tests were performed on two types of single-edge notched-bend (SENB) specimens. The specimens mainly differ by the orientation of the notch. Specimens with height, *H*, of 12.63 mm, width, *W*, of 12.63 mm, and length, *L*, of 76 mm, were used. The specimens were tested using the Instron 5848 MicroTester (Instron, Canton, MA) instrumented with a 500 N load cell. The specimens were loaded monotonically to failure at a loading rate of 0.1 $N.s^{-1}$, with a loading span of 35 mm. An initial notch, with a notch-to-width ratio (*a/W*) of ~ 0.25, was introduced at the center of the specimens. Fracture toughness, K_{Ic}, was determined from the following expression (ASTME, 1990; Saadaoui *et al.*, 1991):

$$K_{Ic} = \frac{PS}{BW^{3/2}} \times f\left(\frac{a}{W}\right) \tag{3}$$

where *a* is the crack length (depth of the notch), $f\left(\frac{a}{W}\right)$ is the compliance function.

4.2.6 Resistance-Curve Measurements

Resistance-curve experiments were also performed on the same type of SENB specimens that were used in the fracture toughness measurements. The experiments were performed under three-point bend loading. Crack growth was monitored with Krak gages (KG-A05, Hartrun Corp., Eden Prairie, MI) bonded to the specimen surfaces with the Epotek 353ND (Epoxy Technologies Inc., Billerica, MA). After curing for 24 hours, four wires were soldered on to the

Krak gage and connected to a FRACTOMAT system (Model 1288, Hartrun Corp., Eden Prairie, MI), which is a two-channel microprocessor-based instrument for monitoring crack growth.

The FRACTOMAT system was connected to a NI CB-68LP board (National Instrument, Austin, TX) that was linked to a computer with LABView software package (National Instruments, Austin, TX). The latter was used to collect the voltage data (due to crack growth) as a function of time. The specimens were loaded in incremental steps to peak loads below the critical loads. The loads were then increased in incremental steps, while the corresponding incremental crack growths were monitored using the *in-situ* Krak gages. This was continued until the crack growth reached the steady-state regime. In this way, the resistance curves were obtained for all the porous ceramics.

4. 3 Modeling

4. 3.1 Crack-tip Shielding

The resistance of the porous ceramic to crack growth was quantified in this section using a combination of small- and large-scale crack bridging models. For small scale bridging, where it is assumed that the bridging zone is small compared to the crack size ($\Delta a < 0.5$ mm), the toughening due to small to small-scale crack bridging, ΔK_{ssb}, is given by:

$$\Delta K_{ssb} = \sqrt{\frac{2}{\pi}} \int_0^{l_B} \alpha V_B \frac{\sigma(x)}{\sqrt{x}} dx \qquad (4)$$

where l_B is the bridge length (which is equal to the distance from the crack-tip to the last unfractured reinforcement), $\sigma(x)$ represents the bridging traction across the ductile reinforcement, x is the distance from the crack face behind the crack-tip, α is the triaxiality/constraint factor (Fett, 2008), and V_B is the volume fraction of the ligaments.

In the case where the bridging zone is comparable to the overall crack dimensions ($\Delta a \geq 0.5$ mm), large scale bridging models are used to estimate the shielding contributions from crack bridging. The shielding due to large-scale bridging, ΔK_{lsb}, is given by (Baker *et al.*, 2006; Lou *et al.*, 2003):

$$\Delta K_{lsb} = \int_0^L \alpha V_B \sigma(x) h(a,x) dx \quad (5)$$

where L is the length of the bridging zone, α is the constraint/triaxiality factor, V_b is the volume fraction of bridging ligaments, $\sigma(x)$ is traction function along the bridge zone, and $h(a,x)$ is a weighting function given by Fett and Munz (Fett & Munz, 1997).

The overall resistance curve behavior may be estimated by the application of the principle of linear superposition. This gives:

$$K_{app} = K_{tip} + \Delta K \quad (6)$$

where K_{app} is the applied stress intensity factor, K_{tip} is the initiation toughness and ΔK is the toughening due to small-scale crack bridging ($\Delta a < 0.5$ mm) or large-scale bridging ($\Delta a \geq 0.5$ mm) as the case may be.

4.3.2 Finite Element Analysis

The objective of Finite Element Analysis (FEA) is to optimize the geometry and supporting configuration of the water filters under the effects of hydrostatic pressure. The finite element software ABAQUS™ v6.9-EF2 (ABAQUS, Inc., Pawtucket, RI) was used in the study. Axisymmetric finite element models of filters were developed as shown in Figure 4.1. A 4-node linear axisymmetric element was used. The mesh was refined at the corners as in Figure 4.1(a). The diameter, thickness, height and angle of the frustum model (Figure 4.1(a)) are the same as that of typical CWFs, as described in Section 4.2.1.

Figure 4.2(a) – 4.2(g) shows the different support configuration that was used in the modeling of the frustum-shaped filter. Models of potential uniform thickness filter model, ellipsoidal filter model, semi-spherical filter model, cylindrical filter model, and inverted frustum filter model, were also built, as shown in Figures 4.1(b) – 4.1(e), respectively. The same wall thicknesses and heights were used in all the filter models.

The measured mechanical properties of the 65-35 filter, such as Young's modulus, density and porosity, were used for this study (Table 4.2 and Table 4.3). It was assumed that all the materials exhibited isotropic elastic behavior. The axisymmetric boundary condition was also applied at the symmetry axis. The bottoms of the filter lips were fixed to have no displacements or rotations. A hydrostatic pressure load was applied on the inner surface of each filter to simulate the effects of water in the filter. In this way, the stress distributions were computed for the possible filter designs. A body force was applied on each filter to simulate the effects of the filter self-weight and the weight of water contained within the filter during operation. In this way, the stress distributions were computed for the different filter designs.

4.4 Results and Discussion

4.4.1 Materials Characterization

Figure 4.3(a) is the environmental scanning electron micrograph of the woodchips (sawdust) used in making the porous ceramics. The surface morphology of the porous clay ceramic is given in Figure 4.3(b). The bulk density and skeletal density (using HP and MP) are found to increase with increasing sawdust content (Table 4.2). One hypothesis is that the greenware with higher sawdust content, burns off quicker than a greenware with lower sawdust content. This is because of larger pathways/channels available expulsion of the combustion products (mainly carbon dioxide). As a result, the greenware with the higher sawdust content has more time to sinter (due to the relatively early eviction of the sawdust).

Furthermore, the skeletal density measured by the helium pycnometer (HP) was greater than that measured by the mercury porosimeter (MP). This suggests that the porous ceramic had pore sizes below the detectable limits of the MP method. This higher skeletal density measured by the HP resulted in a higher porosity, compared with the values for MP (Table 4.2). This is because of helium gas has a small atomic radius (~ 31 pm) and is thus able to seep through pico-scale pores. The mercury porosimetry on the other hand is only effective for pores diameters greater 3 nm. The linear relation between the two types of porosities is shown in Figure 4.4. This exhibits a correlation coefficient, R^2, of about 0.995. Both the MP and HP porosities were found to increase with increasing sawdust content (that was used in fabricating the porous ceramic). No apparent trends were observed between the measured porosities and the average pore sizes (Table 4.2).

The firing of the CWFs is sometimes carried out under controlled conditions that result in carbon residues from the sawdust. However, the EDX analysis revealed no trace of carbon, meaning all of the sawdust was completely burnt off during the firing process (See supporting information Figure S4.1). Also, the EDX is a necessary prerequisite to X-ray diffraction. The X-ray diffraction analyses of the redart clay and the porous ceramics are presented in Figure 4.5. The results show that the redart clay and porous ceramic exhibit similar diffraction patterns. The redart clay structure consists predominantly of illite and kaolinite mineral. Above 500°C, the kaolinite mineral (which has a weight percent of about 10%) undergoes an endothermic dehydroxylation process. This transforms it into a disordered alumino-silicate, metakaolinite (Bellotto *et al.,* 1995; Kingery *et al.,* 1976). The kaolin clay, which was originally crystalline, is now transformed into metakaolin ,which is amorphous. This explains the shorter peaks in the porous ceramics, and why some of the peaks (that existed in the redart clay) are missing in the porous ceramics.

4.4.2 Modulus and Hardness

Elastic modulus and hardness are not strictly functions of porosity but also depend on pore morphology, pore size distribution (and arrangement) and microstructure (Deng *et al.,* 2001; Knudsen, 1959; Rice, 1996a,1996b). The unrelaxed moduli and hardnesses of the porous ceramics, indented using a spherical (conical) indenter, are plotted as a function of porosity and average pore size in Figures 4.6 (a) – 4.6(b). The results showed that the modulus and hardness do not have any clear relationship with porosity but increase as the average pore size is decreased.

4.4.3 Compressive and Flexural Strength

The compressive strengths decreased linearly ($R^2 = 0.9997$) with increasing porosity (Figure 4.7). A better fit can be obtained considering a wider range of porosities, the problem however is that making filters below porosity of ~35% significantly decreases the flow rate of CWFs and porosity above ~50% significantly reduces the strength of the filter and may drastically reduce its microbial efficacy. The flexural strength (MOR) of the porous ceramic is also seen to decrease with decreasing porosity (Figure 4.8). Similar trends have been observed by other researchers (Knudsen, 1959; Liu, 1997; Wagh *et al.*, 1991). It was also observed that the MORs of the "S-Type" specimen were somewhat greater than those of the "T-Type" specimens. This is because the flexural strength largely depends on surface condition and the "S-Type" surface is relatively denser compared to the "T-Type" due to nature of sintering. Both the compressive and flexural strengths are generally attributed to stress concentration phenomena (Boccaccini, 1998; Duran & Fernndez, 1993; Rice, 1993).

4.4.4 Fracture Toughness and Resistance-curve Behavior

The fracture toughness (of both specimen types) decreases with increasing porosity (Figure 4.9). Similar trends have been reported by other researchers (Rice, 1996b). The fracture toughness for the "T-Type" specimen fell sharply for porosities of ~36% and ~41%. This may be due to a reduction in crack deflection and the critical strain energy release rate. At $\Phi = 40.3\%$, the porous ceramic material becomes isotropic with respect to fracture toughness. The resistance-curve behavior of the ceramic obtained using the Krak gage is given in Figure 4.10. The result shows that the porous ceramic exhibited very limited crack growth resistance as is typical of brittle

materials. The limited crack growth resistance was attributed largely to crack bridging. Evidence of crack-tip shielding by crack bridging is presented in Figure 4.11.

4.4.5 Modeling of Filter Stress

4.4.5.1 Effects of supporting configurations

Table 4.4 shows the maximum principal stress at the lip edge and bottom edge for the filter under two extreme conditions: when dry and when filled with water. Also shown in the table is the variation of maximum principal stress with different support conditions. It is seen that the maximum principal stress at the bottom edge (for both the dry and filled filter) has a weak dependence on the support configuration. This may be because the bottom edge is far away from the filter lip which is being supported. For the dry filter, for any given support system the maximum principal stress at the lip edge was generally greater than the maximum principal stress at the bottom edge. The reverse is true for the filter when it is filled with water. This is because when the filter is dry, i.e. during storage and transportation, the lip undergoes greater stress than the bottom. Also, when water is added to the filter, it increases the bending moment on the bottom section, by a lot, and makes it much larger than that in the lip. This indicates that the filter is more likely to fail at the lip when it is dry. It is also more likely to fail at the bottom, when it is wet, i.e. during use.

Figure 4.12 shows the maximum principal stress as a function of hydrodynamic head of the water (measured from the base of the filter up). This mimics the change in maximum principal stress as the filter is drained. The graph also shows the variation of the maximum principal stress with support configuration. For any support configuration, the maximum principal stress at the

bottom edge is more or less the same as shown by the dash line in Figure 4.12. From both Figure 4.12 and Table 4.4, it is apparent that the closer the support is to the (side of the) filter, the lower the stress at its lip edge. This is because closer support gives a smaller bending moment to the lip. The worst scenario is when the support was at the "fourth quarter". Not only does it have the highest maximum principal stress at any given pressure head, it has the longest range of maximum principal stress per cycle. A cycle is defined as the time it takes a filter that is completely filled with water to empty out its content. Also, the best support configuration is the one that spans the entire lip of the filter. In this case the applied bending moment is minimized.

4.4.5.2 Effects of filter geometries

Figure 4.13 shows the maximum principal stress as a function of hydrodynamic head of the water. The modeling was carried out with support fully spanning the entire lip. For reasons mentioned in section 4.5.1, for any given filter model (and for the same pressure head) the maximum principal stress on the filter lip is generally greater than that at the bottom of the filter. Figure 4.13 also shows that the uniform frustum shaped model is better than the regular frustum shaped filter. This is because it has a higher second moment of area (due to higher thickness). In terms of stresses on the filter bottom edge, the general order (from best to worst) is as follows: ellipsoidal model > semi-spherical model > uniform thickness frustum shaped model > frustum shaped model > inverted frustum model > cylindrical model. Ellipsoidal and semi-spherical filters have lower stress concentration because of the roundness its bottom edge. Uniform thickness frustum filter has thicker wall than the frustum filter, and therefore have a greater stiffness. The cylindrical filter appears to be the worst because of effects of bending moments. In terms of stresses on the filter lip edge, the order (from best to worse) is as follows: frustum

shaped model > ellipsoidal model > uniform thickness frustum shaped model > cylindrical model > inverted frustum model. This is largely because of effect of bending moments due to a combination of filter self-weight and hydrostatic pressure. It is hard to rank the semi-spherical model. It appears to be better at handling stress at lower pressure head and worse at handling stress at higher pressure head.

4.4.6 Implications

The implications of the current work are quite significant. First, the result shows clearly that the mechanical properties of porous ceramics are not a simple function of its density but depends largely on porosity, except for modulus and hardness which were more or less a function of the average pore size. Other possible factors that affect the mechanical strength of porous ceramics include: surface and internal defects (such as cracks) during processing (thermal shock), transportation (mechanical vibration) and usage (hydrostatic force). One way of solving this problem is to fabricate CWFs from homogeneous mixtures of clay and sawdust.

Future work should include research on porous ceramic structures that can offer greater resistance to crack growth during transportation, usage and processing. One way of improving the mechanical properties of the filter is to optimize the porous structure of the filters (Deng *et al.*, 2001). Future ceramic water filters should also be made such that they have uniform thicknesses. Furthermore, if they are to be fabricated into "curvy" shapes, they have to be "as ellipsoidal as possible". Also, the receptacle has to span the entire lip of the filter and be as close to the side of the filter as possible. Future work is also needed to study the effects of doping and

the effects of hydration on the structure and mechanical properties of porous clay ceramics. These are clearly some challenges for future work.

4.5 Conclusions

The porosity of clay ceramics increases with increasing volume fraction of sawdust. The higher skeletal density of HP reveals that the porous material has pore sizes that are smaller than what MP is capable of detecting. The modulus and hardness are functions of the average pore size. The strengths (compressive and flexural) and fracture toughness decrease with increasing porosity. The porous clay ceramic materials exhibit resistance-curve behavior that is typical of brittle materials, with limited crack growth resistance attributed to shielding by crack bridging. The shielding due to crack bridging can be predicted using a combination of SSB and LSB models. The wider the support provided by the receptacle, and the closer it is to the side of the filter, the better. Also, the more uniformly thick a filter is the better. Finally, if a filter has to be fabricated to be “curvy”, the more ellipsoidal it is the better.

References

ASTME. (1990). ASTME 399-90: Standard Test Method for Plane Fracture Toughness of Metallic Materials. Philadelphia.

Baker, T. J., Zimba, J., Akpan, E. T., Bashir, I., Watola, C. T., & Soboyejo, W. O. (2006). Viscoelastic toughening of aluminosilicate refractory ceramics. Acta Materialia, 54(10), 2665-2675.

Bellotto, M., Gualtieri, A., Artioli, G., & Clark, S. M. (1995). Kinetic-Study of the Kaolinite-Mullite Reaction Sequence .1. Kaolinite Dehydroxylation. Physics and Chemistry of Minerals, 22(4), 207-214.

Boccaccini, A. R. (1998). Influence of stress concentrations on the mechanical property-porosity correlation in porous materials. Journal of Materials Science Letters, 17(15), 1273-1275.

Deng, Z. Y., Fukasawa, T., Ando, M., Zhang, G. J., & Ohji, T. (2001). Microstructure and mechanical properties of porous alumina ceramics fabricated by the decomposition of aluminum hydroxide. Journal of the American Ceramic Society, 84(11), 2638-2644.

Duran, P., & Fernndez, J. F. (Eds.). (1993). Third Euro-Ceramics, Engineering Ceramics (Vol. 3). Madrid: Faenza Editrice Iberica S.L.

Fett, T. (2008). Stress intensity factors, T-stresses, Weight functions. IKM 50,Universitätsverlag Karlsruhe, Karlsruhe

Fett, T., & Munz, D. (1997). Stress intensity factors and weight functions. Southampton, UK ; Boston, Mass. USA: Computational Mechanics Publications.

Kingery, W. D., Bowen, H. K., & Uhlmann, D. R. (1976). Introduction to ceramics (2d ed.). New York: Wiley.

Knudsen, F. P. (1959). Dependence of Mechanical Strength of Brittle Polycrystalline Specimens on Porosity and Grain Size. Journal of the American Ceramic Society, 42(8), 376-387.

Liu, D. M. (1997). Influence of porosity and pore size on the compressive strength of porous hydroxyapatite ceramic. Ceramics International, 23(2), 135-139.

Lou, J., Bhalerao, K., Soboyejo, A. B. O., & Soboyejo, W. O. (2003). An investigation of fracture initiation and resistance-curve behavior in concrete. Cement & Concrete Composites, 25(6), 599-605.

Rice, R. W. (1993). Comparison of stress concentration versus minimum solid area based mechanical property-porosity relations. Journal of Materials Science, 28(8), 2187-2190.

Rice, R. W. (1996a). Grain size and porosity dependence of ceramic fracture energy and toughness at 22 degrees C. Journal of Materials Science, 31(8), 1969-1983.

Rice, R. W. (1996b). Porosity dependence of physical properties of materials: A summary review. Porous Ceramic Materials, 115, 1-19.

Saadaoui, M., Orange, G., Olagnon, C., & Fantozzi, G. (1991). Crack Resistance Curves of Ceramics Determined on Notched and Precracked Bend Bars. Journal of Materials Science Letters, 10(18), 1090-1092.

Wagh, A. S., Poeppel, R. B., & Singh, J. P. (1991). Open Pore Description of Mechanical-Properties of Ceramics. Journal of Materials Science, 26(14), 3862-3868.

Component	*SiO_2*	*Al_2O_3*	*Fe_2O_3*	*TiO_2*	*MgO*	*CaO*	*Na_2O*	*K_2O*	*Other*	*LOI**
Fraction (wt. %)	64.2	16.4	7	1.1	1.6	0.2	0.4	4.1	0.1	4.9

*LOI = Loss on ignition

Table 4.1: Chemical composition of redart clay raw material

Porous Ceramic Type	***Volume Fraction of Sawdust (%)***	***Average Pore Diameter (µm)***	***Bulk Density (g/cm3)***	***Skeletal Density (g/cm3)***		***Porosity (%)***	
				MP	***HP***	***MP***	***HP***
75:25	25	0.61	1.50	2.36	2.72	36.38	44.85
65:35	35	0.55	1.42	2.41	2.73	40.89	47.85
50:50	50	1.07	1.29	2.42	2.74	46.96	53.10

Table 4.2: Physical properties of porous ceramic. MP is Mercury Porosimeter and HP is Helium Pyncnometer

Porous Ceramic Type	*Volume Fraction of Sawdust (%)*	*Porosity (%)*	*Average Pore Diameter (μm)*	*Compressive Strength (MPa)*	*Young's Modulus (GPa)*	*Hardness (MPa)*	*Specimen Type*	*MOR (MPa)*	*Fracture Toughness, KIc (MPa)*
75:25	25	36.38	0.61	9.11 ± 0.47	1.66 ± 0.44	22.93 ± 9.66	T	5.39 ± 1.72	0.61 ± 0.03
							S	7.16 ± 2.26	0.47 ± 0.09
65:35	35	40.89	0.55	7.41 ± 0.84	3.06 ± 0.73	39.15 ± 12.72	T	4.22 ± 0.12	0.40 ± 0.05
							S	4.64 ± 1.16	0.43 ± 0.03
50:50	50	46.96	1.07	5.25 ± 0.19	1.36 ± 0.20	20.36 ± 8.94	T	3.89± 0.09	0.35 ± 0.02
							S	4.29 ± 0.53	0.37 ± 0.02

Table 4.3: Summary of mechanical properties of the porous ceramics

Support Condition	Dry		Filled to the brim with Water	
	Lip Edge	Bottom Edge	Lip Edge	Bottom Edge
	22.18	14.83	92.68	162.22
	25.38	14.83	101.17	162.22
	32.82	14.83	129.04	162.23
	44.71	14.83	175.44	162.24
	22.18	14.83	92.68	162.22
	18.55	14.83	71.23	162.21
	16.58	14.83	61.14	162.21
	15.71	14.83	56.98	162.21

Table 4.4: The maximum principal stress (in kPa) in the "lip edge" and "bottom edge" of the frustum-shaped filter under different support condition

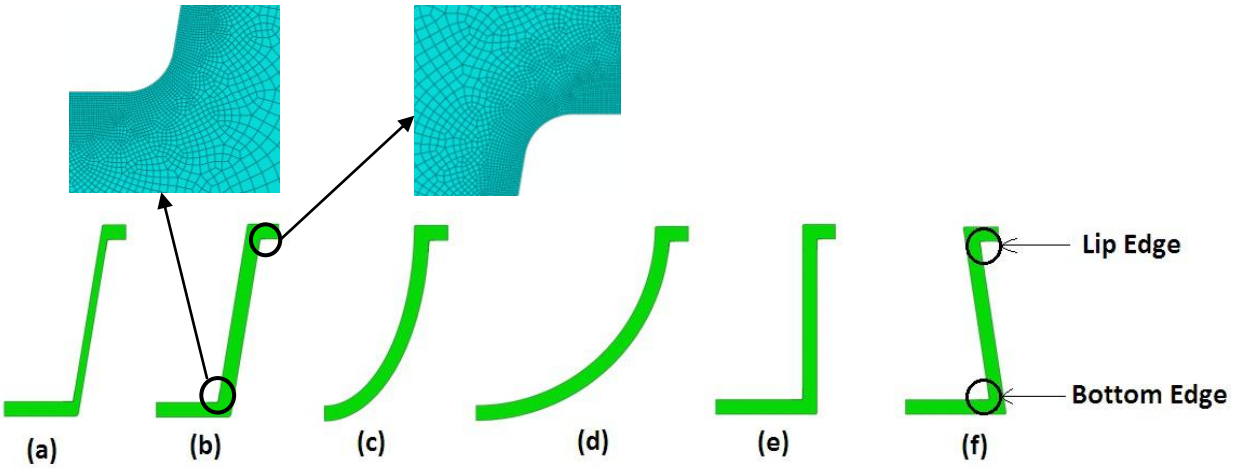

Figure 4.1: Finite element models of the filters for (a) frustum filter model, (b) uniform thickness frustum filter model, (c) ellipsoid filter model, (d) semi-spherical filter model, (e) cylindrical filter model, and (f) inverted frustum filter model

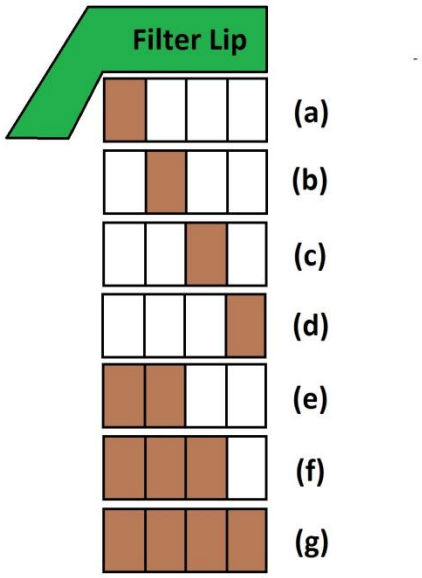

Figure 4.2: Different support configurations modeled. Figure shows support spanning (a) first quarter of lip, (b) second quarter of lip, (c) third quarter of lip, (d) fourth quarter of lip, (e) half of lip, (f) three-quarter of lip and (g) the entire lip

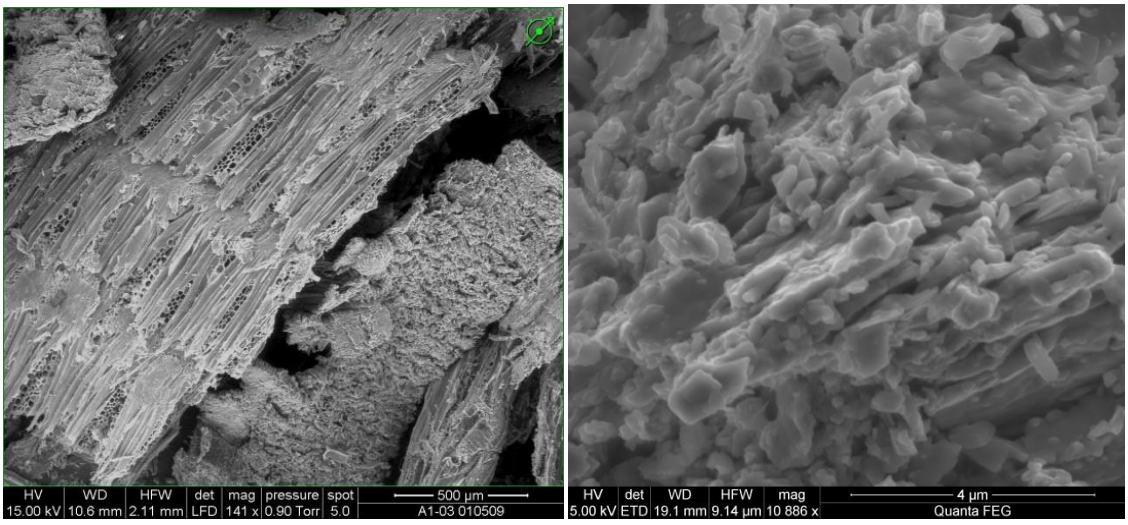

(a) (b)

Figure 4.3: Environmental scanning electron microscopy micrographs of (a) the woodchips (sawdust) used and (b) a typical pore structure of the porous ceramics

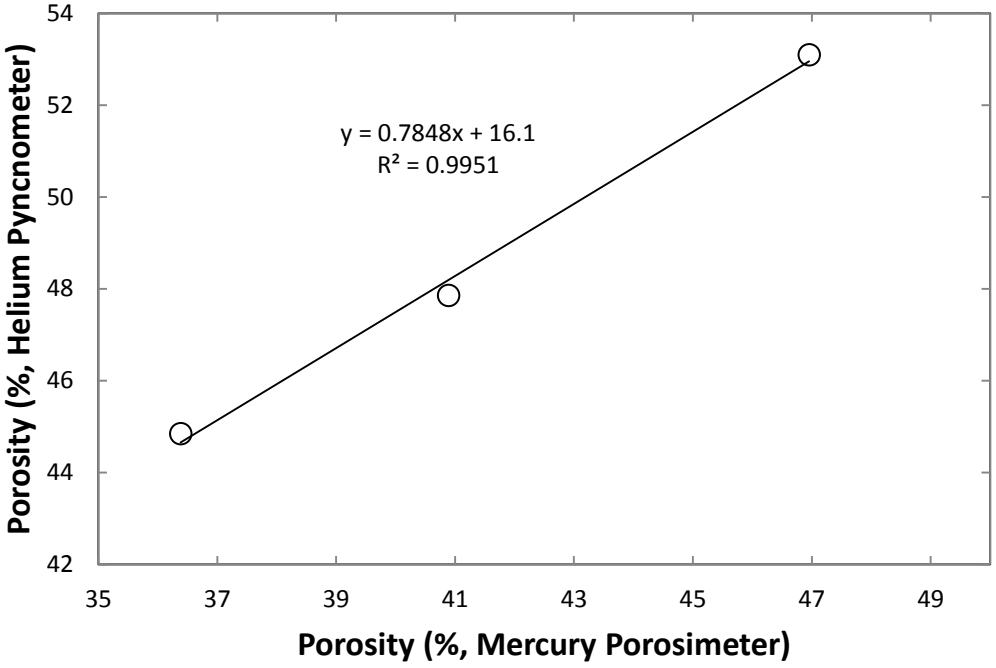

Figure 4.4: Linear relationship between porosity measured using helium pycnometer and mercury porosimeter

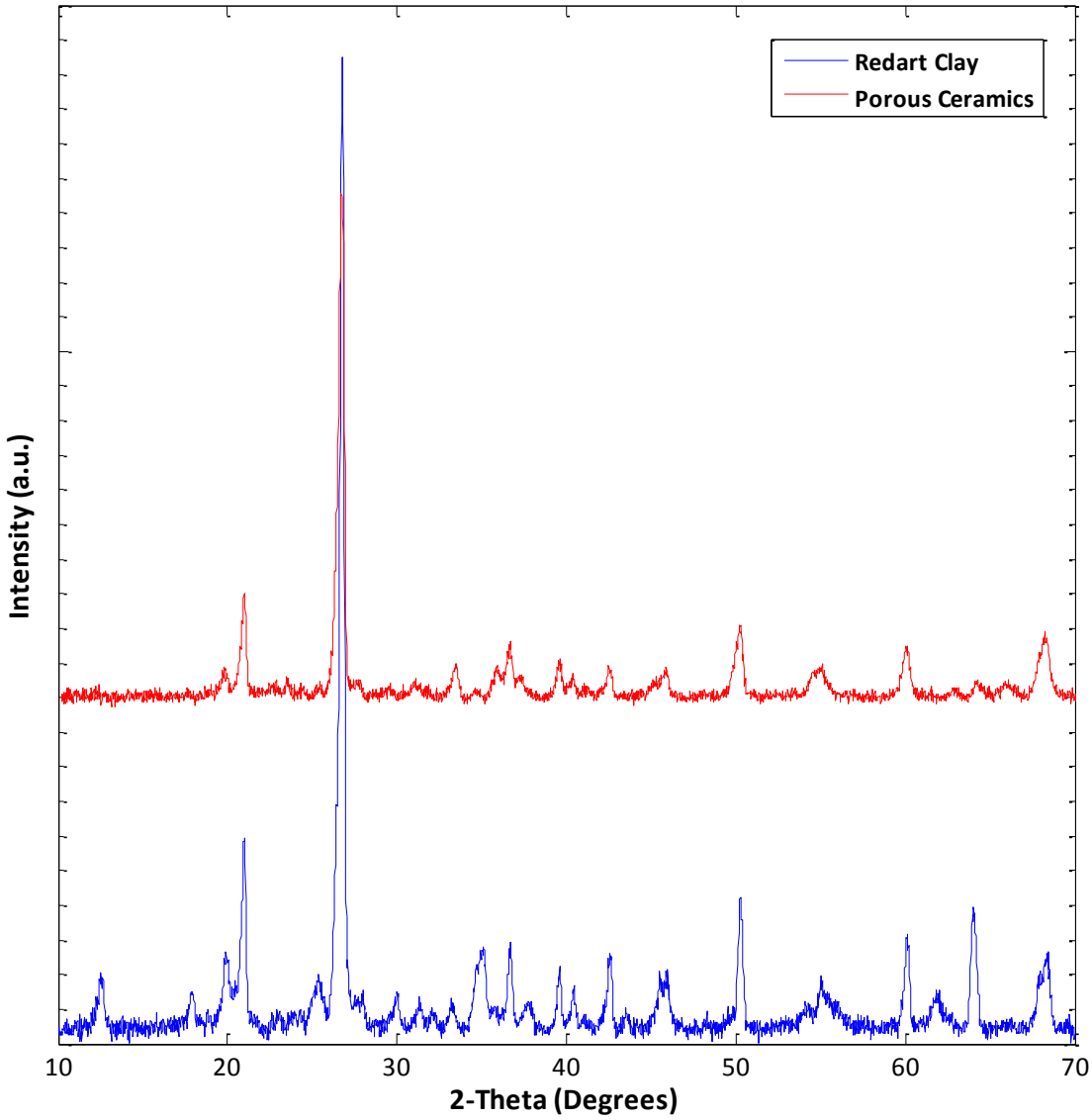

Figure 4.5: XRD pattern of Redart clay (bottom/blue) and the porous ceramic (top/red)

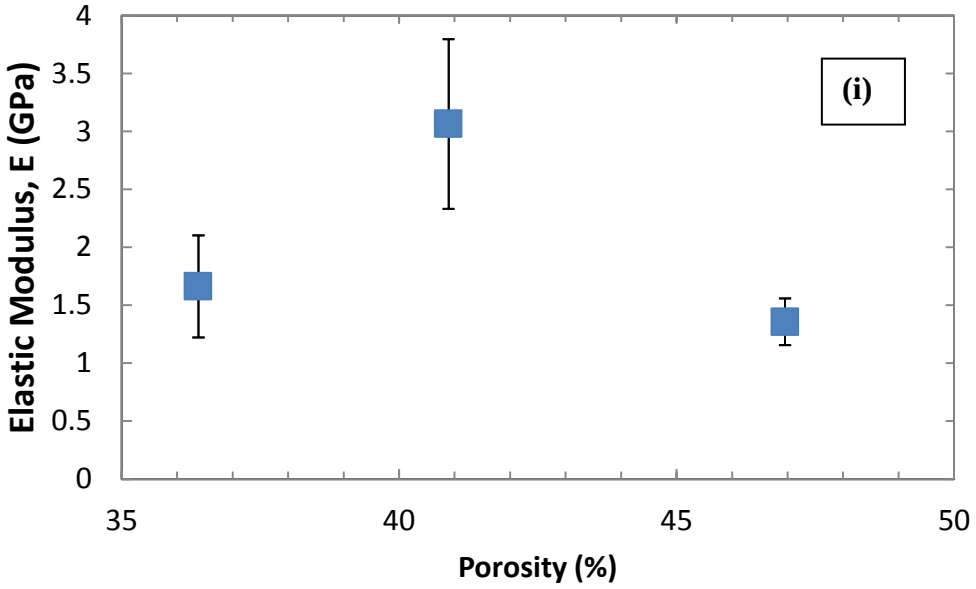

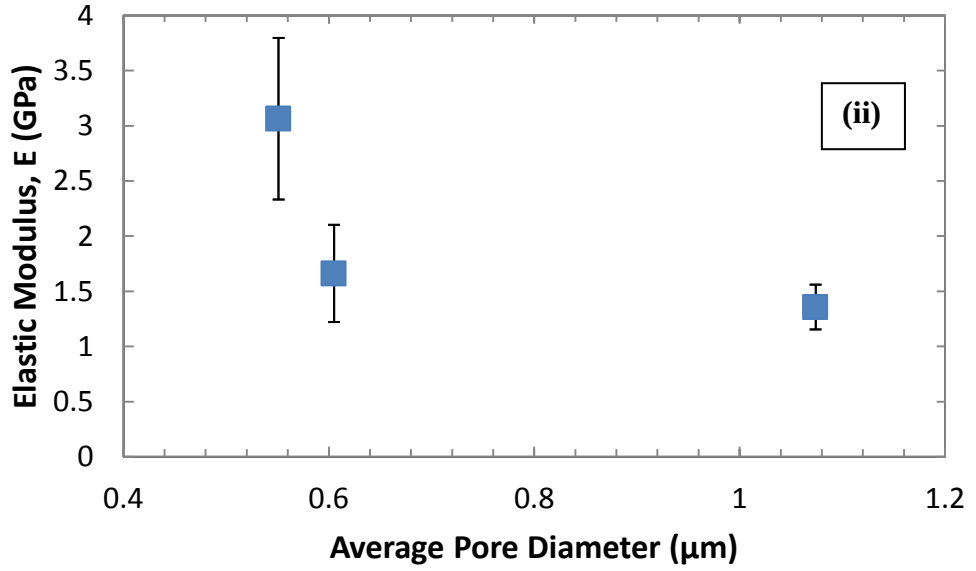

Figure 4.6 (a): Variation of elastic modulus with (i) porosity and (ii) average pore diameter

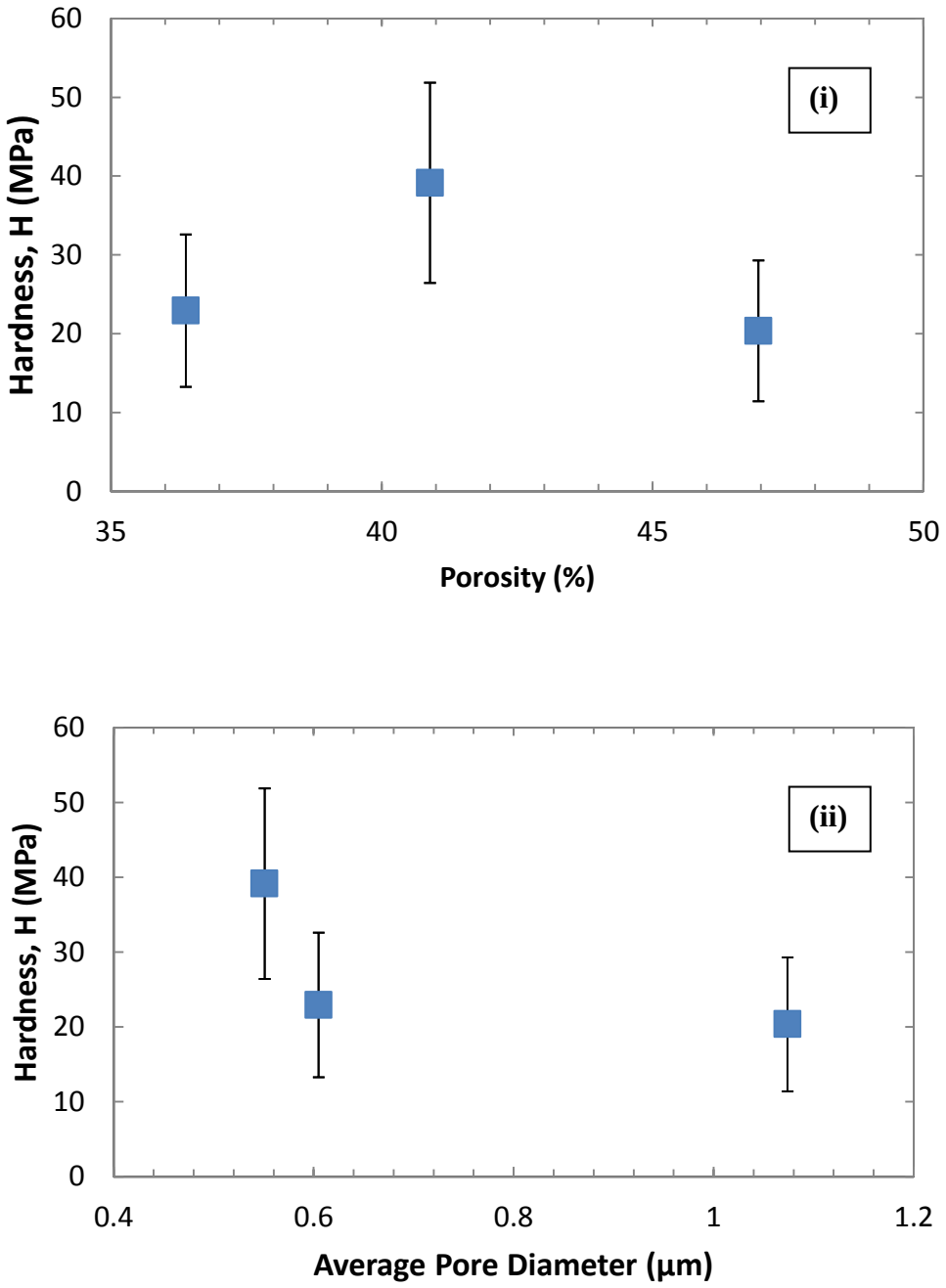

Figure 4.6 (b): Variation of hardness with (i) porosity, (ii) average pore diameter

Figure 4.6: Variation of elastic modulus and hardness with porosity and average pore diameter

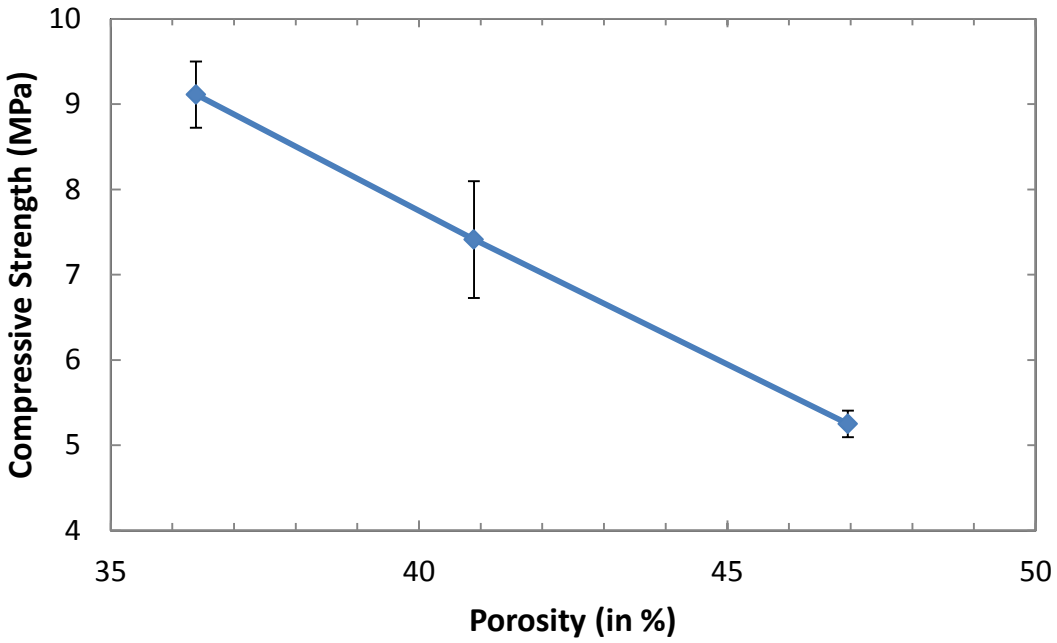

Figure 4.7: Dependence of compressive strength on porosity of the porous ceramics

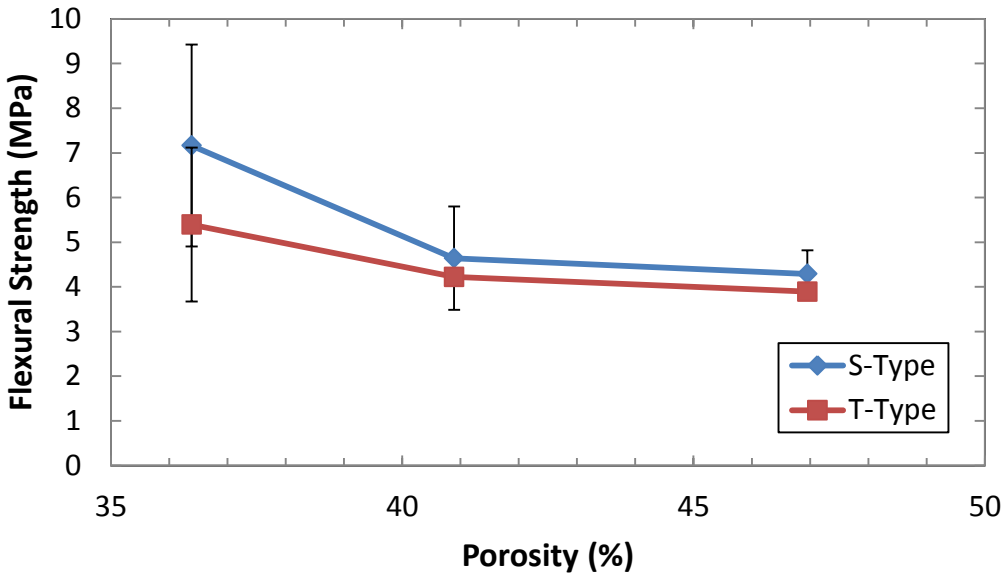

Figure 4.8: Dependence of flexural strength on porosity of the porous ceramics

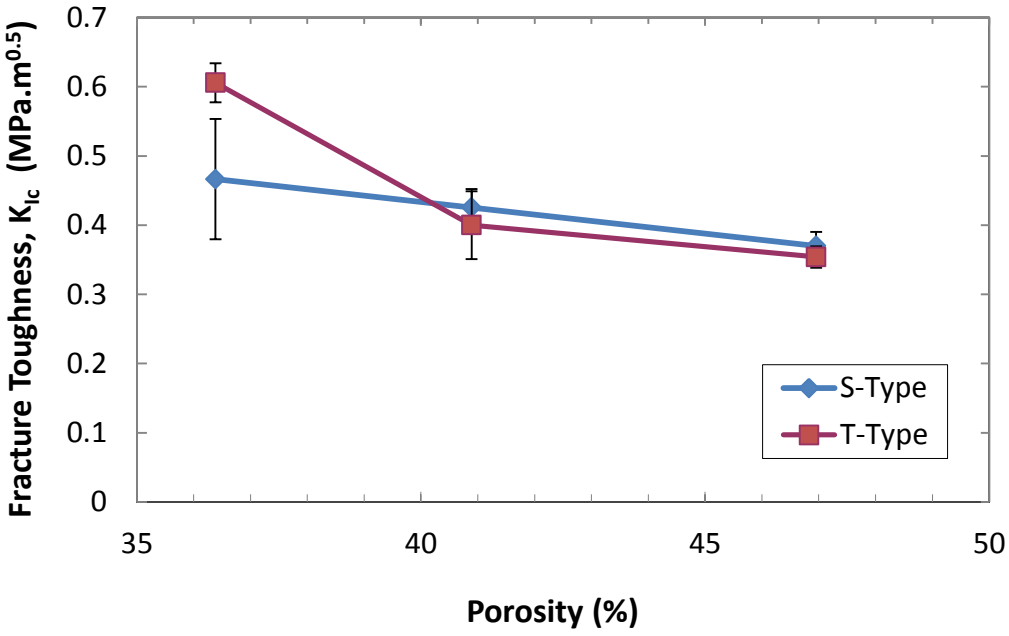

Figure 4.9: Dependence of fracture toughness on porosity of the porous ceramic

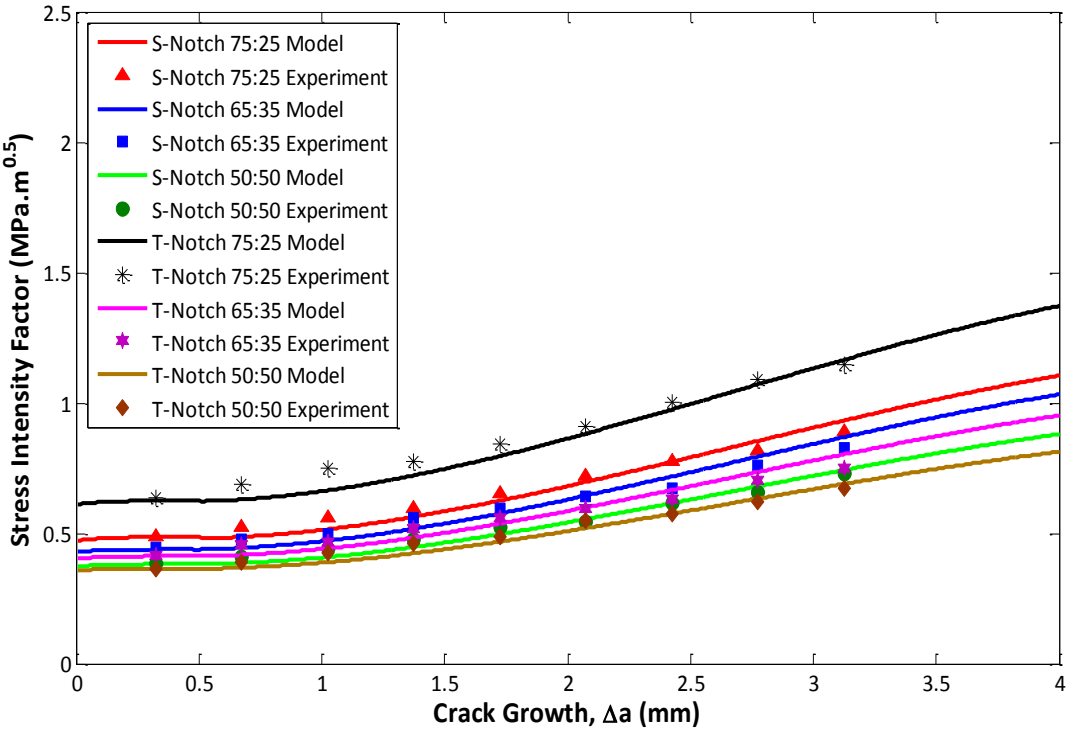

Figure 4.10: Resistance curve behavior of the porous ceramic

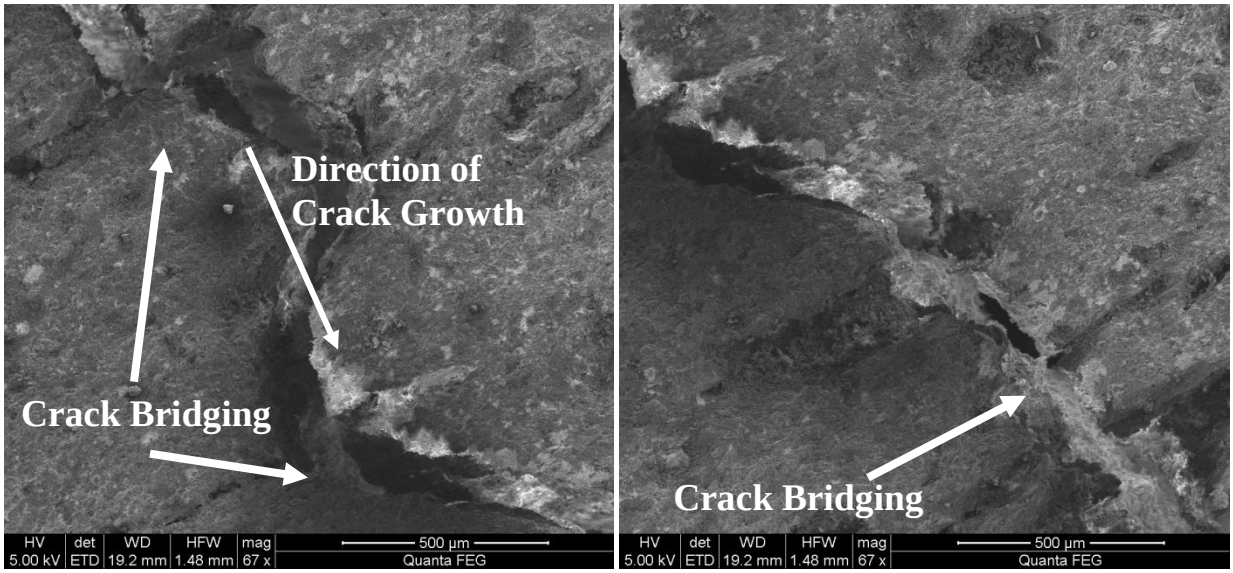

Figure 4.11: ESEM image of a porous ceramic showing evidence of crack bridging

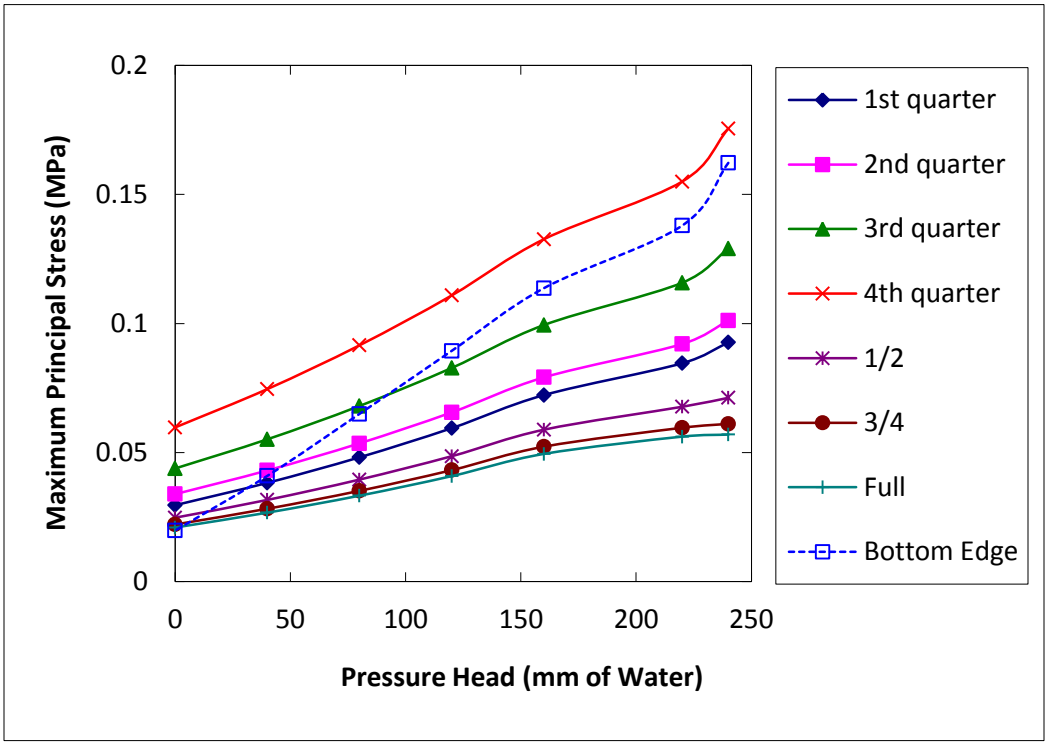

Figure 4.12: Variation of the maximum principal stress on the "lip edge" and the "bottom edge" of the frustum-shaped filter as the pressure head of water changes

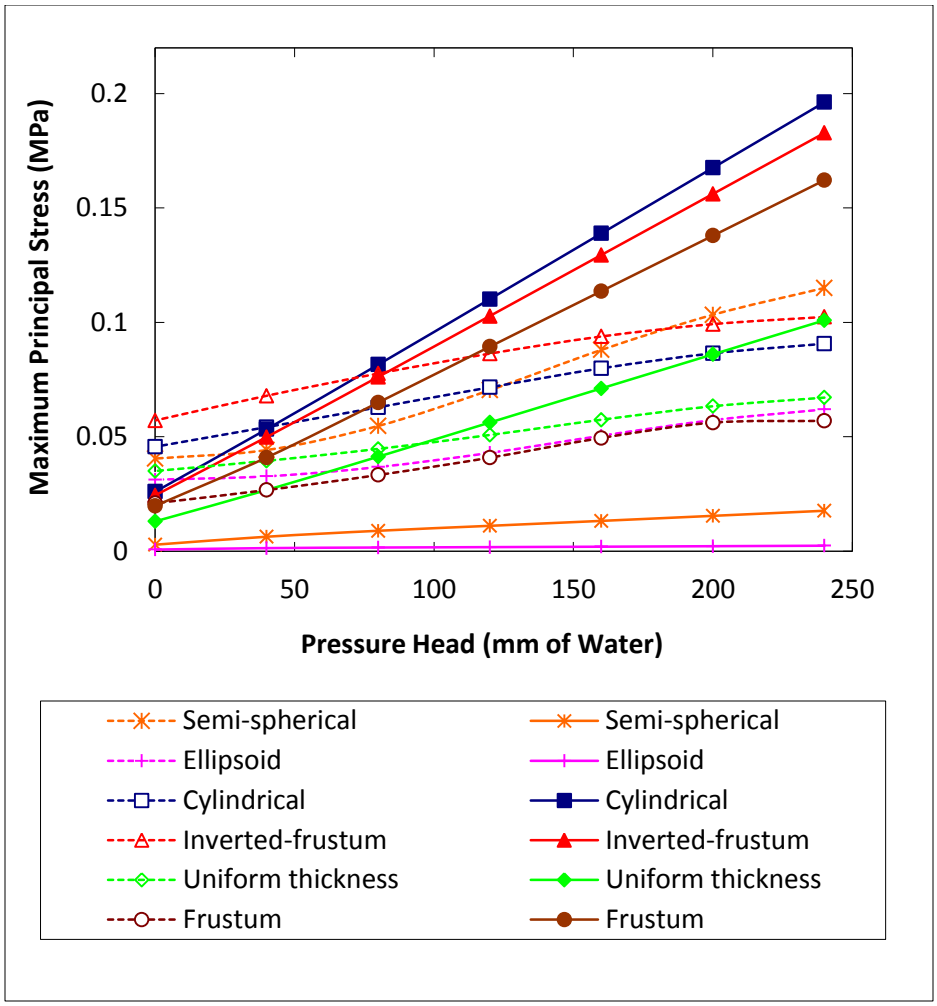

Figure 4.13: Variation of the maximum principal stress on the "lip edge" (dash lines) and "bottom edge" (solid lines) of the filter models as the pressure head of water changes

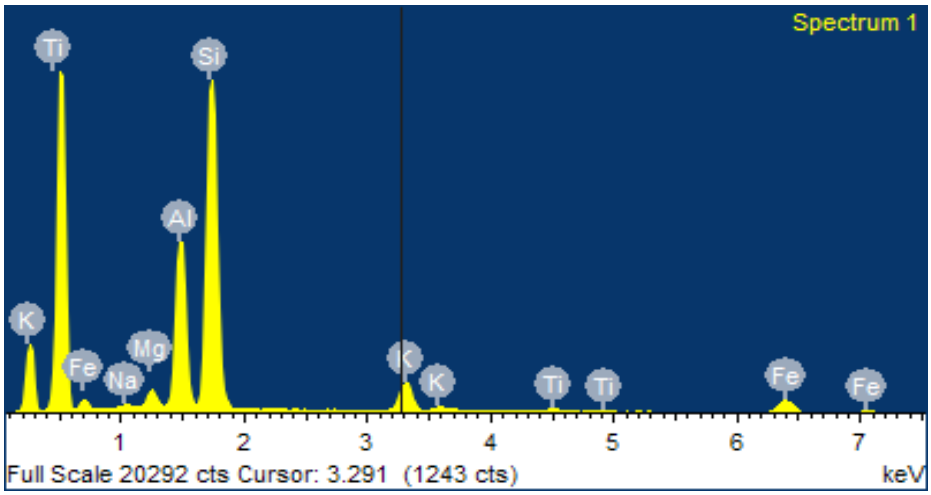

(a)

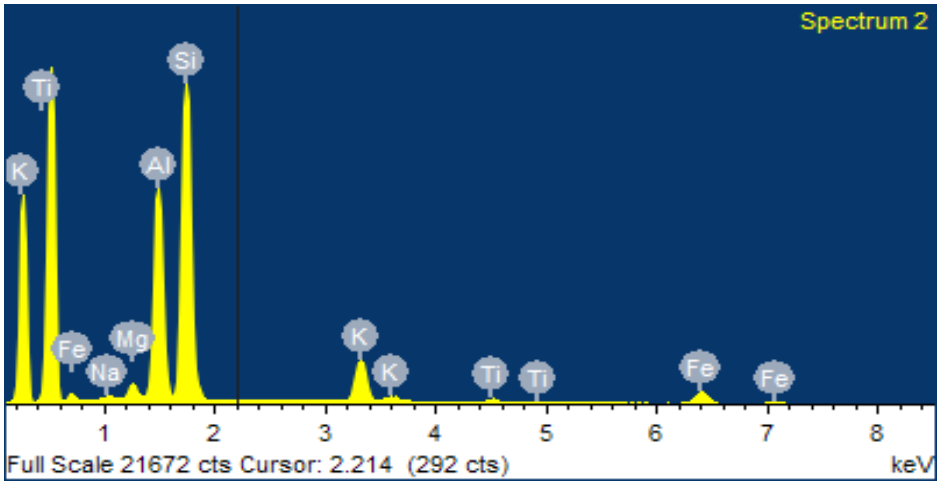

(b)

Supporting Information - Figure S4.1: EDX analysis of (a) redart clay and (b) porous ceramic

Chapter 5

Adhesion of *E.coli* Bacteria to Silver - or Copper - Coated Porous Ceramic Surfaces

5.1 Introduction

About 884 million people worldwide lack access to improved water supplies and over 3 million people, mostly children, die every year from water related diseases (UNICEF, 2008; WHO/UNICEF, 2010). The ceramic water filter (CWFs) is one of the few types of point-of-use (POU) water purification systems that is currently been used to tackle this scourge. CWFs are fabricated by mixing clay with a combustible or pore forming material (usually sawdust, flour and rice husk) with a binder (water). The filter is normally coated with colloidal silver (either by dip coating or by painting with a brush). This is done in order to prevent the growth of microbes that are trapped in the micro- and nano-scale pores of the clay based CWFs.

However, other metals such as silver, copper and zinc, have been shown to exhibit anti-microbial activity (Kim *et al.*, 1998; Lansdown, 2002; Ruparelia *et al.*, 2008; Top & Ulku, 2004; Yoon *et al.*, 2007). Silver nanoparticles have also been used to coat hydroxyapaptite (Yang *et al.*, 2007) and polyurethane water filters (Jain & Pradeep, 2005). Also, copper nanoparticles embedded in sepiolite have been shown to reduce *E.coli* concentration by 99.9% (Esteban-Cubillo *et al.*, 2006). Furthermore, it has been reported that the bactericidal effect of nanoparticles is dependent on their shapes, sizes (Pal *et al.*, 2007; Panacek *et al.*, 2006), and also on the type or strain of microorganism (Morones *et al.*, 2005).

While the specific nanoparticle disinfection pathways are still a subject of debate, it has been shown that the high surface areas and small sizes allows the nanoparticles to interact with the cell membranes. This interaction has been shown to disrupt membrane function, leading ultimately to rupture and cell death (Cho *et al.*, 2005; Morones *et al.*, 2005; Sondi & Salopek-Sondi, 2004). There has also been evidence of nanoparticle endocytosis. Such nanoparticle entry into cells has been shown to kill the cells via interactions with sulfur- and phosphorus-containing compounds, such as DNA (Alcamo, 1997; Feng *et al.*, 2000; Morones *et al.*, 2005; Sondi & Salopek-Sondi, 2004).

However, the role of colloidal silver in the filtration of pathogenic bacteria using CWFs is still not well understood. It is uncertain if the bacterial removal is caused by filtration/sorption, deactivation by colloidal silver, or some combination of these processes (Oyanedel-Craver & Smith, 2008). Furthermore, the author of this dissertation is unaware of prior work to assess the relative adsorption strengths between the antimicrobial agents, the *E.coli* bacteria and the porous ceramic surface.

Although AFM was originally designed as a high resolution scanning machine (Magonov & Whangbo, 1996; Wiesendanger, 1994), it is also a powerful tool for the measurement of the adhesion force between AFM tips and substrates (Prater *et al.*, Bruker). When the surfaces of the AFM tips and substrates are coated with similar or different materials, AFM can be used for force spectroscopy at the nanoscale (Butt *et al.*, 2005; Hartley *et al.*, 1999). This has been applied to the nanoscale mapping of biological interaction forces (Dupres *et al.*, 2005; Hinterdorfer *et al.*, 2001), measurement of the adhesion between biological cells and specific peptides or antibodies (Dupres *et al.*, 2005; Li *et al.*, 2003; Meng *et al.*, 2010; Wojcikiewicz *et al.*, 2004) and have been used to measure the adhesion interaction between *E.coli* bacteria and different surfaces (Cao *et al.*, 2006; Li & Logan, 2004; Lower *et al.*, 2000; Ong *et al.*, 1999; Razatos *et al.*, 1998). AFM can be used to measure the adhesion force between AFM tips and various substrates; adhesion forces down to about 10 pN can be measured using the AFM technique (Kobayashi *et al.*, 2010; Viani *et al.*, 1999).

This chapter presents the results of an experimental study of adhesion forces that are relevant to point-of-use ceramic water filters. They include: (a) Colloidal silver, metallic silver, copper and porous ceramic interactions with *E.coli* bacteria and (b) Colloidal silver, metallic silver, copper and *E.coli* bacteria interactions with porous ceramic surfaces. Since AFM measurements are highly sensitive to roughness and surface asperities, the AFM tip radii, as well as the substrate roughnesses, were measured and incorporated into models that were used to obtain the interaction energies for the bi-material pairs that were examined.

5.2 Theory

5.2.1 Adhesion Force Measurement

The adhesion interactions between bi-material pairs (or surfaces) can be found using contact mode atomic force microscopy. The various stages involved in the measurement of adhesion force are shown schematically in Figure 5.1 (Shahin *et al.*, 2005). The AFM tip is lowered closer to the sample surface at a constant speed (A). Various short-and long-range attractive forces act on the tip and it jumps into contact (B) as soon as the total force gradient exceeds the stiffness of the cantilever. As the scanner head is lowered further, the cantilever deforms elastically (C). The retraction/withdrawal process is not exactly opposite to the approach/extension process. At some distance along curve (C) the AFM tip forms a bond with the sample surface, this causes the scanner head to move some distance further than the initial contact point (B) during the retraction process. As the scanner head continues to move away from the sample (D), the adhesive interactions between the tip and the sample surface are overcome at point (E) as the tip returns to its original position. The adhesion force between the tip and the sample surface can be obtained from Hooke's law. This gives:

$$F_{adh} = k_c \delta \tag{1}$$

where F_{adh} is the adhesion (or pull-off) force, k_c is the spring constant of the AFM tip cantilever and δ is the cantilever deflection during pull-off.

The accuracy of the adhesion force depends largely on the spring constant of the AFM tip. While the manufacturer provides spring constants for AFM tip cantilevers the actual values usually differ from manufacturer's batch measurement. Furthermore, the coating or functionalization of the AFM tip can significantly alter its spring constant. It is, therefore, important to determine

the spring constant of AFM tips prior to adhesion measurement. This was done using the thermal tune method. This technique involves the thermal agitation of the tip (usually in air) prior to fitting a Lorentzian line to the resulting frequency spectrum of harmonic oscillations. This was used to obtain an accurate estimate of the spring constant (Serry, 2005).

5.2.2 Adhesion Energy

The energy required to separate two surfaces in contact may be found from their adhesion force. From fracture mechanics, for two dissimilar surfaces *i* and *j*, with respective surface energy $\gamma_{surface\,i}$ and $\gamma_{surface\,j}$, the adhesion energy (or work of adhesion) is given by (Tong *et al.*, 2009):

$$G_{adh} \cong G_{elastic} = \gamma_{surface\,i} + \gamma_{surface\,j} - \gamma_{surface\,ij} \quad (2)$$

In this study, interfacial fracture mechanics concepts were combined with the adhesion theories of Derjaguin, Muller and Toporov (DMT) and Johnson, Kendall and Roberts (JKR) (Leite & Herrmann, 2005). For small particles or spheres, with high elastic moduli or hard surface with low surface energies and weak adhesive interactions, the DMT model gives the adhesion energy as (Derjaguin *et al.*, 1994):

$$\gamma_{DMT} = \frac{F_{adh}}{2\pi R_{eff}} \quad (3)$$

where, F_{adh} is the adhesion force and the effective radius, R_{eff}, is given by:

$$R_{eff} = \left(\frac{1}{R_t} + \frac{1}{R_{rms}}\right)^{-1} \quad (4)$$

Where, R_t is the AFM cantilever tip radius and R_{rms} is the root mean square (rms) roughness of sample surface.

In the case of large spheres or particles, with low elastic moduli or soft materials, materials and strong adhesive interactions the JKR model gives the adhesion energy as (Johnson *et al.*, 1971):

$$\gamma_{JKR} = \frac{F_{adh}}{1.5\pi R_{eff}} \tag{5}$$

Following the suggestion of Tabor (Tabor, 1977), a parameter, μ, was used to decide on which models were applicable. This is given by:

$$\mu = 2.92 \left(\frac{G_{adh}^2 R_{eff}}{z_o^3 K^2}\right)^{1/3} \tag{6}$$

where z_o is the equilibrium separation between the atoms of contacting surfaces and K is the reduced Young's modulus given by:

$$K = \left[\frac{(1-v_1^2)}{E_1} + \frac{(1-v_2^2)}{E_2}\right]^{-1} \tag{7}$$

Values of $\mu \ll 1$ corresponds to the DMT theory while $\mu \gg 1$ corresponds to JKR theory. The Maugis-Dugdale (MD) model is used for scenarios that lie between the two limiting cases (i.e. when $\mu \approx 1$). The MD model expressed as (Johnson, 1998):

$$\lambda = \sigma_o \left(\frac{9R_{eff}}{2\pi G_{adh} K^2}\right)^{1/3} = 1.16\mu \quad (8)$$

or equivalently by:

$$\lambda = \frac{2.06}{z_o}\left(\frac{R_{eff} G_{adh}^2}{\pi K^2}\right)^{1/3} \quad (9)$$

The adhesion energy is given by the MD model to be:

$$\gamma_{MD} = \frac{F_{adh}}{\pi R_{eff} \bar{F}_{adh}} \quad (10)$$

where, λ is the elasticity parameter, σ_o is the so-called Dugale stress and $\bar{F}_{adh}$ is a non-dimensional parameter known as the reduced load or the net compressive load on the contact, which Carpick *et al.* (Carpick *et al.*, 1999) found empirically to be given by:

$$\bar{F}_{adh} = \frac{1}{4}\left(\frac{4.04\lambda^{1.4} - 1}{4.04\lambda^{1.4} + 1}\right) - \frac{7}{4} \quad (11)$$

The empirical value of the adhesion energy can be obtained by substituting equation (11) in equation (10). However, when plastic deformation occurs, equations (3), (5) and (10) do not hold. In such cases when full plasticity occurs, the Maugis-Pollock (MP) model (Maugis & Pollock, 1984) may be used to find the adhesion energy. This gives:

$$\gamma_{MP} = \frac{F_{adh}}{1.5K} H^{1.5} \sqrt{\frac{\pi}{P}} \quad (12)$$

where, *H* is the hardness of the material and *P* is the applied load.

The above expressions were used to obtain estimates of the adhesion energies that are presented in this study.

5.3 Experimental Procedures

5.3.1 Materials

Two types of uncoated antimony (n) doped silicon AFM tips, MPP-11100-10 and MPP-31100-10, were purchased from Bruker Probes (Camarillo, CA). The MPP-11100-10 tips were used for tapping mode AFM, while the MPP-31100-10 tips were used for contact mode AFM. The colloidal silver was purchased from Argenol Laboratories (French IX Edition, Zaragoza, Spain), since they generally supply colloidal silver to most of the CWF factories in the developing world. Silver (0.5mm thick, CAS: 7440-22-4, Ward Hill, MA) and copper foils (0.5mm thick, CAS: 7440-50-8, Ward Hill, MA) were procured from Alfa Aesar (Ward Hill, MA), while glass slides were procured from Fisher Scientific (12-549-3, Pittsburg, PA). The porous ceramic that was used in this study was cut from the base of a regular frustum-shaped ceramic water filter that was produced by the sintering of clay and sawdust. A full description of the manufacturing process is given elsewhere in chapter 3. Luria-Broth (LB) was purchased from Sigma-Aldrich (L3522-1KG, Saint Louis, MO), while the non-pathogenic K-12 strain of W3110 *E.coli* bacteria was obtained from N. Ruiz (The Ohio State University).

5.3.2 Sample Preparation

The MPP31100-10 AFM tips were coated with: colloidal silver; silver; copper and clay. The colloidal silver coated AFM tips and clay coated AFM tips were prepared by dip-coating method

(Meng *et al.*, 2010; Tong *et al.*, 2009; Wolf *et al.*, 2008). The silver and the copper coated AFM tips were prepared by sputter coating.

To coat the AFM tips with colloidal silver, 2 grams of colloidal silver were dissolved in deionized water from a Barnstead water purification system (Model D8611, Barnstead/Thermolyne, Hampton, NH). This was used to dissolve a concentration of about 1g/mL of colloidal silver in water. Deionized water was used to avoid the introduction of contaminants into the solution. The AFM tips were then immersed in the solution for about 2 hours to maximize the AFM tip surface contact with solution and to promote the self-assembly of the colloidal silver particles onto the tip.

To coat the tips with clay, material cut from a regular CWF was first crushed into fine powder using a mortar and a pestle. Deionzed water was then added to the pulverized clay until the mixture just became plastic. Too much water usually resulted in difficulty in coating the AFM tip, due to the surface tension of water. A water-to-clay ratio of about 1 gram to 1.4 mL was found to be sufficient.

Bare AFM tips were coated with silver and copper by sputter coating silver and copper foil, respectively, from an ion beam sputterer (VCR Group Incorporated, IBS/TM 200S, San Francisco, CA). The tips were coated with ~100 Å of material. During the coating process, the AFM cantilever was protected from contact with the coating material. This was done to avoid changes in the laser/AFM tip interactions. In all cases, clay substrates with length, *L*, of 35 mm, width, *W*, of 12.63 mm, and breadth, *B*, of 12.63 mm were used.

A simple fixation process was used to prepare the E.coli bacteria for the AFM experiments. The *E.coli*, K-12 strain W3110 (Bachmann, 1972), were grown in Miller's LB Broth (Miller, 1972) at

37°C for 18-24 hours. The growth was done under vigorous aeration by stirring with a VWR digital stirrer/hotplate (Model 735-HPS, VWR, West Chester, PA). About 1,000 µL of this stationary phase culture was pipetted on to a microscope glass slide. This was then incubated at 37°C at normal atmospheric conditions for about 12 hours, after which it was kept in the refrigerator at -4°C prior to use in the adhesion experiments.

5.3.3 Materials Characterization

After the coating process, the AFM tips were kept in a vacuum chamber to minimize the possible extent of oxidation prior to testing. An Environmental SEM (Quanta 200 FE-ESEM, FEI, Hillboro, OR) equipped with Oxford EDX detector (Oxford Instruments, Oxfordshire, UK) was used to characterized the AFM tips. Since the AFM measurements were highly sensitive to surface roughness, the ESEM was used to measure the AFM tip radii before and after the AFM adhesion force experiments to take into account the potential tip deformation during the course of the tests. The substrate root mean squared (rms) surface roughness values of the substrate materials were also measured using a Digital Instruments Dimension 3000 atomic force microscope (Bruker, Camarillo, CA) that was operated under the tapping mode. Three substrates or surfaces were studied i.e. porous clay, *E.coli* and glass (a control). At least 15 height images were used to determine the surface roughness values.

The Oxford energy dispersive X-ray spectroscopy (EDX) detector was used to confirm whether the AFM tip was successfully coated. Since poor adhesion between the AFM tips and the coatings may result in the detachment of the coatings from the AFM tips (during handling or pull-off testing), EDX analysis was also carried out on the AFM tips after force measurement

experiments. This was used to ensure that the coatings were still attached to the AFM tips after the adhesion force measurements.

The spring constants of the AFM tips cantilever (coated and uncoated) were measured experimentally using the thermal tune method. This was carried out using a Digital Instruments Nanoscope IIIa AFM (Bruker, Camarillo, CA). This was done to quantify the actual spring constants that were used in the calculation of the pull-off forces. Such measurements are also needed to account for the effects of coating on the cantilever stiffness and also the batch-to-batch variations in the spring constants (Wolf *et al.*, 2008).

5.3.4 AFM Measurements

AFM contact mode experiments were carried out using the Dimension 3000 atomic force microscope. The entire operation was performed in air under ambient conditions (room temperature range of 23 - 27 ^{o}C and a relative humidity range of 48 - 55%). Prior to the adhesion force measurements, the photodetector sensitivity of the atomic force microscope was calibrated on a stiff quartz surface (Bhushan, 1995). The adhesive interactions were measured for the following four configurations:

(a) The interactions between (colloidal silver or silver or copper or clay ceramic) - coated AFM tips and *E.coli* substrates;
(b) The interactions between (colloidal silver or silver or copper) - coated AFM tips and clay ceramic substrates;
(c) The interactions between (colloidal silver or silver or copper or clay ceramic) - coated AFM tips and bare silica glass and

(d) The interactions between uncoated (or bare) AFM tips and *E.coli* or clay ceramic substrates.

The third and fourth configurations were tested as the controls. At least twenty five adhesion force curves were obtained for each pair of interactions. These were obtained from at least three tips, with each tip being tested at several different locations on the substrates. Figure 5.2 is a schematic showing the different adhesive interactions.

5.4 Results and Discussions

5.4.1 Characterization of AFM tip and substrate

ESEM images and the corresponding EDX spectra obtained for bare and coated AFM tips are presented in Figure 5.3(a) – 5.3(e). The images reveal that the bare tip (Figure 5.3(a)) is smooth and that the sputter coated AFM tips (Figure 5.3(b) and 5.3(c)) are evenly coated. The dip coated AFM tips (Figure 5.3(d) and 5.3(e)) were also shown by ESEM/EDX to contain coatings. The oxygen detected by the EDX technique is attributed to the tenacious formation of a surface oxide on silicon surfaces.

It is important to note here that the interaction volume of the beam of electron (from the electron gun) meant that materials beneath the coating could be detected. This is why silicon, carbon and oxygen from the original (bare) tip were still detected, even after the tip was coated (Figure 5.3(b) – 5.3(e)). However, the colloidal silver was found to contain more than just the silver element for the following reasons. Colloidal silver, collargol, is usually produced from aqueous phase reduction of silver nitrate by ascorbic acid (Oyanedel-Craver & Smith, 2008; Sondi *et al.*,

2003). However, the acidity of the mixture is increased due to the release of protons. Also, in the case of other reducing agents, which are only effective in basic or neutral solutions (such as hydrazine, N_2H_4), a base will be used to control the acidity. Hence, 0.1 normal of sodium hydroxide (0.1N of NaOH) was used by Argenol laboratory in their production of colloidal silver (Argenol-Laboratories, 2011). Therefore, the sodium and nitrogen observed in the EDX spectra obtained for the colloidal silver coated tips are believed to be due to the reducing agent, and the stabilizing agent. Note that the hydrogen in NaOH and N_2H_4 was not detected by the EDX detector because of the small diameter of the hydrogen orbital. Furthermore, the EDX analyses of the tips before and after the adhesion measurements did not reveal any evidence of coating delamination from the AFM tips. This confirms that the tip pull-off force measurements were due to the detachment of the coated AFM tips from the substrates.

An ESEM micrograph of a typical AFM tip that was used for the measurement of tip radii is presented in Figure 5.4. The tip radius of the metallic silver coated tip shown was found to be ~ 87 nm. The roughness value of the substrate was determined with the atomic force microscope operating in tapping mode. A typical 3D morphology of the substrates is presented in Figure 5.5 and the roughness values are presented in Table 5.1. The porous ceramic is the most rough (179.71 ± 88.16 nm), followed by *E.coli* coated glass slide (87.69 ± 68.82 nm) and plain glass slide (3.77 ± 0.54 nm).The tip radii and substrate rms surface roughness were used in finding the adhesion energies.

5.4.2 Adhesion Forces

The spring constant of the bare tip and uncoated tip was found using the thermal tune method. The results are presented in Table 5.2. The values of the spring constant are different from the value of 0.9 N/m quoted by manufacturer. The spring constant for the bare tip (control tip) was 0.65 ± 0.03 N/m. This is much lower than the tip stiffness summarized in Table 5.3 for the coated AFM tips. The increased stiffnesses of the coated tips is attributed to the stiffening of the tips by the deposited or dip coated materials. These increase the effective second moment of area, and thus the effective AFM tip stiffness.

Typical force-displacement plots are presented in Figures 5.6 ((a) and (b)). Figure 5.6(a) shows the adhesion curve for the interaction between a copper coated AFM tip and a clay ceramic substrate. This similar typical force-displacement curve was obtained for all the other pair-wise interactions, except for those between the different tips (bare AFM tips or copper coated tips or silver coated tips) and *E.coli*. A typical force displacement plot obtained in the latter case is presented in Figure 5.6(b). This shows an example of a force-displacement obtained for the interaction between copper coated tips and *E.coli*.

The pull-off deflections were multiplied by the spring constant of the AFM tip (Table 5.2) to obtain the pull-off forces (Equation 1). The measured pull-off forces are divided into two main types of interactions and presented in Figures 5.7(a) and 5.7 (b), and Table 5.3. Figure 5.7(a) shows the interactions of metallic materials (colloidal silver, silver and copper) and the porous clay ceramic with *E.coli,* while Figure 5.7(b) presents the pair wise interaction between the metals or *E.coli* with the porous clay ceramic.

Figure 5.7(a) shows that the porous clay ceramic exhibited the highest adhesion force of 157 ± 27 nN. The adhesion force between colloidal silver and *E.coli* is lower (67 nN to 113 nN), as is the interaction between copper and *E.coli* (92 nN to 113 nN). Furthermore, the metallic silver has a higher (average) adhesion force (133 nN) with *E.coli* than that between the colloidal silver and *E.coli* (90 nN) and that between copper and *E.coli* (104 nN). However, the scatter in the data is quite significant.

Different trends were observed in the clay ceramic adhesive forces (Figure 5.7(b)). First, the surface pair interactions exhibited a much wider range of adhesive forces. The adhesion force between the colloidal silver and clay ceramic (125 ± 32 nN) was greater than that between silver and clay ceramic (29 ± 11 nN) and copper and clay ceramic (37 ± 15nN). Also, the adhesion force between the colloidal silver and clay ceramic is over three times greater than the force between copper and the clay ceramic. Furthermore, the average adhesion force between copper and the clay ceramic (37 nN) is greater than that between the silver and the clay ceramic (29 nN). However, the standard deviations are large (Figure 5.7(b)). The above adhesion forces are attributed largely to van der Waals interactions between the bi-material pairs. Capillary forces and electrostatic forces may also occur for the interactions between colloidal silver - or silver - or copper - coated AFM tips and *E.coli* substrates. Furthermore, contact forces may be masked by the larger liquid bridge effects. However, van der Waals forces should be the dominant forces in most of the interactions studied, especially for smooth contacts. Long range electrostatic forces appear to operate only for limited range of surfaces and relative humidities (Jones *et al*., 2002).

5.4.3 Adhesion Energies

Some of the differences in the measured interactions became even more apparent after the adhesion energies were determined from the measured pull-off forces and surface profiles. By carrying out iterative calculations using Equations 3 - 11, the Tabor parameter, μ, was found to be within the range ~ 10^{-8} - 10^{-16}. Hence, the Tabor parameter is $\ll 1$, for of all the bi-material pairs that were studied. Furthermore, using the elasticity parameter, λ, it is clear that as $\lambda \rightarrow 0$, hence the MD model (Equation 10) reduces to the DMT model. Both parameters (μ and λ), indicated that the interactions should be characterized by the DMT model (Equation 3).

The resulting adhesion energies are presented in Figure 5.8(a) and 5.8(b). The trends in the adhesion energies are similar to those of the adhesion forces presented earlier (Figures 5.7(a) and 5.7(b)). However, the adhesion energies are also influenced by the surface roughness presented in Table 5.1. Hence, the relative values of the adhesion forces are different from those of the adhesion energies. For example, the ratio of the adhesion force for the silver - *E.coli* and the adhesive force interaction for colloidal silver –*E.coli* was ~ 1.5, while the corresponding ratio of adhesion energies was ~ 1.3. The clay ceramic - *E.coli* interaction had the highest adhesion energy, 0.46 J/m^2, while the silver – ceramic interaction had the lowest adhesion energy, 0.06 J/m^2. The latter was just below that of copper – ceramic interaction, 0.07 J/m^2. The measured adhesion energies are attributed largely to van der Waals interactions between the bi-material pairs.

5.4.4 Implications

The implications of the above force microscopy results are quite significant. First, the results can be used for the ranking of the adhesion between the different material pairs that are relevant to water purification using ceramic water filters. Such ranking is important in selection of bactericidal materials that coat and impregnate the filter. These kill entrapped bacteria and reduce the proliferation of bacteria at entrapped sites. Strong adhesion of silver, colloidal silver and copper nanoparticles to clay ceramic substrates is good because it reduces the leaching of these materials into the filtered water. The high levels of adhesion to the clay ceramic by colloidal silver and the copper and silver nanoparticles are therefore important for the long term health and safety of those that consume the filtered water from the coated CWFs. For example, ingesting water containing colloidal silver may lead to argyria (Wadhera & Fung, 2005), which is a condition in which the skin turns blue or bluish-grey.

Furthermore, the adhesion between colloidal silver and *E.coli* is in the same range as the adhesion between copper and *E.coli*. This implies that colloidal silver may be replaced with copper as the disinfectant coating ceramic water filters. This could help to reduce the cost of ceramic water filters, since copper nanoparticles are cheaper than colloidal silver. However, since the adhesion energies between the clay ceramic surfaces and the colloidal silver or silver nanoparticles were greater than those with copper nanoparticles, this suggests that a higher incidence of leaching should be expected from copper nanoparticle coated clay ceramic surfaces.

Further work is clearly needed to study the effects of adhesion on the leaching of silver, colloidal silver and copper nanoparticles. There is also a need for further studies to explore the adhesion between other clay ceramic materials and *E.coli* and other microbial pathogens that are relevant to clay ceramic water purification. These are clearly some of the challenges for future work.

5.5 Conclusions

This chapter presents the results of an experimental study of the adhesion of bi-material pairs that are relevant to clay ceramic water purification. These include adhesion forces/energies for surfaces between disinfectant coatings (silver, colloidal silver and copper) and clay ceramic surface as well as the adhesion between *E.coli* and surfaces/materials that are relevant to point-of-use ceramic water filters. The results show that pure silver coatings have the strongest adhesion to *E.coli*. It is, therefore, more likely to attract *E.coli* than colloidal silver or copper nanoparticle coatings. Colloidal silver adhere best to the clay ceramic that was studied. It is therefore less likely to leach into the filtrate than the pure silver or copper nanoparticles that have lower adhesion forces/energies. Hence, colloidal silver or silver nanoparticles are more adherent coatings than alternative copper nanoparticle coatings that could reduce the overall costs of point-of-use clay ceramic water filters.

References

Alcamo, I. E. (1997). *Fundamentals of microbiology* (5th ed.). Menlo Park, Calif.: Benjamin Cummings.

Argenol-Laboratories. (2011). Retrieved from http://www.laboratorios-argenol.com/fi-colargoli.htm

Bachmann, B. J. (1972). Pedigrees of some mutant strains of Escherichia coli K-12. *Bacteriol Rev, 36*(4), 525-557.

Bhushan, B. (1995). *Handbook of micro/nanotribology*. Boca Raton: CRC Press.

Butt, H. J., Cappella, B., & Kappl, M. (2005). Force measurements with the atomic force microscope: Technique, interpretation and applications. *Surface Science Reports, 59*(1-6), 1-152.

Cao, T., Tang, H. Y., Liang, X. M., Wang, A. F., Auner, G. W., Salley, S. O., & Ng, K. Y. S. (2006). Nanoscale investigation on adhesion of E-coli surface modified silicone using atomic force microscopy. *Biotechnology and Bioengineering, 94*(1), 167-176.

Carpick, R. W., Ogletree, D. F., & Salmeron, M. (1999). A general equation for fitting contact area and friction vs load measurements. *Journal of Colloid and Interface Science, 211*(2), 395-400.

Cho, K. H., Park, J. E., Osaka, T., & Park, S. G. (2005). The study of antimicrobial activity and preservative effects of nanosilver ingredient. *Electrochimica Acta, 51*(5), 956-960.

Derjaguin, B. V., Muller, V. M., & Toporov, Y. P. (1994). Effect of Contact Deformations on the Adhesion of Particles. *Progress in Surface Science, 45*(1-4), 131-143.

Dupres, V., Menozzi, F. D., Locht, C., Clare, B. H., Abbott, N. L., Cuenot, S., Bompard, C., Raze, D., & Dufrene, Y. F. (2005). Nanoscale mapping and functional analysis of individual adhesins on living bacteria. *Nat Methods, 2*(7), 515-520.

Esteban-Cubillo, A., Pecharroman, C., Aguilar, E., Santaren, J., & Moya, J. S. (2006). Antibacterial activity of copper monodispersed nanoparticles into sepiolite. *Journal of Materials Science, 41*(16), 5208-5212.

Feng, Q. L., Wu, J., Chen, G. Q., Cui, F. Z., Kim, T. N., & Kim, J. O. (2000). A mechanistic study of the antibacterial effect of silver ions on Escherichia coli and Staphylococcus aureus. *Journal of Biomedical Materials Research, 52*(4), 662-668.

Hartley, P. G., Grieser, F., Mulvaney, P., & Stevens, G. W. (1999). Surface forces and deformation at the oil-water interface probed using AFM force measurement. *Langmuir, 15*(21), 7282-7289.

Hinterdorfer, P., Schutz, G., Kienberger, F., & Schindler, H. (2001). Detection and characterization of single biomolecules at surfaces. *Journal of Biotechnology, 82*(1), 25-35.

Jain, P., & Pradeep, T. (2005). Potential of silver nanoparticle-coated polyurethane foam as an antibacterial water filter. *Biotechnol Bioeng, 90*(1), 59-63.

Johnson, K. L. (1998). Mechanics of adhesion. *Tribology International, 31*(8), 413-418.

Johnson, K. L., Kendall, K., & Roberts, A. D. (1971). Surface Energy and Contact of Elastic Solids. *Proceedings of the Royal Society of London Series a-Mathematical and Physical Sciences, 324*(1558), 301-&.

Jones, R., Pollock, H. M., Cleaver, A. S., & Hodges, C. S (2002). Adhesion forces between glass and silicon surfaces in air studied by afm: effects of relative humidity, particle size, roughness, and surface treatment. *Langmuir, 18*, 8045-8055

Kim, T. N., Feng, Q. L., Kim, J. O., Wu, J., Wang, H., Chen, G. C., & Cui, F. Z. (1998). Antimicrobial effects of metal ions (Ag+, Cu2+, Zn2+) in hydroxyapatite. *J Mater Sci Mater Med, 9*(3), 129-134.

Kobayashi, N., Li, Y. J., Naitoh, Y., Kageshima, M., & Sugawara, Y. (2010). High force sensitivity in Q-controlled phase-modulation atomic force microscopy. *Applied Physics Letters, 97*(1).

Lansdown, A. B. (2002). Silver. I: Its antibacterial properties and mechanism of action. *J Wound Care, 11*(4), 125-130.

Leite, F. L., & Herrmann, P. S. P. (2005). Application of atomic force spectroscopy (AFS) to studies of adhesion phenomena: a review. *Journal of Adhesion Science and Technology, 19*(3-5), 365-405.

Li, F., Redick, S. D., Erickson, H. P., & Moy, V. T. (2003). Force measurements of the alpha5beta1 integrin-fibronectin interaction. *Biophysical Journal, 84*(2 Pt 1), 1252-1262.

Li, X., & Logan, B. E. (2004). Analysis of bacterial adhesion using a gradient force analysis method and colloid probe atomic force microscopy. *Langmuir, 20*(20), 8817-8822.

Lower, S. K., Tadanier, C. J., & Hochella, M. F. (2000). Measuring interfacial and adhesion forces between bacteria and mineral surfaces with biological force microscopy. *Geochimica Et Cosmochimica Acta, 64*(18), 3133-3139.

Magonov, S. N., & Whangbo, M.-H. (1996). *Surface analysis with STM and AFM : experimental and theoretical aspects of image analysis*. Weinheim ; New York: VCH.

Maugis, D., & Pollock, H. M. (1984). Surface Forces, Deformation and Adherence at Metal Microcontacts. *Acta Metallurgica, 32*(9), 1323-1334.

Meng, J., Paetzell, E., Bogorad, A., & Soboyejo, W. O. (2010). Adhesion between peptides/antibodies and breast cancer cells. *Journal of Applied Physics, 107*(11).

Miller, J. H. (1972). *Experiments in molecular genetics*. Cold Spring Harbor, N.Y.: Cold Spring Harbor Laboratory.

Morones, J. R., Elechiguerra, J. L., Camacho, A., Holt, K., Kouri, J. B., Ramirez, J. T., & Yacaman, M. J. (2005). The bactericidal effect of silver nanoparticles. *Nanotechnology, 16*(10), 2346-2353.

Ong, Y. L., Razatos, A., Georgiou, G., & Sharma, M. M. (1999). Adhesion forces between E-coli bacteria and biomaterial surfaces. *Langmuir, 15*(8), 2719-2725.

Oyanedel-Craver, V. A., & Smith, J. A. (2008). Sustainable colloidal-silver-impregnated ceramic filter for point-of-use water treatment. *Environmental Science & Technology, 42*(3), 927-933.

Pal, S., Tak, Y. K., & Song, J. M. (2007). Does the antibacterial activity of silver nanoparticles depend on the shape of the nanoparticle? A study of the gram-negative bacterium Escherichia coli. *Applied and Environmental Microbiology, 73*(6), 1712-1720.

Panacek, A., Kvitek, L., Prucek, R., Kolar, M., Vecerova, R., Pizurova, N., Sharma, V. K., Nevecna, T., & Zboril, R. (2006). Silver colloid nanoparticles: Synthesis, characterization, and their antibacterial activity. *Journal of Physical Chemistry B, 110*(33), 16248-16253.

Prater, C. B., Maivald, P. G., Kjoller, K. J., & Heaton, M. G. (Bruker). Retrieved from www.bruker.com

Razatos, A., Ong, Y. L., Sharma, M. M., & Georgiou, G. (1998). Evaluating the interaction of bacteria with biomaterials using atomic force microscopy. *Journal of Biomaterials Science-Polymer Edition, 9*(12), 1361-1373.

Ruparelia, J. P., Chatterjee, A. K., Duttagupta, S. P., & Mukherji, S. (2008). Strain specificity in antimicrobial activity of silver and copper nanoparticles. *Acta Biomater, 4*(3), 707-716.

Serry, F. M. (2005). Improving the accuracy of AFM force measurements: The thermal tune solution to the cantilever spring constant problem *In Veeco Application Notes* (Vol. AN90). Santa Barbara, CA: Veeco Instrument Inc.

Shahin, V., Ludwig, Y., Schafer, C., Nikova, D., & Oberleithner, H. (2005). Glucocorticoids remodel nuclear envelope structure and permeability. *J Cell Sci, 118*(Pt 13), 2881-2889.

Sondi, I., Goia, D. V., & Matijevic, E. (2003). Preparation of highly concentrated stable dispersions of uniform silver nanoparticles. *Journal of Colloid and Interface Science, 260*(1), 75-81.

Sondi, I., & Salopek-Sondi, B. (2004). Silver nanoparticles as antimicrobial agent: a case study on E-coli as a model for Gram-negative bacteria. *Journal of Colloid and Interface Science, 275*(1), 177-182.

Tabor, D. (1977). Surface Forces and Surface Interactions. *Journal of Colloid and Interface Science, 58*(1), 2-13.

Tong, T., Babatope, B., Admassie, S., Meng, J., Akwogu, O., Akande, W., & Soboyejo, W. O. (2009). Adhesion in organic electronic structures. *Journal of Applied Physics, 106*(8).

Top, A., & Ulku, S. (2004). Silver, zinc, and copper exchange in a Na-clinoptilolite and resulting effect on antibacterial activity. *Applied Clay Science, 27*(1-2), 13-19.

UNICEF. (2008). UNICEF Handbook on Water Quality. *United Nations Children's Fund (UNICEF), New York*.

Viani, M. B., Schaffer, T. E., Chand, A., Rief, M., Gaub, H. E., & Hansma, P. K. (1999). Small cantilevers for force spectroscopy of single molecules. *Journal of Applied Physics, 86*(4), 2258-2262.

Wadhera, A., & Fung, M. (2005). Systemic argyria associated with ingestion of colloidal silver. *Dermatol Online J, 11*(1), 12.

WHO/UNICEF. (2010). Progress on Drinking Water and Sanitation: World Health Organization and United Nations Children's Fund Joint Monitoring Programme for Water Supply and Sanitation. Geneva, Switzerland.

Wiesendanger, R. (1994). *Scanning probe microscopy and spectroscopy : methods and applications*. Cambridge England ; New York: Cambridge University Press.

Wojcikiewicz, E. P., Zhang, X., & Moy, V. T. (2004). Force and Compliance Measurements on Living Cells Using Atomic Force Microscopy (AFM). *Biol Proced Online, 6*, 1-9.

Wolf, K. V., Zong, Z., Meng, J., Orana, A., Rahbar, N., Balss, K. M., Papandreou, G., Maryanoff, C. A., & Soboyejo, W. (2008). An investigation of adhesion in drug-eluting stent layers. *Journal of Biomedical Materials Research Part A, 87A*(1), 272-281.

Yakub, I., Plappally, A., Leftwich, M., Malatesta, K., Friedman, K. C., Obwoya, S., Nyongesa, F., Maiga, A. H., Soboyejo, A. B. O., et al. (Submitted for publication). Porosity and Filtration Characteristics of Frustum-Shaped Ceramic Water Filters.

Yang, L., Ning, X., Xiao, Q., Chen, K., & Zhou, H. (2007). Development and characterization of porous silver-incorporated hydroxyapatite ceramic for separation and elimination of microorganisms. *J Biomed Mater Res B Appl Biomater, 81*(1), 50-56.

Yoon, K. Y., Byeon, J. H., Park, J. H., & Hwang, J. (2007). Susceptibility constants of Escherichia coli and Bacillus subtilis to silver and copper nanoparticles. *Science of the Total Environment, 373*(2-3), 572-575.

Material	Roughness (nm)
Glass	3.77 ± 0.54
E.coli	87.69 ± 68.82
Ceramic	179.71 ± 88.16

Table 5.1: Average rms roughness values

AFM tip	Average spring constant (N/m)
Bare tip	0.65 ± 0.03
Colloidal silver coated tip	0.81 ± 0.06
Silver coated tip	0.80 ± 0.02
Copper coated tip	1.00 ± 0.05
Ceramic coated tip	0.93 ± 0.07

Table 5.2: Spring constants of the bare and coated AFM tips

	Interaction	Average adhesion force (nN)
(a)	Colloidal silver - E.coli	90 ± 23
	Silver - E.coli	133 ± 21
	Copper - E.coli	104 ± 12
	Ceramic - E.coli	157 ± 27
(b)	Colloidal silver - Ceramic	125 ± 32
	Silver - Ceramic	29 ± 11
	Copper - Ceramic	37 ± 15
	E.coli - Ceramic	157 ± 27

Table 5.3: Adhesion force between coated AFM tips and substrate for (a) *E.coli* bacteria interactions and (b) Ceramic interactions

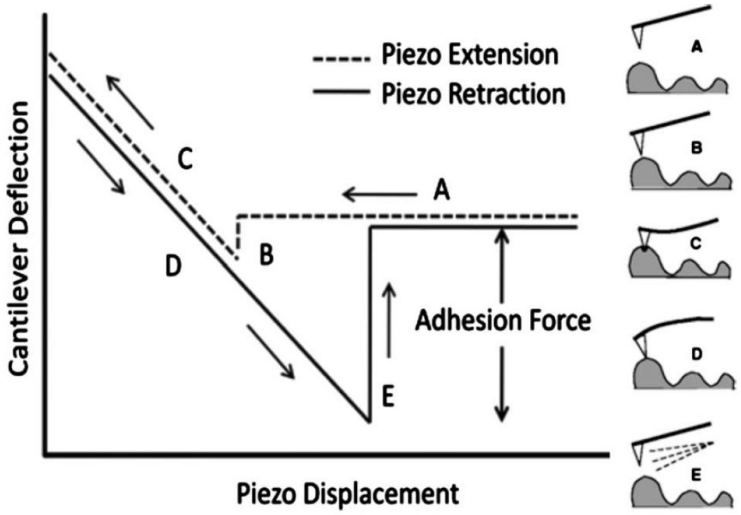

Figure 5.1: Schematic of a typical cantilever deflection-displacement plot with highlights of the various stages (A-E) of the AFM tip as it is brought into and out of sample at a fixed point (adapted from Shahin et al., 2005)

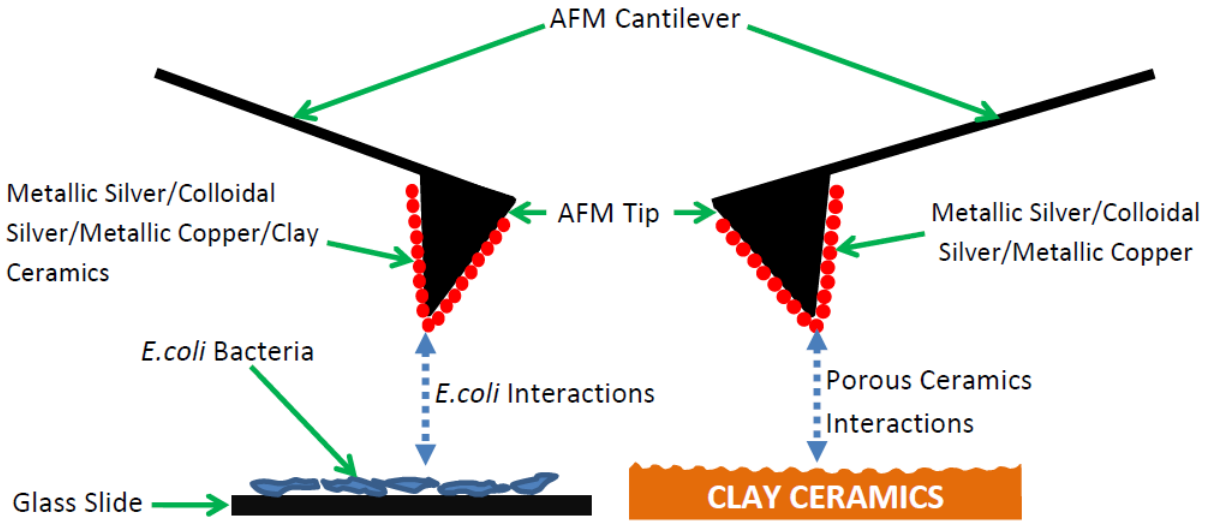

Figure 5.2: Schematic illustration of adhesion between coated AFM tips and surfaces relevant to ceramic water filter

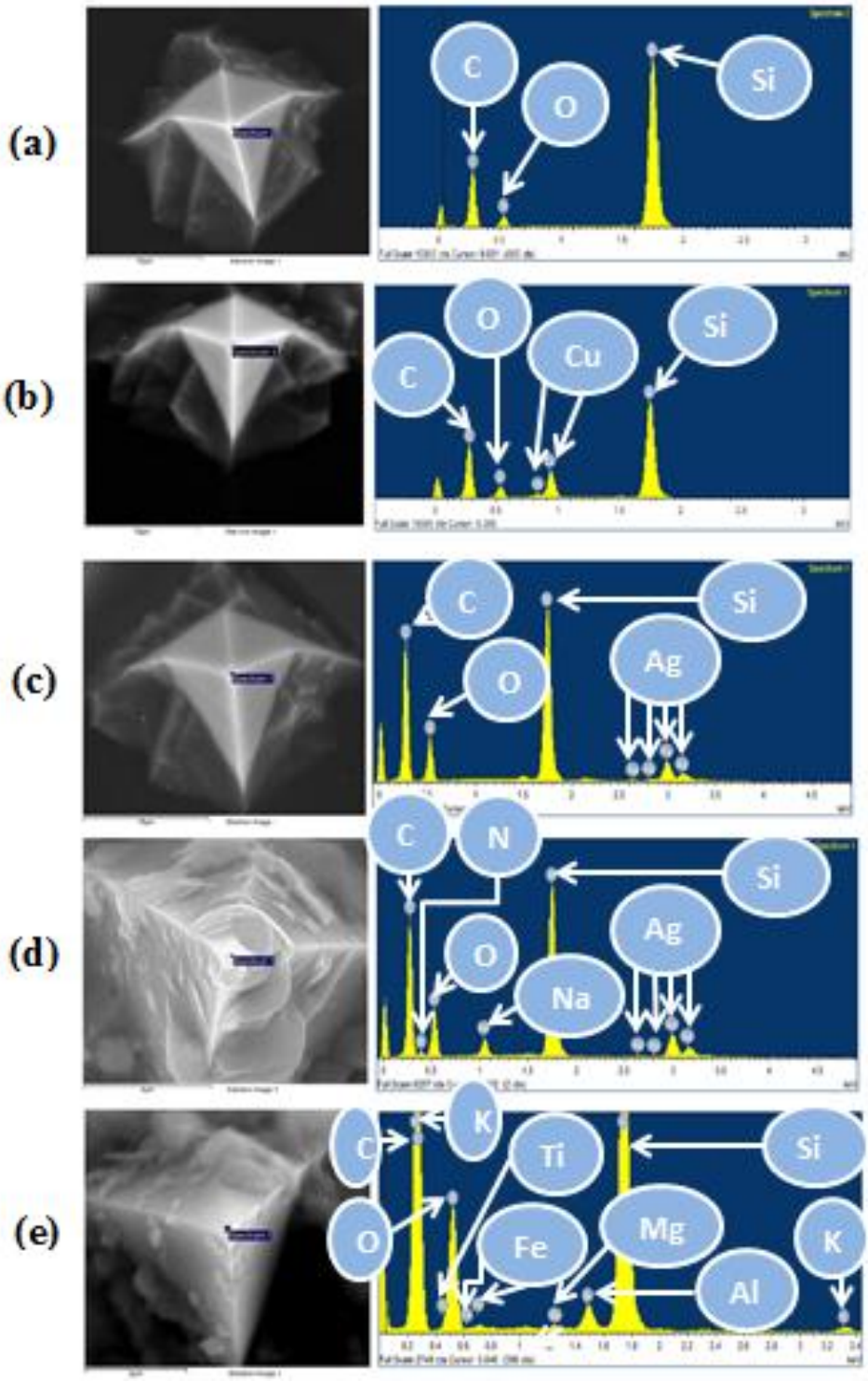

Figure 5.3: ESEM images and EDX spectrum of (a) uncoated tip, (b) copper coated tip, (c) silver coated tip, (d) colloidal silver coated tip, and (e) ceramic coated tip

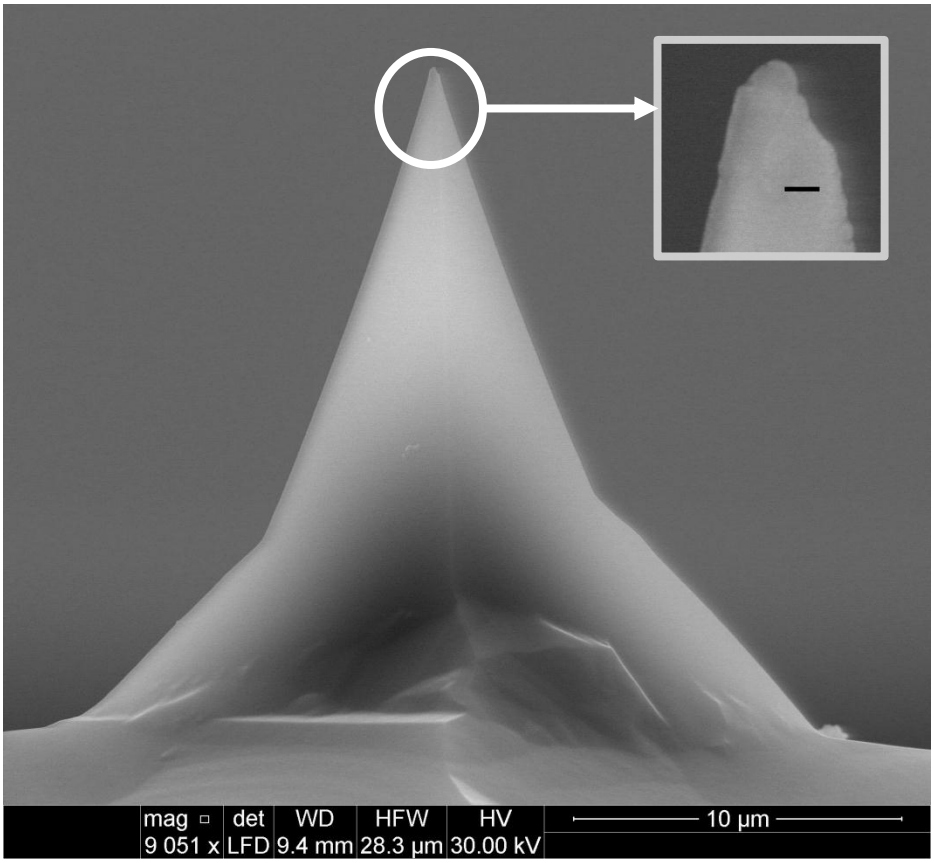

Figure 5.4: Measurement of AFM tips radii using ESEM micrograph (scale bar of insert = 100 nm). The metallic silver coated AFM tip shown has a tip radius of ~ 87 nm.

(a) (b)

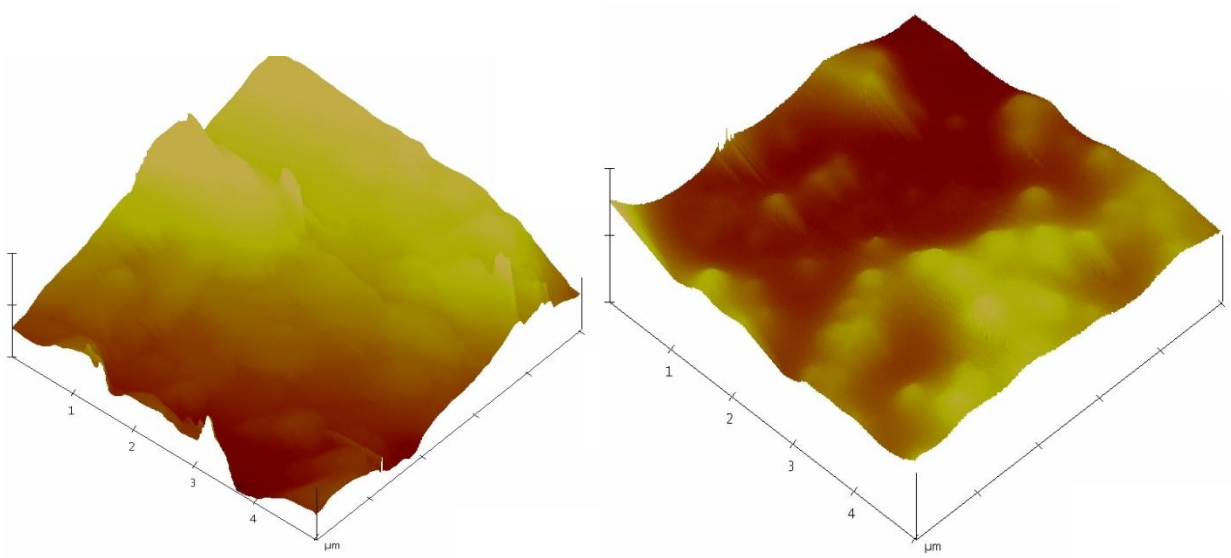

Figure 5.5: Sample of 5µm AFM tapping mode image of (a) porous ceramic and (b) *E.coli* bacteria surfaces

(a)

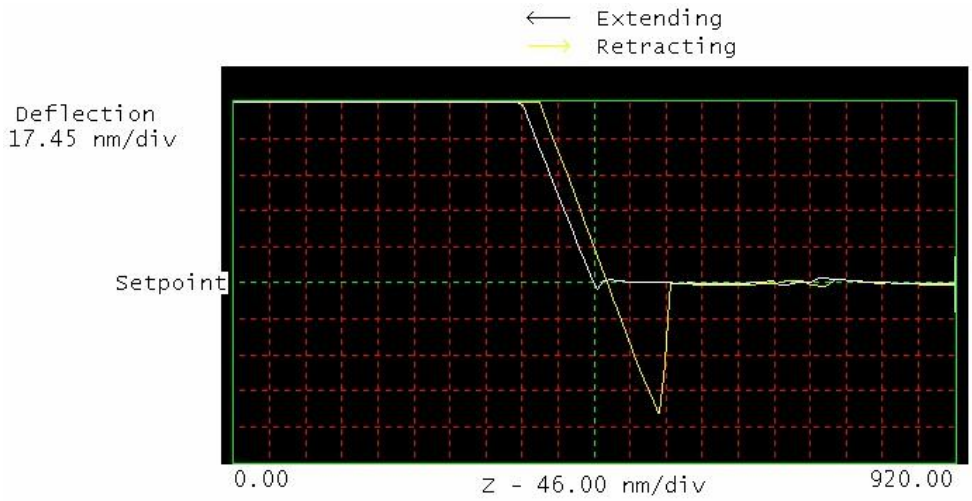

(b)

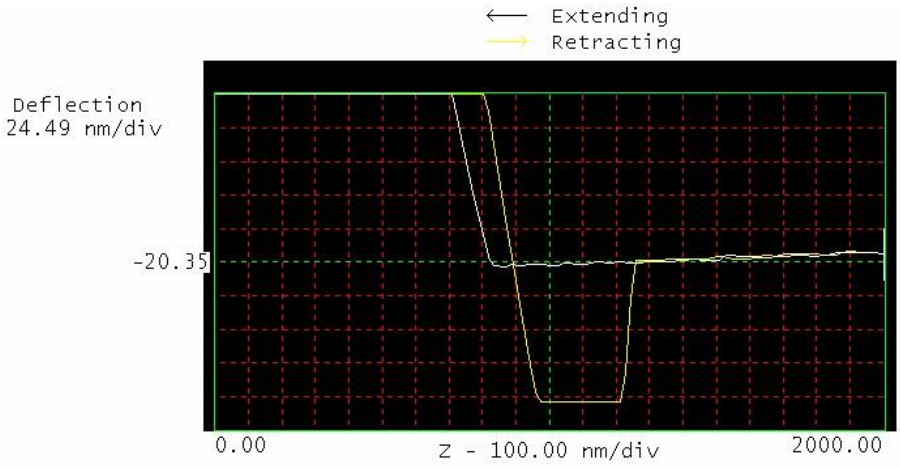

Figure 5.6: Typical AFM force-displacement characteristics for copper coated tip and (a) porous ceramics and (b) *E.coli* bacteria

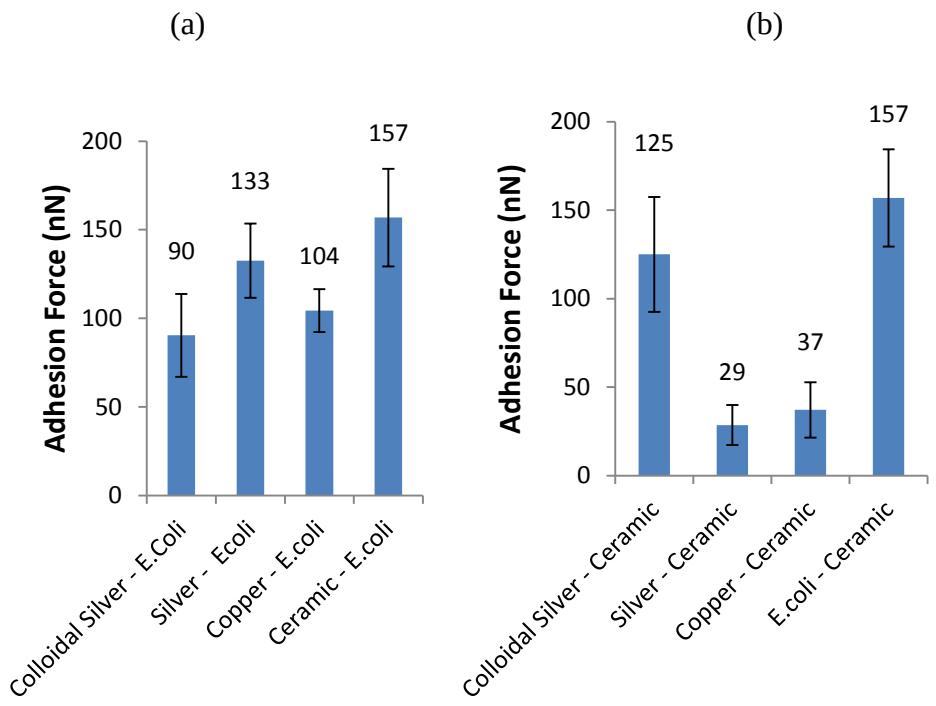

Figure 5.7: Comparison of adhesion force obtained for (a) *E.coli* interactions and (b) Porous ceramics interactions

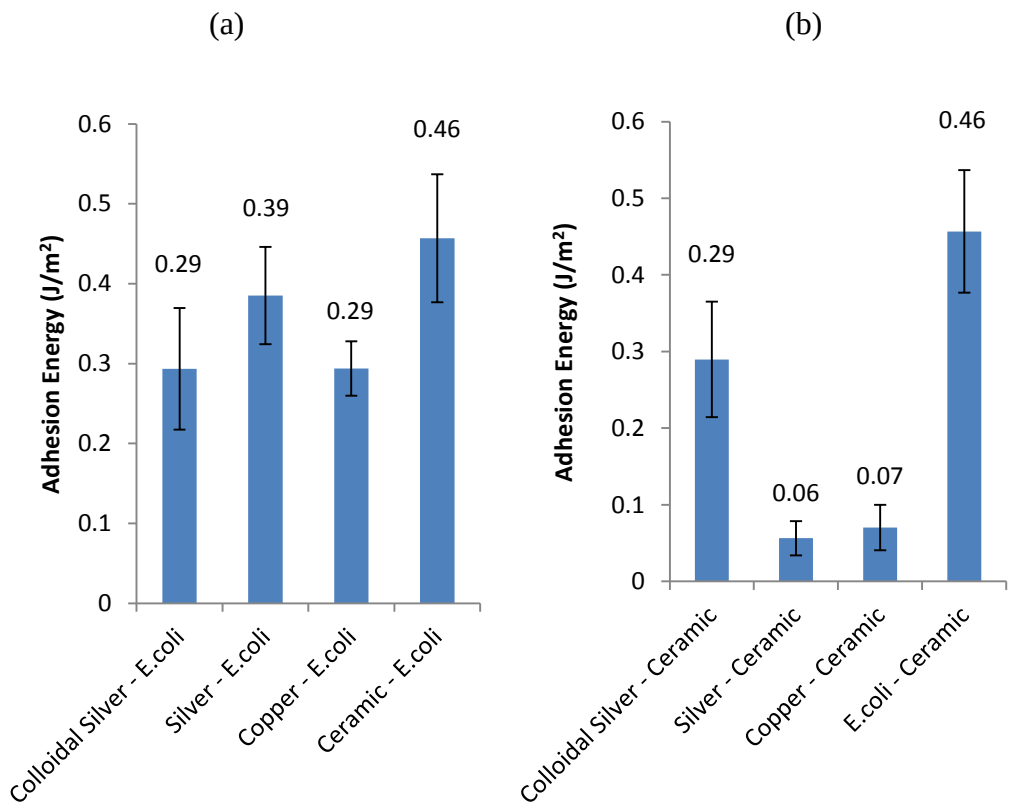

Figure 5.8: Adhesion energies obtained for (a) *E.coli* interactions and (b) Porous ceramics interactions

Chapter 6

Adsorption of Fluoride from Water using Sintered Clay-Hydroxyapatite Composites

6.1 Introduction

Ingesting water containing fluoride of concentration around 1.5 mg/L (as recommended by the World Health Organization) has a number of beneficial effects. This includes promoting healthy teeth and preventing dental cavities (MRC, 2002). However, fluoride contaminated water can also have detrimental effects on the human health, including fluorosis, if concentrations greater than ~ 1.5 mg/L are consumed over a prolonged period of time. Dental fluorosis is characterized by the staining, pitting and mottling of the dental enamel. However, much higher concentrations (about 4mg/L) and longtime exposure can lead to crippling skeletal fluorosis and osteoporosis (Inyang, 2004; Mandinic *et al.*, 2010). Depending on body weight, the consumption of excessive amounts of fluoride (about 300 to 750 mg) in a single dose can also result in acute toxicity

associated with nausea or vomiting (NebGuide, 1998). It is also known to have adverse effects on the kidneys (Waldbott, 1973).

Fluoride is found in all natural waters at some concentration (Mandinic *et al.*, 2010). However, in many parts of the world, elevated levels of fluoride are present in water due to either anthropogenic sources (industrial and agricultural activities, e.g. during the production of aluminium, use of some pesticides etc), natural causes (volcanic activity, sediments of marine origin, granitic and gneissic rocks), or a combination of both. High levels of fluoride in drinking water and cases of fluorosis have been reported in many countries across the world (Murray *et al.*, 1986; USEPA, 1996). These include: United States of America, Germany, Saudi Arabia, South Africa, Nigeria, Kenya, Tanzania, China and India (Akpata *et al.*, 1997; al-Khateeb *et al.*, 1991; Latham & Grech, 1967; McCaffrey & Willis, 1997; Nair *et al.*, 1984; Queste *et al.*, 2001; Segreto *et al.*, 1984; UNICEF, 1999 ; Wongdem *et al.*, 2000). In China, endemic fluorosis has been reported in all 28 provinces, autonomous regions and municipalities, except Shanghai (Mandinic *et al.*, 2010). It was also reported in 1999 that, 17 of India's 32 states and territories, have naturally high fluoride levels in water (FRRDF, 1999; UNICEF, 1999 ; Yadav *et al.*, 1999).

The major mechanisms by which fluoride is removed from the water include: adsorption, precipitation and ion exchange. Different types adsorbents and methods have already been explored to achieve this objective. These include the use of kaolinite (Chaturvedi *et al.*, 1988; Srimurali *et al.*, 1998), montmorillite (Agarwal *et al.*, 2002; Mlilo *et al.*, 2010), goethite (Mlilo *et al.*, 2010), hematite (Mlilo *et al.*, 2010), Soil (Mlilo *et al.*, 2010; Wang & Reardon, 2001), non-sintered forms of hydroxyapatite (Alagumuthu & Rajan, 2010; Fan, 2003; Sundaram *et al.*, 2008), bone char (Abe *et al.*, 2004; Brunson & Sabatini, 2009; Kaseva, 2006; Medellin-Castillo *et al.*, 2007; Mlilo *et al.*, 2010; Mwaniki, 1992), ion-exchangers (Chubar *et al.*, 2005), activated

carbon, alumina and carbon nanotubes (Y Li *et al.*, 2001; Li *et al.*, 2003; Ramos, 1999) and other types of adsorbents (Ayoob & Gupta, 2009; Srimurali *et al.,* 1998). However, there are no filters reported to fluoride and microbial pathogens from contaminated water.

In this chapter, we present a novel adsorbent that can remove both fluoride and microbial pathogens, such as bacteria, from contaminated water. The adsorbent is processed by the sintering of a mixture of clay and hydroxyapatite that removes fluoride from water. The porous structure also effectively removes bacteria (and other microbial pathogens) that may be present in water. Adsorption experiments were also performed to explore the potential of the redart clay and hydroxyapatite composite mixtures to remove fluoride from water. Finally, a proof-of-concept frustum-shaped filter is shown to remove both fluoride and *E.coli* from fluoride- and microbe - contaminated water.

6.2 Experimental

6. 2.1 Materials and Processing

The HA used in this chapter was synthesized by adding phosphoric acid to a calcium hydroxide solution, as described by Vermilghen *et al.* (Verwilghen *et al.,* 2007). The resulting HA was allowed to dry under constant exposure to solar lamps with an incident power of 1000 W/m^2. The dried HA was crushed using a mortar and pestle and then sieved using a sieve with a nominal opening of 500 µm.

For the study of adsorption, small pellets of C-HA were made by sintering a mixture of HA, redart clay (Cedar Heights Redart Airfloated Clay, Pittsburgh, PA) and sawdust (Hamilton Building Supplies, Trenton, NJ) in different proportions. Five different types of adsorbent were produced, by varying the proportion of clay to HA. First, clay was added to HA in different ratios by volume (0:100, 75:25, 80:20, 90:10 and 100:0). Sawdust, obtained from a local sawmill, consisting of 80% oak and 20% Spanish cedar, was added in a ratio of 2:1 ("Clay + HA": Sawdust) by volume, in order to introduce a porous network into the resulting pellet (Table 6.1). Prior to mixing, the sawdust was manually sieved using a sieve with a nominal opening of 125 μm.

Water was used as the binding agent. Water was added until the mixture turned plastic. The resulting mixtures were then molded into a disc, using a cylindrical mold with internal dimension of ~ 50 mm in diameter and ~ 10 mm in depth. They were then allowed to dry for about 2 days before sintering in a furnace (Type F6000 Ashing Furnace, Barnstead/Thermolyne Corporation, Dubuque, IA). The mixtures were sintered at a rate of 3°C/min until they reached the peak sintering temperatures. The furnace was then turned off and allowed to cool down to room temperature. The maximum sintering temperatures were 500°C, 600°C, 700°C, 800°C and 900°C. After sintering, the resulting C-HA pellets had diameters of ~ 42 ± 3 mm and thicknesses of ~ 9 ± 1mm.

In an effort to explore the potential use of the C-HA structures in water filtration, frustum-shaped C-HA filters were produced. Two types of filters were made with clay to HA volume ratios of 75:25, and 80:20. Sawdust was added in the ratio, by volume, of 2:1 ("Clay + HA": Sawdust). The process of making the filter is described in detail by Yakub *et al.* (Yakub *et al.*, submitted for publication). It involved mixing of constituents (clay, HA and sawdust) with water in an

industrial mixer (Model A-200, The Hobart Manufacturing Company, Troy, OH) until the mixture became plastic. About 12 pounds of the mixture was then manually formed into a ball, which was then compacted in a two-piece aluminum mold, using a 50 ton hydraulic press (TRD55002, Torin Jacks, Inc., Ontario, Canada). The greenware that was formed was then allowed to dry in laboratory air (~ 25°C at ~ 40% relative humidity) for about 8 days, after which they were sintered in an electric kiln ("That Pottery Place", Princeton Junction, NJ). The C-HA was fired at a rate of ~3°C/min until a peak temperature of ~861°C (cone 012) was reached. It was then held at this temperature for 4 hours before cooling to room-temperature.

6.2.2 Materials Characterization

The chemical constituents of the ingredients used (HA and redart clay) in making the adsorbent and C-HA adsorbent were characterized using the Oxford energy dispersive X-ray spectroscopy (EDX) detector (Oxford Instruments, Oxfordshire, UK) in an Environmental Scanning Electron Microscope (ESEM) (Quanta 200 FE-ESEM, FEI, Hillboro, OR). The crystalline phases present were also determined using X-ray Diffraction (Rigaku Miniflex, Texas, US). The morphologies of the ingredients and the adsorbent were studied using the Backscattered Electron and the Scanning Transmission Electron Microscope (Quanta 200 FE-ESEM, FEI, Hillboro, OR).

X-ray diffraction (XRD) was performed on powders of the ingredients used and, while C-HA adsorbents were used to determine phase compositions. A Rigaku Miniflex (Rigaku, Texas, US) working at 30 kV, 15mA and using the Cu-Kα radiation (λ=0.15418 nm) was used for this purpose. The scanning rate was 0.8 deg (2θ)/min over the interval shown in Figure 6.2 (a) – 6.2(c).

6.2.3 Adsorption and Kinetics Studies

Fluoride solution was prepared by either dissolving the appropriate mass of NaF (Fisher Scientific, Fair Lawn, NJ) in deionized water, or by serial dilution. The pH of the solution was not adjusted. For the batch adsorption experiments, 0.25 g of the adsorbent was added to 30 mL of fluoride solution and agitated using a rotary shaker ("Rugged Rotator", Glas-Col, Terre Haute, IN) at 80 revolutions per minute (rpm) for 24 hours. The suspension was then filtered through a 0.22 µm filter (Millex-GP, Millipore Corp, Billerica, MA) attached to a syringe. The equilibrium concentration of fluoride was measured using the Hach fluoride probe (Model 51928 Platinum Series Fluoride Electrode, Hach Company, Loveland, CO) attached to an ion-selective electrode (ISE) meter (sensION™ pH/ISE Meter, Hach Company, Loveland, CO). For the adsorption kinetics experiments, C-HA = 0:100 and C-HA = 75:25 sintered at 500°C was studied. 0.25 g of adsorbent was added to 50 mL of water with a fluoride concentration of ~ 60 mg/L. The amount of fluoride removed by the adsorbent was determined at different time intervals until the equilibrium concentration was reached.

6.2.4 Proof-of-Concept Study

The C-HA filter was placed in a plastic receptacle that was fitted with a large plastic funnel. The filter and receptacle-funnel were suspended above an empty collection vessel. For the fluoride removal test, water containing fluoride concentration of 2.5 mg/L and 20 mg/L was used. The filtrate was collected at intervals corresponding to volumes of 25 mL. In addition to measuring the concentration of fluoride, the pH of water was measured before and after treatment. This was done using a pH probe (Model 51910 Platinum Series pH Electrode, Hach Company, Loveland, CO) attached to the ISE meter. Non-pathogenic *E.coli* K-12 strain W3110 (Obtained from N.

Ruiz, The Ohio State University) was used for the bacterial filtration test. A full description of the procedure is given elsewhere (Yakub *et al.*, submitted for publication). It basically involves growing the bacteria strain at 37°C for 18-24 hrs in Miller's LB Broth. This is followed by mixing of the bacteria with 4 L of sterile, purified water to produce a pre-filtrate suspension containing about 10^{6} - 10^{7} cells/mL. The 4 L of pre-filtrate was then poured into the C-HA filter, which was placed on a plastic receptacle. The latter was lined with a sterile plastic bag that was used to collect the filtrate.

6.3 Results and Discussion

6.3.1 Characterization of Adsorbent

The EDX analyses of the HA adsorbent revealed the presence of calcium, phosphorus and oxygen [Figure 6.1(a)]. The EDX spectra obtained for the HA adsorbent sintered at 500°C are presented in Figure 6.1(b). The presence of the carbon peak verifies that the woodchips were not been completely burnt off during the sintering process. Figure 6.1(c) shows the elemental composition for the C-HA = 75:25 adsorbent. It also verifies the co-sintering of the HA and clay. The carbon peak is also present in this figure. Figures 6.1(d) and 6.1(e) show the EDX results obtained for the C-HA adsorbent after the adsorption experiments. They reveal the capture of fluorine.

Figure 6.2(a) shows the XRD pattern of the HA that was used in making the adsorbent. The peaks present correspond to those of the crystalline hydroxyapatite structure (File No.73-0293, ICDD; Jie & Yubao, 2004; Sundaram, 2008). The XRD analysis of the sintered HA, i.e. C–HA =

0:100, is presented in Figure 6.2(b). The figure shows no marked change in the pattern for all of the sintering temperatures that were considered (500°C, 600°C, 700°C, 800°C and 900°C) (Koumoulidis *et al.*, 2006). Figure 6.2(c) shows the XRD pattern obtained for the C-HA adsorbent (in this case, C–HA = 75:25). A similar pattern was observed for other adsorbent containing clay. Only a couple of peaks, corresponding to HA (co-sintered with clay) peaks, could be spotted on the XRD pattern. This is because of their small intensities relative to the peaks of the sintered clay structure. Hence, the presence of HA is masked by the presence of the crystalline peaks of the clay. XRD analysis was also carried out for adsorbent, which has been treated with fluorine (result not shown). There was no observable difference between the pattern of the adsorbent treated with or without fluoride (Díaz-Nava *et al.*, 2002; Sundaram *et al.*, 2008).

A typical STEM micrograph of the HA that was used in making adsorbents is presented in Figure 6.3(a). The particles of the HA powder are acicular, with diameters of about ~ 40 nm and lengths of ~ 200 nm. Similar results were obtained for C-HA = 0-100 [See Figure 6.3(b)]. Figure 6.3(c) shows an image of C-HA = 75:25. The images reveal clay particles with different shapes and sizes. Alumina-silica plates were also observed. EDX revealed that the cylindrical rod like shapes are HA-rich, while other types of shapes are HA-lean. A backscattered electron (BSE) micrograph of the C-HA adsorbent used is presented in Figure 6.4. It shows the surface morphology of the sintered C-HA prior to crushing/preparation for adsorption study. The brighter areas are the HA-rich areas.

6.3.2 Effect of Sintering Temperature

The amount of fluoride adsorbed at equilibrium, q_e (mg/g), which is defined as the mass of fluoride adsorbed per unit mass of adsorbent, was found using (Mlilo *et al.*):

$$q_e = \frac{10^{-3}(C_i - C_e)V}{m} \quad (1)$$

where C_i (mg/L) is the initial concentration of fluoride, C_e (mg/L) is the concentration of fluoride at equilibrium, V is the volume of the fluoride solution, and m (mg) is the mass of the adsorbent used.

Plots of the amount of fluoride adsorbed with sintering temperature for fluoride concentration of 10 mg/L are presented in Figure 6.5 (a). A similar trend was observed for adsorbent treated at other concentrations [Figure 6.5(b) – 6.5(e)]. As shown, the adsorption capacity of the "HA only" adsorbent decreases in a step-wise manner, with increasing sintering temperature. During sintering, sawdust is known to burn off at a temperature of about 450°C – 550°C (Maritan *et al.*, 2006). However, the EDX analysis revealed that some of sawdust is left behind as some sort of carbon residue (see Section 3.1). This is evidence in the traces of carbon that were observed at all the temperatures that were used. Evidence of carbon was also observed visually in the sintering of "C-HA = 0:100" (HA only). The HA produced was white in color. However, after sintering with sawdust, the HA became dark in color. The color of the sintered HA also became progressively lighter with sintering temperature, and it was almost completely white after sintering at 900°C. Hence, the higher the sintering temperature, the less the carbon residue that was left behind. This residual carbon, may be partly responsible for the high adsorption of the HA sintered at low temperature, and partly the reason why the adsorption capacity decreases as

the sintering temperature is increased. Besides the "HA only" adsorbent, other adsorbent showed no clear dependence on temperature [Figure 6.5 (a) – 6.5 (b)].

The XRD results (Figure 6.2(a) and 6.2(b)) also revealed that the higher the sintering temperature, the more crystalline the adsorbent. This is one of the reasons for the decrease in adsorption with increasing sintering temperature. Jha *et al*. (Jha *et al.*, 2008) have also found that the adsorption band of gehlenite ($Ca_2Al_2SiO_7$) decreases with increasing sintering temperature, and almost disappears at temperatures greater than 850^oC. This was because the strong and broad band in the amorphous samples was split into several bands by the crystallization of gehlenite. In their paper, the amount of Ni^{2+} adsorbed by the amorphous sample was greater than that of the crystalline counterpart given the same initial concentration of Ni^{2+} (Table 1, Jha *et al*., 2008)

6.3.3 Effect of HA Content

The results presented in Figure 6.5(a) – 6.5(e) showed that, in general, the higher the HA content, the higher the amount of fluoride that is adsorbed. This is not surprising, since HA is well-known to be effective in removal of fluoride ions from water. It does so by a combination of three main mechanisms: formation of fluroapatite; ion exchange mechanism (substitution of F^- ions for OH^- ions) and formation of calcium fluoride. Clays have also been shown to have fluoride removal capabilities. In this case, redart clay, which is composed mainly of illite and kaolinite. Kaolinite is a hydrated alumino-silicate, which, when treated with fluorine ion, exchanges its OH^- for fluorine. It has also been shown that, at low fluoride concentration the F^- /OH^- ion exchange that occurs is due to the presence of Al-OH in clay (Bower & Hatcher, 1967).

Another possible mechanism of fluoride removal is the hydration of metal oxides in aqueous solution. The fluoride ion present in the aqueous solution then replaces the hydroxyl ions in the metal crystal lattice, without disrupting the crystal structure of the compound. This is because F^- and OH^- have comparable ionic radii (1.36 Å and 1.40 Å, respectively). The fluoride ion is also capable of being adsorbed by Coulombic attractions due to the positive charge on alumina surface sites. The "C-HA= 100:0" (or clay only) adsorbent was the least effective at removing fluoride especially at higher sintering temperatures. This is consistent with findings by Hauge *et al*. (Hauge *et al.*, 1994) working with ordinary potter's clay.

6.3.4 Adsorption Isotherm

The experimental data obtained for the adsorption of fluoride by the C-HA adsorbent at equilibrium were fitted to the Freundlich isotherm:

$$q_e = K_f \, C_e^{1/n} \tag{2}$$

where $1/n$ and K_f ($mg^{1-1/n}L^{1/n}g^{-1}$) are Freundlich constants related to adsorption intensity and adsorption capacity, respectively.

Taking the logarithm of both sides gives the following linearized form:

$$\ln(q_e) = \frac{1}{n}\ln(C_e) + \ln(K_f) \tag{3}$$

where the Freundlich constants are obtained from the plots of $\ln(q_e)$ versus $\ln(C_e)$ (Figure 6.6a-e). The measured data are summarized in Table 6.2.

It is clear from Table 6.1 that the Freundlich model sufficiently describes the C:HA adsorbent – fluoride interaction. The correlation coefficient obtained from the Freundlich fits were ~ 0.864 – 0.999. This suggests that the adsorption process was heterogeneous. In contrast, the data were not well described by the Langmuir isotherm (results not published). Hence, heterogeneous nature of our adsorbent, violates the fundamental assumption of the Langmuir isotherm that all the adsorption sites have equal affinities for molecules of the adsorbate.

6.3.5 Change in Free Energy

The change in free energy of the C-HA adsorbent – fluoride system was obtained from the following expression:

$$\Delta G = -RT\ lnK_o \qquad (4)$$

where ΔG (kJ/mol) is the change in free energy, R (8.314J/mol-K) is the universal gas constant, T (Kelvin) is the absolute temperature and $K_o$is the thermodynamic distribution coefficient for the adsorption process. The latter is determined from the intercept of the plot of $\ln(q_e/C_e)$ against C_e (Khan & Singh, 1987). With the exception of adsorbent C:HA = 100:0 sintered at 900°C, negative values of free energy were obtained for all the adsorbent type (Table 6.1). This implies a spontaneous nature of the process. This degree of spontaneity increases as the sintering temperature of the C-HA = 0:100 adsorbent decreases. However, there was no clear trend in the dependence of free energy on sintering temperature for all other adsorbent types.

6.3.6 Adsorption Kinetics

The amount of fluoride adsorbed with time for two adsorbents (C-HA = 0:100 and C-HA = 75:25) is presented in Figure 6.7(a). To understand the adsorption kinetics of the adsorbent, the following two diffusion-based models were explored:

$$\ln(1-\alpha) = -k_p t \quad (5)$$

and

$$q_t = k_d t^{0.5} \quad (6)$$

where, α is the fractional attainment of equilibrium, i.e, the ratio of the amount of fluoride ion removed from water at any given time, *t* (min), to that removed from water at equilibrium; q_t is the amount of fluoride adsorbed at any given time, k_p (min^{-1}) is particle rate constant and k_d (mg/g $min^{½}$) is the intra particle rate constant. Equation 5 was developed by Chanda *et al.* (Chanda *et al.*, 1983) for particle diffusion-controlled adsorption processes, while equation 6, developed by Weber and Morris (Weber & Morris, 1964), is the widely applied intraparticle diffusion equation (Ho *et al.*, 2000). Both equations have been applied to the adsorption kinetics data (Figure 6.7(b) and 6.7(c)) obtained from this study.

The fits to the above two models are summarized in Table 6.3. The intraparticle diffusion model provided a better fit. This means that the adsorption process is not only a surface phenomenon, but also a rate-limiting process in the micro- and nano- porous structure. Furthermore, Figure 6.7(c) suggests that the adsorption process occurs in three major stages. The first stage involves bulk diffusion of fluoride ion to the surface of the adsorbent, while the second stage involves intraparticle or pore diffusion processes that lead ultimately to the third stage, the equilibrium

adsorption stage. Similar trends have been observed by other researchers (Chen *et al.*, 2010; Meenakshi *et al.*, 2008). It is important to note the slope of the second stage yields the intraparticle rate constant, k_d .

6.3.7 Frustum-Shaped C-HA Filter

The fluoride and bacteria removal efficacy of the frustum-shaped C-HA based filter was evaluated, as described in section 2.4. Figures 6.8 (a) and 6.8(b) show the amount of fluoride removed with cumulative volume of water. The results are summarized in Table 6.4. Studies have shown that the more HA in the matrix of the C-HA filter, the less porous the entire structure is (Friedman, 2010). Hence, the frustum shaped "C-HA=75:25" is more porous (and more permeable) than the "C-HA=80:20" filter. This implies that it will take a longer time for the water to flow through the "C-HA=80:20" filter. The increased contact time is therefore the key reason why the "C-HA = 80:20" removed more fluoride from water with a low concentration of fluoride, C_o = 2.5 mg/L [Figure 6.8(a)].

The rate of fluoride removal was fairly constant over time [Figure 6.8(a)]. The hump observed in Figure 6.8(a) is attributed to nature of the frustum shape of the filter. Since the thickness of the sides of the filter (~10mm) is much smaller the thickness of the base of the filter (~15mm), the water seeps more quickly through the sides. However, after a while, some sort of equilibrium is reached. At higher fluoride concentrations, the "C-HA = 75:25" was the better filter (Figure 6.8(b)). The reason is because at low concentrations of fluoride, adsorption of the fluorine ion to HA to form fluoroapaptite, and the F^-/OH^- ion exchange process, are the dominant process. However, at higher fluoride concentrations, an abrupt increase in fluoride uptake is observed due

to the formation calcium fluoride (Lin *et al.*, 1981). Therefore, for high concentrations of fluoride, the higher the HA content in the filter, the better.

The concentration of fluoride is also seen to increase linearly with the cumulative volume of water collected [Figure 6.8(b)]. The optimum filter would have to be the one with a high HA content and reduced porosity. The pH of the water also increased from ~ 6 to ~ 12 (Table 6.3). This is largely due to the F^-/OH^- ion exchange process which results in the presence of excess OH^- ions in the filtrate. This is also the reason why the higher the HA content, the higher the final pH. Finally, the fact that the final pH of the solution is lower, for the higher concentration of fluoride, also lends credence to the formation of calcium fluoride at high concentrations of fluoride.

Despite the high CFU/mL of *E.coli* in the pre-filtrate (Table 6.3), no *E.coli* was present in the filtrate. One explanation is that all of the bacteria might have been trapped (and possibly killed) inside the pores of the C-HA filter. Another explanation for the absence of the bacteria in the pre-filtrate can be linked to the pH of the solution (Table 6.3). Even if some of the bacteria do manage to make it through the filter, the pH of the filtrate may have resulted in their death. More work needs to be done to ascertain the true mechanism of filtration of *E.coli* bacteria, using the C-HA filter.

6.3.8 Implications

The implications of the current work are quite significant. There are three main types of contaminants in water. These are: radiological, chemical and biological contaminants. Although drinking water may contain radioactive substances that could present a risk to human health,

except in extreme circumstances, those risks are small, compared to the risks from chemicals and microbes that may be present in the water (WHO, 2011). This chapter has shown that both chemically and microbiologically contaminated water can be purified by creating a heterogeneous adsorbent using the simple process of co-sintering (in this case, the sintering of a matrix material (clay) with a well-known defluoridating material (hydroxyapaptite)). This is one great leap towards making a "universal water filter", that is cheap, locally producible, re-useable, sustainable and eco-friendly.

This work shows that the adsorption capacity of C-HA adsorbent depends on the concentration of fluoride, the sintering temperature, the HA content and the contact time. Furthermore, the proof-of-concept study suggests that porosity, initial fluoride concentration and contact time are important factors in the design of future point-of-use type fluoride/bacteria removal filters. The author of this chapter would like to stress that the C-HA filter is not ready to be used in the field. One drawback of the C-HA filter is that it increases the pH of water. Such water should be tested for the potential (short and long term) effects on human health, if any. The rise in the pH of water is mainly due to the hydroxyl ions of the hydroxyapatite. The control of the pH of the filtrate should be investigated. This may be done by running the contaminated water through C-HA filters connected in series. The filter may also by doped with materials capable of adsorbing hydroxyl ions. Juices of some citrus fruits, such as lime, may also be used to control the pH of the pre-filtrate and filtrate. The efficacy of the C-HA filter over a long period of time ($\geq$ 2 years) should also be studied.

6.4 Conclusions

The “HA only” adsorbent exhibits a strong dependence on sintering temperature, while the other types of adsorbent exhibit a weak temperature dependence. The adsorption capacity of the adsorbent increases with increasing fluoride concentration and HA content. The Freundlich isotherm model provides a good fit to the experimental data obtained for the C-HA adsorbent. The adsorption process is also spontaneous. Furthermore, the adsorption of fluorine ion onto the C-HA surfaces follows the intraparticle (pore) diffusion model. The proof-of-concept study of a frustum-shaped C-HA based filter suggests that the filter may be considered as a point-of-use water purification technique for the removal of fluoride and microbial pathogens such as *E.coli*.

References

Abe, I., Iwasaki, S., Tokimoto, T., Kawasaki, N., Nakamura, T., & Tanada, S. (2004). Adsorption of fluoride ions onto carbonaceous materials. *Journal of Colloid and Interface Science, 275*(1), 35-39.

Agarwal, M., Rai, K., Shrivastav, R., & Dass, S. (2002). A study on fluoride sorption by montmorillonite and kaolinite. *Water Air and Soil Pollution, 141*(1-4), 247-261.

Akpata, E. S., Fakiha, Z., & Khan, N. (1997). Dental fluorosis in 12-15-year-old rural children exposed to fluorides from well drinking water in the Hail region of Saudi Arabia. *Community Dent Oral Epidemiol, 25*(4), 324-327.

al-Khateeb, T. L., al-Marsafi, A. I., & O'Mullane, D. M. (1991). Caries prevalence and treatment need amongst children in an Arabian community. *Community Dent Oral Epidemiol, 19*(5), 277-280.

Alagumuthu, G., & Rajan, M. (2010). Equilibrium and kinetics of adsorption of fluoride onto zirconium impregnated cashew nut shell carbon. *Chemical Engineering Journal, 158*(3), 451-457.

Ayoob, S., & Gupta, A. K. (2009). Performance evaluation of alumina cement granules in removing fluoride from natural and synthetic waters. *Chemical Engineering Journal, 150*(2-3), 485-491.

Bower, C. A., & Hatcher, J. T. (1967). Adsorption of Fluoride by Soils and Minerals. *Soil Science, 103*(3), 151.

Brunson, L. R., & Sabatini, D. A. (2009). An Evaluation of Fish Bone Char as an Appropriate Arsenic and Fluoride Removal Technology for Emerging Regions. *Environmental Engineering Science, 26*(12), 1777-1784.

Chanda, M., Odriscoll, K., & Rempel, G. (1983). Sorption of phenolics onto cross-linked poly(4-vinyl pyridine). *Reactive Polymers, Ion Exchangers, Sorbents, 1*(4), 281-293.

Chaturvedi, A. K., Pathak, K. C., & Singh, V. N. (1988). Fluoride removal from water by adsorption on china clay. *Applied Clay Science, 3*(4), 337-346.

Chen, N., Zhang, Z. Y., Feng, C. P., Sugiura, N., Li, M., & Chen, R. Z. (2010). Fluoride removal from water by granular ceramic adsorption. *Journal of Colloid and Interface Science, 348*(2), 579-584.

Chubar, N., Samanidou, V., Kouts, V., Gallios, G., Kanibolotsky, V., Strelko, V., & Zhuravlev, I. (2005). Adsorption of fluoride, chloride, bromide, and bromate ions on a novel ion exchanger. *Journal of Colloid and Interface Science, 291*(1), 67-74.

Díaz-Nava, C., Olguín, M. T., & Solache-Ríos, M. (2002). Water Defluoridation by Mexican Heulandite–Clinoptilolite. *Separation Science and Technology, 37*(13), 3109-3128.

Fan, X. (2003). Adsorption kinetics of fluoride on low cost materials. *Water Research, 37*(20), 4929-4937.

Friedman, K. C. (2010). *Design and Characterization of Hydroxyapatite-Clay Filters for Water Purification.* Bachelor of Science in Engineering Princeton University, Princeton, NJ.

FRRDF. (1999). *State of Art Report on the Extent of Fluoride in Drinking Water and the Resulting Endemicity in India.* Fluorosis Research and Rural Development Foundation, New Delhi.

Hauge, S., Osterberg, R., Bjorvatn, K., & Selvig, K. A. (1994). Defluoridation of Drinking-Water with Pottery - Effect of Firing Temperature. *Scandinavian Journal of Dental Research, 102*(6), 329-333.

Ho, Y. S., Ng, J. C. Y., & McKay, G. (2000). Kinetics of Pollutant Sorption by Biosorbents: Review. *Separation & Purification Reviews, 29*(2), 189-232.

Inyang, H. I. (2004). Geochemical and Health Policy Dimensions of the Controversy about Fluorides in Water Resources. *Journal of Environmental Engineering, 130*(2), 113.

Jha, V. K., Matsuda, M., & Miyake, M. (2008). Sorption properties of the activated carbon-zeolite composite prepared from coal fly ash for Ni2+, Cu2+, Cd2+ and Pb2+. *Journal of Hazardous Materials, 160*(1), 148-153.

Kaseva, M. E. (2006). Optimization of regenerated bone char for fluoride removal in drinking water: a case study in Tanzania. *J Water Health, 4*(1), 139-147.

Khan, A. A., & Singh, R. P. (1987). Adsorption Thermodynamics of Carbofuran on Sn(Iv) Arsenosilicate in H+, Na+ and Ca-2+ Forms. *Colloids and Surfaces, 24*(1), 33-42.

Koumoulidis, G. C., Trapalis, C. C., & Vaimakis, T. C. (2006). Sintering of hydroxyapatite lath-like powders. *Journal of Thermal Analysis and Calorimetry, 84*(1), 165-174.

Latham, M. C., & Grech, P. (1967). Effects of Excessive Fluoride Intake. *American Journal of Public Health and the Nations Health, 57*(4), 651-&.

Li, Y.-H., Wang, S., Cao, A., Zhao, D., Zhang, X., Xu, C., Luan, Z., Ruan, D., Liang, J., et al. (2001). Adsorption of fluoride from water by amorphous alumina supported on carbon nanotubes. *Chemical Physics Letters, 350*(5-6), 412-416.

Li, Y. H., Wang, S., Zhang, X., Wei, J., Xu, C., Luan, Z., Wu, D., & Wei, B. (2003). Removal of fluoride from water by carbon nanotube supported alumina. *Environmental Technology, 24*(3), 391-398.

Lin, J., Raghavan, S., & Fuerstenau, D. W. (1981). The Adsorption of Fluoride Ions by Hydroxyapatite from Aqueous-Solution. *Colloids and Surfaces, 3*(4), 357-370.

Mandinic, Z., Curcic, M., Antonijevic, B., Carevic, M., Mandic, J., Djukic-Cosic, D., & Lekic, C. P. (2010). Fluoride in drinking water and dental fluorosis. *Science of The Total Environment, 408*(17), 3507-3512.

Maritan, L., Nodari, L., Mazzoli, C., Milano, A., & Russo, U. (2006). Influence of firing conditions on ceramic products: Experimental study on clay rich in organic matter. *Applied Clay Science, 31*(1-2), 1-15.

McCaffrey, L. P., & Willis, J. P. (1997). *Distribution and origin of fluoride in rural drinking water supplies in the Western Bushveld Areas of South Africa*. 4th International Symposium on Environmental Geochemistry

Medellin-Castillo, N. A., Leyva-Ramos, R., Ocampo-Perez, R., Garcia de la Cruz, R. F., Aragon-Piña, A., Martinez-Rosales, J. M., Guerrero-Coronado, R. M., & Fuentes-Rubio, L. (2007). Adsorption of Fluoride from Water Solution on Bone Char. *Industrial & Engineering Chemistry Research, 46*(26), 9205-9212.

Meenakshi, S., Sundaram, C. S., & Sukumar, R. (2008). Enhanced fluoride sorption by mechanochemically activated kaolinites. *Journal of Hazardous Materials, 153*(1-2), 164-172.

Mlilo, T. B., Brunson, L. R., & Sabatini, D. A. (2010). Arsenic and Fluoride Removal Using Simple Materials. *Journal of Environmental Engineering-Asce, 136*(4), 391-398.

MRC. (2002). *Water fluoridation and health*. London: Medical Research Council Working Group Report.

Murray, J. J., International Dental Federation., World Health Organization., & W.K. Kellogg Foundation. (1986). *Appropriate use of fluorides for human health*. Geneva Albany, NY: World Health Organization ; WHO Publications Center USA distributor.

Mwaniki, D. L. (1992). Fluoride Sorption Characteristics of Different Grades of Bone Charcoal, Based on Batch Tests. *Journal of Dental Research, 71*(6), 1310-1315.

Nair, K. R., Manji, F., & Gitonga, J. N. (1984). The Occurrence and Distribution of Fluoride in Groundwaters of Kenya. *East African Medical Journal, 61*(7), 503-512.

NebGuide. (1998). *Drinking water: Fluoride*. Lincoln: Nebraska Cooperative Extension G98-1376-A.

Queste, A., Lacombe, M., Hellmeier, W., Hillermann, F., Bortulussi, B., Kaup, M., Ott, K., & Mathys, W. (2001). High concentrations of fluoride and boron in drinking water wells in the Muenster region--results of a preliminary investigation. *Int J Hyg Environ Health, 203*(3), 221-224.

Ramos, R. (1999). Adsorption of fluoride from aqueous solution on aluminum-impregnated carbon. *Carbon, 37*(4), 609-617.

Segreto, V. A., Collins, E. M., Camann, D., & Smith, C. T. (1984). A current study of mottled enamel in Texas. *J Am Dent Assoc, 108*(1), 56-59.

Srimurali, M., Pragathi, A., & Karthikeyan, J. (1998). A study on removal of fluorides from drinking water by adsorption onto low-cost materials. *Environmental Pollution, 99*(2), 285-289.

Sundaram, C. S., Viswanathan, N., & Meenakshi, S. (2008). Defluoridation chemistry of synthetic hydroxyapatite at nano scale: Equilibrium and kinetic studies. *Journal of Hazardous Materials, 155*(1-2), 206-215.

UNICEF. (1999). *State of the art report on the extent of fluoride in drinking water and the resulting endemicity in India*. New Delhi.

USEPA. (1996). *R.E.D. FACTS: Cryolite.* United States Environmental Protection Agency. Retrieved from http://www.epa.gov/oppsrrd1/REDs/factsheets/0087fact.pdf

Verwilghen, C., Rio, S., Nzihou, A., Gauthier, D., Flamant, G., & Sharrock, P. J. (2007). Preparation of high specific surface area hydroxyapatite for environmental applications. *Journal of Materials Science, 42*(15), 6062-6066.

Waldbott, G. L. (1973). *Health effects of environmental pollutants*. Saint Louis,: Mosby.

Wang, Y., & Reardon, E. J. (2001). Activation and regeneration of a soil sorbent for defluoridation of drinking water. *Applied Geochemistry, 16*(5), 531-539.

Weber, W. J., & Morris, J. C. (1964). Equilibria and capacities for adsorption on carbon. *J. Sanitary Eng. Div, 90*(SA3), 79-107.

WHO. (2011). *Guidelines for Drinking-Water Quality* (4 ed.). Geneva, Switzerland.

Wongdem, J. G., Aderinokun, G. A., Sridhar, M. K., & Selkur, S. (2000). Prevalence and distribution pattern of enamel fluorosis in Langtang town, Nigeria. *Afr J Med Med Sci, 29*(3-4), 243-246.

Yadav, S., Khan, T. I., Gupta, S., Gupta, A. B., & Yadava, R. N. (1999, 18-21st October). *Fluorosis in India with special reference to Rajasthan.* Proceedings of the International Conference on Water, Environment, Ecology, Socioeconomics and Health Engineering (WEESHE), Seoul National University.

Yakub, I., Plappally, A., Leftwich, M., Malatesta, K., Friedman, K. C., Obwoya, S., Nyongesa, F., Maiga, A. H., Soboyejo, A. B. O., et al. (submitted for publication). Porosity and Filtration Characteristics of Frustum-Shaped Ceramic Water Filters.

Clay-Hydroxyapatite (C-HA) Adsorbent					
Clay to HA ratio (by volume)*	100:0	90:10	80:20	75:25	0:100
Nomenclature	C-HA = 100:0 OR "Clay only" OR "No HA"	C-HA = 90:10	C-HA = 80:20	C-HA = 75:25	C-HA = 0:100 OR "HA only" OR "No Clay"

Table 6.1: Different types of adsorbent studied. *Sawdust was added to the matrix (i.e. Clay and HA) in a ratio of 2 to 1 by volume. The adsorbent was sintered at five different temperatures of 500°C, 600°C, 700°C, 800°C and 900°C.

Adsorbent Type	Sintering Temperature (°C)	Freundlich isotherm parameters			ΔG (kJ/mol)
		K_f	1/n	R^2	
C-HA = 0:100	500	0.714	0.523	0.982	-4.360
	600	0.657	0.524	0.987	-4.308
	700	0.235	0.746	0.993	-3.935
	800	0.219	0.742	0.956	-3.887
	900	0.072	0.977	0.957	-3.507
C-HA = 75:25	500	0.027	1.130	0.934	-3.156
	600	0.032	1.103	0.983	-3.222
	700	0.008	1.500	0.906	-2.808
	800	0.012	1.398	0.972	-2.927
	900	0.011	1.398	0.962	-2.893
C-HA = 80:20	500	0.008	1.500	0.906	-3.297
	600	0.030	1.120	0.937	-3.197
	700	0.010	1.375	0.969	-2.842
	800	0.009	1.439	0.939	-2.894
	900	0.007	1.482	0.971	-2.779
C-HA = 90:10	500	0.005	1.603	0.988	-2.517
	600	0.010	1.398	0.995	-2.773
	700	0.002	1.823	0.993	-2.122
	800	0.003	1.637	0.999	-2.376
	900	0.004	1.555	0.97	-2.358
C-HA = 100:0	500	0.006	1.404	0.911	-2.387
	600	0.003	1.542	0.864	-1.959
	700	0.001	1.870	0.941	-1.495
	800	0.002	1.723	0.96	-1.750
	900	0.000	2.853	0.931	0.399

Table 6.2: The Freundlich Isotherm parameters and Gibbs free energy obtained for all adsorbent type.

Adsorbent Type	$k_p \times 10^3$	R^2	$k_d \times 10^3$	R^2
C-HA = 0:100	11.1	0.846	153.5	0.915
C-HA = 75:25	28.5	0.958	242.0	0.989

Table 6.3: Particle- and intra – particle rate constant for two adsorbents (C-HA = 0:100 and C-HA = 75:25)

Clay to HA Ratio	**Pre-filtrate concentration of E.coli (CFU/mL) x 10^6**	**Initial Fluoride Concentration, C_o (mg/L)**	**Final Fluoride Concentration,* C_f (mg/L)**	**Initial pH**	**Final pH***
75:25	2.207± 0.007	2.5	0.265 ± 0.043	6.332 ± 0.009	12.443 ± 0.127
		20	2.026 ± 1.144		11.493 ± 0.544
80:20	2.175 ± 0.050	2.5	0.157 ± 0.015		12.199 ± 0.083
		20	2.333 ± 1.150		11.053 ± 0.531

Table 6.4: Proof-of-concept results using frustum-shaped C-HA filter. *Averaged over a cumulative volume of ~500mL

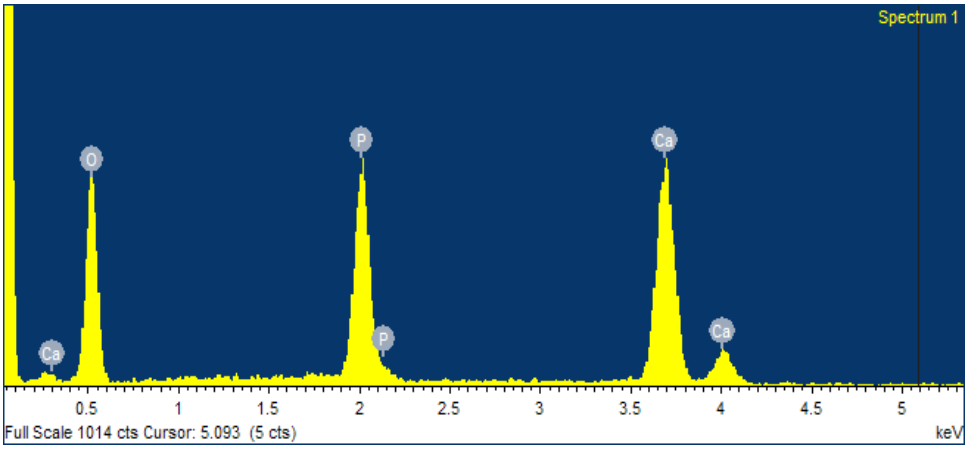

Figure 6.1(a): HA after making (before mixing or sintering)

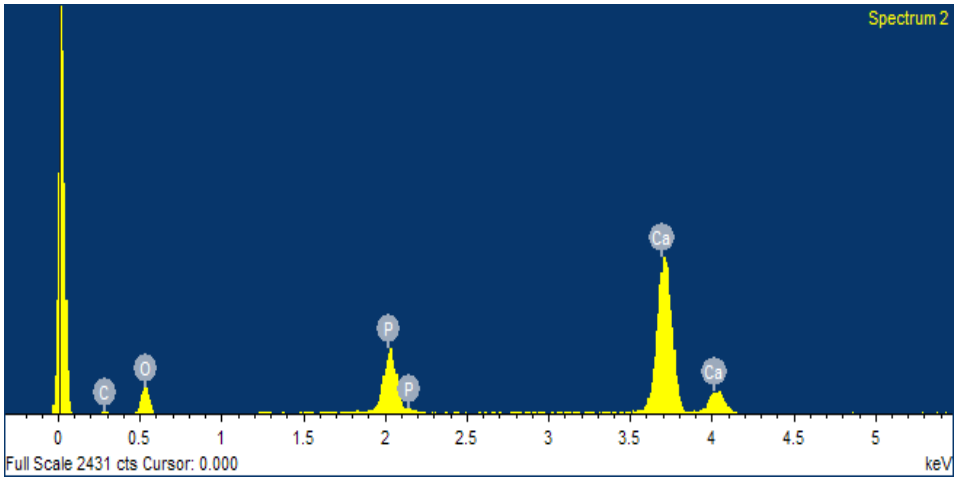

Figure 6.1(b): C-HA = 0:100 (HA only) sintered at 500°C

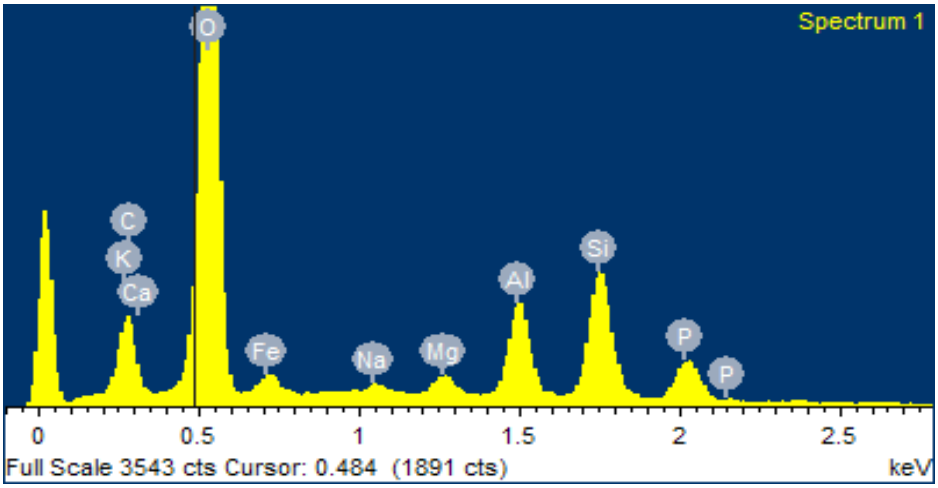

Figure 6.1(c): C-HA = 75:25 sintered at 500°C

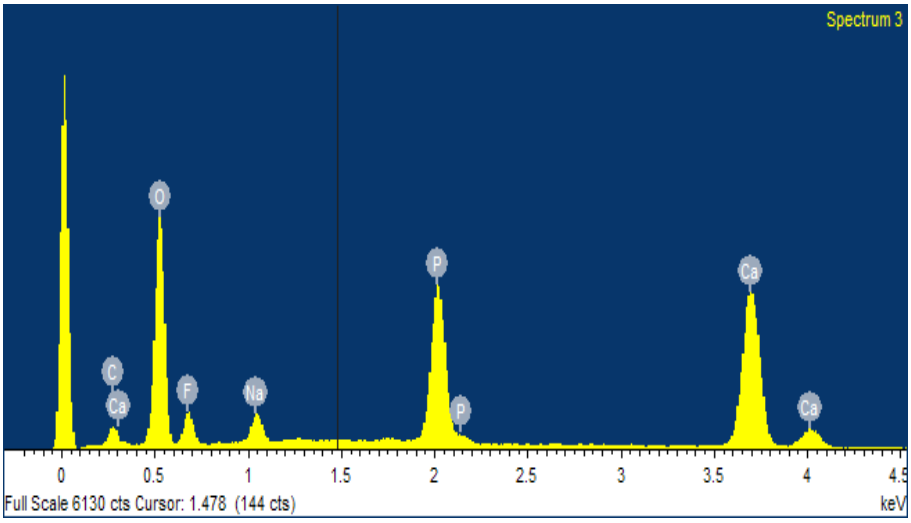

Figure 6.1(d): EDX of C-HA adsorbent after adsorption test, in this case C-HA = 0:100

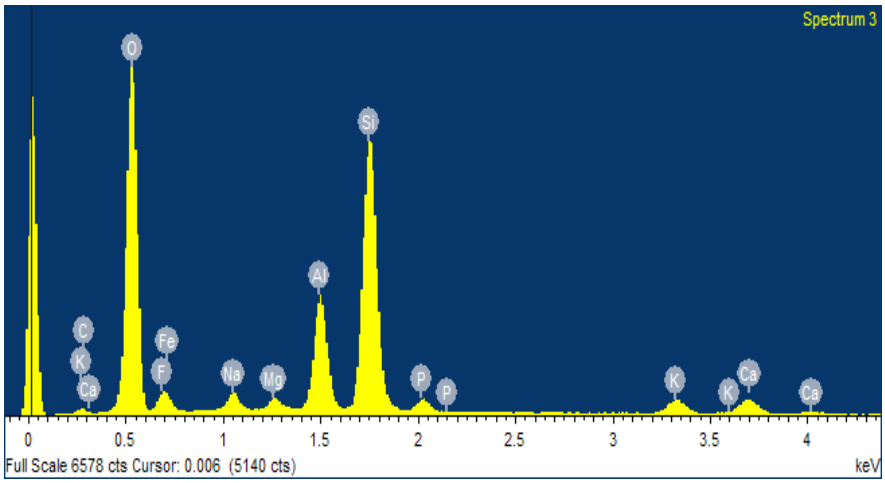

Figure 6.1(e): EDX of C-HA adsorbent after adsorption test, in this case C-HA = 75:25

Figure 6.1: EDX analysis of C-HA adsorbent

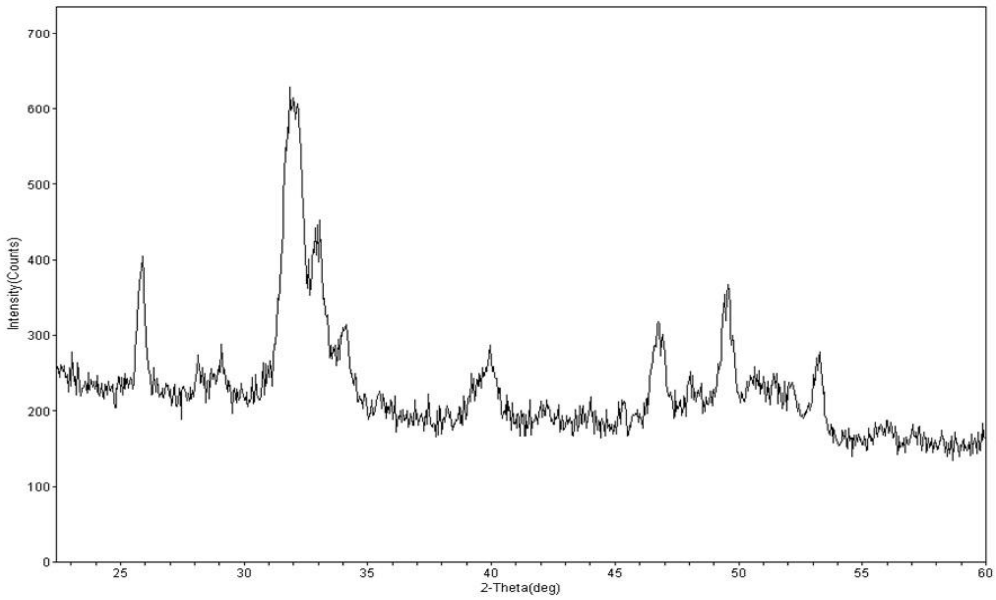

Figure 6.2(a): XRD of HA used to make the adsorbents

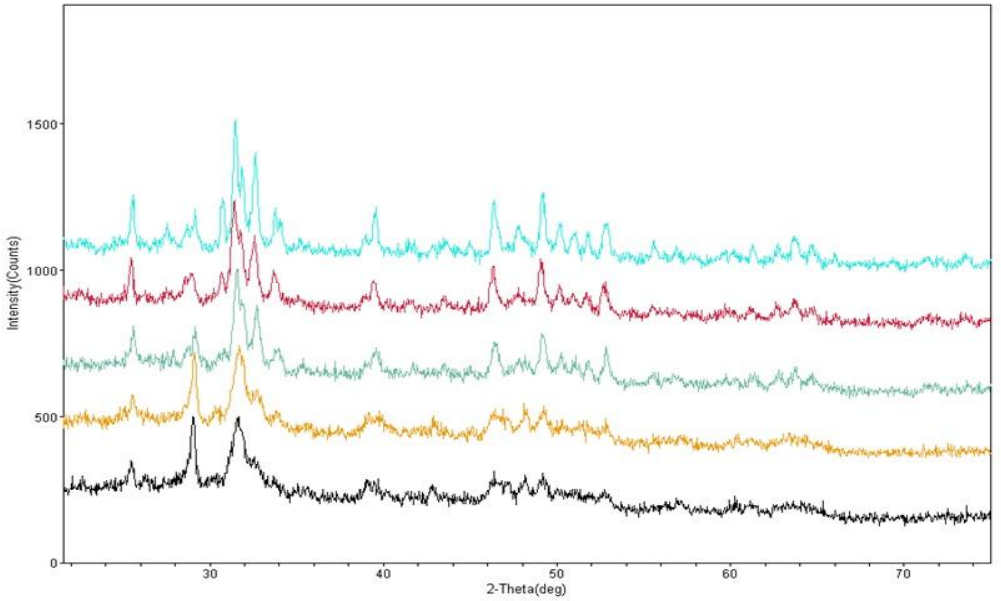

Figure 6.2(b): C–HA = 0:100 (HA only) sintered at 500°C, 600°C, 700°C, 800°C and 900°C (from bottom to top).

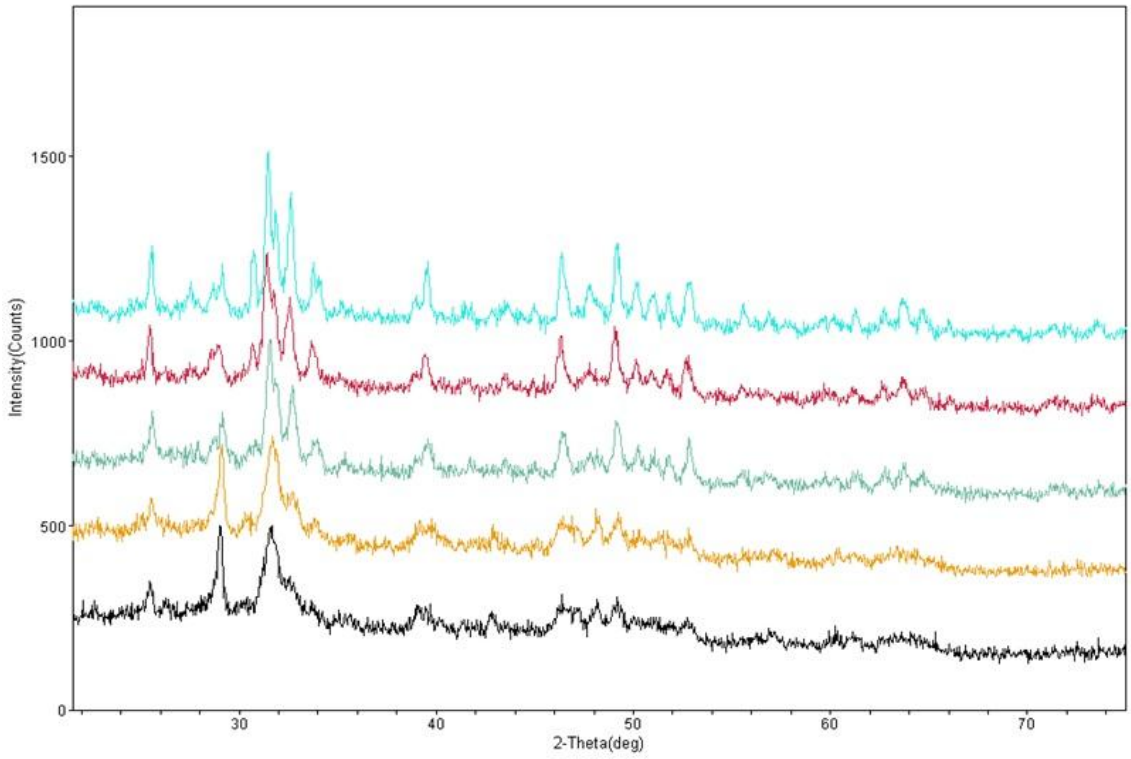

Figure 2(c): XRD pattern for C-HA adsorbent (in this case C–HA = 75-25) sintered at 500oC, 600oC, 700oC, 800oC and 900oC (from bottom to top). Similar pattern was observed for other adsorbent containing clay (results not published). The peaks of the HA structure (co-sintered with clay) cannot be identified because of their low/short intensities relative to the peaks of redart clay structure.

Figure 6.2: XRD analysis of C-HA adsorbent

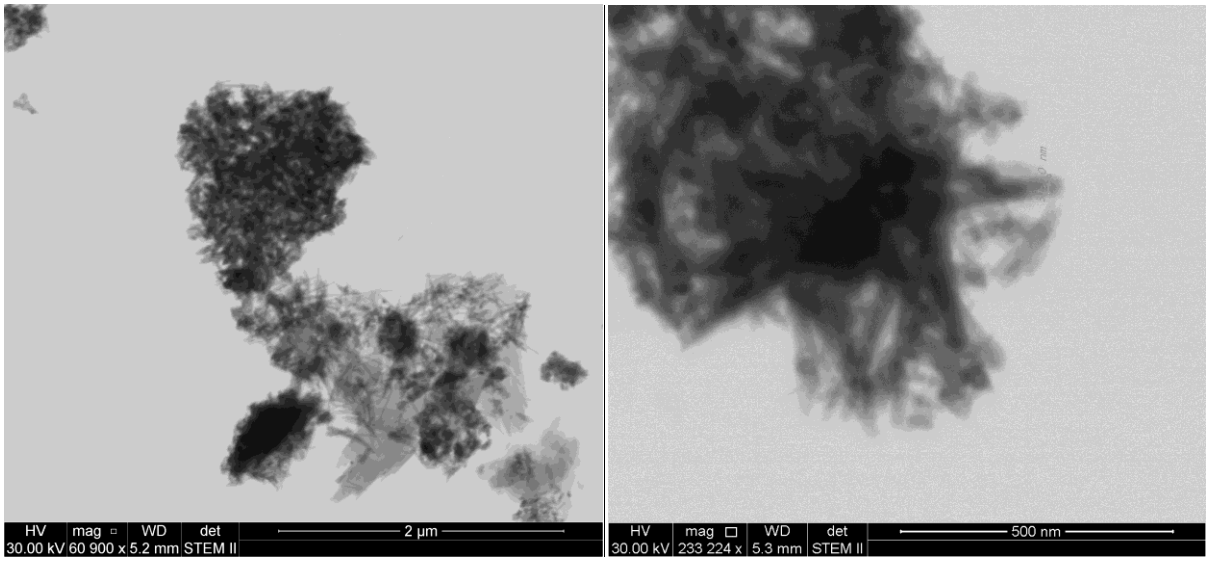

Figure 3(a): STEM image of HA used in making the adsorbent

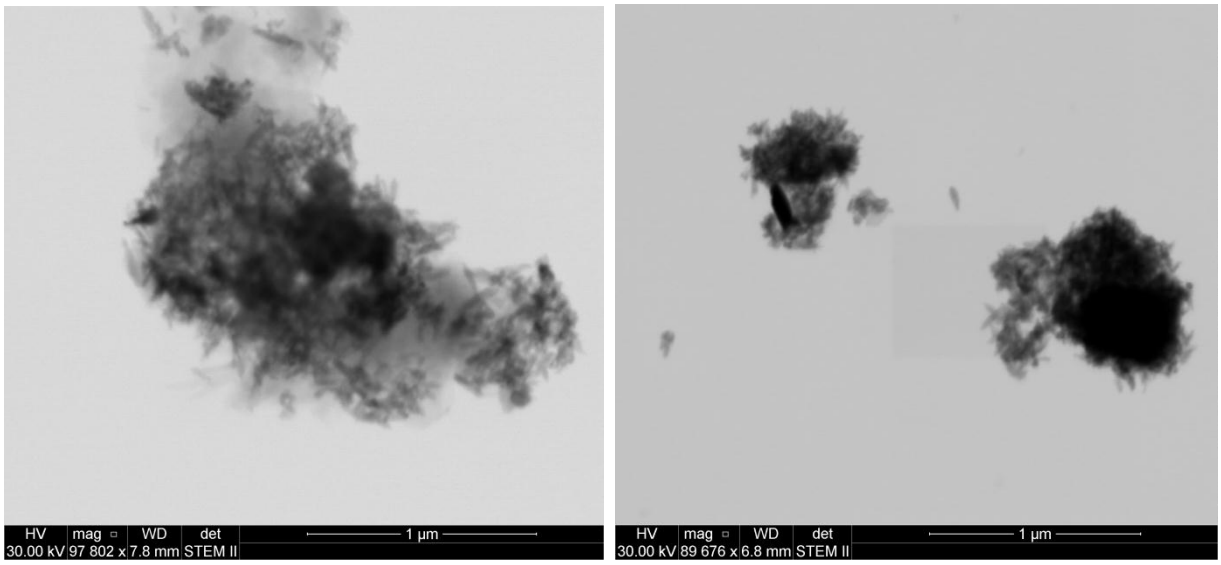

Figure 3(b): STEM image of C-HA = 0:100

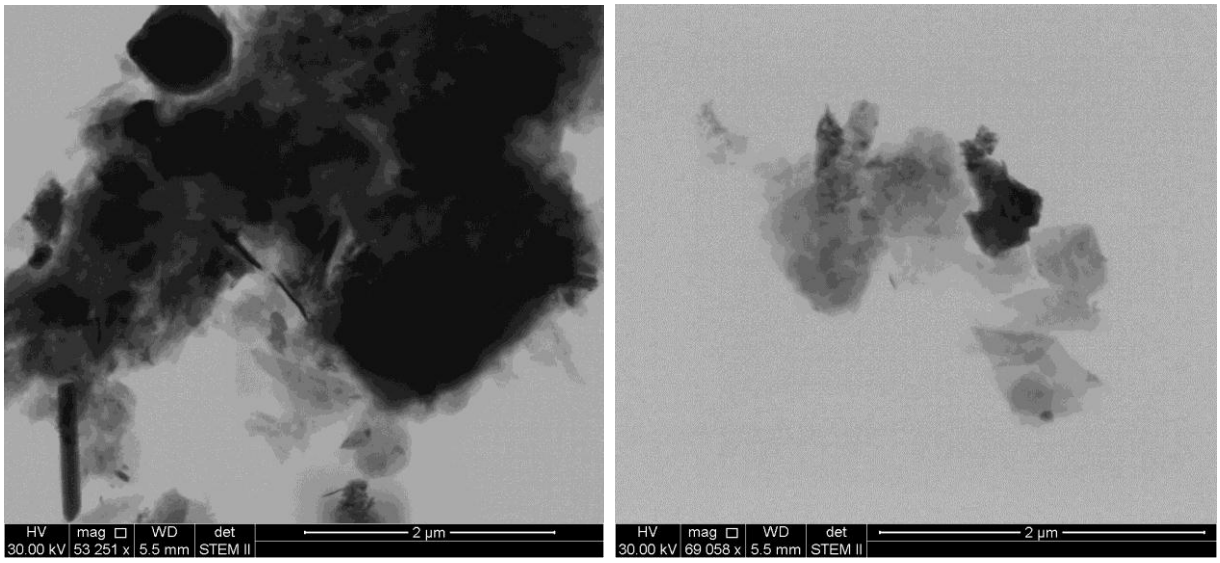

Figure 6.3(c): STEM image of C-HA = 75:25

Figure 6.3: STEM image of the HA used in making the C-HA adsorbents, the C-HA = 0:100 adsorbent and the C-HA = 75:25 adsorbent

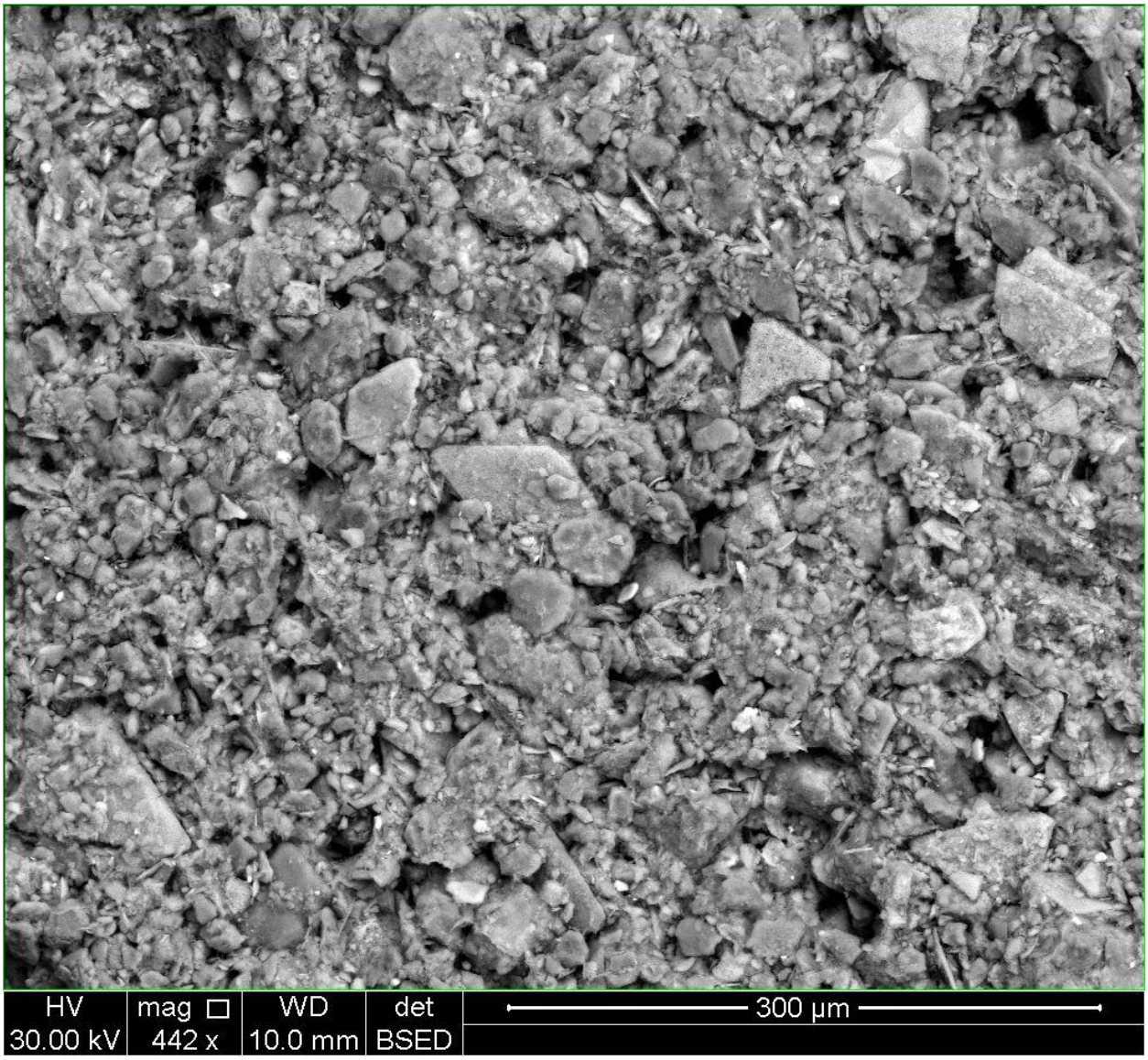

Figure 6.4: Backscattered electron (BSE) image of the C-HA adsorbent in this case C-HA = 75:25

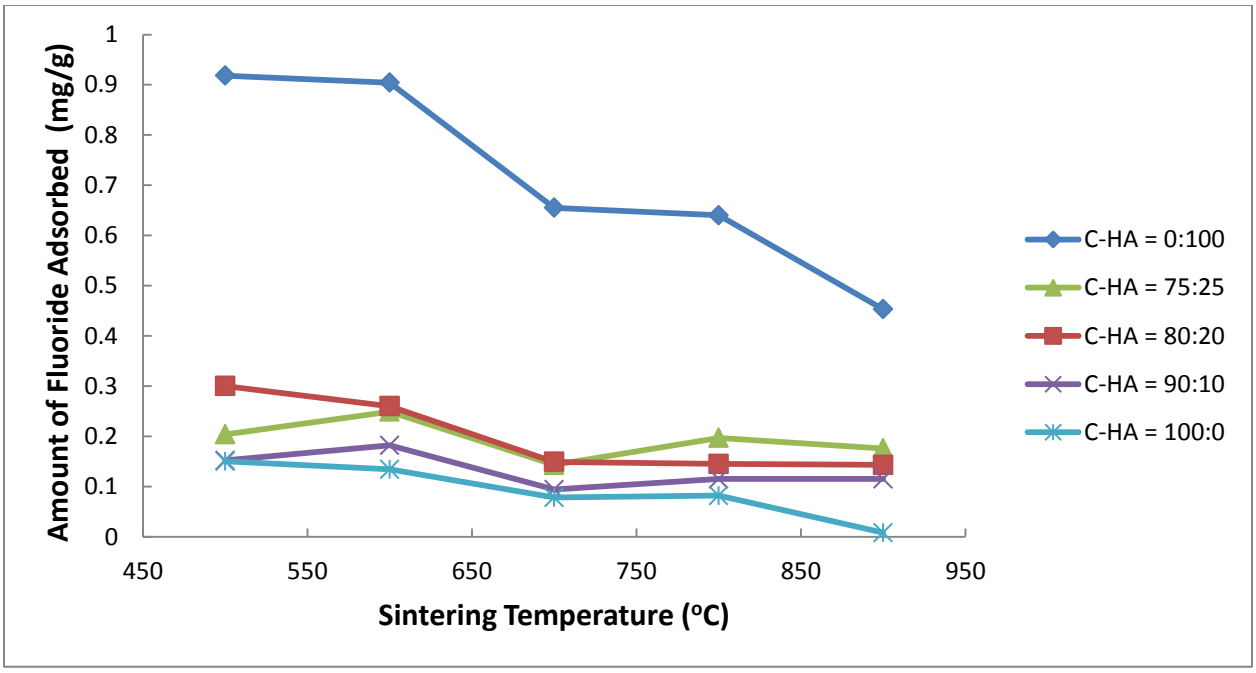

Figure 6.5(a): Effect of sintering temperature of the adsorbent on the amount of fluoride that is adsorbed from water with an initial fluoride level of 10mg/L

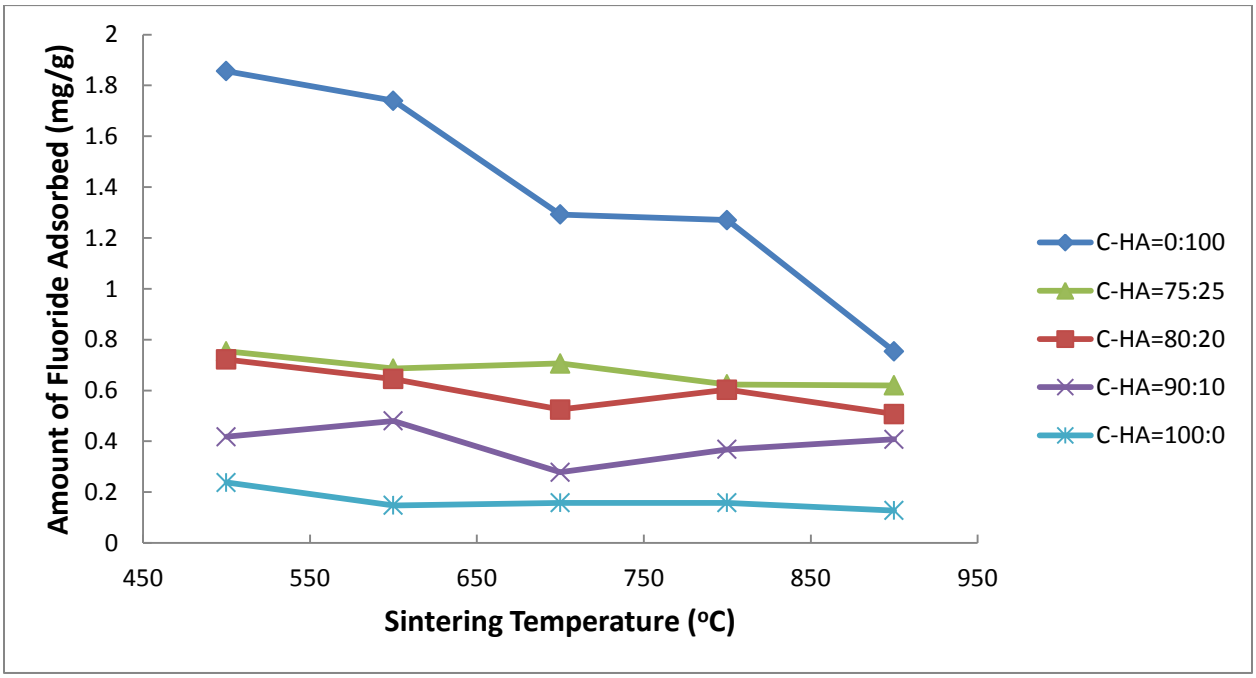

Figure 6.5(b): Effect of sintering temperature of the adsorbent on the amount of fluoride that is adsorbed from water with at an initial fluoride level of 20mg/L

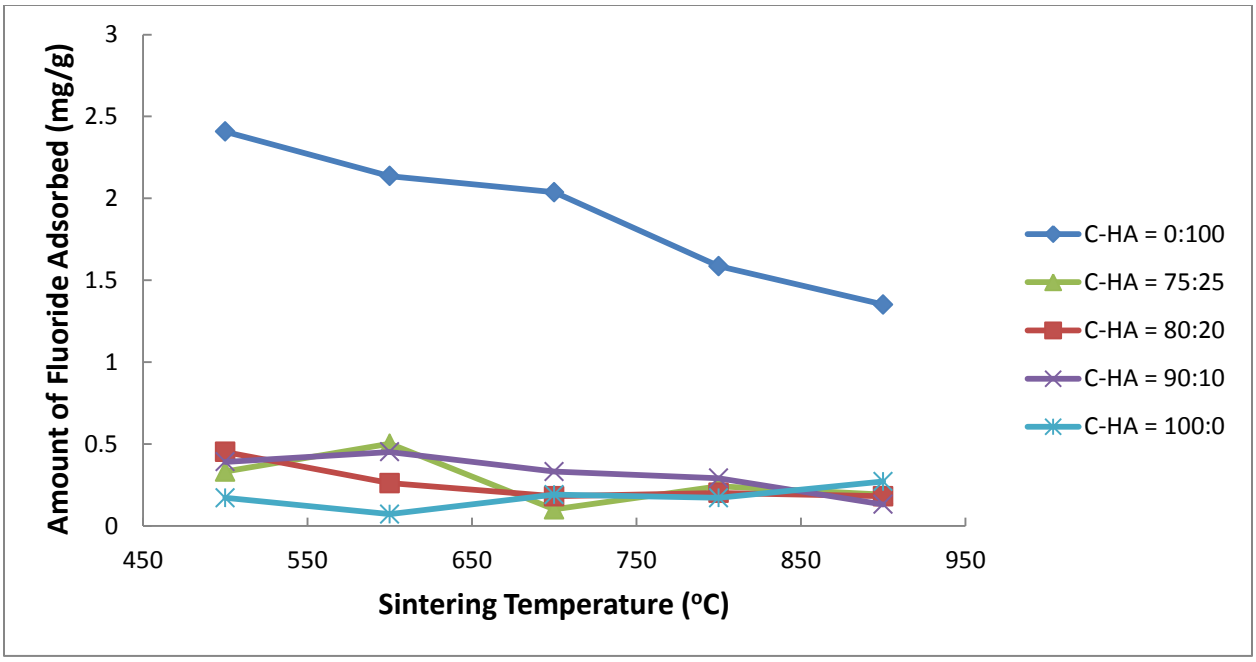

Figure 6.5(c): Effect of sintering temperature of the adsorbent on the amount of fluoride that is adsorbed from water with at an initial fluoride level of 30mg/L

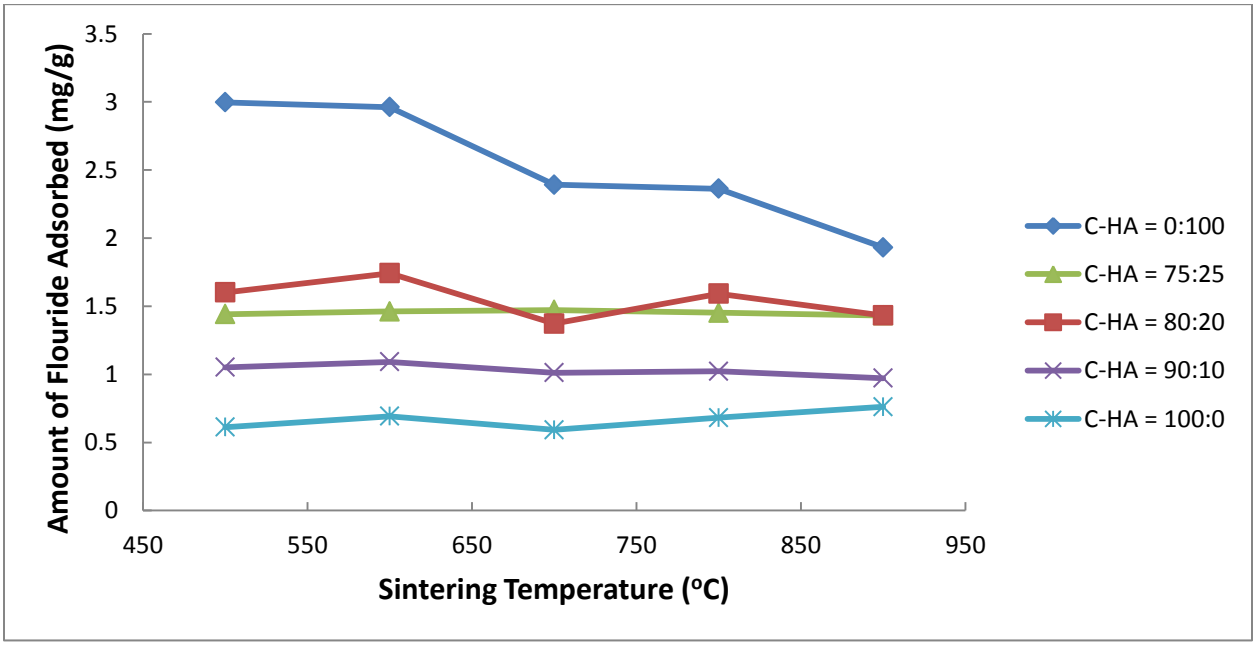

Figure 6.5(d): Effect of sintering temperature of the adsorbent on the amount of fluoride that is adsorbed from water with at an initial fluoride level of 40mg/L

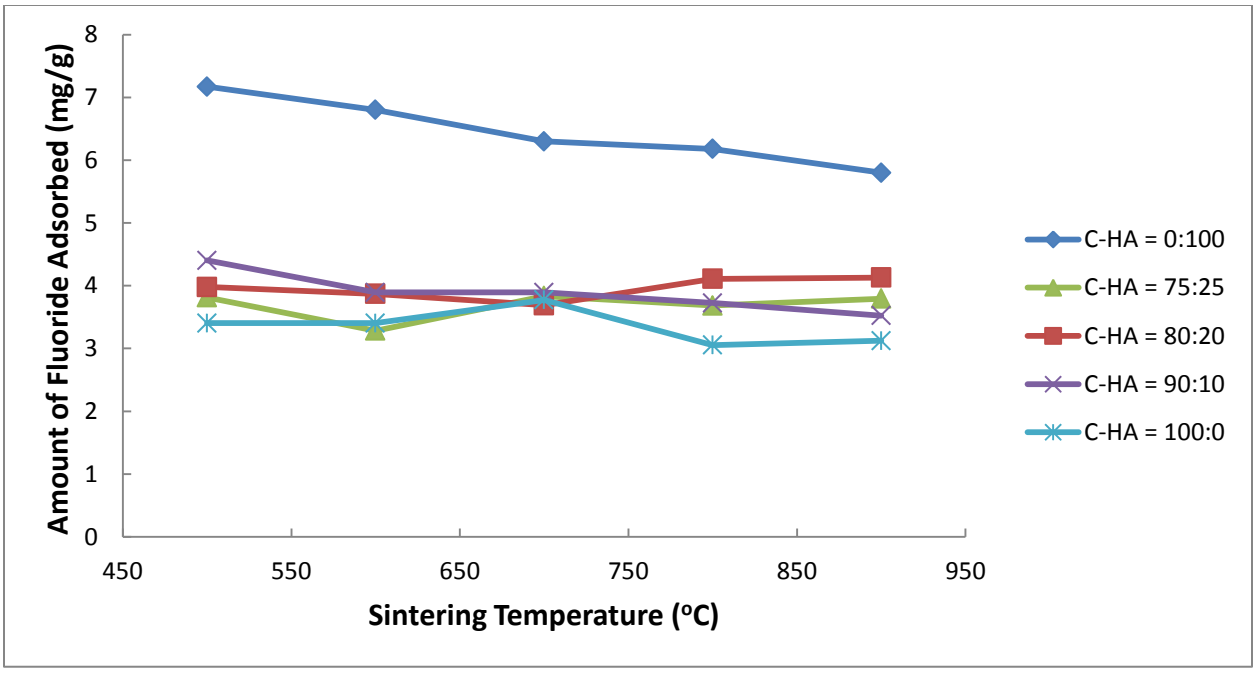

Figure 6.5(e): Effect of sintering temperature of the adsorbent on the amount of fluoride that is adsorbed from water with at an initial fluoride level of 100mg/L

Figure 6.5: Effect of sintering temperature of the adsorbent on the amount of fluoride that is adsorbed from water with at an initial fluoride level of: (a) 10mg/L; (b) 20mg/L; (c) 30mg/L; (d) 40mg/L and (e) 100mg/L

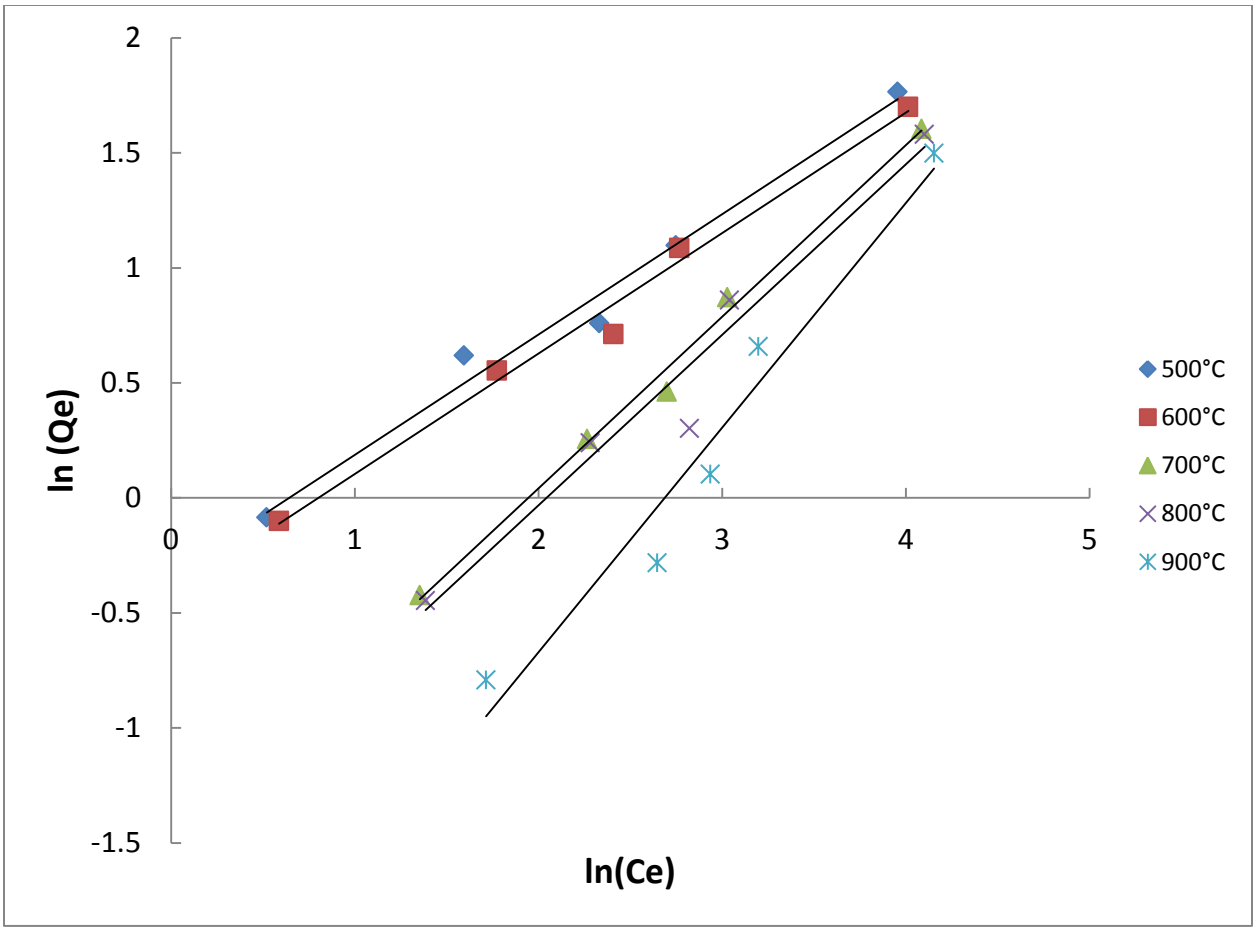

Figure 6.6(a): Freundlich Isotherm for C-HA = 0:100

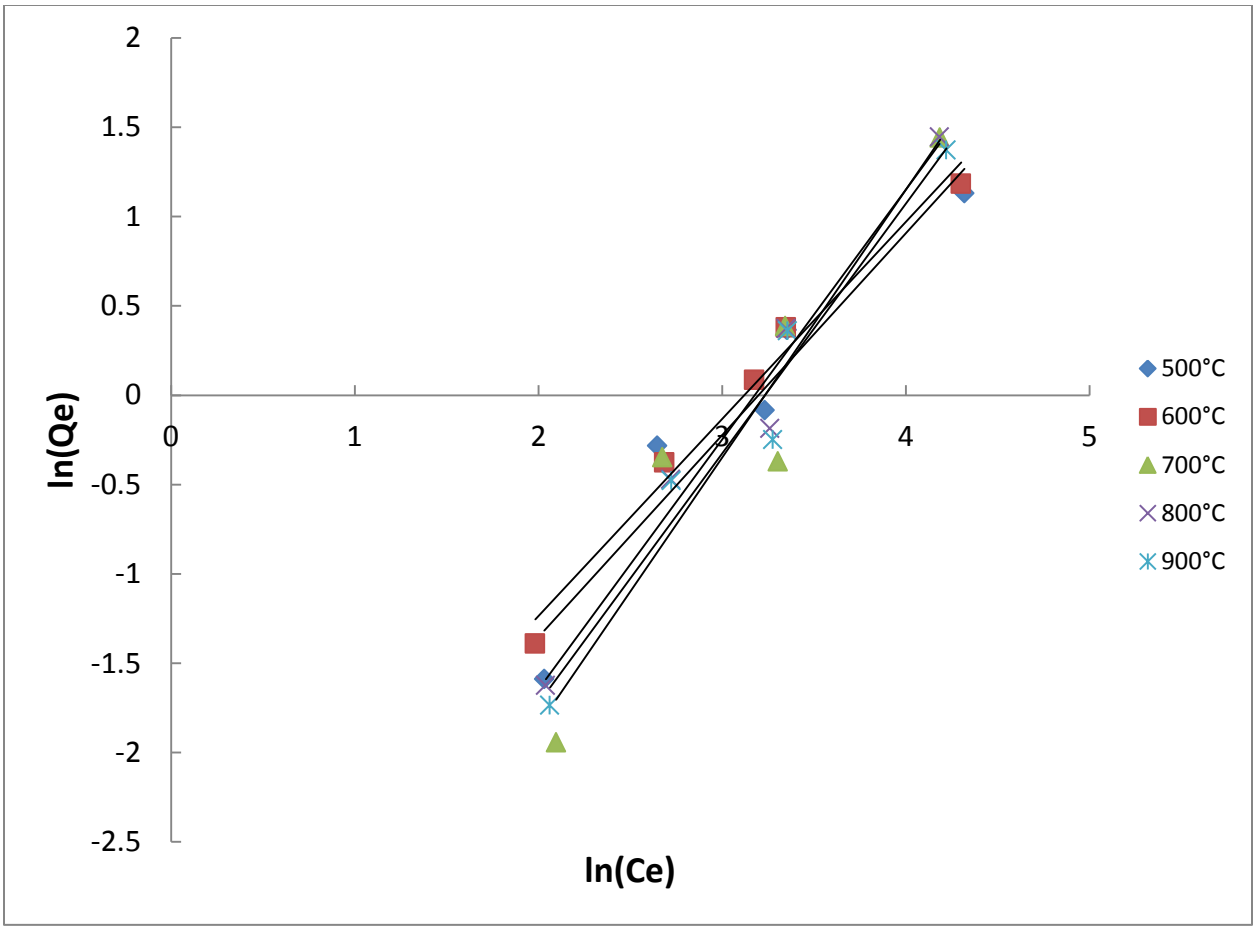

Figure 6.6(b): Freundlich Isotherm for C-HA = 75:25

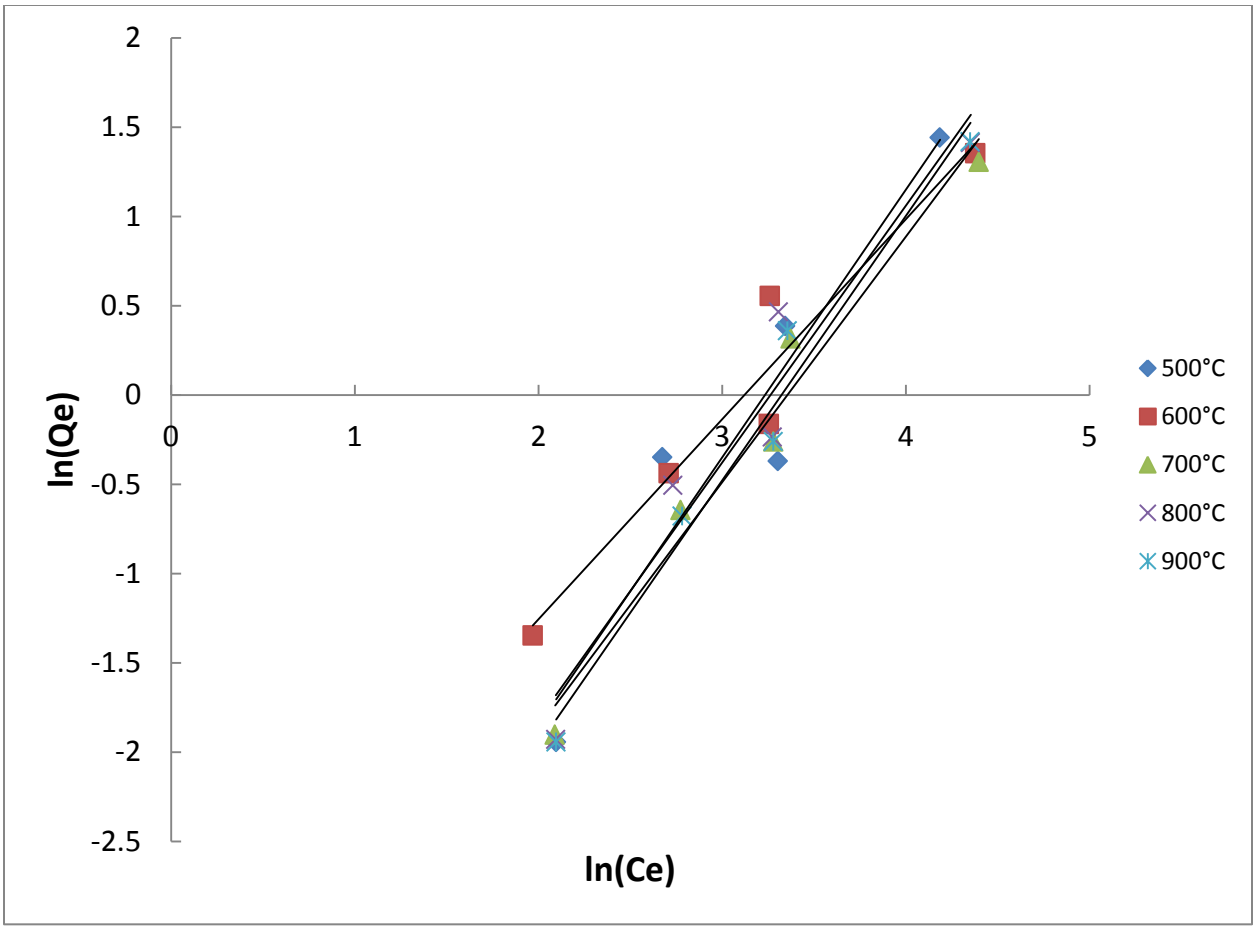

Figure 6.6(c): Freundlich Isotherm for C-HA = 80:20

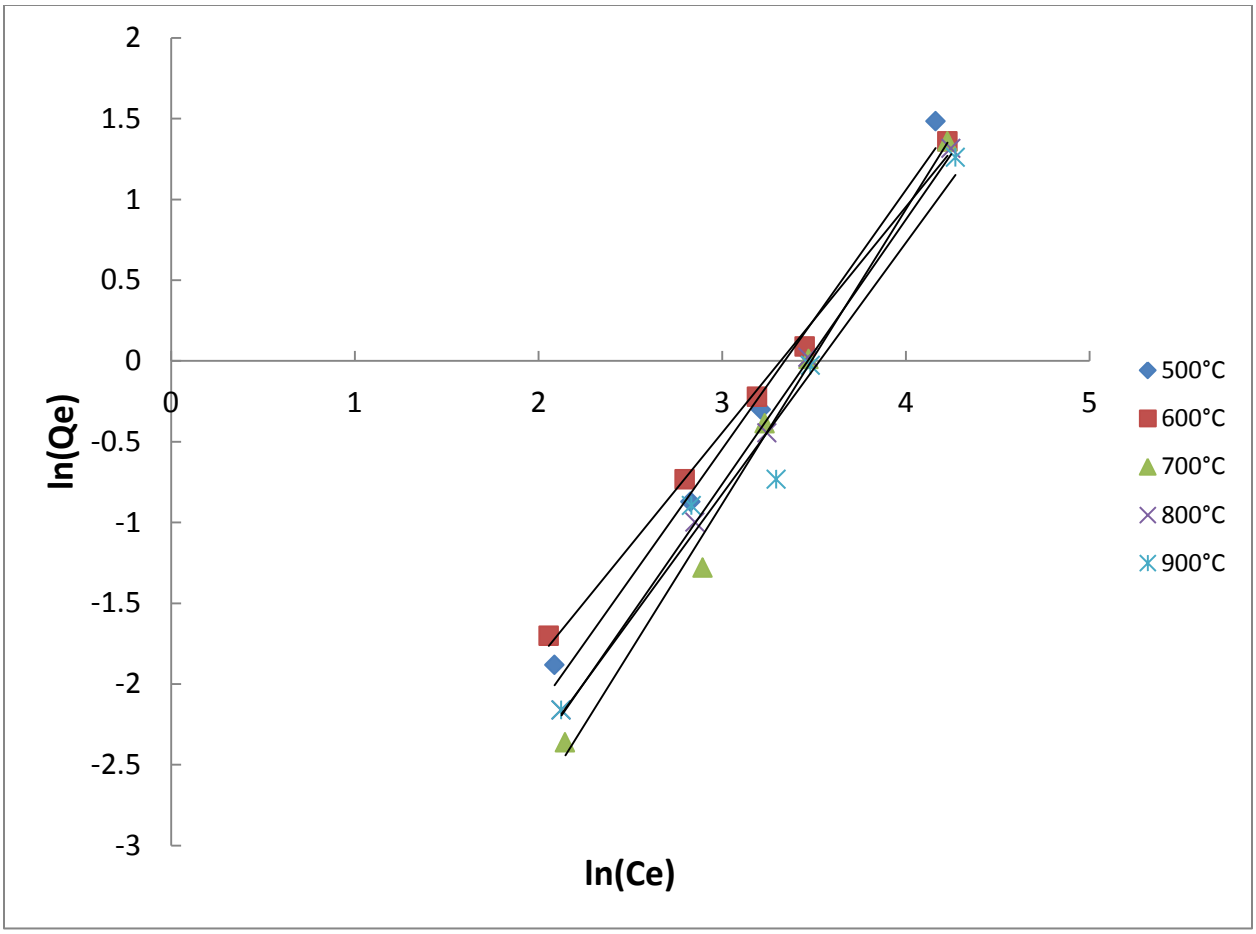

Figure 6.6(d): Freundlich Isotherm for C-HA = 90:10

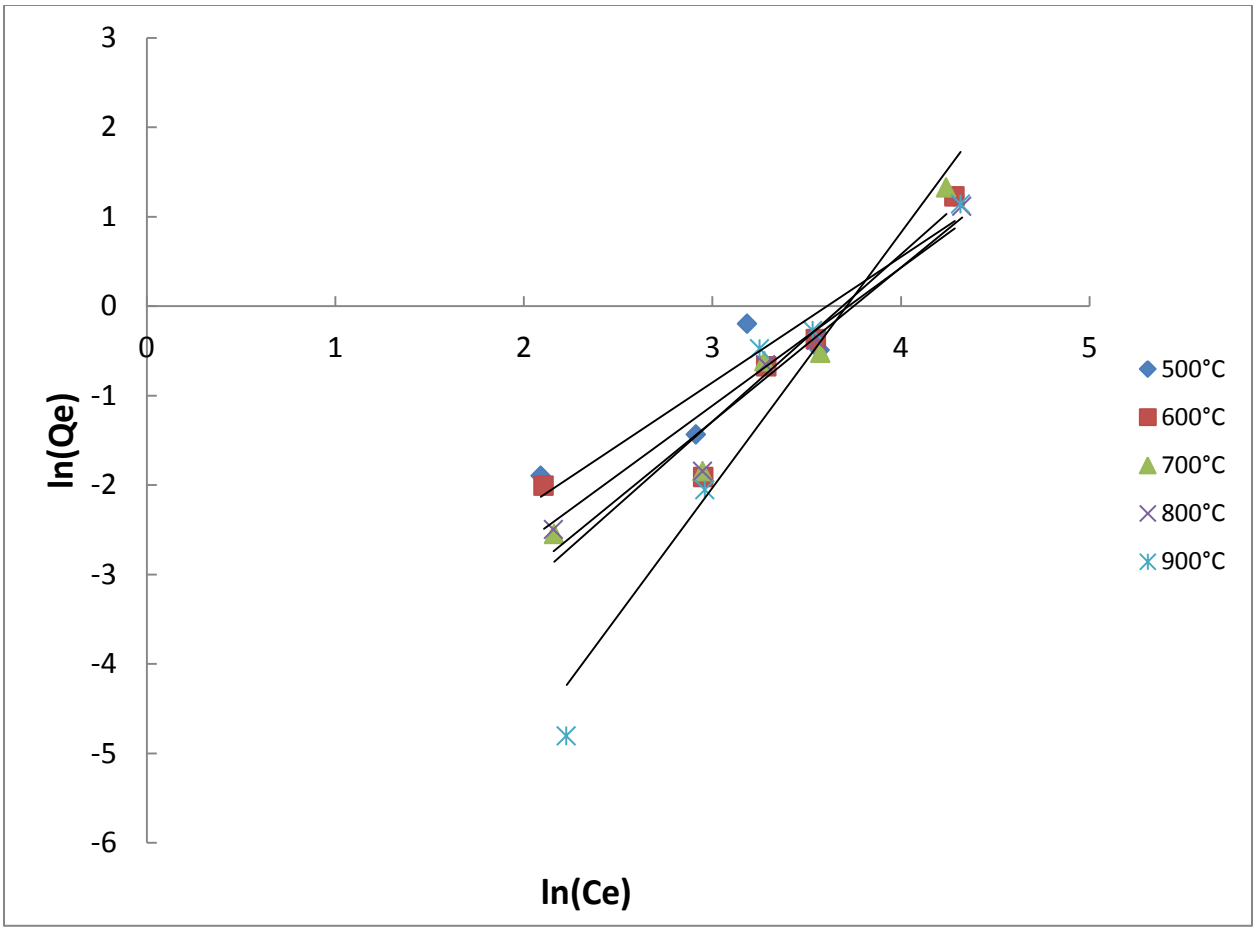

Figure 6.6(e): Freundlich Isotherm for C-HA = 100:0

Figure 6.6: Freundlich Isotherm for C-HA adsorbent

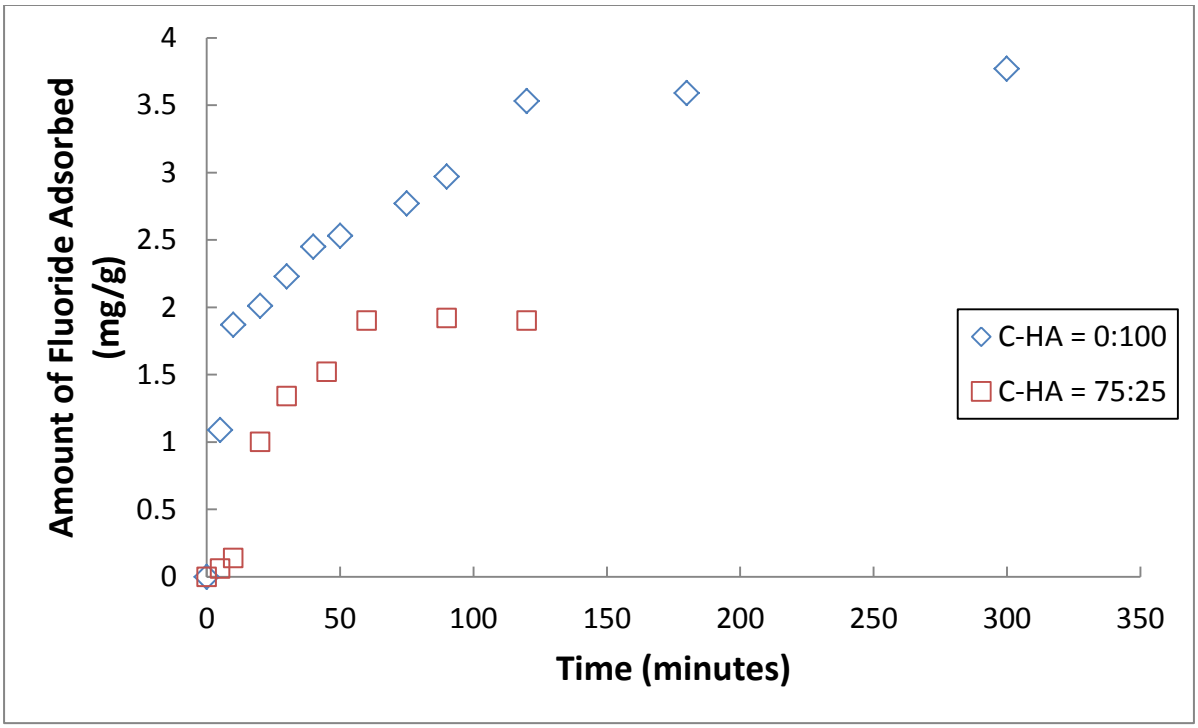

Figure 6.7(a): Amount of fluoride adsorbed with time for two adsorbents (C-HA = 0:100 and C-HA = 75:25)

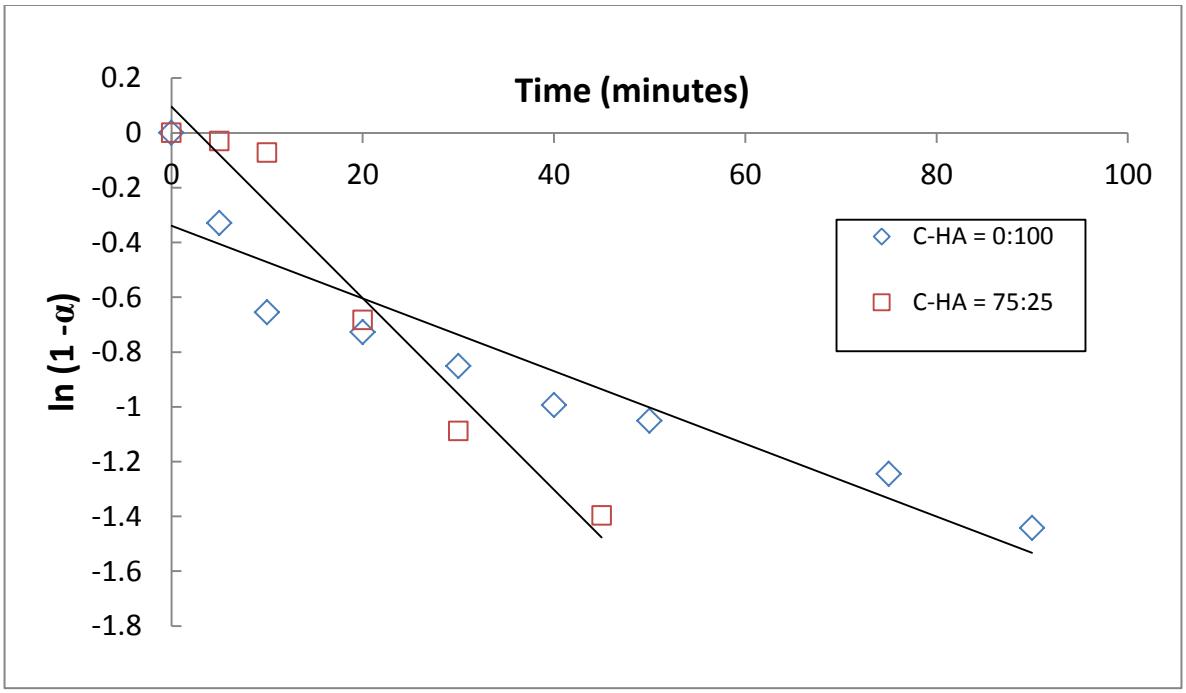

Figure 6.7(b): Particle diffusion modeling for two adsorbents (C-HA = 0:100 and C-HA = 75:25)

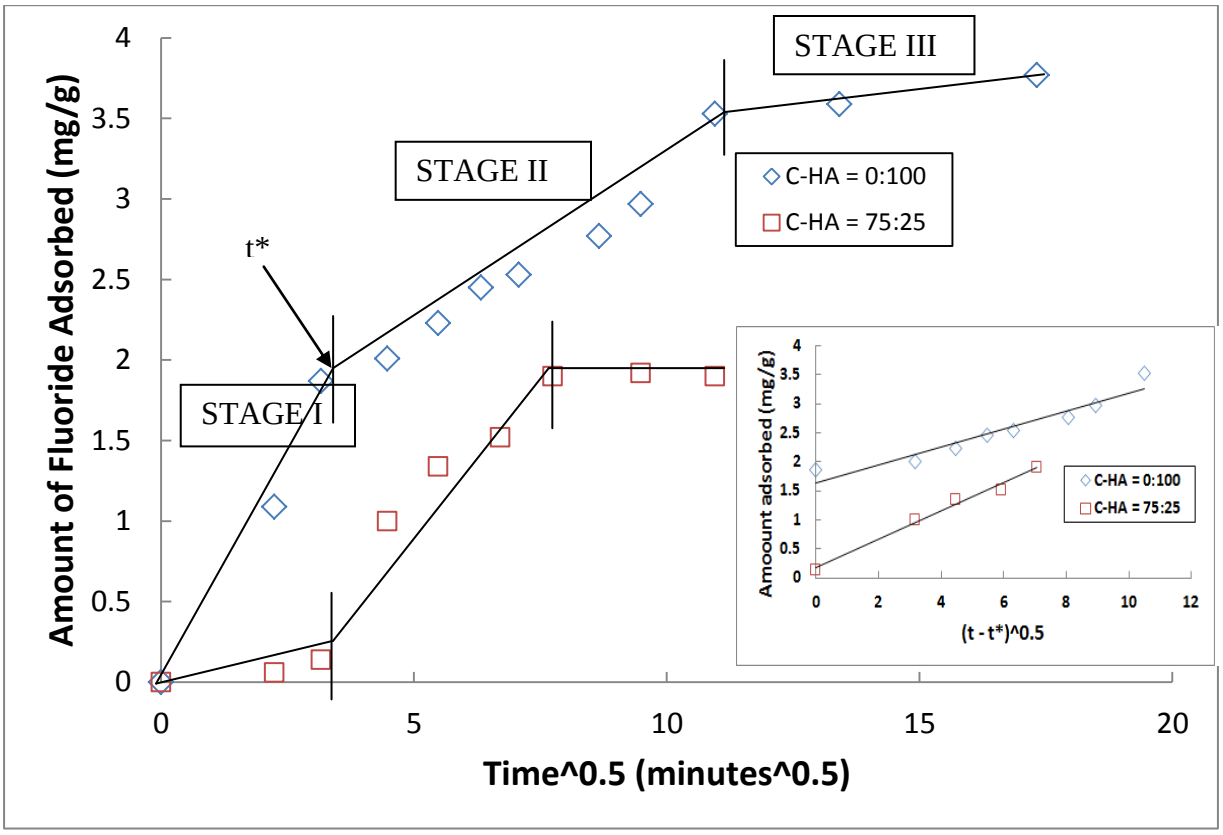

Figure 6.7(c): Intraparticle/pore (Weber and Morris) diffusion modeling for two adsorbents (C-HA = 0:100 and C-HA = 75:25) was carried out on the "Stage II" of the process (see insert, where t* is the time at which the intraparticle diffusion process began).

Figure 6.7: C-HA adsorption kinetics

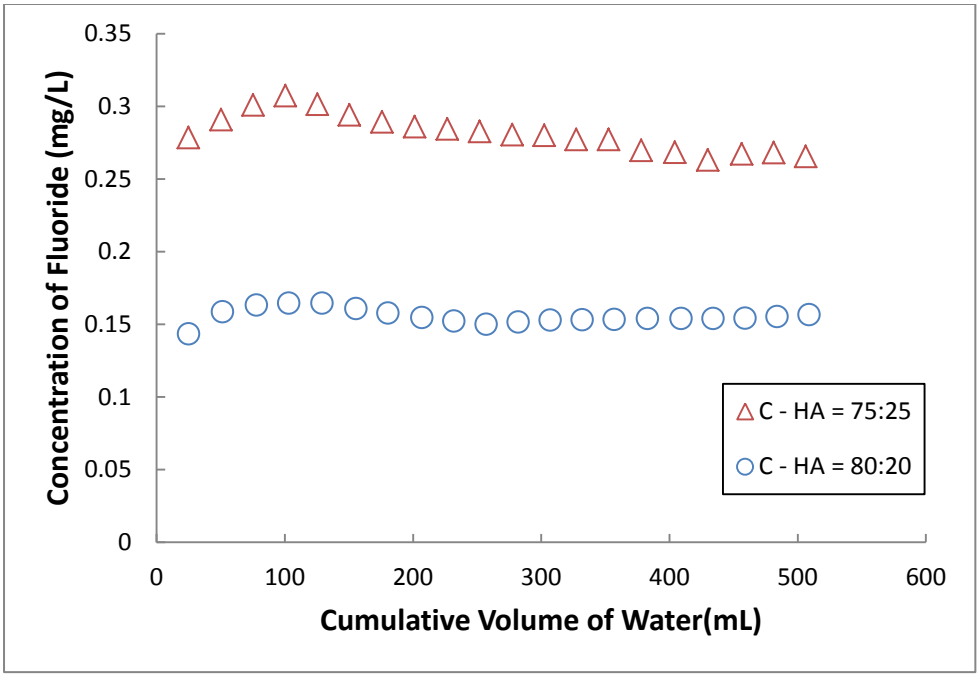

Figure 6.8(a): Change in concentration of fluoride with cumulative volume of water collected for C_o = 2.5mg/L

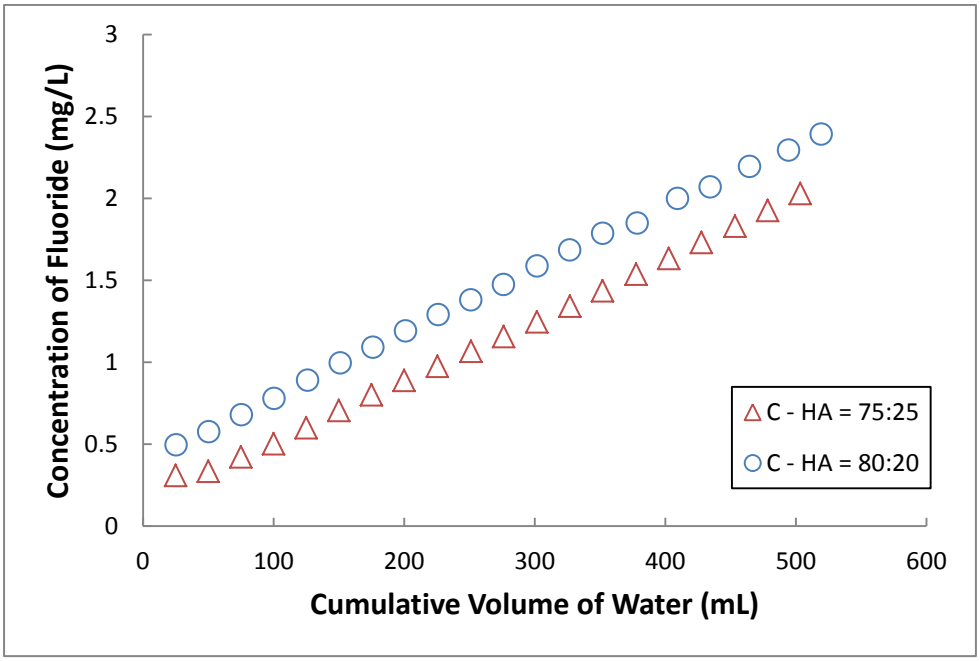

Figure 6.8(b): Change in concentration of fluoride with cumulative volume of water collected for C_o = 20mg/L

Figure 6.8: Change in concentration of fluoride with cumulative volume of water collected for: (a) C_o = 2.5mg/L and (b) C_o = 20mg/L.

Chapter 7

Removal of Fluoride from Water Using the "Buckyweb"

7.1 Introduction

Many different types of adsorbent and methods have been explored as defluorinating agents, and for removal of other chemicals from water, but none have shown more promise than the use of carbon-based materials. Carbon, in the form of activated carbon/charcoal, is the most widely used industrial adsorbent for removal of contaminants and pollutants from gaseous, aqueous, and nonaqueous solutions because of its large surface area, complex porous structure, with associated energetic as well as chemical heterogeneities (Brennan *et al.*, 2001; Colella *et al.*, 1998; Nevskaia *et al.*, 2004; Roque-Malherbe, 2007; Singh *et al.*, 1996).

However, the discovery of carbon nanotubes (CNT) (Iijima, 1991) has attracted the attention of many scientists due to its unique mechanical, electronic, thermal (Ruoff & Lorents, 1995; Salvetat *et al.*, 1999; Xie *et al.*, 2000), physical (large specific surface area), and chemical properties (surface chemistry) (Loh *et al.*, 2010; Tasis *et al.*, 2006). The last two properties are of great significant interest to researchers interested in fundamental studies of the adsorption

characteristics of CNTs (Y.-H. Li *et al.*, 2001; Y. H. Li *et al.*, 2003; Pan & Xing, 2008) and those interested turning it into a filter (Srivastava *et al.*, 2004) to mention a few. The discovery of graphene (Novoselov *et al.*, 2004) also attracted a lot of attention (Geim & Novoselov, 2007). Like CNTs, graphene has a number of unique properties (Castro Neto *et al.*, 2009; Frank *et al.*, 2007; Salvetat *et al.*, 1999) including having a specific surface area that is more than double that of finely divided activated carbon used in water purification (D. Li & Kaner, 2008).

This chapter explores the potential use of a mixture of carbon nanotubes and graphene for removal of fluoride from water. The study was carried out under various conditions in which the concentrations of fluoride, pH of solution and contact time were varied. The equilibrium and kinetic data were fitted to models, and then discussed. The implications of the current results for the potential use of buckywebs in point-of-use water purification technologies were also discussed.

7.2 Experimental

7.2.1 Material Processing

The buckyweb used in this chapter was produced at the Princeton Plasma Physics Laboratory (Princeton, NJ). A schematic of the set-up of the arc-discharge method used in the production of the adsorbent is presented in Figure 7.1. The anode was placed on a positioner, which is free to move forward and backward, through a feedback controller. This ensures that a constant power is maintained by controlling the gap between the anode and cathode. The anode was a graphite rod with a catalyst, usually Y-Ni, embedded. The cathode was a disc-shaped copper metal. Upon

ignition, the high temperature of the discharge causes the consumption (vaporization) of the graphite material, which is then deposited on the cathode in the form of soot. The entire experiment was carried out with an arc voltage of around 20 – 30 V, arc current of around 80 A. The experiment were performed in a chamber filled with helium gas (any other inert gas may be used) at a pressure below atmospheric pressure (Raitses *et al.*, 2008).

7.2.2 Materials Characterization

The buckyweb was imaged using a field emission gun Scanning Transmission Electron Microscope (STEM) (Quanta 200 FE-ESEM, FEI, Hillboro, OR). A high resolution TEM (CM100 FEG-TEM, Philips, Andover, MA) was also used to study the buckyweb structure. The chemical constituents of the buckyweb were characterized after adsorption using the Oxford EDX detector (Oxford Instruments, Oxfordshire, UK) attached to the Quanta 200 FE-ESEM (Hillboro, OR). Although Volotskova *et al.* (Volotskova *et al.*, 2010) has previously shown that the buckyweb structure contains graphene and carbon nanotubes (Figure 7.2), there is no information on the presence of catalyst in the material. The presence of catalyst in the material may have profound effects on the adsorption capacity of the material. There is also a need to conduct EDX analysis to ascertain the capture of fluorine.

7.2.3 Adsorption and Kinetics Studies

Fluoride solution was prepared by either dissolving the appropriate mass of NaF (Fisher Scientific, Fair Lawn, NJ) in deionized water or by serial dilution. The pH of the solution was adjusted to the desired level using 0.1 M NaOH or 0.1 M HNO3 solutions. Moreover, fluoridated

deionized water (i.e. water with fluoride in which the pH has not been adjusted) was also used. The pH of this water was found to be ~ 6.5.

For the batch adsorption experiments, 0.02 g of the adsorbent was added to 30 mL of fluoride solution and agitated using a rotary shaker ("Rugged Rotator", Glas-Col, Terre Haute, IN) at 80 revolution per minute (rpm) for 36 hours. The suspension was then filtered through a 0.22 µm filter (Millex-GP, Millipore Corp, Billerica, MA) attached to a syringe. The equilibrium concentration of fluoride was measured using the Hach fluoride probe (Model 51928 Platinum Series Fluoride Electrode, Hach Company, Loveland, CO) attached to an ion-selective electrode (ISE) meter (sensION™ pH/ISE Meter, Hach Company, Loveland, CO).

For the kinetic experiments, 0.02 g of adsorbent was added to 30 mL of water with an initial fluoride concentration of ~100 mg/L and pH of 6.5. The amount of fluoride removed by the adsorbent was taken at different time intervals until an asymptote was reached. The experiments were carried out with water at temperature of 20 ± 2°C.

7.3 Results and Discussion

7.3.1 Characterization of Adsorbent and the Effect of Inclusions

Figure 7.3a and 7.3b, shows that, in addition to CNTs and graphene, the buckyweb contains traces of the Y-Ni catalysts that were used in the production of the web. The EDX analysis (Figure 7.4a, 7.4b and Table 7.1) also corroborates this. Moreover, the EDX analysis confirms the capture of fluoride ion by the buckyweb. Furthermore, since the fluoride solution was prepared by dissolving NaF in deionized water, the EDX spectrum also reveals that the adsorbent

adsorbed some of the sodium in the water. The silicon found in the spectrum is an artifact of the glass slide on which the treated adsorbent was laid during the analysis.

EDX mapping (Figure 7.4b) revealed that the capture of fluorine, with some areas appearing to have higher density of capture than others. Furthermore, on close inspection, Figure 7.4b suggests that many of the carbon sites have a similar affinity for fluorine and sodium. This suggests that the adsorption mechanism of the material may also be due to precipitation processes. There is also the possibility that the sodium ion may be competing with fluorine ion for adsorption. This point is further elaborated in the next sub-section. The Y-Ni catalyst was sparsely distributed (Figure 7.4b) across the buckyweb samples.

7.3.2 Adsorption Isotherm

The amount of fluoride adsorbed at equilibrium, q_e (mg/g), is defined as the mass of fluoride adsorbed per unit mass of adsorbent. This is given by:

$$q_e = \frac{10^{-3}(C_i - C_e)V}{m} \qquad (1)$$

where C_i (mg/L) is the initial concentration of fluoride, C_e (mg/L) is the concentration of fluoride at equilibrium, V (mL) is the volume of the fluoride solution, and m (mg) is the mass of the adsorbent used.

The variation of the amount of fluoride adsorbed with initial concentration of fluoride for the different pH is presented in Figure 7.5. The amount of fluoride adsorbed generally increased with increasing initial concentration of fluoride. However, the dependency of adsorption capacity on pH of the solution is a strong function of the initial concentration of fluoride. At an initial

concentration of fluoride less than ~ 38 mg/L, the adsorption capacity of the material followed the trend (from highest to lowest): pH 6.5 > pH 3 > pH 5 > pH 7 > pH 11. However, at an initial concentration of fluoride greater than ~ 43 mg/L, the adsorption capacity followed a slightly different trend of: pH 6.5 > pH 11 > pH 3 > pH 5 > pH 7. The major difference in the trend is the behavior of the adsorbent, in a solution with pH value of 11, between fluoride concentrations of 38 – 43 mg/L. The trends observed may be explained in terms of what is known as the isoelectric point (IEP). The IEP may be defined as the pH at which the surface of the adsorbent carries no net charge. The IEP of carbon is usually around the neutral pH. When a solution is at a pH below the IEP, the net charge of the adsorbent surface is positive which is favorable for removal of negatively charged ion (anions), such as fluorine, from water. The farther away from the IEP, the higher the surface charge density. This may explain why in general, the adsorption capacity of buckyweb followed the pattern: pH = 3 > pH = 5 > pH = 7. It is important to re-state that, while the other solutions were adjusted to the desired pH using 0.1 M NaOH or 0.1 M HNO3 solutions, the solution with pH = 6.5 was not. This means that it has the least competing ions compared to the other solutions. This, we believe, is one of the reasons that the solution at pH = 6.5 exhibited the highest adsorption capacity over the pH range that was studied.

Furthermore, when a solution is at a pH above the IEP, the net charge of the adsorbent surface is negative and tends to favor the adsorption of positively charged ion (cations), such as the sodium ion, from water. This may explain why the adsorption capacity of the buckyweb is low at low fluoride concentrations for the solution with a pH of 11.

The equilibrium adsorption data (Figure 7.5) were fitted to the Freundlich isotherm. The mathematical representation of the model is giving as:

$$q_e = K_f\, C_e^{1/n} \qquad (2)$$

where $1/n$ and K_f ($mg^{1-1/n}L^{1/n}g^{-1}$) are Freundlich constants related to adsorption intensity and adsorption capacity, respectively.

The linearized form of equation 2 is:

$$\ln(q_e) = \frac{1}{n}\ln(C_e) + \ln(K_f) \qquad (3)$$

The Freundlich constants obtained for the adsorbents treated at different pH values were obtained from the plots of $\ln(q_e)$ versus $\ln(C_e)$ (Figure 7.6). The results are summarized in Table 7.2. They showed that the adsorbent has the highest adsorption intensity (2.7) at pH 11, and the highest affinity of the binding sites (1.2 $mg^{1-1/n}L^{1/n}g^{-1}$) at pH 3. With the exception of the values of K_f obtained for pH 7 and 11, the values of the Freundlich constants (K_f and 1/n) are similar to those observed by Li *et al.* (2003). The correlation coefficient for the fit is between 0.886 – 0.964.

The Langmuir isotherm model was also used (results not shown). However, in general, the model did not provide an adequate fit of the data. It either provided a very low value of correlation coefficient or gave negative values of the Langmuir isotherm, which is physically impossible. We suspect this is so because of the heterogeneous nature of our adsorbent, which violates the fundamental assumption of the Langmuir isotherm that all the adsorption sites have equal affinities for molecules of the adsorbate.

7.3.3 Change in Free Energy

The changes in the free energy of the C-HA adsorbent – fluoride system were obtained from the following equation:

$$\Delta G = -RT\, lnK_o \qquad (4)$$

where ΔG (kJ/mol) is the change in free energy, R (8.314J/mol-K) is the universal gas constant, T (Kelvin) is the absolute temperature and $K_o$is the thermodynamic distribution coefficient for the adsorption process which is determined from the intercept of the plot of $\ln(q_e/C_e)$ against C_e (Khan, 1987) (Figure 7.7). The adsorbent was found to have negative values of free energy for all pH value (Table 7.1). This implies that the adsorption process is spontaneous in nature. This degree of spontaneity, in general, increases as the pH of the solution is decreased, with the exception of pH of 5.

7.3.4 Adsorption Kinetics

Figure 7.8 presents the result of the adsorption kinetics of fluoride onto the buckyweb. The figure also shows the amount of fluoride adsorbed by the material at any given time for a solution of with an initial fluoride concentration of ~ 100 mg/L and a pH value of 6.5. These show that fluoride is rapidly adsorbed onto the adsorbent within the first 180 min. The adsorption process then slows down and only increases by about 6 – 7% in the next 270 min. Two types of models were applied to the adsorption kinetic data in order to understand the adsorption mechanism of the adsorption-adsorbent system, viz: diffusion-based models and reaction-based models. These will be discussed in the next two sections.

7.3.4.1 Diffusion-based models

To understand the adsorption kinetics of the adsorbent, two diffusion based model were explored:

$$\ln(1-\alpha) = -k_p t \qquad (5)$$

$$\mathrm{Q_t} = k_d t^{0.5} \qquad (6)$$

where, α is the fractional attainment of equilibrium, i.e., the ratio of the amount of fluoride ion removed from water at any given time, *t* (min), to that removed from water at equilibrium; Q_t is the amount of fluoride adsorbed at any given time, k_p ($\mathrm{min^{-1}}$) is the particle rate constant and k_d ($\mathrm{mg/g\ min^{½}}$) is the intra particle rate constant.

Equation 5 was developed by Chanda *et al.* (1983) for particle diffusion-controlled adsorption processes, while equation 6, developed by Weber and Morris (1964), is the widely applied intraparticle diffusion equation (Ho, Ng, & McKay, 2000). The values of k_p and k_d (and the correlation coefficient, R^2) obtained from the two fits, Figure 7.9(a) and 7.9(b), respectively are: k_p = 7.8 x 10^{-3} $\mathrm{min^{-1}}$, R^2 = 0.966 and k_d = 288.9 x 10^{-3} mg/g $\mathrm{min^{½}}$, R^2 = 0.988. The similar equal correlation coefficients suggest that there is likelihood that the adsorption process been controlled by both particle and intraparticle (pore) diffusion processes. This means that the adsorption process is not only a surface phenomenon, but also a rate-limiting process by the micro-and-nano porous nature of the adsorbent. Figure 7.9(b) suggests that the adsorption process occurs in two major stages. The first stage is a combination of the bulk diffusion of fluoride ions into the surface of the adsorbent and the intra-particle or pore diffusion processes.

The second stage is the equilibrium adsorption stage. The slope of the first stage of Figure 7.9(b) yields the intraparticle rate constant, k_d .

7.3.4.2 Reaction-based models

Two reaction-based models were fitted to data obtained from the adsorption kinetics experiments, viz: pseudo-first-order reaction and pseudo-second-order reaction model. The Lagergren rate equation is the most widely used rate equation for adsorption of a solute from liquid solution (Ho *et al.*, 2000) and formed the basis from which the pseudo-first-order rate equation is derived. The latter equation may be expressed as (Fan *et al.*, 2003):

$$log(Q_e - Q_t) = logQ_e - K_1 t \qquad (7)$$

where, K_1 (min^{-1}) is the equilibrium rate constant of pseudo-first-order rate adsorption. The constant K_1 can be found from the slope of the plot of $log(Q_e - Q_t)$ against *t* (Figure 7.10(a)).

One of the four linear forms of pseudo-second-order adsorption model (Ho, 2006), is:

$$\frac{1}{Q_e - Q_t} = \frac{1}{Q_e} + K_2 t \qquad (8)$$

where, K_2 (g/mg·min) is the equilibrium rate constant of pseudo-second-order rate adsorption and the other parameters have their usual meanings. The constant K_2 can be found from the slope of the plot of $1/(Q_e - Q_t)$ against *t* (Figure 7.10(b)).

The respective values of K_1 and K_2 (and the correlation coefficients, R^2) obtained from Figure 7.10(a) and 7.10(b), respectively, is 1.5 x 10^3 min^{-1} (R^2 = 0.840) and 4 x 10^{-4} g/mg·min (R^2 =

0.920). This means that the removal of fluoride from water by buckyweb can be described by the pseudo-second-order rate equation. Furthermore, the larger the value of $K_{1,}$ the faster the adsorption rate. Also, the smaller the value of $K_{2,}$ the faster the adsorption rate (Fan *et al.*, 2003).

7.3.6 Implications

The results show that the buckyweb is capable of removing fluoride from water over a wide range of pH. The pH of most natural water, determined by relative concentration of dissolved carbon dioxide, carbonate ions and hydrogen carbonate ions, is around 6 – 8 (Thurman, 1985). However, in some places around the world, the pH of water is much lower or higher than this value. This may be due to a number of factors, one of which is the effect of the rainwater – which is a water with a pH of 4.5 – 5.6 (Charlson & Rodhe, 1982). Another factor is the presence of high levels metallic oxides, largely due to weathering of rocks in natural water, causing the water to have an unusually high alkaline level (Khoury *et al.*, 1985). Therefore, in addition to having to having an adsorbent that is capable of removing fluoride over a wide range of fluoride concentration, it is important for the adsorbent to be able to do so over a wide range of pH values.

The EDX analysis showed that the buckyweb filter adsorbed sodium from water. This implies that the adsorbent may be used, not only as a means of removal of anions (such as fluorine) from water, but can be also be explored in removal/controlling the concentration of cations in water. Future work should look into the removal of other chemical and heavy metal contaminants, such as, arsenic, nitrate, mercury, lead, and halogenated organics, that may be found in water, and are

capable of causing serious health problems, when present beyond the permissible dose and taken for a prolonged period of time (Pradeep & Anshup, 2009).

Adsorption from the liquid phase depends on the system conditions such as initial concentration of fluoride, type and surface area of adsorbent, adsorbent surface chemistry, mass of adsorbent (or solid-liquid ratio), solution pH, ionic strength of solution, contact time, solubility of adsorbate in the solvent, and temperature (Bower & Hatcher, 1967; Chen *et al.*, 2010; Díaz-Nava *et al.*, 2002; Hamdi & Srasra, 2007; Roque-Malherbe, 2007; Sundaram *et al.*, 2008).

One main advantage of the graphene and nanotube filters over other types of filters is the fact that they can be cleaned after use and this can be done by the simple process of ultrasonication and autoclaving (Srivastava *et al.*, 2004). Also, the adsorption capacity and bactericidal properties of the buckyweb may be enhanced through surface functionalization and increasing or decreasing, as the case may be, the isoelectric potential of the material (Boehm, 1994; Holzinger *et al.*, 2001; Lau *et al.*, 1986; J. Li *et al.*, 2005; Quintana *et al.*, 2010). These are clearly some of the challenges for future work.

7.4 Conclusions

The current study of buckyweb material has shown that it can adsorb fluoride from water. The adsorption capacity of the adsorbent increases with increasing fluoride concentration but is dependent on the pH of the solution. The EDX analysis confirmed the removal of fluoride from water. It also confirmed the capture of sodium, which means that the carbon web may be used to remove either positively charge ions and negatively charged ions from water. The Freundlich isotherm model provides a good fit to the experimental data. The kinetic studies revealed that the

uptake of fluoride from water is controlled by both particle and pore diffusion mechanism and follows a pseudo-second-order equation. Negative values of the standard free energy indicate that the buckyweb interaction with fluoride is spontaneous with high affinity for fluoride. Also, the values of the standard free energy suggest that the maximum adsorption is obtained in solutions with pH values of 3.

References

Boehm, H. P. (1994). Some aspects of the surface chemistry of carbon blacks and other carbons. *Carbon, 32*(5), 759-769.

Bower, C. A., & Hatcher, J. T. (1967). Adsorption of Fluoride by Soils and Minerals. *Soil Science, 103*(3), 151-&.

Brennan, J. K., Bandosz, T. J., Thomson, K. T., & Gubbins, K. E. (2001). Water in porous carbons. *Colloids and Surfaces a-Physicochemical and Engineering Aspects, 187*, 539-568.

Castro Neto, A. H., Guinea, F., Peres, N. M. R., Novoselov, K. S., & Geim, A. K. (2009). The electronic properties of graphene. *Reviews of Modern Physics, 81*(1), 109-162.

Charlson, R. J., & Rodhe, H. (1982). Factors Controlling the Acidity of Natural Rainwater. *Nature, 295*(5851), 683-685.

Chen, N., Zhang, Z. Y., Feng, C. P., Sugiura, N., Li, M., & Chen, R. Z. (2010). Fluoride removal from water by granular ceramic adsorption. *Journal of Colloid and Interface Science, 348*(2), 579-584.

Colella, L. S., Armenante, P. M., Kafkewitz, D., Allen, S. J., & Balasundaram, V. (1998). Adsorption isotherms for chlorinated phenols on activated carbons. *Journal of Chemical and Engineering Data, 43*(4), 573-579.

Díaz-Nava, C., Olguín, M. T., & Solache-Ríos, M. (2002). Water Defluoridation by Mexican Heulandite–Clinoptilolite. *Separation Science and Technology, 37*(13), 3109-3128.

Fan, X., Parker, D. J., & Smith, M. D. (2003). Adsorption kinetics of fluoride on low cost materials. *Water Research, 37*(20), 4929-4937.

Frank, I. W., Tanenbaum, D. M., Van der Zande, A. M., & McEuen, P. L. (2007). Mechanical properties of suspended graphene sheets. *Journal of Vacuum Science & Technology B, 25*(6), 2558-2561.

Geim, A. K., & Novoselov, K. S. (2007). The rise of graphene. *Nature Materials, 6*(3), 183-191.

Hamdi, N., & Srasra, E. (2007). Removal of fluoride from acidic wastewater by clay mineral: Effect of solid–liquid ratios. *Desalination, 206*(1-3), 238-244.

Ho, Y. S. (2006). Second-order kinetic model for the sorption of cadmium onto tree fern: A comparison of linear and non-linear methods. *Water Research, 40*(1), 119-125.

Ho, Y. S., Ng, J. C. Y., & Mckay, G. (2000). Kinetics of pollutant sorption by biosorbents: Review. *Separation and Purification Methods, 29*(2), 189-232.

Holzinger, M., Vostrowsky, O., Hirsch, A., Hennrich, F., Kappes, M., Weiss, R., & Jellen, F. (2001). Sidewall functionalization of carbon nanotubes. *Angewandte Chemie-International Edition, 40*(21), 4002-+.

Iijima, S. (1991). Helical Microtubules of Graphitic Carbon. *Nature, 354*(6348), 56-58.

Khoury, H. N., Salameh, E., & Abduljaber, Q. (1985). Characteristics of an Unusual Highly Alkaline Water from the Maqarin Area, Northern Jordan. *Journal of Hydrology, 81*(1-2), 79-91.

Lau, A. C., Furlong, D. N., Healy, T. W., & Grieser, F. (1986). The Electrokinetic Properties of Carbon-Black and Graphitized Carbon-Black Aqueous Colloids. *Colloids and Surfaces, 18*(1), 93-104.

Li, D., & Kaner, R. B. (2008). Materials science - Graphene-based materials. *Science, 320*(5880), 1170-1171.

Li, J., Vergne, M., Mowles, E., Zhong, W., Hercules, D., & Lukehart, C. (2005). Surface functionalization and characterization of graphitic carbon nanofibers (GCNFs). *Carbon, 43*(14), 2883-2893.

Li, Y.-H., Wang, S., Cao, A., Zhao, D., Zhang, X., Xu, C., Luan, Z., Ruan, D., Liang, J., et al. (2001). Adsorption of fluoride from water by amorphous alumina supported on carbon nanotubes. *Chemical Physics Letters, 350*(5-6), 412-416.

Li, Y. H., Wang, S., Zhang, X., Wei, J., Xu, C., Luan, Z., Wu, D., & Wei, B. (2003). Removal of fluoride from water by carbon nanotube supported alumina. *Environmental Technology, 24*(3), 391-398.

Loh, K. P., Bao, Q. L., Ang, P. K., & Yang, J. X. (2010). The chemistry of graphene. *Journal of Materials Chemistry, 20*(12), 2277-2289.

Nevskaia, D. M., Castillejos-Lopez, E., Munoz, V., & Guerrero-Ruiz, A. (2004). Adsorption of aromatic compounds from water by treated carbon materials. *Environmental Science & Technology, 38*(21), 5786-5796.

Novoselov, K. S., Geim, A. K., Morozov, S. V., Jiang, D., Zhang, Y., Dubonos, S. V., Grigorieva, I. V., & Firsov, A. A. (2004). Electric field effect in atomically thin carbon films. *Science, 306*(5696), 666-669.

Pan, B., & Xing, B. S. (2008). Adsorption Mechanisms of Organic Chemicals on Carbon Nanotubes. *Environmental Science & Technology, 42*(24), 9005-9013.

Pradeep, T., & Anshup. (2009). Noble metal nanoparticles for water purification: A critical review. *Thin Solid Films, 517*(24), 6441-6478.

Quintana, M., Spyrou, K., Grzelczak, M., Browne, W. R., Rudolf, P., & Prato, M. (2010). Functionalization of Graphenevia1,3-Dipolar Cycloaddition. *Acs Nano, 4*(6), 3527-3533.

Raitses, Y., Skinner, C. H., Jiang, F., & Duffy, T. S. (2008). Raman spectroscopy of carbon dust samples from NSTX. *Journal of Nuclear Materials, 375*(3), 365-369.

Roque-Malherbe, R. M. A. (2007). *Adsorption and diffusion in nanoporous materials*. Boca Raton: CRC Press.

Ruoff, R. S., & Lorents, D. C. (1995). Mechanical and Thermal-Properties of Carbon Nanotubes. *Carbon, 33*(7), 925-930.

Salvetat, J. P., Bonard, J. M., Thomson, N. H., Kulik, A. J., Forro, L., Benoit, W., & Zuppiroli, L. (1999). Mechanical properties of carbon nanotubes. *Applied Physics a-Materials Science & Processing, 69*(3), 255-260.

Singh, B., Madhusudhanan, S., Dubey, V., Nath, R., & Rao, N. B. S. N. (1996). Active carbon for removal of toxic chemicals from contaminated water. *Carbon, 34*(3), 327-330.

Srivastava, A., Srivastava, O. N., Talapatra, S., Vajtai, R., & Ajayan, P. M. (2004). Carbon nanotube filters. *Nature Materials, 3*(9), 610-614.

Sundaram, C. S., Viswanathan, N., & Meenakshi, S. (2008). Defluoridation chemistry of synthetic hydroxyapatite at nano scale: Equilibrium and kinetic studies. *Journal of Hazardous Materials, 155*(1-2), 206-215.

Tasis, D., Tagmatarchis, N., Bianco, A., & Prato, M. (2006). Chemistry of carbon nanotubes. *Chemical Reviews, 106*(3), 1105-1136.

Thurman, E. M. (1985). *Organic geochemistry of natural waters*. Dordrecht ; Boston Hingham, MA, USA: M. Nijhoff ; Distributors for the U.S. and Canada, Kluwer Academic.

Volotskova, O., Levchenko, I., Shashurin, A., Raitses, Y., Ostrikov, K., & Keidar, M. (2010). Single-step synthesis and magnetic separation of graphene and carbon nanotubes in arc discharge plasmas. *Nanoscale, 2*(10), 2281-2285.

Xie, S. S., Li, W. Z., Pan, Z. W., Chang, B. H., & Sun, L. F. (2000). Mechanical and physical properties on carbon nanotube. *Journal of Physics and Chemistry of Solids, 61*(7), 1153-1158.

Element	Weight (%)	Atomic (%)
C	76.18	88.01
O	7.22	6.26
F	1.7	1.24
Na	1.02	0.61
Al	0.11	0.06
Si	1.42	0.70
S	0.68	0.30
Cl	0.37	0.30
K	0.75	0.26
Ti	0.21	0.06
Ni	9.13	2.16
Y	1.23	0.19

Table 7.1: Chemical composition of the treated buckyweb

pH	Actual pH	Freundlich isotherm parameter			Δ*G* (kJ/mol)
		R^2	1/n	K_f	
3	2.999 ± 0.004	0.920	0.699	1.222	- 16.135
5	4.996 ± 0.006	0.964	1.414	0.036	-11.221
6.5	6.571 ± 0.228	0.886	0.746	1.083	-15.784
7	7.190 ± 0.140	0.956	1.668	0.001	-8.729
11	11.016 ± 0.021	0.900	2.685	0.001	-4.993

Table 7.2: The Freundlich Isotherm parameters and Gibbs free energy obtained for the adsorbent treated with different pH

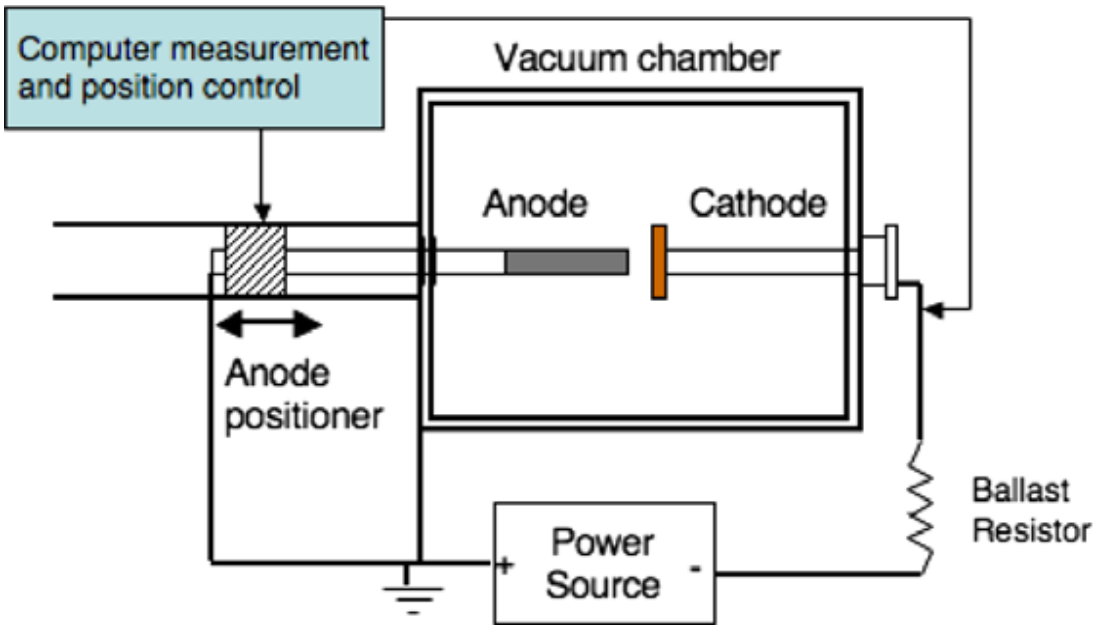

Figure 7.1: Schematics of set up used for making buckyweb (Raitses *et al.*, 2008)

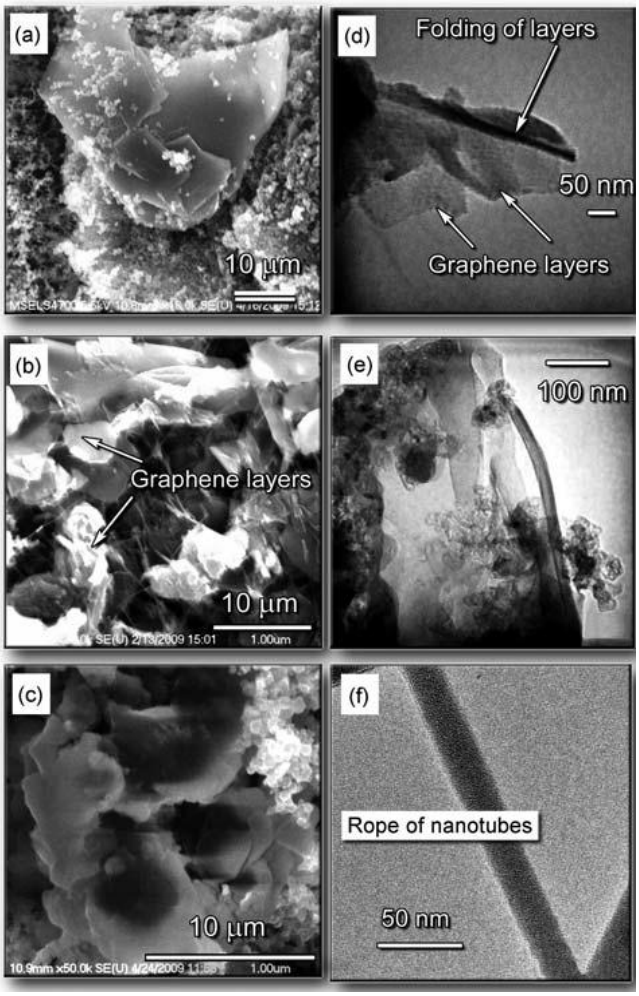

Figure 7.2: Representative SEM and TEM images of various carbon deposits collected in different collection areas. (a–c) Low-, medium-, and high magnification SEM images of the samples containing graphene layers, collected from the top and side surfaces of the magnet. (d, e) TEM image of folded graphene layers in the carbon sample collected from the top and side surfaces of the magnet, respectively. (f) TEM image of the sample containing carbon nanotube bundles

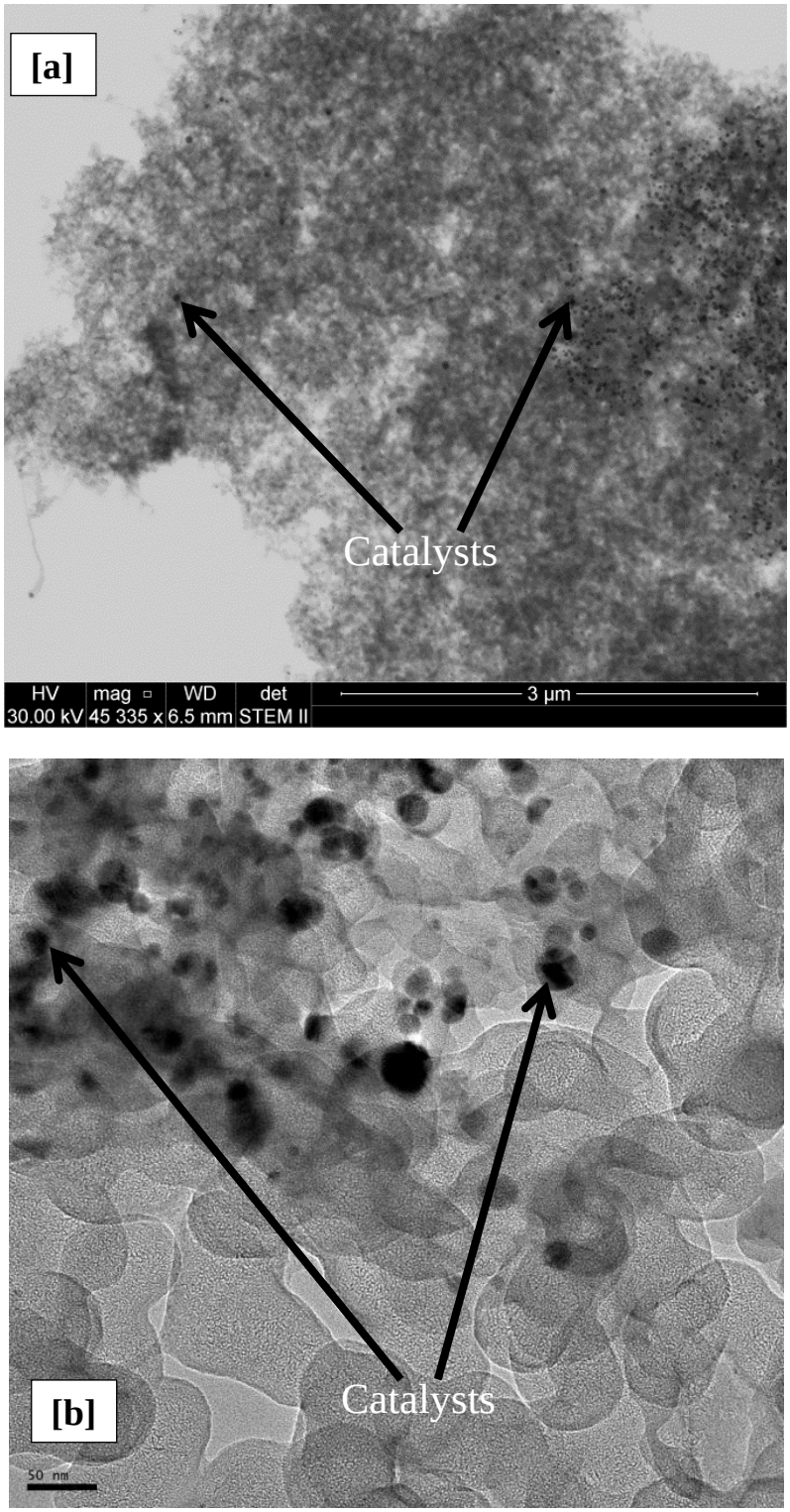

Figure 7.3: STEM and TEM micrograph of buckyweb: [a] STEM image showing ropes of carbon and catalyst deposits (scale bar = 3 µm), and [b] TEM image showing graphene sheets and catalyst deposits (scale bar = 50 nm)

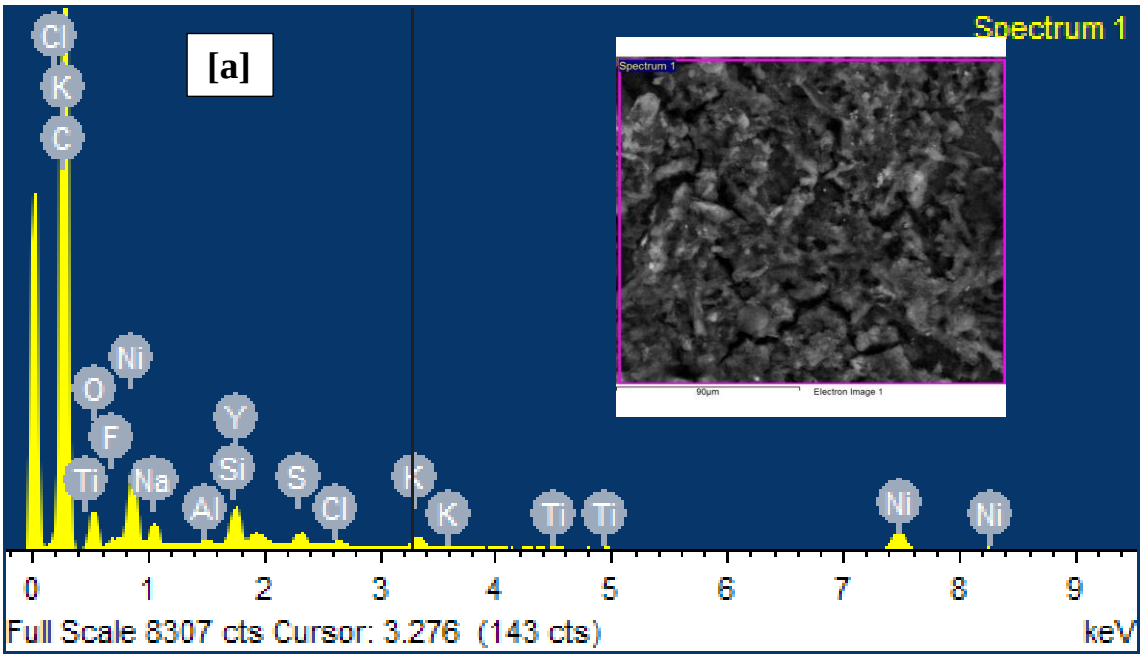

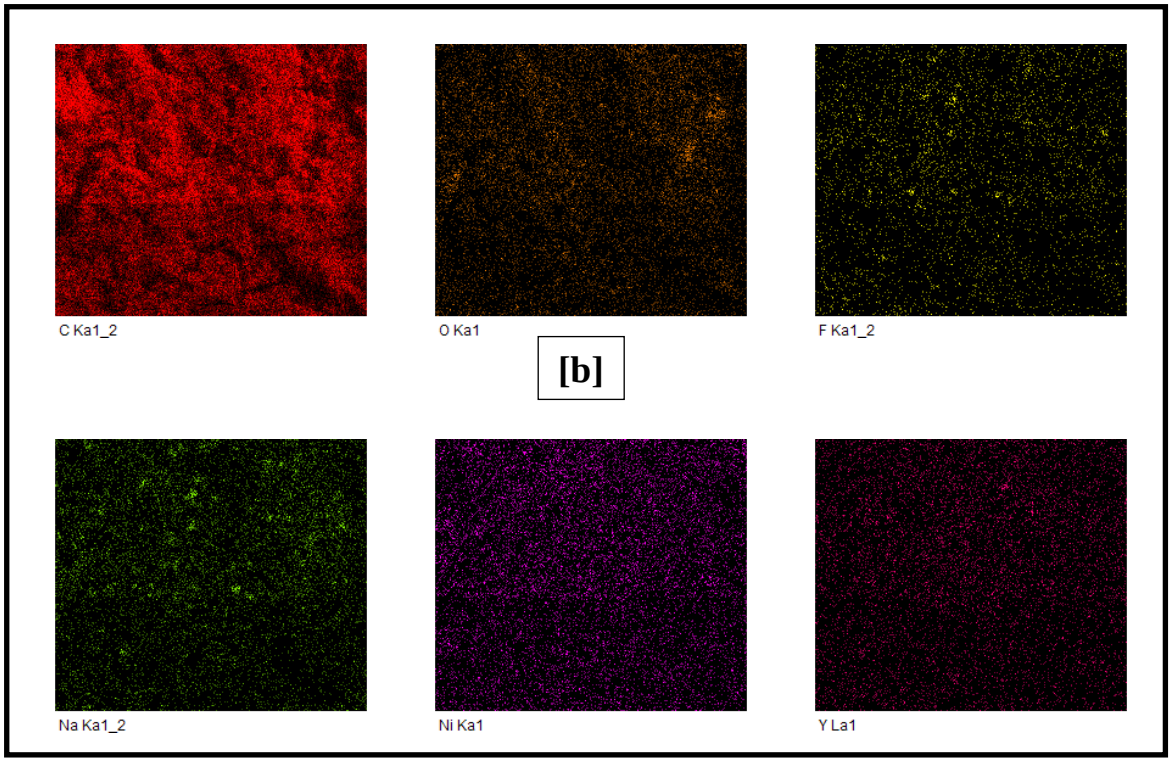

Figure 7.4: Chemical composition analysis: [a] EDX spectrum of buckyweb (Insert: Environmental Scanning Electron Image of the treated web) and [b] EDX mapping of Carbon, Oxygen, Fluorine, Sodium, Nickel and Yttrium (from top to bottom)

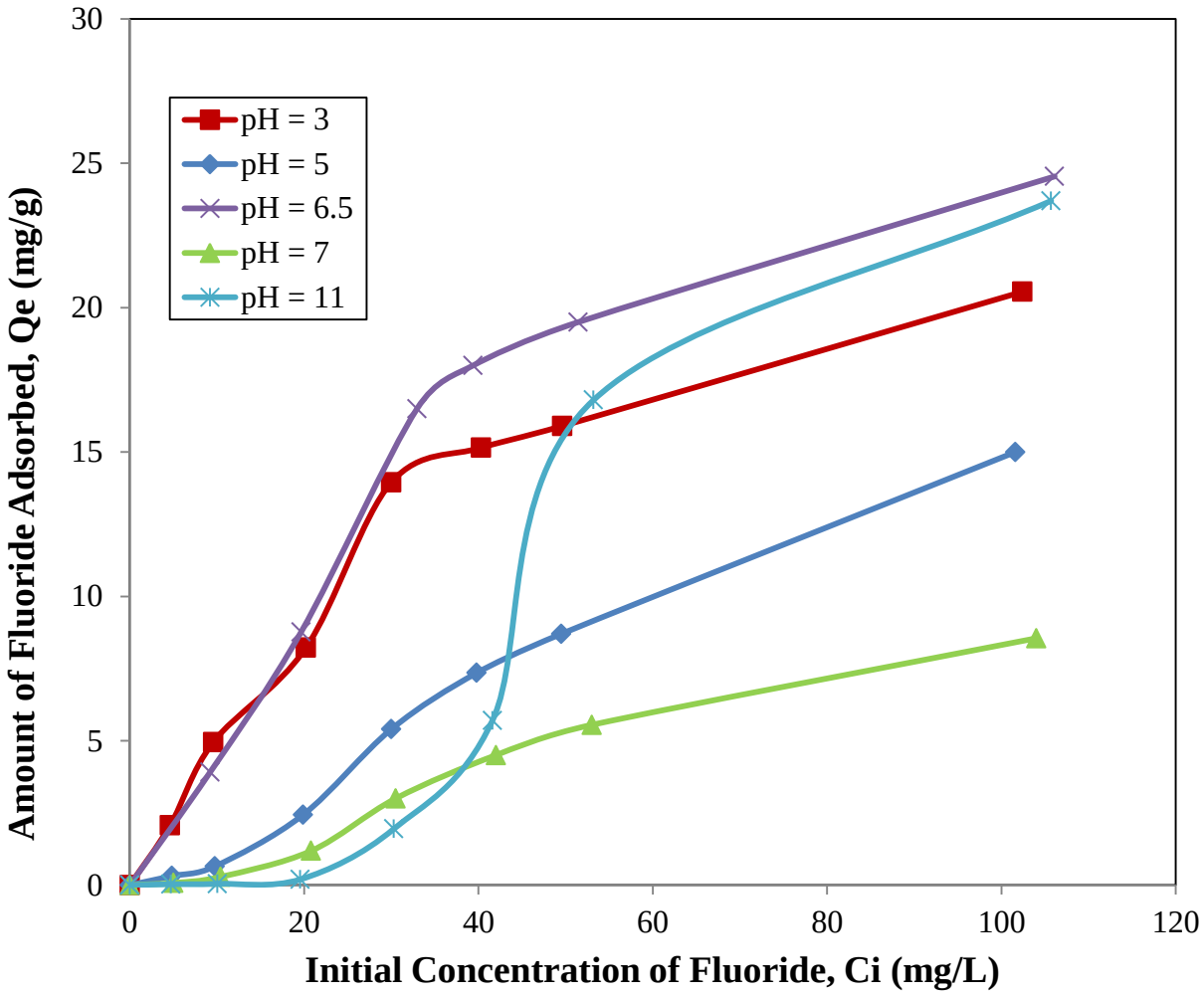

Figure 7.5: Variation of amount of fluoride adsorbed as a function of pH values

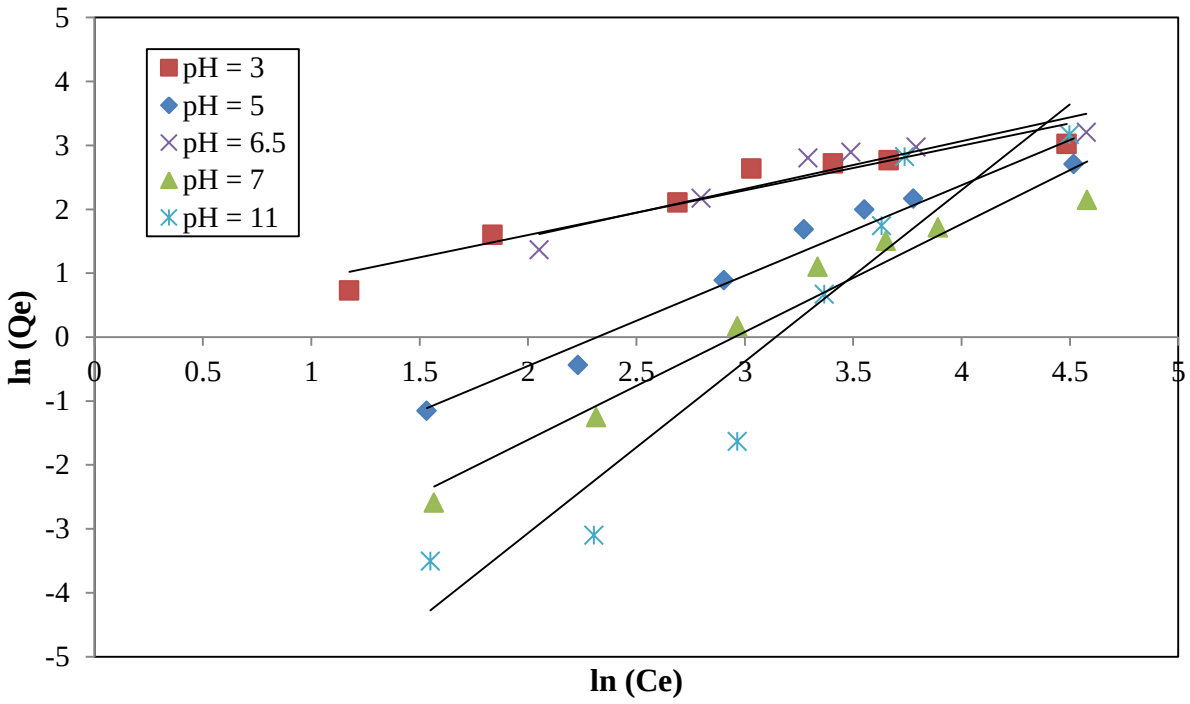

Figure 7.6: Freundlich Isotherm for the fluoride adsorption on buckyweb

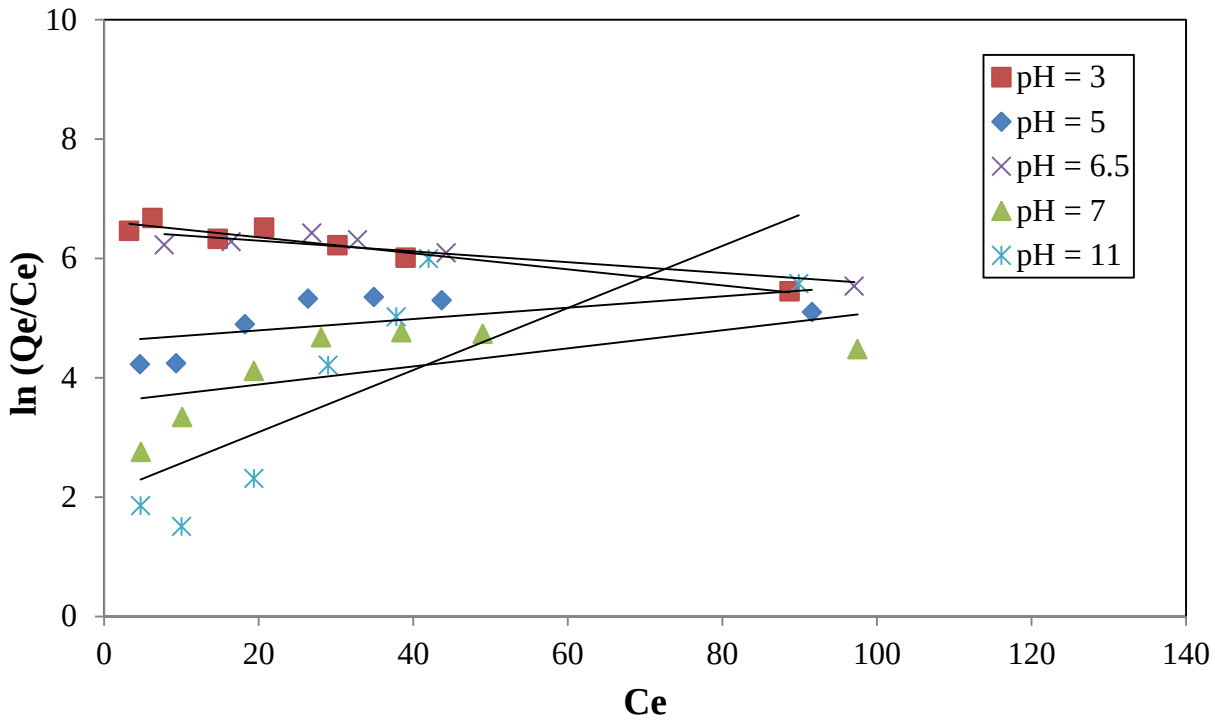

Figure 7.7: The intercept of the plot of ln(Qe/Ce) against Ce is an indication of the thermodynamic distribution coefficient of the adsorption process (Khan, 1987)

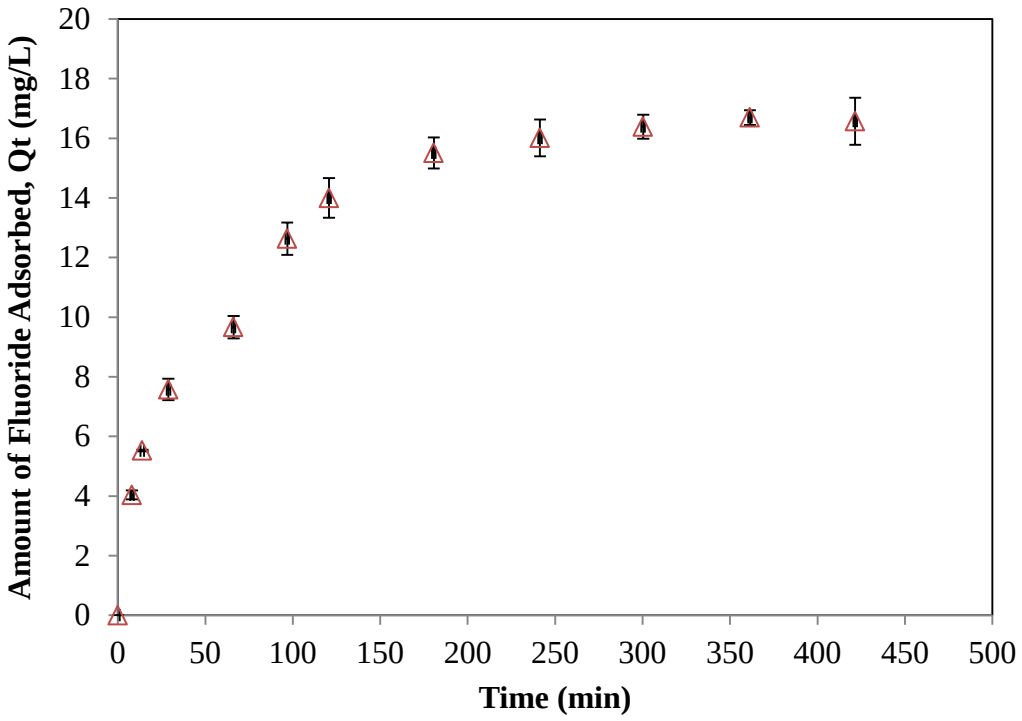

Figure 7.8: Amount of fluoride adsorbed with time on buckyweb at pH 6.5

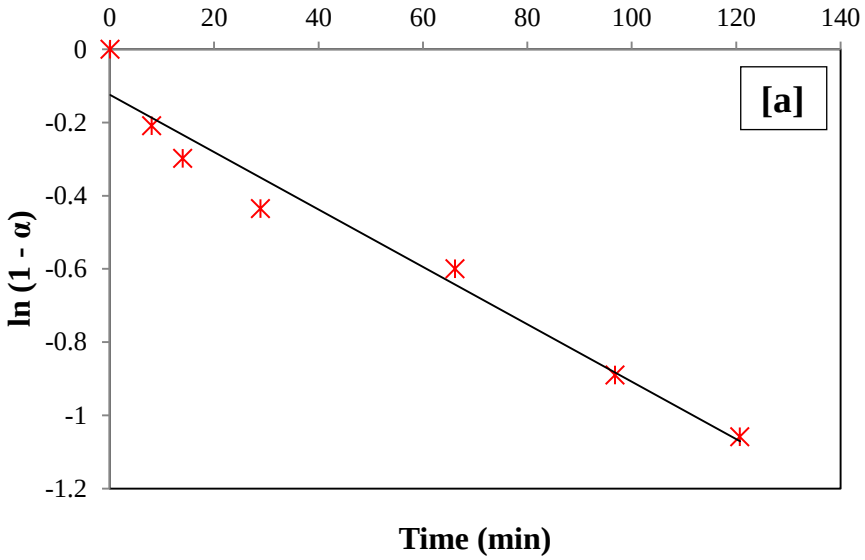

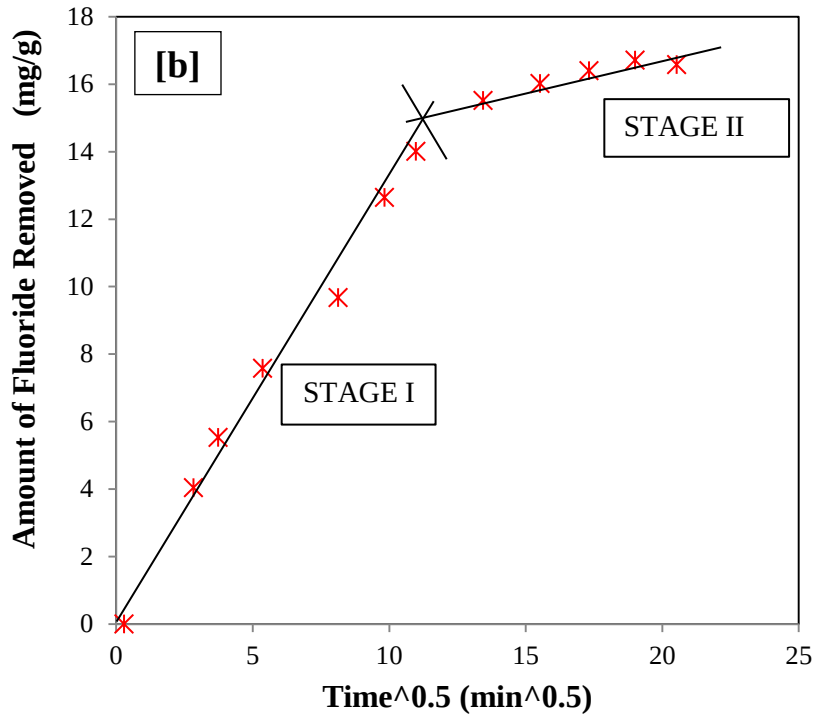

Figure 7.9: Diffusion-based models: [a] Particle diffusion modeling and [b] Intraparticle/pore diffusion modeling for the buckyweb at pH 6.5

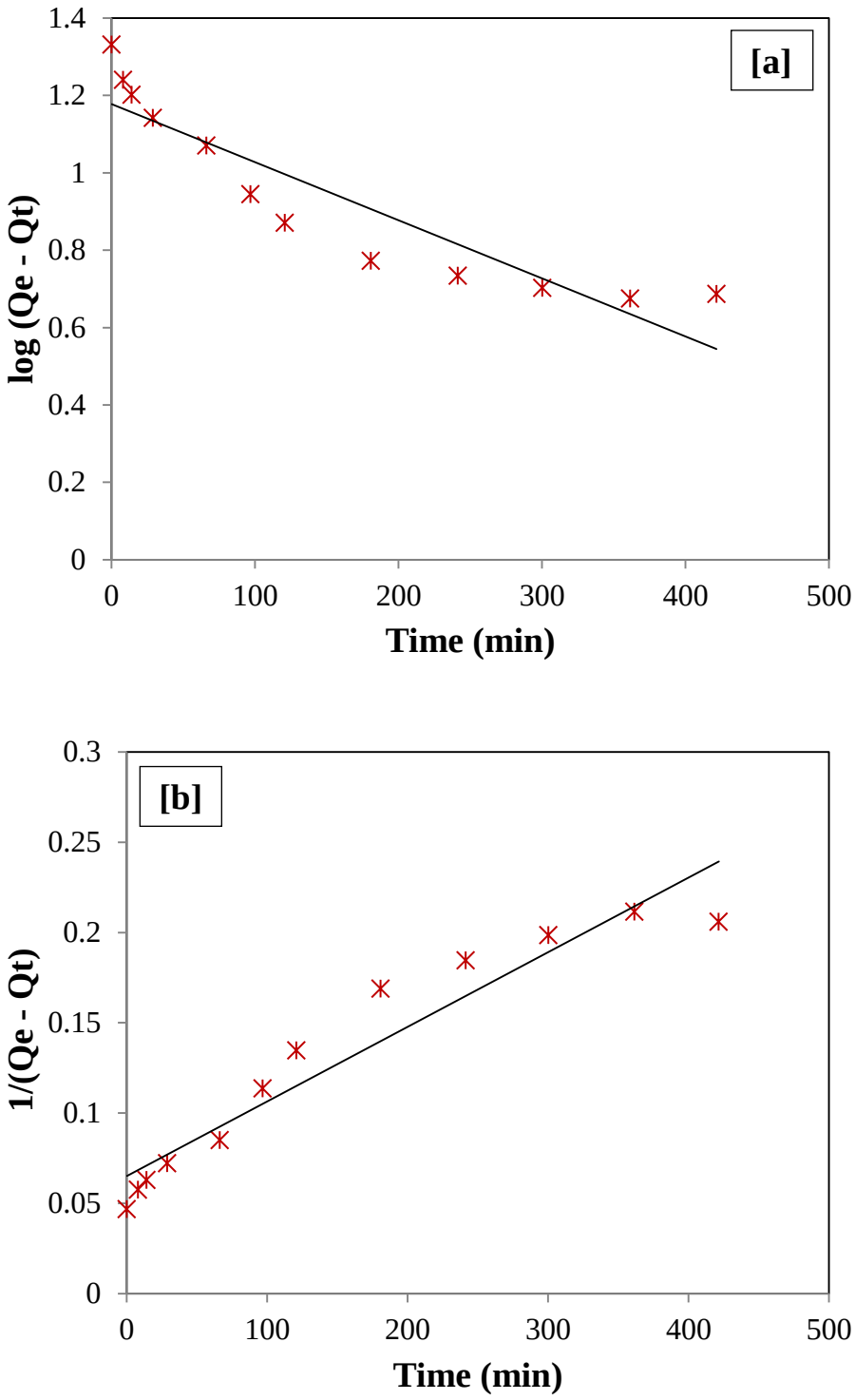

Figure 7.10: Reaction-based models: [a] Pseudo-first-order kinetic model and [b] Pseudo-second-order model of fluoride adsorption kinetics on the buckyweb at pH 6.5

Chapter 8

Concluding Remarks and Suggestions for Future Work

8.1 Concluding Remarks

This dissertation presents the results of an experimental and theoretical computation study of point-of-use water filters. These include: porous clay-based ceramics; porous clay-hydroxyapatite composite and the "buckyweb" structures. While the first material is capable of removing bacteria and some viruses from water, the last two materials are capable of removing both bacteria and negatively charged ions from water. The salient conclusions arising from this study are summarized below:

1. The porosity in the frustum-shaped ceramic water filters ranges in size from the nano- to the micron-scale. The effective porosity also increases with the volume fraction of sawdust. The pore sizes are also in a range in which they can occlude microbial pathogens and viruses.

2. Flow through the CWFs is well described by Darcy's law. This can be used to describe the volumetric flow of water through the filters, and to extract the effective permeability. The intrinsic permeability found using this model compares well with that from the Katz-Thompson

method, using the mercury intrusion data. In general, for the same pressure head, the flow through the filter increases with increasing porosity and permeability. However, the materials tortuosity decreases with increasing porosity and permeability.

3. Atomic force microscopy has been used to quantify the adhesion forces and adhesion energies for bi-material pairs that are relevant to water purification with porous clay-based ceramics. Of the three metals studied colloidal silver exhibits the highest adhesion to the clay ceramic surfaces. However, pure silver has the highest adhesion to *E.coli*. Considering potential issues of cost, colloidal silver is a very good choice for the impregnation of the ceramic water filter with particles that can disinfect water.

4. The compressive strength, flexural strength and fracture toughness of the porous ceramics decreased with increasing porosity. This is attributed largely to stress concentration effects. However, the elastic modulus and hardness of the material, determined from nanoindentation studies, were strongly influenced by the average pore size rather than the materials porosity. The material exhibited limited fracture toughness and toughening was attributed to the crack bridging mechanism. This toughening was predicted by small- and large-scale bridging models.

5. Finite element simulations of possible filter geometries suggest that the current frustum-shaped filter is a robust design and capable of withstanding stresses better than inverted frustum and cylindrical shaped design. However, the more uniformly thick a frustum shaped filter is, the better. The wider the receptacle (or support) is, the better. Also, the closer the support is to the side (or surface) of the filter, the better. Finally, if a porous ceramic filter has to be fabricated to be “curvy”, the more ellipsoidal the shape is, the lower the overall levels of stress concentration.

6. A new material, clay-hydroxyapatite (C-HA) composite, was developed for the removal of both fluoride and bacteria from water. The defluoridation associated with varying clay to hydroxyapatite ratios and sintering temperature was investigated in terms of concentration of fluoride and contact time. The adsorption capacities of the C-HA adsorbent were found to increase with increasing hydroxyapatite (HA) content and decreasing sintering temperature. The adsorbent adsorption capacity increased with increasing concentration of fluoride and was well modeled by the Freundlich adsorption isotherm. The changes in the free energy revealed that the adsorption process occurred spontaneously. Also, the adsorption of fluoride ion on the C-HA occurs through intraparticle (pore) diffusion mechanism. A proof-of-concept study on frustum-shaped C-HA filter revealed that the filters are capable of effectively removing fluoride from water with initially low concentration of fluoride. The filtration experiments on the device also suggest that the porous C-HA adsorbent is also capable of removing bacteria from water.

7. A “buckyweb” foam, comprising carbon nanotubes and graphene, was studied for its potential use in defluoridation. The adsorption capacity of the buckyweb was studied as function of fluoride concentration, contact time and solution pH. The adsorption capacity of the material increased with initial fluoride concentration. The kinetic (or contact time) studies revealed that the adsorption process is controlled by both particle and pore diffusion mechanism and follows a pseudo-second-order equation. However, there was no clear relationship between the adsorption capacity of the adsorbent and the pH solution. The presence of catalyst particles and the variations in the carbon nanotube – graphene mixture ratio are the most probable explanation. The results suggest that the buckyweb foams have the potential for future application in fluoride filters.

8.2 Suggestions for Future Work

To extend the work presented in this dissertation, the following possible future directions are suggested:

1. The clay used in this dissertation is the redart clay (Cedar Heights Redart Airfloated Clay, Pittsburgh, PA). Future work should investigate the effect of different clay types on the flow properties, filtration efficiencies, adhesion properties and mechanical properties of compositional different filters. Also, the effect of different clay types on the adsorption capacity of clay – hydroxyapatite composite should be studied. The C-HA composite was found to have much better adsorption capacity for fluoride at low sintering temperature. Future generations of C-HA filters may be made by other processing techniques such as high pressure compaction or sol-gel processing.

2. The mechanical properties of the filters presented in this dissertation were obtained in the dry condition. Although the ceramic filters are often transported under such dry conditions, the filters are hydrated during operation. Therefore, future research should investigate the strengths of the porous clay-based ceramics under hydrated conditions. The strengths should also be studied at different levels of saturation, and compared to the results obtained from this dissertation. The adhesion studies should also be carried out under hydrated conditions. The result of the adhesion study should be compared with results obtained from shear assay methods and finite element modeling. The effects of different pore forming agents such as flour, rice husks and tea leaves should also be studied.

3. The ceramic water filter should be toughened to resist cracking. This may be done by making clay-based composites from a mixture of clay and cement material and/or metals. Also, future

filters may be made by mixing clays with different particle sizes together. This may lead to toughening by self-bridging. Toughening may also be achieved by the using fibers that are capable of withstanding high sintering temperatures without disintegrating. The filtration and leaching characteristics of the resulting filters should be elucidated.

4. One drawback of the C-HA filter is that it increases the pH of water. Such water should be tested for the potential (short and long term) effects on human health, if any. The rise in the pH of water is mainly due to the hydroxyl ions of the hydroxyapatite. This may be controlled by doping the composite with metallic oxides, such as sodium oxide (Na_2O). Juices of some citrus fruits, such as lime, may also be used to control the pH of the pre-filtrate and filtrate. The efficacy of the C-HA filter over a long period of time ($\geq$ 2 years) should also be studied.

5. Buckywebs with different carbon nanotube to graphene ratios and also webs of high purity (i.e. webs composed entirely of carbon nanotube or graphene only) should be made and rigorously tested against water pre-contaminated with different concentration of fluorine, nitrate and arsenic (the three most common chemical contaminants in water). A buckyweb filter device should be made and studied. The long term leaching and filtration characteristics should also be studied using a combination of experiments and models.